



Delft University of Technology

On-Chip Solutions for Future THz Imaging Spectrometers

Pascual Laguna, A.

DOI

[10.4233/uuid:512da833-dc9d-4301-b566-35243d2f1f9b](https://doi.org/10.4233/uuid:512da833-dc9d-4301-b566-35243d2f1f9b)

Publication date

2022

Document Version

Final published version

Citation (APA)

Pascual Laguna, A. (2022). *On-Chip Solutions for Future THz Imaging Spectrometers*. [Dissertation (TU Delft), Delft University of Technology]. <https://doi.org/10.4233/uuid:512da833-dc9d-4301-b566-35243d2f1f9b>

Important note

To cite this publication, please use the final published version (if applicable).
Please check the document version above.

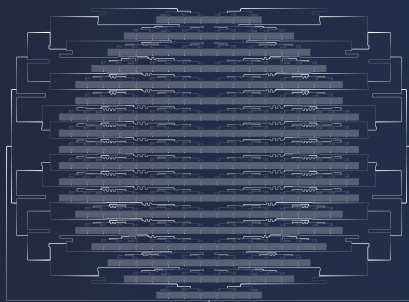
Copyright

Other than for strictly personal use, it is not permitted to download, forward or distribute the text or part of it, without the consent of the author(s) and/or copyright holder(s), unless the work is under an open content license such as Creative Commons.

Takedown policy

Please contact us and provide details if you believe this document breaches copyrights.
We will remove access to the work immediately and investigate your claim.

On-chip Solutions for Future THz Imaging Spectrometers



Alejandro Pascual Laguna



On-Chip Solutions for Future THz Imaging Spectrometers

On-Chip Solutions for Future THz Imaging Spectrometers

DISSERTATION

for the purpose of obtaining the degree of doctor
at Delft University of Technology
by the authority of the Rector Magnificus, Prof. dr. ir. T. H. J. J. van der Hagen,
Chair of the Board for Doctorates,
to be defended publicly on
Friday 11 February 2022 at 12:30

by

Alejandro PASCUAL LAGUNA

Master of Science in Electrical Engineering,
Delft University of Technology, the Netherlands,
born in Madrid, Spain.

This dissertation has been approved by the promotores.

Composition of the doctoral committee:

Rector Magnificus,	Chairman
Prof. dr. ir. J. J. A. Baselmans,	Delft University of Technology, promotor
Prof. dr. ing. A. Neto,	Delft University of Technology, promotor

Independent members:

Prof. dr. A. G. Yarovoy	Delft University of Technology
Prof. dr. N. Llombart Juan	Delft University of Technology
Dr. E. Shirokoff	The University of Chicago, USA
Dr. A. Freni	University of Florence, Italy
Dr. A. Endo	Delft University of Technology



The work presented in this thesis has been performed at Delft University of Technology and SRON Netherlands Institute for Space Research, and financed by the European Research Council Consolidator Grant (ERC-2014-CoG MOSAIC), no. 648135 and co-supported by the European Research Council Starting Grant (ERC-2014-StG LAATHz-CC), no. 639749.

Keywords: antenna, array, astronomy, broadband, filter-bank, Fabry-Pérot, on-chip, phase-shifter, spectrometer, superconductor, THz

Cover design: The different shades of the cosmic infrared waves are captured by the electrically beam-steered focused connected array antenna (front) coupled to an MKID filter-bank (back). Cover design by Alejandro Pascual Laguna & Ángela M. Moncaleano Novoa.

Printed by: Gildeprint – The Netherlands

Copyright © 2022 by A. Pascual Laguna. All rights reserved.

An electronic version of this dissertation is available at <https://repository.tudelft.nl/>

ISBN 978-94-6384-298-3

*A la memoria de mi abuela Maribel,
por ‘padecer’ su tercera generación de ingenieros.*

Contents

Preface	xi	
1	Introduction	1
1.1	The Colors of the Universe	1
1.2	Observing the Early Universe	2
1.3	THz Instrumentation for Astronomy	5
1.3.1	Cameras	5
1.3.2	Spectrometers	5
1.3.3	Imaging spectrometers	6
1.4	Broadband THz On-chip Imaging Spectrometers	7
1.5	Outline of this Thesis	9
2	Superconducting Circuits at High Frequencies	11
2.1	Introduction	11
2.2	Superconductivity	12
2.3	Superconducting Resonators	16
2.4	Microwave Kinetic Inductance Detector	18
2.5	Conclusions	21
I	Towards a Broadband THz Superconducting On-chip Filter-Bank	23
3	THz Superconducting On-chip Filter-Bank Spectrometers	25
3.1	Introduction	25
3.2	On-Chip Filter-Bank Spectrometer	27
3.3	Resonator as a THz Band-Pass Filter	29
3.3.1	Energy Perspective	31
3.3.2	Circuit Perspective	33
3.4	Filter-bank Circuit Model Analysis	34
3.5	Conclusions	43

4 Co-planar THz Band-Pass Filters	45
4.1 DESHIMA 1.0	45
4.2 Bridges on a CPW Line	47
4.3 CPW Turns	49
4.4 Meandered-Slot as a Band-Pass Filter.	51
4.5 Radiation Loss in Co-Planar THz Filter-Banks.	54
4.6 Conclusions	56
5 Microstrip THz Band-Pass Filters	59
5.1 On-Chip Technology: CPW vs. Microstrip	60
5.2 Band-Pass Filter Design	61
5.3 Sparse Filter-Bank Chip	63
5.3.1 Fabrication	65
5.3.2 Frequency Response Measurements	65
5.3.3 Optical Efficiency Measurements	71
5.3.4 Discussion	75
5.4 Conclusions and Outlook.	76
6 Design and Optimization of the I-Shaped Microstrip Resonator	79
6.1 Coupler at the Through-Line Side.	82
6.2 Coupler at the MKID Side.	83
6.3 Tuning the Resonance Frequency	84
6.4 Blind Design of a THz Filter at 350 GHz	84
6.5 Empirical Design Optimization	86
6.6 Conclusions	90
II Towards a Broadband THz Superconducting On-Chip Beam-Steering Antenna	93
7 Focused Connected Array Antenna	95
7.1 Introduction.	95
7.2 Near-Field Focused Aperture	97
7.2.1 Focusing Currents	98
7.2.2 Broadband and Highly-Efficient Quasi-Optical Coupling.	101
7.2.3 Scanning Capabilities Inside a Focusing System	103
7.2.4 Prototype Dimensioning	103
7.3 Focused Connected Array of Slots.	105
7.3.1 Array Unit Cell	105
7.3.2 Corporate Feeding Network	107
7.3.3 Finite Array Simulations	107
7.4 Measurements.	111
7.5 Conclusions and Outlook.	117

8 On-Chip Superconducting Phase Shifters at THz Frequencies	119
8.1 Introduction	119
8.2 Electronic Beam-Steering of a Superconducting Phased-Array Antenna	121
8.2.1 Scanning a 1-D Conventional Phased-Array	123
8.2.2 Scanning a Focused Connected Array	124
8.3 Current-Biased Fabry-Pérot Resonator	125
8.3.1 Fabry-Pérot Resonator	126
8.3.2 Fabry-Pérot Design	127
8.3.3 Fabry-Pérot Implementation	132
8.3.4 Low-Pass Filter Design Procedure	133
8.3.5 Filter Design for the Tunable Fabry-Pérot Resonator	137
8.3.6 DC Current Injection Point	138
8.4 Chip Design	142
8.4.1 Critical Current Avoidance	143
8.4.2 Expected Performance	144
8.5 Conclusions	146
9 Conclusions and Outlook	149
9.1 High-Frequency Superconducting Circuits	149
9.2 Superconducting On-Chip Filter-Bank Spectrometers	150
9.2.1 Filter-Bank of Half-Wavelength Resonators	150
9.2.2 Co-Planar Filter-Bank	151
9.2.3 Microstrip Filter-Bank	152
9.3 Broadband Beam-Steering Reflector Feed	153
9.3.1 Focused Connected Array	154
9.3.2 Superconducting Phase-Shifters	155
9.4 Outlook	156
9.5 Impact of the Research	157
A Modeling Superconducting Films	159
B Fabrication of a Microstrip On-Chip Filter-Bank Spectrometer	161
C S-parameters of a shunt resonator in terms of its quality factors	169
C.1 Two-port network of a quarter-wavelength resonator in shunt	169
C.2 Three-port network of a half-wavelength resonator in shunt	171
C.3 Maximum power transfer to the detector	172
Bibliography	173
Summary	193
Samenvatting	195
List of Publications	199

Propositions Accompanying the Doctoral Thesis	205
Acknowledgements	207
About the author	211

Preface

This dissertation describes the research work carried out over a period of almost five years (from December 2016 to August 2021) in the frame of a close collaboration between the THz Sensing group of the Delft University of Technology and the Technology group of the Netherlands Institute for Space Research (NWO-I SRON), both in the Netherlands. This project was financed by the European Research Council under the Consolidator Grant ERC-2014-CoG MOSAIC, no. 648135. Besides, this work was co-financed in part by the European Research Council under the Starting Grant ERC-2014-StG LAATHz-CC, no. 639749.

*Alejandro Pascual Laguna
Delft, August 2021*

Chapter 1

Introduction

1.1. The Colors of the Universe

In the darkness of a cold night by a campfire, the faint light of the night sky slowly emerges as the fire fades out. A myriad of stars, like tiny burning fires, now light up the sky to our naked eyes. At the same time, the consuming campfire turns redder as it cools. At some point the ashes appear to cease glowing while the warmth remains. These invisible ‘calorific rays’, that we nowadays call infrared light, were discovered by W. Herschel with his experiments measuring the thermal energy of the different colors composing the light of our nearby star, the Sun [1]. Such experiments evidenced that the nature of those ‘calorific rays’ was the same as for the visible light, and in fact for the whole electromagnetic spectrum as J. C. Maxwell would demonstrate later in [2]. However, the actual radiant energy distribution with color found by W. Herschel would only be understood with the work of J. Stefan [3], L. Boltzmann [4] and M. Planck [5], who postulated the relation between the temperature of a body and its radiation. Such radiation of thermal origin was predicted to permeate the sky as a remnant of the hot and dense conditions in the early Universe by R. A. Alpher and R. C. Herman [6], but only years later would the group led by R. H. Dicke find evidence for this [7] in the excess noise temperature of 3.5 ± 1.0 K in the microwave antenna measurements by A. A. Penzias and R. W. Wilson [8]. This was the discovery of the Cosmic Microwave Background, which was crucial for supporting the Big Bang theory describing how the Universe expanded from an initial state of high density and temperature.

With the copious astronomical observations obtained over the last century, an estimate of the total cosmic background radiation has been obtained over a large part of the electromagnetic spectrum [9] as shown in Fig. 1.1. The three main contributions to the background radiation of the Universe are the Cosmic Microwave Background (CMB), which is the afterglow of the Big Bang; the Cosmic Infrared Background

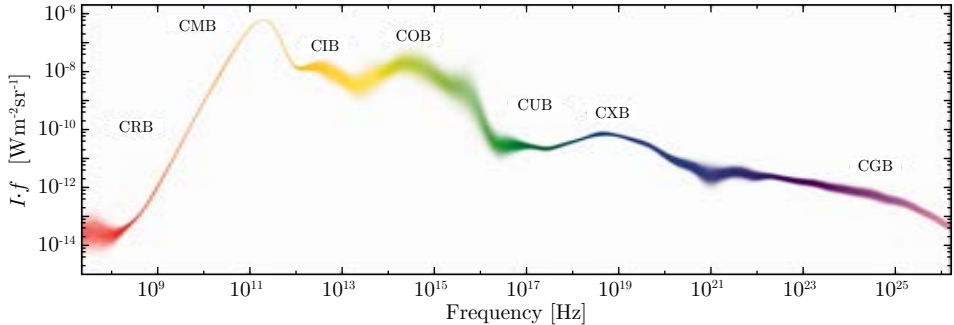


Figure 1.1: Frequency-scaled specific intensity estimate of the cosmic background with its various parts being referred to as the cosmic radio, microwave, infrared, optical, ultraviolet, X-ray, and γ -ray backgrounds; whose acronyms and ranges are respectively CRB ($< 10^{10}$ Hz), CMB (10^{10} – 10^{12} Hz), CIB (10^{12} – 10^{14} Hz), COB (10^{14} – 10^{15} Hz), CUB (10^{15} – 10^{16} Hz), CXB (10^{16} – 10^{19} Hz), and CGB ($> 10^{19}$ Hz). The spread in this splatter plot is proportional to the uncertainty. Figure adapted from [9] with permission.

(CIB), which originates from the heated dust in star-forming galaxies [10]; and the Cosmic Optical Background (COB), which is the mostly visible¹ starlight. Each wavelength range probes different objects and physical processes, which can often take place in the same object or structure. As a result, multi-wavelength astronomy, combining observations across the electromagnetic spectrum are becoming key to advance our understanding of the Universe.

1.2. Observing the Early Universe

Due to the finite speed of light and the vast distances of the Universe², the light emitted shortly after the Big Bang (roughly 13.8 billions years ago) still reaches us today, allowing us to see the cosmological evolution of the past. On top of this, because the Universe expands [11–15], the radiation emitted a long time ago has stretched along with the space it travels through. This results in the so-called cosmological redshift, by which the light emitted in the early Universe has shifted to lower, i. e. redder, frequencies. The redshift z is defined as

$$z = \frac{f_{\text{emit}}}{f_{\text{obs}}} - 1, \quad (1.1)$$

¹The ‘calorific rays’ discovered by W. Herschel were in the proximity of the visible spectrum, in the near-infrared (2.14×10^{14} – 4×10^{14} Hz), and thus are classified as part of the COB, not the CIB.

²The current estimate of the observable radius of the Universe is about 46.9 billion lightyears (or about 4.4×10^{26} m), which is given by the *cosmic light horizon*.

where f_{emit} is the rest frame emission frequency and f_{obs} the observed frequency upon redshift. The higher the redshift, the longer the radiation has traveled since emitted, and thereby the further apart in time and space the emission point is from the observation point.

The furthest observable in the Universe in the electromagnetic spectrum is the CMB (see Fig. 1.2(a)), at a redshift of about $z \approx 1100$. The assembly of the first galaxies in the early Universe is currently estimated to occur only at $z \approx 11$ [16, 17], roughly 400 million years after the Big Bang or 13.4 billion years ago. However, the process of the distribution of matter from the largely uniform primordial condensate of hot (~ 3000 K) and dense (~ 200 particles/cm 3) gas [18], and the subsequent creation and evolution of those ancient galaxies remain largely unknown. Since the observations by FIRAS in the 1990s, it has been known that a large fraction of the star formation in the early Universe is obscured by dust [19, 20]. In such dust-rich environments, starlight is effectively blocked; making the infrared re-radiation of the heated dust, the emission lines from the excited gas clouds and the synchrotron radiation the only proxies for the intense star formation in these regions [21–23]. Subsequent observations by Hubble and ALMA have shown that in fact galaxies in the early Universe are typically very bright in the far-infrared regime, but show no counterparts elsewhere in the electromagnetic spectrum as can be noticed in Fig. 1.2(b): the purple-, blue-, and yellow- colored galaxies observed in the 435 nm–1.6 μm (187.4–689.2 THz) band by Hubble do not overlap with the observations by ALMA at 231.2 GHz shown in orange. Thereby, to study galaxy formation and evolution, observations in both the optical and (far-)infrared are crucial.

As can be seen from Fig. 1.3, apart from the continuum emission caused by the heated dust, the spectra of star-forming galaxies contain a plethora of emission lines in the terahertz (THz) regime (or equivalently far-infrared), which is loosely defined as the 0.1–10 THz band. The study of these emission lines provides detailed information about these astronomical objects in terms of their age, distance, structure, dynamics, energy, chemistry, and physical conditions such as density, temperature and ionization. Some of the brightest lines probing star formation are [CII], [OIII] and the ‘CO ladder’ [27]. On top of this, the continuum THz spectrum of these galaxies has an interesting feature that makes their study feasible despite their vast distances. Normally, the flux reduces quadratically with increasing distance, i. e. for higher redshifts. However, at (sub-)millimeter wavelengths, the cosmological dimming of more distant sources is partially compensated by the peak of the spectral energy distribution shifting into the longer wavelengths, as can be seen in Fig. 1.3. As a result very distant star-forming galaxies are relatively easy to observe at these long wavelengths.

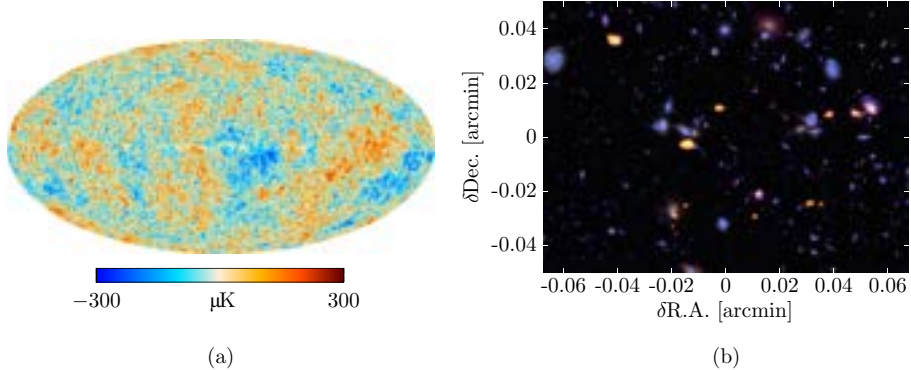


Figure 1.2: Panel (a) is the all-sky Cosmic Microwave Background (CMB) observed by the Planck space telescope. This map shows the anisotropy of the temperature of the CMB, which has a mean value of 2.725 K [24]. The density fluctuations are thought to be the seeds for all future structure in the Universe. Image adapted from [25] with permission. Panel (b) is a sector (centered at R.A. 3:32:37.93, Dec. -27:46:33.03) of the Hubble Ultra Deep Field false-colored in purple (435 and 606 nm), blue (775, 814 and 850 nm) and yellow (1.05, 1.25 and 1.6 μ m) overlaid with the observations by ALMA, false-colored in orange (231.2 GHz or 1.3 mm). Image adapted from [26].

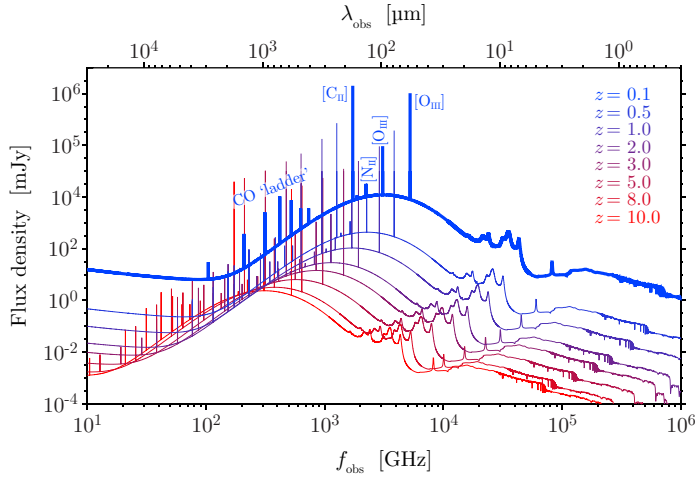


Figure 1.3: Typical spectrum of an infrared galaxy adapted from [28]. The continuum emission, peaking in the infrared, capitalizes on the dusty nature of this galaxy. The emission lines stand out over the continuum, showcasing a plethora of proxies for the study of such galaxies. Note the largely redshift-independent flux density around 100–1000 GHz. The flux density unit Jansky (Jy) is related to SI units as $1 \text{ Jy} = 10^{-26} \text{ W m}^{-2} \text{ Hz}^{-1}$.

1.3. THz Instrumentation for Astronomy

The very faint signals from astronomical sources require very sensitive detectors. Astronomical instrumentation in the ultraviolet, optical and near infrared is very mature and gigapixel charge coupled devices (CCD's) with near single-photon read noise and negligible dark current can be commercially obtained. In the far infrared such technology cannot be used because the low photon energies of the longer wavelength radiation cannot directly³ excite photoelectrons in semiconductors. In general, to obtain the best possible noise performance, THz detectors need to be cryogenically cooled to reduce their intrinsic noise and thereby allow a lower detection threshold. In practice, superconducting detectors give the best noise performance and scaling capabilities (ease of fabrication, integration and multiplexing) for the demanding science cases of THz astronomy. There are two detector variants: coherent detectors, which are phase-preserving systems, and incoherent detectors, which sense only power.

Independently from the detector technology used, there are various ways to probe the distant astronomical objects and their physical processes by means of the electromagnetic spectrum. We can distinguish three main types of instruments according to their function: photometric (cameras), spectrometric (spectrometers), or a combination of the two (imaging spectrometers).

1.3.1. Cameras

Cameras perform photometric measurements of sectors of the Universe to produce images that allow to spatially-resolve different astronomical objects. Such instruments are characterized by a high pixel count but typically have no or very limited color-discriminating capabilities ($R = f/\delta f \sim 10^0\text{--}10^1$). Examples in the THz regime are the cameras Bolocam [29], AzTEC [30], LABOCA [31], EBEX [32], ACTPol [33], SPTpol [34], SCUBA-2 [35], BICEP/Keck [36–38], NIKA2 [39]; and the cameras in preparation POLARBEAR-2 [40], AMKID [41], LiteBIRD [42], TolTEC [43].

1.3.2. Spectrometers

Spectrometers resolve spectral features of a particular astronomical object. This type of instrument typically has a single pixel. We may distinguish two sub-types according to the nature of the detectors:

³Thermal-mediated detection with semiconducting bolometers is still possible but superconducting bolometers have become the preferred option since they are easier to integrate and read out in large systems.

1 **Coherent spectrometers** provide exquisite spectral resolution $R = f/\delta f \sim 10^6 - 10^7$, but are narrow band at THz frequencies because they typically require frequency down-conversion (heterodyning) prior to detection. As a result they are slow for blind spectroscopic surveys over large bandwidths. Examples of THz coherent spectrometers are HIFI [44], EMIR [45] and interferometric arrays like ALMA, NOEMA and SMA.

Incoherent spectrometers can achieve moderate spectral resolution $R = f/\delta f \sim 10^2 - 10^3$ over a wideband detection bandwidth. Since the phase information is lost in a direct detector, light is dispersed prior to detection with e.g. gratings, filter-banks and interferometers like the Fourier-Transform Spectrometer (FTS) or the Fabry-Pérot Interferometer (FPI). This type of spectrometers offer three major advantages over coherent spectrometers: (1) the detection bandwidth is decoupled from the readout bandwidth, allowing a broad detection band to be read with a moderate readout bandwidth; (2) the noise performance can be background limited, unlike coherent detectors which suffer from the fundamental noise floor given by the uncertainty principle [46]; and (3) the integration is typically easier thanks to the avoidance of the mixing stages. The main disadvantage is that much higher resolution spectrometers will become infeasible due to their large size and enormous amount of detectors needed, since each spectral band requires an individual detector. Examples of THz incoherent spectrometers are Z-Spec [47], ZEUS-2 [48], and DESHIMA [49], which have had first light; and CAMELS [50], WSPEC [51], μ -Spec [52] and SuperSpec [53], which are under development.

1.3.3. Imaging spectrometers

Imaging spectrometers simultaneously conduct photometric and spectroscopic observations. These instruments are composed of several spatial pixels, or ‘spaxels’, each with spectroscopic capabilities. An illustration is given in Fig. 1.4. We may distinguish two sub-types according to their operation: the integral field unit (IFU) and the multi-object spectrometer (MOS). IFU’s employ a ‘camera-like’ array of spaxels sampling (part of) the field of view of a telescope, thereby enabling ‘blind’ spectral surveys when there is no a-priori knowledge of both the source position and its spectrum. Instead, each spaxel of a MOS is dynamically and independently aimed at pre-mapped sources, whose position must be known a-priori from images obtained from cameras operating in the same band and with the same spatial resolution. These instruments are wildly successful in optical astronomy [54] but only a handful of small scale IFU’s exist to date in the THz domain. Examples of THz IFU’s based on coherent receivers are CHAMP⁽⁺⁾ [55, 56], BEARS [57], Pole STAR [58], Desert STAR

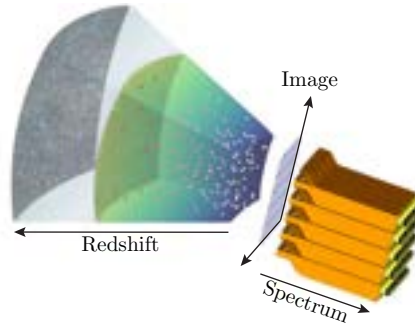


Figure 1.4: Conceptualization of an imaging spectrometer with 5×5 modules (or spaxels) observing a 3D sky, where the depth may be retrieved by the redshift of the observations.

[59], SMART [60], HERA [61], HARP [62], SuperCam [63] and (up)GREAT [64, 65]. These THz imaging spectrometers are based on heterodyne receivers and thus are effectively limited to narrow instantaneous operational bandwidths and to small spaxel counts given the system complexity. On the other hand, IFU's based on direct detectors also exist, examples of which are FIFI LS [66], PACS [67], SPIRE [68] and ZEUS-2 [48]. It is worth noting that all these incoherent THz imaging spectrometers use quasi-optical dispersion mechanisms (FTS or gratings), thereby resulting in bulky systems with limited operational bandwidth, spectral resolution and a large focal plane size. Currently, there are several proposals of miniaturized incoherent THz imaging spectrometers that could largely reduce the instrument footprint [69–73], being the on-chip spectrometer the most widely used.

1.4. Broadband THz On-chip Imaging Spectrometers

With the on-sky demonstration of DESHIMA [74] and the many related developments [50–53], the technology of broadband THz on-chip spectrometers has arrived. This technology has the potential to create very compact imaging spectrometers, where the dispersion and detection takes place on the detector chip. This will allow the construction of on-chip spectrometers with different combinations of N on-sky pixels over the field of view, with an instantaneous bandwidth B and a spectral resolution R . These three properties are in trade-off since they all increase the number of detectors required and thus affect the instrument footprint and the complexity of the readout. As an illustration, several instrument designs, and the science cases that could become possible, are discussed below. For such instruments, we shall assume the following somewhat arbitrary design considerations based upon what is currently feasible:

- An instrument design with two imaging spectrometer arrays coupled to the same optics using a polarizing grid. This implies singly-polarized radiation coupling for each spaxel.
- A maximum detector count of 20000, which is limited both by the available wafer area ($\varnothing 4''$) and the readout complexity.
- A maximum instantaneous input bandwidth of an octave (2:1) for each beam. Two octaves (4:1) could also be obtained if polarization discrimination is not needed, making each on-sky pixel couple through the polarizing grid to two singly-polarized spaxels, each covering an octave of instantaneous bandwidth.
- Each spaxel has approximately R channels⁴ or detectors whose spectral resolution is R .

Redshift Machine

$N = 25$, $B = 4:1$ (two single-pol. octave bands), $R = 500 \rightarrow 17350$ detectors

Quantifying dust-obscured star-formation in the early Universe is currently hampered by the slow redshift-measurement of the 10000's of dusty star-forming galaxies identified with THz cameras. Large-span redshift measurements with coherent spectrometers for all of these sources is impossibly time-consuming. Instead, a multi-object spectrometer (MOS) redshift machine, with a few spaxels that can be independently and electronically steered to pre-mapped sources on-sky, will quickly measure the redshift and the full emission/absorption line spectrum over a large bandwidth for many sources simultaneously, identifying thereby the exact lines that merit interferometric follow-ups. Another advantage of such a system is fast electronic beam-chopping for the calibration of the instrument. Besides, each pixel could be set to observe with different settings over its corresponding patrol sector of the field of view.

Additionally, galaxies with weak emission in the continuum but strong line-emission are currently overlooked [75]. As a result there is the need for unbiased (i.e. with no a-priori information from continuum photometric observations) tomographic surveys of the early Universe [76, 77]. An instrument with similar detector count, but with closely-spaced non-steerable spaxels, commonly known as an integral field unit (IFU), could target these blind spectroscopic surveys. More specific science cases, when some constraining information is available, would be possible by trading off the spatial and spectral coverage with the number of spaxels and their bandwidth.

⁴In reality the total number of channels for a full spectral sampling is given by the expression in (3.2). For an octave bandwidth this results in 347 channels of $R = 500$, or 70 channels of $R = 100$ or 8 channels of $R = 10$.

Sunyaev–Zeldovich Mapper

$N = 1250$, $B = 4:1$ (two single-pol. octave bands), $R = 10 \rightarrow 20000$ detectors

The Sunyaev–Zeldovich (SZ) effect [78] observed at THz frequencies probes the hot intergalactic matter in galaxy clusters by measuring the distortion of the CMB spectrum in a complementary way to traditional X-ray observations [79]. Because the strength of the SZ effect is redshift-independent, it is ideal for studying the emergence of galaxy clusters at redshifts out of the range of X-ray observations. Such an instrument will do targeted observations on known clusters, which are typically of a size well matched to the field of view of current ground-based observatories. A quite similar technology, but then polarization sensitive, could be used as a building-block for future space-borne observatories observing the polarization of the CMB [80].

Line Intensity Mapper

$N = 142$, $B = 4:1$ (two single-pol. octave bands), $R = 100 \rightarrow 19880$ detectors

This instrument would use a new technique that measures the brightness fluctuation of emission lines without resolving individual galaxies [81]. By probing interstellar matter below the detection limit of individual galaxies, this low spectral-resolution, wide field-of-view instrument can efficiently map the evolution of the three-dimensional large-scale structure of the interstellar matter, the fuel of star-formation. This type of instrument trades off resolution and bandwidth for more pixels.

1.5. Outline of this Thesis

This dissertation discusses the two key technological developments needed to make a broadband on-chip imaging spectrometer in the THz regime a reality: a broadband on-chip spectrometer and a broadband antenna with electronic beam-steering.

Prior to the chapters with novel contributions in this dissertation, we describe in Chapter 2 the foundations of superconductivity that are relevant for the high-frequency designs presented in this work. After that comes the first part of the dissertation, which includes chapters 3 through 6, and deals with the design of on-chip broadband superconducting filter-banks. The second part, which includes chapters 7 and 8, discusses the building blocks for a broadband electrically-steered antenna serving as a reflector feed. A more detailed description of the content of each chapter is given next.

1 **Chapter 2** describes the electrodynamic properties of superconductors and how they should be accounted for in electromagnetic solvers when operated at very low temperatures both below and above the gap frequency. Furthermore, we describe the implications of these properties for superconducting resonators and their application to the detectors used in the THz devices of this dissertation.

Chapter 3 investigates the concept of a fully-sampled moderate spectral resolution filter-bank using half-wavelength resonators as the building blocks. We build a circuit model that allows the characterization of the frequency response of these entities in isolation and when arrayed into a large filter-bank configuration. This chapter sets the foundations for such a device irregardless of the technology used.

Chapter 4 explains the performance of a pre-existing filter-bank realized in co-planar technology used for the first generation of the on-chip spectrometer DESHIMA. This chapter showcases the loss problems incurred by such technological choice and the limited free-spectral range limitation of the particular filter geometry employed.

Chapter 5 proposes a new band-pass filter design based on a half-wavelength resonator in microstrip technology. We demonstrate the superior performance of a microstrip filter-bank with the measurements of a spectrally-sparse filter-bank using this filters. We also introduce a new measurement strategy that makes use of the peaks in the filter-coupled detectors and the dips in the wideband-coupled detectors. We employ the well-established optical efficiency measurements as a confirmation for our measurement results.

Chapter 6 describes in detail the procedure to design the newly-introduced filters of Chapter 5. Furthermore, we provide the characterization of other less performing filter-bank batches to motivate our design choices from the gained insights.

Chapter 7 proposes an efficient reflector feed concept with broadband imaging capabilities and easy on-chip integration for superconducting instruments. The concept is based on a connected array antenna which focuses its steerable beam in the focal plane of the reflector system, thereby achieving imaging capabilities in the sky. We demonstrate the concept with low-frequency prototype.

Chapter 8 discusses a phase-shifting concept based on the non-linear response of the kinetic inductance of a current-biased superconducting line. This concept has application in the electronic beam-steering of the antenna array presented in Chapter 7. To quantify the achievable phase-shift in superconducting lines at THz frequencies we have designed biased on-chip Fabry-Pérot resonators.

Chapter 9 concludes the dissertation with an overview of the achieved results and provides an outlook for future research opportunities stemming from this work.

Chapter 2

Superconducting Circuits at High Frequencies

2.1. Introduction

When a superconducting material is cooled below its critical temperature T_c , its direct current (dc) resistance abruptly drops to zero. This is caused by the pairing of electrons with opposite spin and momentum, which are responsible for the transport of charge without any resistance. As illustrated in Fig. 2.1, this interaction is made possible from the wake of positive charge left behind an electron moving through the lattice of a superconductor, which attracts a second electron to lower its potential energy in the deformed lattice [82]. Simultaneously, an energy gap appears in the density of free-electron states, with the consequence that the number of unpaired electrons decreases exponentially with temperature. At very low temperatures ($T \ll T_c$) hardly any unpaired electrons are left and therefore the charge transport becomes virtually lossless. This enables electrically-long and efficient circuitry that would be impossible with normal conductors. However, as we will see in Section 2.2, the alternating current (ac) response of a superconductor is different from the perfect electrical conductor (PEC) abstraction often used in electromagnetic simulators. Since paired electrons do not collide with the metallic lattice, their accrued kinetic energy results in an inductive behavior that has to be taken into account to correctly model superconductors. In Section 2.3 we demonstrate that the negligible loss in superconductors also allows the construction of extremely high quality-factor resonators. In Section 2.4 we discuss one such superconducting resonator, the Microwave Kinetic Inductance Detector, which is the detector of choice for the superconducting devices designed in this dissertation.

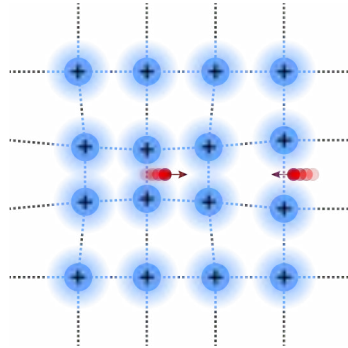


Figure 2.1: Illustration of the net attractive interaction of two electrons due to the positive wake left with their movement along the ionic lattice of a superconductor operated below its critical temperature.

This chapter gives the foundations for the proper modeling of thin film superconductors in electromagnetic solvers. In particular, the designs presented in this thesis are made of thin niobium-titanium nitride (NbTiN) films ranging from 35 nm to 300 nm, with critical temperatures of 14.3–15 K and normal state resistivities of 90–135 $\mu\Omega$ cm. For the sub-millimeter wave frequencies of operation of our devices, the energies are smaller but not much smaller than 2Δ , requiring a full treatment of the electrical properties of the superconducting films using Mattis-Bardeen theory.

2.2. Superconductivity

A metal is composed of an ionic lattice with a cloud of free electrons very weakly coupled to each positive nucleus [83, 84]. The conduction of electricity occurs due to the movement of free electrons along the lattice of the metal. During this process, the electrons collide with the thermally-excited ions of the lattice, thus transforming their kinetic energy into further lattice vibrations and thus heat. This gives rise to the concept of resistance. By cooling a normal conductor, the resistance decreases until a saturation point where the impurities in the sample dominate the collisions. Superconducting metals follow the same trend when cooled down until a critical temperature T_c , where the resistance vanishes completely [85], the magnetic field is expelled out of the conductor (perfect diamagnetism down to dc or Meissner effect) [86, 87] and an energy gap 2Δ appears in the density of free-electron states. This energy gap is reminiscent of the gap between the conduction and valence bands of semiconductors, although 2Δ is typically about three orders of magnitude smaller than the gap in semiconductors. As a result, only excitations with an energy larger than 2Δ will

affect a superconductor, which for electromagnetic radiation sets a gap frequency of

$$f_{\text{gap}} = \frac{2\Delta}{h}, \quad (2.1)$$

where h is the Planck constant.

The London brothers gave a phenomenological electromagnetic explanation for the Meissner effect, the zero resistance and the inductive response in the superconducting state [88]. The microscopic foundation of the superconducting phenomenon was derived later by J. Bardeen, L. N. Cooper and J. R. Schrieffer with their BCS theory [89]. One of the key elements of this theory is the assumption that, in the superconducting state, pairs of electrons tend to have a net attractive interaction despite their repulsion due to Coulomb's law thanks to the electron-phonon interaction qualitatively explained in Fig. 2.1. These pairs of electrons with opposite spin and momentum form Cooper pairs, coined after L. N. Cooper who first described them [90]. Cooper pairs are bosonic particles and will condense into a single macroscopic quantum state at the Fermi energy which is coherent throughout the entire electrical circuit. Local disturbances do not interact with this quantum state, hence the charge transport without dissipation. The energy gap of 2Δ represents in the superconductor also the energy required to break a Cooper pair into two single-particle excitations called quasiparticles. At finite temperatures, there is a residual number of quasiparticles N_{qp} , whose density in a superconductor volume V is exponentially dependent on temperature due to the presence of the energy gap and it is given by [89]

$$n_{\text{qp}} = \frac{N_{\text{qp}}}{V} \approx 2N_0 \sqrt{2\pi k_B T \Delta_0} e^{-\Delta_0/k_B T} \quad (2.2)$$

for $k_B T \ll \Delta$; with k_B the Boltzmann constant, $2\Delta_0 \approx 3.52 k_B T_c$ the energy band gap at absolute zero temperature [89] and N_0 the single-spin density of states at the Fermi surface.

Following the BCS theory, D. C. Mattis and J. Bardeen subsequently explained the electrodynamic properties of superconductors in [91], where they gave an expression for the complex conductivity $\sigma = \sigma_1 - j\sigma_2$ that reads

$$\begin{aligned} \sigma_1 &= \frac{2}{\rho_n h f} \int_{\Delta}^{\infty} (F(E) - F(E + hf)) g_1(E) dE \\ &\quad + \frac{1}{\rho_n h f} \int_{\min(\Delta-hf, -\Delta)}^{-\Delta} (1 - 2F(E + hf)) g_1(E) dE, \end{aligned} \quad (2.3)$$

$$\sigma_2 = \frac{1}{\rho_n h f} \int_{\max(\Delta-hf, -\Delta)}^{\Delta} (1 - 2F(E + hf)) g_2(E) dE, \quad (2.4)$$

where

$$g_1(E) = \frac{E^2 + \Delta^2 + hfE}{\sqrt{E^2 - \Delta^2} \sqrt{(E + hf)^2 - \Delta^2}}, \quad (2.5)$$

$$g_2(E) = \frac{E^2 + \Delta^2 + hfE}{\sqrt{\Delta^2 - E^2} \sqrt{(E + hf)^2 - \Delta^2}} = -jg_1(E). \quad (2.6)$$

In these equations ρ_n is the normal state resistivity (which is the inverse of the normal state conductivity σ_n) and $F(E)$ is the energy distribution function of the quasiparticles at energies E relative to the Fermi energy. In thermal equilibrium, this is given by the Fermi-Dirac distribution

$$F(E) = \frac{1}{1 + e^{E/k_B T}}. \quad (2.7)$$

The real part of the conductivity, σ_1 , accounts for the response of the quasiparticles; whereas the imaginary part, $-\sigma_2$, accounts for the response of the Cooper pairs. In this thesis we will consider superconductors operating at temperatures $T \ll T_c$, where $f_{\text{gap}} = 2\Delta_0/h$. As an example, we illustrate in Fig. 2.2 the complex conductivity $\sigma = \sigma_1 - j\sigma_2$ of a 113 nm-thick NbTiN film¹ ($\rho_n = 135 \mu\Omega \text{ cm}$, $T_c = 15 \text{ K}$) at 0.1 K, which is well below its critical temperature. Using the BCS result of $2\Delta_0 \approx 3.52k_B T_c$, this film has an energy gap of $\Delta_0 \approx 2.27 \text{ meV}$ and thus a gap frequency of $f_{\text{gap}} \approx 1.1 \text{ THz}$. At $T \ll T_c$ there are virtually no quasiparticle excitations and the charge transport is dominated by the Cooper pair condensate for any frequency $f < f_{\text{gap}}$, resulting in an essentially lossless response. The radical change in the conductivity across the gap frequency results from the onset of the pair-breaking mechanism for radiation with an energy larger than the band gap, i. e. at frequencies beyond the gap frequency ($f > f_{\text{gap}}$). For frequencies $f \gg f_{\text{gap}}$, the response becomes mostly resistive, as in the normal state.

The surface impedance of conductive films with arbitrary thickness t in the dirty limit², relevant for the devices reported in this thesis, is given by [92–94]

$$Z_s = \sqrt{\frac{j\omega\mu}{\sigma}} \coth(\sqrt{j\omega\mu\sigma}t) = \sqrt{\frac{j\omega\mu}{\sigma}} \coth\left(\sqrt{1 + j\frac{\sigma_1}{\sigma_2} \frac{t}{\lambda}}\right) = R_s + jX_s, \quad (2.8)$$

where $\omega = 2\pi f$ is the angular frequency and $\lambda = (\omega\mu\sigma_2)^{-1/2}$ is the magnetic penetration depth [95]. The real part of the surface impedance, R_s , is the surface resistance and the imaginary part, X_s , is the surface reactance. For a superconducting film at

¹This superconducting film is used as the top microstrip layer of the on-chip filter-banks discussed in Chapters 5 and 6.

²The dirty limit occurs when the mean free path of the uncondensed electrons is much smaller than the coherence length.

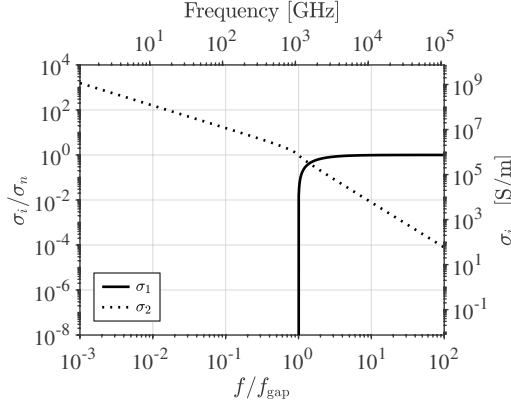


Figure 2.2: Frequency dependence of the complex conductivity $\sigma = \sigma_1 - j\sigma_2$ for a NbTiN film with a thickness $t = 113$ nm, a critical temperature $T_c = 15$ K and normal state resistivity $\rho_n = \sigma_n^{-1} = 135$ $\mu\Omega$ cm. The evaluated temperature is 0.1 K, which is well below the critical temperature. The magnetic penetration depth is $\lambda \approx 315$ nm.

$T \ll T_c$ and $f < f_{\text{gap}}$, when $\sigma_2 \gg \sigma_1$, both parts of the surface impedance can be approximated by [96]

$$R_s = \Re\{Z_s\} \approx \frac{\sigma_1}{\sigma_2} \frac{\beta}{2} \omega \mu \lambda \coth\left(\frac{t}{\lambda}\right), \quad (2.9)$$

$$X_s = \Im\{Z_s\} = \omega L_k \approx \omega \mu \lambda \coth\left(\frac{t}{\lambda}\right); \quad (2.10)$$

where $\beta = 1 + \frac{2t/\lambda}{\sinh(2t/\lambda)}$. Equations (2.9) and (2.10) evidence that a superconducting film at $T \ll T_c$ and $f < f_{\text{gap}}$ should be modeled as an inductive sheet since the ratio σ_1/σ_2 is virtually 0. The surface inductance L_k of such sheet is usually referred to as ‘kinetic inductance’. For low frequencies $f \ll f_{\text{gap}}$ and very low temperatures $T \ll T_c$, the kinetic inductance can be approximated as [97]

$$L_k \approx \frac{\hbar \rho_n}{\pi \Delta_0 t}, \quad (2.11)$$

where $\hbar = h/2\pi$. On the other hand, films operated at $T \ll T_c$ and $f \gtrsim f_{\text{gap}}$ should be modeled with a complex surface impedance obtained by directly evaluating the real and imaginary parts of (2.8) adopting the complex conductivity from the Mattis-Bardeen expressions (2.3) and (2.4), instead of using the simplifications in (2.9) and (2.10). Evaluating the previously introduced NbTiN film yields the surface impedance illustrated in Fig. 2.3(a), which clearly shows the inductive behavior in the superconducting state as emphasized in Fig. 2.3(b). Furthermore, it can be noticed

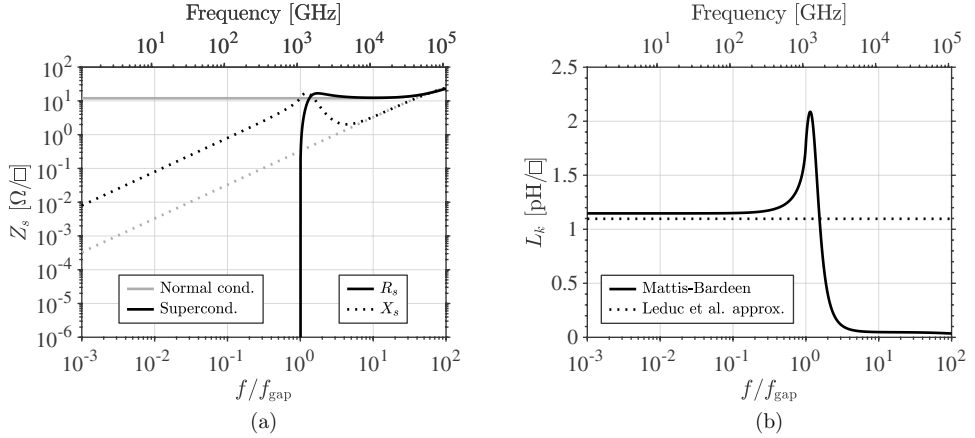


Figure 2.3: Panel (a) shows the complex surface impedance $Z_s = R_s + jX_s$ variation with frequency evaluated using (2.3) and (2.4) in (2.8) (although (2.9) and (2.10) would be accurate up to f_{gap}) for a NbTiN film with thickness $t = 113$ nm, critical temperature $T_c = 15$ K and normal state resistivity $\rho_n = 135 \mu\Omega \text{ cm}$. We also report the behavior expected if the material was a normal conductor with the same thickness and a frequency-independent resistivity $\rho = \rho_n$. Panel (b) shows the kinetic inductance L_k variation with frequency for the same film. We also report the approximation of (2.11). The evaluated temperature for all cases is 0.1 K, which is well below the critical temperature.

that the approximation in (2.11) is only valid for low frequencies ($f \ll f_{\text{gap}}$), becoming inaccurate at the high frequencies just below the gap and thereby requiring the use of the Mattis-Bardeen integrals. Importantly, it becomes apparent that the perfect electrical conductor abstraction, commonly used in electromagnetic solvers, is not a good representation of a superconductor at any frequency. The modeling of a superconducting film employed in this thesis, both in CST Microwave Studio [98] and in Sonnet [99], is described in Appendix A.

2.3. Superconducting Resonators

In this dissertation we will investigate several superconducting resonator circuits, whose quality factor Q_l is generally described as the ratio of the average energy stored $\langle E_{\text{stored}} \rangle$ to power lost P_{lost} at the resonance frequency f_0 [100],

$$Q_l = 2\pi f_0 \frac{\langle E_{\text{stored}} \rangle}{P_{\text{lost}}} = \frac{f_0}{\delta f_0}, \quad (2.12)$$

where δf_0 is the full-width half-maximum response bandwidth around f_0 . The loading of the resonator with its several energy-leaking mechanisms renders a loaded quality

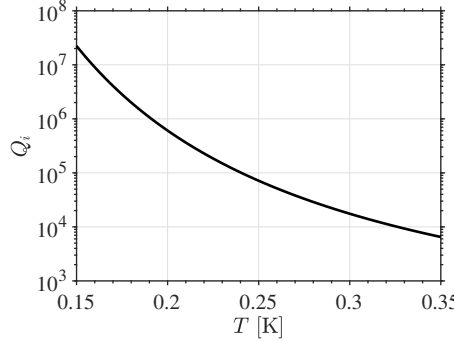


Figure 2.4: Internal quality factor of a 2.2-1.7-2.2 μm -wide, 300-55-300 nm-thick NbTiN-Al-NbTiN CPW on sapphire ($\epsilon_r \approx 10.3$) as a function of temperature T . The material properties are $\rho_n = 0.577 \mu\Omega\text{cm}$ and $T_c = 1.24\text{K}$ for Al, and $\rho_n = 100 \mu\Omega\text{cm}$ and $T_c = 15\text{K}$ for NbTiN. The kinetic inductance fraction for this particular CPW line is $\alpha_k \approx 0.17$, which is calculated using the geometrical scaling factors in [101].

factor given by

$$Q_l^{-1} = Q_i^{-1} + Q_c^{-1}; \quad (2.13)$$

whose comprising terms are the internal quality factor Q_i , accounting for the losses intrinsic to the resonator, and the coupling quality factor Q_c , accounting for the connection strength with the driving system. The internal quality factor due to a superconducting metal is given by [96]

$$Q_i = 2\pi f_0 \frac{1}{\alpha_k} \frac{L_s}{R_s} \approx \frac{2}{\alpha_k \beta} \frac{\sigma_2}{\sigma_1}, \quad (2.14)$$

where the last equality holds for $T \ll T_c$ and $f < f_{\text{gap}}$, when $\sigma_2 \gg \sigma_1$ and the expressions (2.9) and (2.10) may be used. In this equation α_k is the kinetic inductance fraction, which is defined as

$$\alpha_k = \frac{L_k}{L} = \frac{L_k}{L_k + L_g}, \quad (2.15)$$

and it quantifies the contribution to the total inductance L of the kinetic inductance L_k for a particular transmission line with a geometrical inductance L_g . Fig. 2.4 shows the typical Q_i range to be expected from the conductor dissipation in a superconducting (CPW) resonator operated at $T \ll T_c$ and $f < f_{\text{gap}}$. If no other loss mechanism affects the resonating system, the tiny loss contribution from the superconducting metal enables the construction of high quality factor resonators and also ultra low-loss electrical circuits, operating up to 1.1 THz when using NbTiN.

2.4. Microwave Kinetic Inductance Detector

Radiation at frequencies higher than the gap frequency is absorbed in a superconductor by breaking Cooper pairs into quasiparticles. By sensing the changes in the Cooper pair density (and equivalently in the quasiparticle density n_{qp}) in a superconductor, pair-breaking detectors can be engineered. Examples of such type of detectors are the Quantum Capacitance Detector (QCD) [102], the Superconducting Tunnel Junction (STJ) [103] and the Microwave Kinetic Inductance Detector (MKID) [104]. An MKID uses a microwave resonator to probe the change in the complex conductivity caused by radiation absorption at supra-gap frequencies. This radiation absorption can be written in terms of the change in quasiparticle density as [96, 105, 106]

$$\frac{d\sigma_1}{dn_{\text{qp}}} \approx \sigma_n \frac{1}{N_0 hf} \sqrt{\frac{2\Delta_0}{\pi k_B T}} \sinh\left(\frac{hf}{2k_B T}\right) K_0\left(\frac{hf}{2k_B T}\right), \quad (2.16)$$

$$\frac{d\sigma_2}{dn_{\text{qp}}} \approx \sigma_n \frac{-\pi}{2N_0 hf} \left(1 + 2\sqrt{\frac{2\Delta_0}{\pi k_B T}} e^{-hf/2k_B T} I_0\left(\frac{hf}{2k_B T}\right)\right), \quad (2.17)$$

for $k_B T, hf < 2\Delta_0$, where I_0 and K_0 are respectively the modified Bessel functions of first and second kind of zeroth order.

A practical MKID detector [104] consists of a high quality factor microwave superconducting resonator weakly coupled (high Q_c) in shunt to a readout line as schematically shown in Fig. 2.5. The frequency response of the transmission past this resonator for a small frequency shift $df_0 = f - f_0$ is given by [107]

$$S_{21}(f) = \frac{S_{21}(f_0) + j2Q_l \frac{df_0}{f_0}}{1 + j2Q_l \frac{df_0}{f_0}}, \quad (2.18)$$

where the on-resonance transmission is $S_{21}(f_0) = Q_l/Q_i$. Such device allows the sensing of the tiny changes in the complex conductivity upon radiation absorption (according to (2.16) and (2.17)) thanks to its high quality factor resonance, which is enabled by the high Q_i inherent to superconductors (see Fig. 2.4). If the resonator is constructed such that radiation can be efficiently absorbed, the resonator becomes a radiation detector whose resonance frequency f_0 and internal quality factor Q_i vary with the changes in the complex conductivity caused by pair-breaking due to radiation absorption. These changes can be expressed as [96, 106]

$$\frac{df_0}{dN_{\text{qp}}} \approx \frac{\alpha_k \beta f_0}{4|\sigma|V} \frac{d\sigma_2}{dn_{\text{qp}}}, \quad (2.19)$$

$$\frac{dQ_i}{dN_{\text{qp}}} \approx -\frac{\alpha_k \beta Q_i^2}{2|\sigma|V} \frac{d\sigma_1}{dn_{\text{qp}}}. \quad (2.20)$$

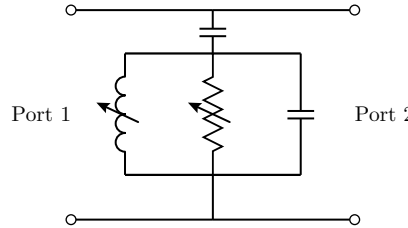


Figure 2.5: Circuit representation of an MKID detector, which is a resonator weakly coupled in shunt to a readout represented here by ports 1 and 2. The resistance and inductance values of the resonator change upon radiation absorption.

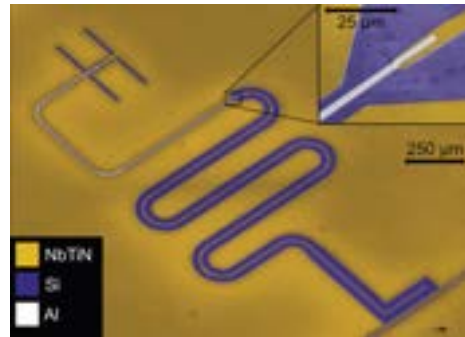


Figure 2.6: Antenna-coupled hybrid MKID detector. Image downloaded with permission from [108].

In this thesis we particularly employ quarter-wavelength CPW hybrid MKID detectors [108]. This MKID variation, illustrated in Fig. 2.6 for an antenna-coupled scenario, combines two superconductors: Al, with a gap frequency of 90 GHz and NbTiN with a gap frequency of 1.1 THz. Al is limited to the central conductor of the CPW at the high-current side (shorted-end) of the MKID, whereas NbTiN is used elsewhere in the device; thereby confining the pair-breaking detection into a small volume. The combination of materials in this hybrid MKID effectively allows to detect radiation at frequencies above 90 GHz, due to pair breaking in the aluminium section, while keeping a conductor-loss free system up to 1.1 THz, due to the use of NbTiN below its gap frequency. The hybrid section of the MKID, where THz radiation is absorbed, is made narrow for two reasons: firstly the Al strip should be narrow and thin to maximize the responsivity of the detector by maximizing α_k ; and secondly, to avoid re-radiation, as we will discuss in Chapter 4. Instead, the NbTiN section should be made wide to minimize the Two-Level System (TLS) noise contributions, which have been shown to depend with the electric field \mathbf{E} as $\propto |\mathbf{E}|^3$ [109].

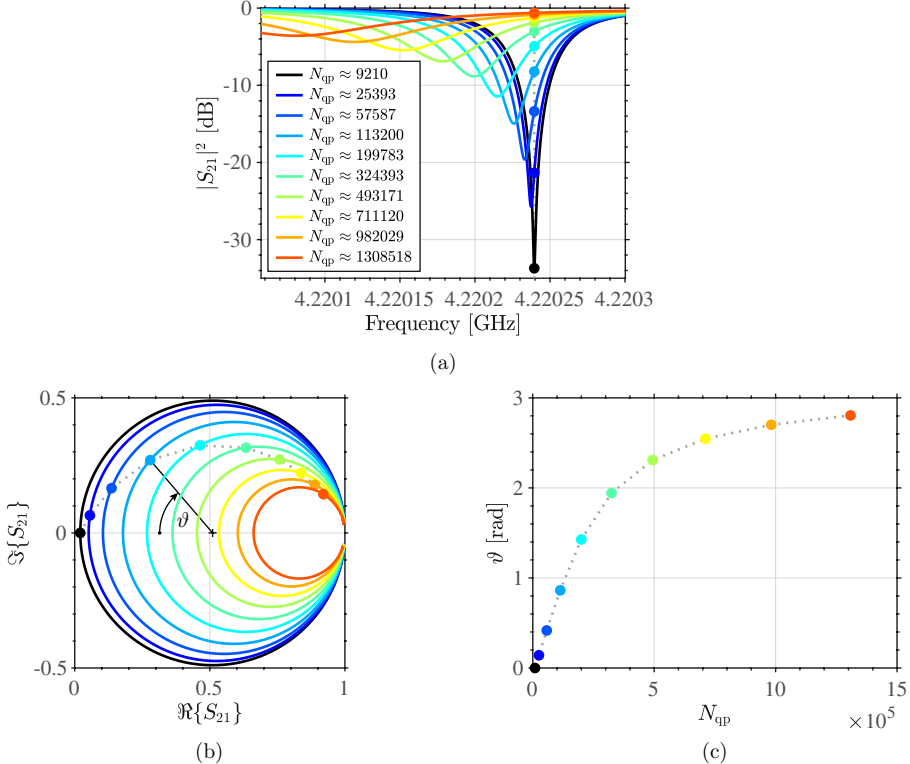


Figure 2.7: Panel (a) shows the simulated transmission response of a quarter-wavelength CPW hybrid MKID for various quasiparticle numbers N_{qp} . The increase in the quasiparticle number incurs in a downward shift of the resonance frequency and a smearing into a shallower dip. Panel (b) shows the IQ-plane of S_{21} around the resonance. Panel (c) shows the phase ϑ of the S_{21} IQ response against the number of quasiparticles. The Al volume is $V \approx 102.85 \mu\text{m}^3$ and its kinetic inductance fraction with respect to the whole resonator is $\alpha_k = 0.03$. The coupling quality factor is $Q_c = 71\,000$.

Fig. 2.7 gives the simulated response of a quarter-wavelength CPW hybrid MKID resonator whose radiation-sensitive part uses a 1.7 μm -wide, 55 nm-thick and 1.1 mm-long Al strip ($T_c = 1.24\text{ K}$, $\rho_n = 0.577 \mu\Omega\text{ cm}$, $N_0 = 1.72 \times 10^{10} \text{ eV}^{-1} \mu\text{m}^{-3}$) and has a kinetic inductance fraction with respect to the whole resonator inductance of $\alpha_k \approx 0.03$. As the number of quasiparticles N_{qp} increases, the dip shifts to lower frequencies and becomes shallower. By sending a probing microwave tone at the nominal resonance frequency of the MKID, a change in amplitude and phase can be sensed as shown in panel (b). In this work we use the phase response (panel (c)) as it gives a monotonic behavior and provides better noise performance [110].

Microwave Kinetic Inductance detectors were pioneered by P. K. Day et al. [104] and they are now used in many astronomical observatories for (sub-)mm wave radiation detection. They are especially interesting due to their intrinsic ease of frequency multiplexing: many resonators with slightly different lengths ring at different microwave resonance frequencies and thus can be coupled to a single readout line. The read-out of such a large array of resonators requires a software defined radio approach [111, 112], where analog and digital electronics provide the capability to generate a microwave readout tone for each resonator to measure simultaneously and in real time the response of all these tones due to radiation absorption in the resonators.

2.5. Conclusions

In this chapter we have shown that superconductors provide extremely low conductor loss, allowing the construction of electrically-long circuits and high quality-factor resonators up to THz frequencies. Despite the apparent resemblance in terms of loss with the ‘perfect electric conductor’ abstraction, a superconductor operated well below its critical temperature and below its gap frequency is different in that it presents an almost purely inductive behavior due to its microscopic nature, where electrons function as pairs. Under these conditions, superconductors should be modeled as inductive sheets. This inductive response to an alternating field is responsible for the slowing down of electromagnetic waves, allowing very compact on-chip solutions of electrically-long components as we will see in this dissertation.

The binding of electrons also results in a small energy band gap of a few meV (c.f. a few eV in semiconductors). Excitations with energies larger than this band gap break Cooper pairs (paired electrons) into quasiparticles (unpaired electrons), altering the conductivity of the superconductor and thus allowing the construction of pair-breaking detectors of frequencies down to a few GHz. The detector used for the THz superconducting devices of this thesis is the MKID, which is a highly-sensitive pair-breaking detector based on a microwave superconducting resonator. This detector naturally offers high frequency-multiplexing capabilities, thereby being very well suited for multi-channel instruments such as the THz imaging spectrometers targeted in this dissertation.

I

Towards a Broadband THz Superconducting On-chip Filter-Bank

Chapter 3

THz Superconducting On-chip Filter-Bank Spectrometers

3.1. Introduction

The physical processes and properties of both the interstellar medium of galaxies as well as the planetary atmospheres can be studied by probing cool gas, which is their most abundant state of matter. This cool gas offers a plethora of emission lines in the terahertz (THz) spectrum (0.1–1 THz) [114], which serve as proxies for astronomy [21–23], meteorology and climatology [115]. In fact, a large fraction of the total brightness of the Universe lays in this far-infrared band [9, 116]. Furthermore, dusty star-forming galaxies in the early Universe can be efficiently observed only in this band, as most of the starlight is absorbed by the dust that enshrouds them [21–23, 116].

Over the last decades, large and very detailed two-dimensional THz maps have been reported [117] employing very wide field-of-view (FoV) cameras [31, 35, 39]. However, these broadband but virtually achromatic instruments lack the capabilities to perform blind spectral surveys, which are crucial for detecting astronomical sources from their emission lines when their continuum emission is too weak to overcome the atmospheric foreground loading or the instrument noise level. Moreover, the understanding of the underlying physics of astronomical sources requires resolving their spectrum to grasp their age, motion and chemical properties.

Conventionally, THz spectrometers based on coherent receivers [44, 118] are aimed at pre-mapped objects to perform narrow band (4–12 GHz) surveys with very fine spectral resolution $R = f_0/\delta f_0 \sim 10^5\text{--}10^6$, where f_0 is the central frequency and δf_0 is the -3 dB pass-band bandwidth. The observation strategy with these instruments

Parts of this chapter have been published in *IEEE Trans. THz Sci. Tech.* [113].

however becomes prohibitively lengthy if the spatial and spectral loci of the targets are unknown a-priori, as it requires the re-aiming of the telescope, and the re-tuning of the local-oscillators for every observation bandwidth. On the contrary, broadband moderate resolution ($R \sim 10^2\text{--}10^3$) incoherent THz spectroscopy allows for fast blind spectroscopic observations of astronomical sources [27].

Spectral imaging instruments like the integral field unit (IFU) [54]—dense spatial sampling—and the multi-object spectrometers (MOS) [119]—sparse spatial sampling with steerable pixels—based on broadband moderate spectral resolution pixels are key to unravel the physics of clustered and redshifted extra-galactic astronomic sources. These type of instruments in the far-infrared spectrum would enable the creation of large tomographic maps of the THz sky [76, 77]. Moreover, these broadband multi-pixel instruments would allow the study of the intra-cluster medium by measuring the Sunyaev-Zeldovich effect [78] as a complementary probe to X-ray observations of the warm and hot gas of galaxy clusters [79, 120]. Additionally, future missions probing the cosmic microwave background (CMB) radiation [42, 121] would benefit from imaging spectroscopy in the 40–600 GHz band.

The scalability of such mid-resolution imaging spectrometers heavily relies on the ability to integrate its comprising units, i. e. highly-efficient broadband single-pixel spectrometers, into compact focal plane arrays. In fact, the dispersion mechanism largely influences the overall spectrometer size given that a signal with wavelength λ needs to be delayed over an average distance $R\lambda$ to achieve a spectral resolution R [122, 123]. Grating spectrometers require quasi-optical path lengths of the order of $R\lambda$, which results in bulky instruments such as Z-Spec [47] and ZEUS [48]. On the other hand, filter-bank spectrometers like the waveguide device WSPEC [51], only require band-pass filters whose size is of the order of λ to achieve a spectral resolution R , since on-resonance the signal is bounced an average of R times. A further footprint reduction can be achieved exploiting the very slow nature of guided waves in thin-film superconductors, making on-chip spectrometers remarkably more compact than non-integrated solutions, as evidenced in Fig. 3.1. On-chip technology has been used for both diffraction gratings, such as μ -Spec [52]; and filter-banks, such as SuperSpec [53], CAMELS [50] and DESHIMA [49]. Superconducting on-chip filter-banks offer the most scalable solution towards multi-pixel spectrometers thanks to their compact size and large instantaneous bandwidth.

The rest of the chapter is organized as follows. In Section 3.2 we discuss the on-chip filter-bank concept for mid-resolution broadband THz spectrometers. We target a coupling efficiency to the detectors as high as possible, an octave of instantaneous bandwidth free from spurious resonances and a moderate spectral resolution of $R = 500$, driven by the typical emission line width of high-redshift galaxies [21]. In Section 3.3 we investigate the foundations of resonators as band-pass filters and construct a circuit model, largely inspired by [124, 125], to study large filter-banks.

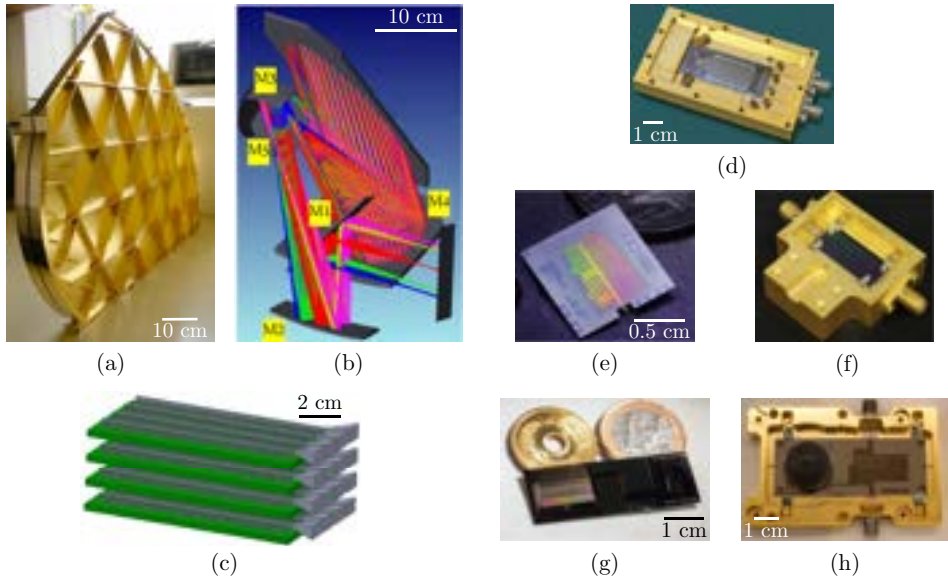


Figure 3.1: Size comparison of state of the art broadband far-infrared spectrometers. Panels (a–c) show non-integrated solutions and panels (d–h) display on-chip spectrometers, with an order of magnitude in footprint reduction. Panels (a) and (b) show the quasi-optical diffraction gratings of the spectrometers Z-Spec [47] and ZEUS-2 [48], respectively. Panel (c) displays the waveguide filter-bank of [51]. Panel (d) shows the on-chip grating spectrometer of μ -Spec [52]. Panels (e–h) contain the on-chip filter-bank spectrometers of SuperSpec [53], CAMELS [50], DESHIMA 1.0 [49] and DESHIMA 2.0, respectively.

In Section 3.4 we analyze the response obtained from the filter-bank circuit model to derive requirements and design considerations for an actual implementation.

3.2. On-Chip Filter-Bank Spectrometer

An on-chip sub-mm wave superconducting filter-bank spectrometer couples THz radiation to the chip with a broadband antenna, which transforms the incoming radiation onto a guided mode. From the antenna, a superconducting transmission line, hereinafter called through-line, guides the wideband signal with virtually no loss of power [126] to the filter-bank, where it is sorted into sub-bands and subsequently detected. Any remaining power undetected by the filter-bank is eventually absorbed in a matched lossy transmission line terminating the through-line to avoid reflections. Before and after the filter-bank there are a few weakly coupled detectors which, thanks

to the their wideband response, serve for calibration and diagnostic purposes. A schematic drawing of such device is shown in Fig. 3.2 and described in detail in [49].

The filter-bank consists of an array of N shunted band-pass filters stemming from the through-line. Each of these filters is tuned to channelize a sub-band of the broadband THz signal from the through-line, on one side, to the detector, on the other side, where the filtered signal is sensed and read out. To minimize the losses, the filters are monotonically ordered along the through-line from the highest frequency (f_{\max}) to the lowest (f_{\min}), starting from the antenna side¹. Since the aim is to fully sample the whole operational bandwidth with a constant spectral resolution $R = f_i/\delta f_i$ and pass-band cross-overs at -3 dB, the i^{th} filter from the entrance of the filter-bank has an exponentially lower central frequency (f_i) and a narrower -3 dB bandwidth (δf_i) following the relation²

$$f_i = f_{\max}(1 + R^{-1})^{-i+1}, \quad (3.1)$$

where $f_{\max} = f_{\min}(1 + R^{-1})^{N-1}$ and the total number of channels is

$$N = \left\lfloor \frac{\log(f_{\max}/f_{\min})}{\log(1 + R^{-1})} + 1 \right\rfloor, \quad (3.2)$$

where $\lfloor \cdot \rfloor$ is the floor function.

Each sub-band is sensed with a Microwave Kinetic Inductance Detector (MKID) [104] behind each THz filter. This type of incoherent detector is a high quality factor superconducting microwave resonator that changes its resonance with the small variations in the complex conductivity of the superconductor upon the absorption of signals with frequencies beyond its gap frequency. In particular, hybrid quarter-wavelength CPW MKIDs [108] are used by combining two superconductors in the resonators: NbTiN, with a gap frequency of $f_{\text{gap}}^{\text{NbTiN}} \approx 1.1$ THz, and an aluminium strip, with $f_{\text{gap}}^{\text{Al}} \approx 90$ GHz, as the absorbing central conductor of the CPW in the shorted-end of the MKID in the proximity of the THz filter. Moreover, to increase the responsivity of the detector, the resonator is narrowed at its shorted-end, and widened elsewhere to reduce two-level system (TLS) noise contributions [109]. By capacitively coupling an array of MKIDs with slightly different lengths to a single readout line, each detector can be simultaneously sensed at a different frequency with a comb of microwave probing tones, allowing a highly frequency-multiplexed readout scheme [111, 112]. This poses a great advantage over coherent detectors as it allows to decouple the observation bandwidth from the detector readout bandwidth. For example, an octave band 220–440 GHz on-chip spectrometer has approximately 350 spectral channels using $R = 500$, which can be read out using approximately 1 GHz of readout bandwidth.

¹We will show later that the reverse ordering is also detrimental for the performance of the high-frequency channels of the filter-bank.

²This definition stems from $f_i = f_{\min}(1 + R^{-1})^{N-i} = f_{\min}(1 + R^{-1})^{N-1}(1 + R^{-1})^{-i+1}$. This choice ensures that the lowest frequency channel $i = N$ has a pass-band exactly centered at $f_N = f_{\min}$.

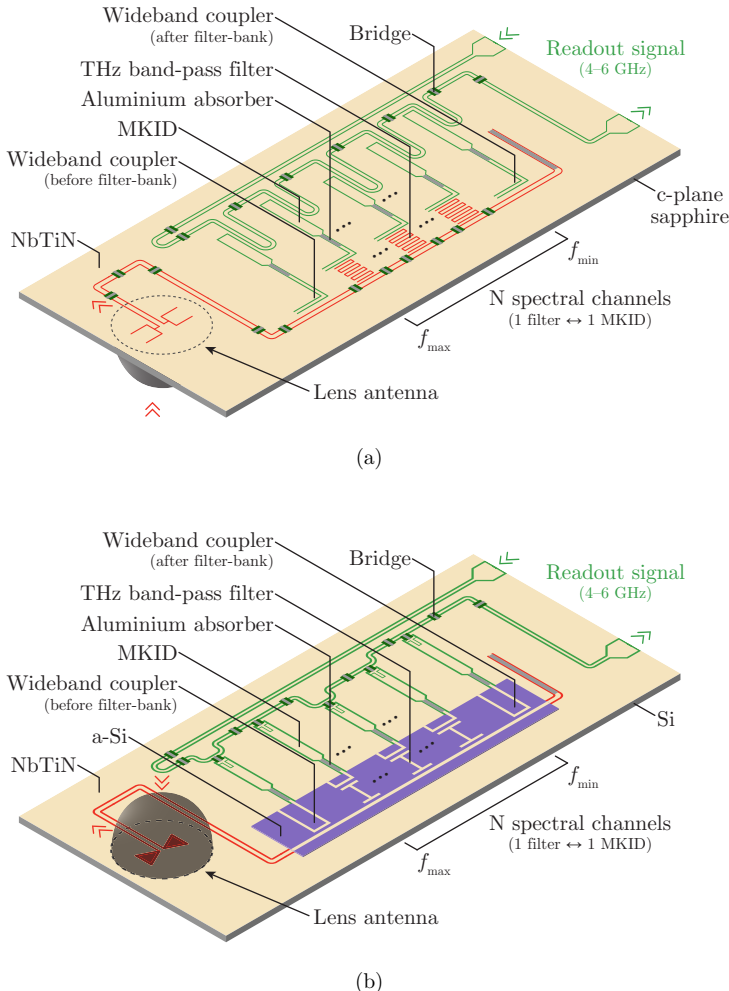


Figure 3.2: Conceptual drawing of a superconducting on-chip filter-bank spectrometer based on MKIDs with (a) co-planar and (b) microstrip THz band-pass filters.

3.3. Resonator as a THz Band-Pass Filter

Each shunted band-pass filter should maximize the coupling efficiency in the pass-band, i.e. the power transferred from the through-line into the MKID; and in the stop-band it should not affect the THz signal on the through-line. The ideal top-hat

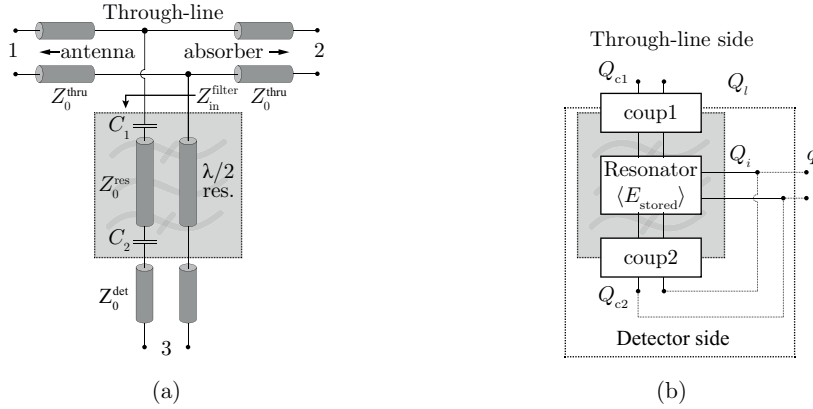


Figure 3.3: A resonator as a band-pass filter from (a) a circuit point of view, and (b) an energetic point of view.

band-pass response could be approximated with multiple filtering elements [127, 128], however to limit the chip complexity, this is not done. Moreover broadband lumped-element solutions like [129] become very complex at THz frequencies due to their electrical length. Thereby, we have investigated resonators as a simple broadband distributed band-pass filter solution, as these naturally provide an octave of spurious-free bandwidth for a half-wavelength resonator. The bandwidth of the Lorentzian pass-band of these resonators is controlled by means of the coupling strength of the surrounding couplers.

By defining the ports of a single band-pass filter coupled to a through-line as in Fig. 3.3(a), the figure of merit to maximize on-resonance is the coupling efficiency or $|S_{31}|^2$; and off-resonance the transmission coefficient $|S_{21}|^2$, so that most of the power is extracted on-resonance and off-resonance the filter does not load the through-line. It turns out that for a lossless filter, if no extra filtering structures like band-stop filters in the through-line are added [51, 130], at most 50% of the input power can be extracted on-resonance ($|S_{31}|^2 = 50\%$). The remaining 50% of the input power is evenly split between reflections ($|S_{11}|^2 = 25\%$) and power let to continue in the through-line ($|S_{21}|^2 = 25\%$). This frequency response is illustrated in Fig. 3.4. In the following we shall see this band-pass filter in two different ways: as a distributed circuit model (Fig. 3.3(a)), and as a resonator with several energy-leaking mechanisms (Fig. 3.3(b)). The energy perspective, described in the next section, allows to derive analytical expressions of the S-parameters of resonator band-pass filters, providing therein insights to their properties as well as fitting functions to facilitate their characterization in a complex measurement setup.

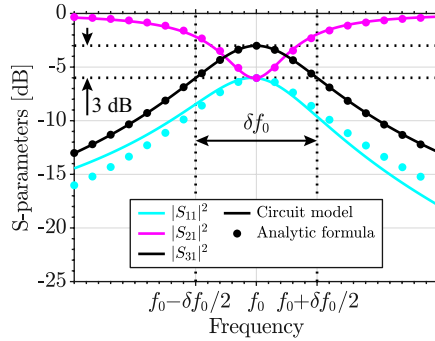


Figure 3.4: Frequency response of a single lossless band-pass filter with spectral resolution R as in Fig. 3.3. The analytical expressions (3.8) to (3.10) are shown with dots and the results of the numerical circuit model are represented with solid lines.

3.3.1. Energy Perspective

The loaded quality factor Q_l of a resonator relates the average energy stored in it $\langle E_{\text{stored}} \rangle$ to the power lost P_{lost} by the energy-leaking mechanisms at its resonance frequency f_0 by the expression [100]

$$Q_l = 2\pi f_0 \frac{\langle E_{\text{stored}} \rangle}{P_{\text{lost}}} = \frac{f_0}{\delta f_0}. \quad (3.3)$$

For the resonator of Fig. 3.3(b), the energy-leaking mechanisms are two couplers and any internal loss mechanism in the resonator. One coupler leaks energy from the resonator to the through-line with an associated quality factor Q_{c1} , and the other coupler to the detector with Q_{c2} . The loss mechanisms, represented by Q_i , will be radiative or dielectric losses for a superconducting device. As a result, the loaded quality factor Q_l of the resonator can be written as

$$Q_l^{-1} = Q_{c1}^{-1} + Q_{c2}^{-1} + Q_i^{-1}. \quad (3.4)$$

Following a similar approach as in [107, 131], the three-port network S-parameters of the shunted half-wavelength resonator of Fig. 3.3 may be approximated for frequencies f around the resonance f_0 by means of the quality factors of its components. This

is detailed in Appendix C. The dots in Fig. 3.4 illustrate the equations of

$$S_{11}(f) \approx \frac{S_{11}(f_0)}{1 + j2Q_l \frac{f-f_0}{f_0}}, \quad (3.5)$$

$$S_{21}(f) \approx \frac{S_{21}(f_0) + j2Q_l \frac{f-f_0}{f_0}}{1 + j2Q_l \frac{f-f_0}{f_0}}, \quad (3.6)$$

$$S_{31}(f) \approx \frac{S_{31}(f_0)}{1 + j2Q_l \frac{f-f_0}{f_0}}, \quad (3.7)$$

being $S_{11}(f_0)$, $S_{21}(f_0)$ and $S_{31}(f_0)$ the values of the S-parameters on-resonance; which in turn are given by

$$S_{11}(f_0) = \frac{-q_i}{Q_{c1} + q_i} = \frac{-Q_i Q_{c2}}{Q_i(Q_{c1} + Q_{c2}) + Q_{c1} Q_{c2}} = \frac{-Q_l}{Q_{c1}}, \quad (3.8)$$

$$S_{21}(f_0) = \frac{Q_{c1}}{Q_{c1} + q_i} = \frac{(Q_i + Q_{c2})Q_{c1}}{Q_i(Q_{c1} + Q_{c2}) + Q_{c1} Q_{c2}} = \frac{Q_l}{q_i}, \quad (3.9)$$

$$S_{31}(f_0) = \frac{\sqrt{2Q_{c1}Q_{c2}}}{Q_{c2} + Q_{c1} \left(1 + \frac{Q_{c2}}{Q_i}\right)}, \quad (3.10)$$

where q_i is the internal quality factor of the equivalent two-port network depicted in Fig. 3.3 and it is defined as

$$q_i = (Q_i^{-1} + Q_{c2}^{-1})^{-1}. \quad (3.11)$$

This allows to re-write (3.4) as

$$Q_l^{-1} = Q_{c1}^{-1} + q_i^{-1}. \quad (3.12)$$

By equating to zero the derivatives of (3.10) with respect to Q_{c1} and Q_{c2} , one can find that the configuration that maximizes the coupling efficiency on-resonance, for a desired loaded quality factor Q_l and a given internal quality factor Q_i , is when the two couplers have the same Q_c with a value of

$$Q_c = Q_{c1} = Q_{c2} = \frac{2Q_i Q_l}{Q_i - Q_l}. \quad (3.13)$$

Under this condition the coupling efficiency in (3.10) is maximized and peaks at

$$|S_{31}^{\max}(f_0)|^2 = \frac{(Q_i - Q_l)^2}{2Q_i^2} = \frac{2Q_l^2}{Q_c^2} = \frac{2Q_i^2}{(2Q_i + Q_c)^2}, \quad (3.14)$$

which is represented in Fig. 3.5 as a function of the internal quality factor Q_i for different values of $Q_c = Q_{c1} = Q_{c2}$. It becomes apparent that to obtain a high coupling efficiency ($|S_{31}(f_0)|^2$), the internal quality factor must be much larger than the targeted loaded quality factor ($Q_i \gg Q_l$).

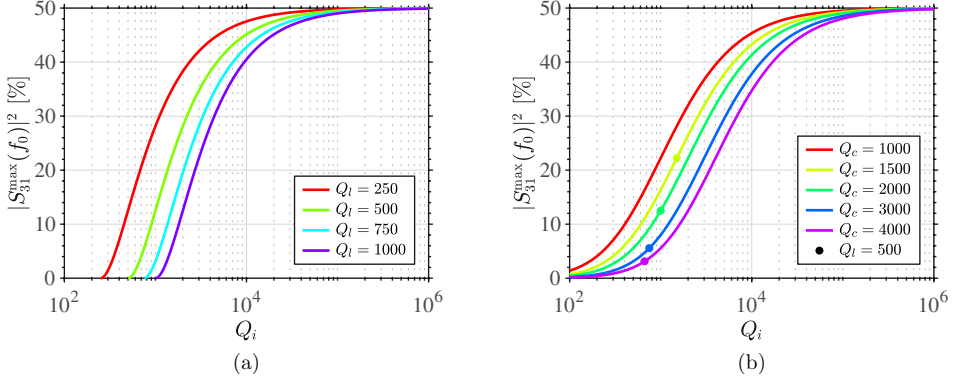


Figure 3.5: Maximum coupling efficiency as a function of the internal quality factor Q_i for (a) several cases of loaded quality factor Q_l and (b) several cases of coupling quality factor $Q_c = Q_{c1} = Q_{c2}$, with the location of $Q_l = 500$ emphasized with dots (the red dot would be located at $Q_i \rightarrow \infty$).

3.3.2. Circuit Perspective

On the other hand, an equivalent circuit representation as in Fig. 3.3(a) also allows us to investigate these resonators with simple microwave analysis techniques. The resonator is represented by a transmission line whose losses are characterized by [100] $Q_i = \beta/(2\alpha)$, relating the real and imaginary parts of the propagation constant $\gamma = \alpha + j\beta$. The length of the resonator is determined by the resonance condition $\Im\{Z_{\text{in}}^{\text{filter}}\} = 0$, which gives a slightly shorter length than $\lambda/2$ due to the detuning introduced by the couplers. The couplers surrounding the half-wavelength resonator are modeled by capacitors, which are designed to provide the coupling quality factor of (3.13) following an energetic approach as in [96] with $Q_c = 2\pi/|S_{ab}|^2$, where $|S_{ab}|^2$ is the transmission through a series capacitor between ports a and b . This transmission can be calculated for a series capacitance C using the following expression relating the S and ABCD parameters [132]:

$$S_{ij} = \frac{2\sqrt{\Re\{Z_0^a\}\Re\{Z_0^b\}}}{Z_0^a + (j\omega C)^{-1} + Z_0^b}, \quad (3.15)$$

where Z_0^a and Z_0^b are the normalizing impedances at ports a and b respectively. The capacitor at the through-line side has $Z_0^a = Z_0^{\text{thru}}/2$ and $Z_0^b = Z_0^{\text{res}}$, whereas the capacitor at the detector side has $Z_0^a = Z_0^{\text{det}}$ and $Z_0^b = Z_0^{\text{res}}$.

From these considerations the unit cell of the filter-bank, the band-pass filter of Fig. 3.3(a), can be fully described in transmission line terminology for a given resonance f_0 and a given resolution $R = Q_l = f_0/\delta f_0$. By cascading a network comprised of these filters branching off a transmission line, a full filter-bank can be

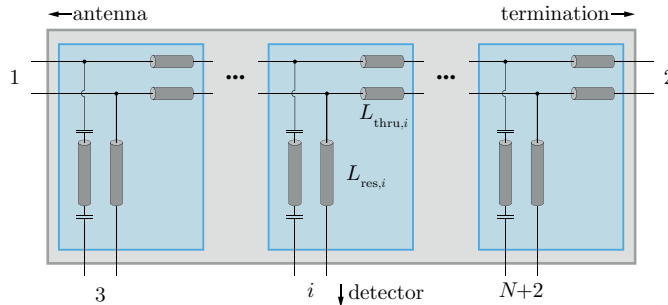


Figure 3.6: Filter-bank circuit model using the unit cell in Fig. 3.3 for each channel.

analyzed with a circuit model as depicted in Fig. 3.6 to obtain the S-parameters relating every port: input, detectors and termination of the filter-bank. To ease the calculations, an ABCD matrix approach was employed to link each pair of ports while the other were kept loaded. The S-parameters of the whole filter-bank can be easily obtained by means of the transformations in [132].

3.4. Filter-bank Circuit Model Analysis

We analyze the response of the circuit model in Fig. 3.6 for a filter-bank fully sampling the octave band 220–440 GHz with 347 band-pass filters designed to have a spectral resolution in isolation of $R = Q_i = 500$. The response of the lossless ($Q_i \rightarrow \infty$) filter-bank is depicted in Fig. 3.7 for an inter-filter separation along the through line of $L_{\text{thru},i} = \lambda_{\text{thru},i}/4$, where $\lambda_{\text{thru},i}$ is the effective wavelength of the microstrip mode propagating in the through-line at the resonance frequency of the i^{th} filter. Sub-figure (a) shows the frequency response of the S-parameters of the filter-bank: the reflections at its entrance ($|S_{11}|^2$), the transmission to the absorber behind it ($|S_{21}|^2$) and the response of all the filter-coupled detectors ($|S_{i1}|^2$) color-coded by their central frequency f_i . We have also emphasized in bold the channels around 250, 300, 350 and 400 GHz to showcase the response tails that are otherwise concealed by the neighboring spectral channels. Furthermore we have plotted the aggregated response of all the filter-coupled detectors ($\sum_{i=3}^{N-2} |S_{i1}|^2$) to exhibit the fraction of the available power at the filter-bank entrance that is actually coupled to the detectors. Sub-figure (b) shows a zoom-in of panel (a) to appreciate the tight spectral sampling with the overlap of the different channels. Sub-figure (c) over-plots all the filter-coupled responses with the frequency axis normalized by each filter central frequency f_i to emphasize the similar spectral resolution between the channels and how their Lorentzian profiles get distorted by the interactions between the filters. Sub-figure

(d) shows the obtained loaded quality factor Q_l for each filter-coupled channel. Sub-figure (e) displays the in-band coupling efficiency of each filter $\eta_{\text{filter},i}^{\text{FWHM}}$, which is the fraction of the available power at the input of the filter-bank that couples to the i^{th} detector within its half-power pass-band δf_i , and it is given by

$$\eta_{\text{filter},i}^{\text{FWHM}} = \frac{P_{\text{filter},i}^{\text{FWHM}}}{P_{\text{available}}^{\text{FWHM}}} = \frac{\int_{f_i-\delta f_i/2}^{f_i+\delta f_i/2} |S_{11}(f)|^2 df}{\delta f_i}. \quad (3.16)$$

This efficiency should become 100% for an ideal boxcar filter response. Instead, the response of our filters has a Lorentzian response (see (3.7)), thereby this ratio should be compared with the in-band coupling efficiency of an isolated³ shunted band-pass filter $\eta_{\text{filter}}^{\text{FWHM}}$, whose response is given by (3.7). The resulting expression for $\eta_{\text{filter}}^{\text{FWHM}}$ is analytic and it is given by

$$\eta_{\text{filter}}^{\text{FWHM}} = \frac{P_{\text{filter}}^{\text{FWHM}}}{P_{\text{available}}^{\text{FWHM}}} = \frac{\int_{f_0-\delta f_0/2}^{f_0+\delta f_0/2} |S_{31}(f)|^2 df}{\delta f_0} = \frac{\pi}{4} \frac{(Q_i - Q_l)^2}{2Q_i^2}, \quad (3.17)$$

peaking at 39.27% (-4.06 dB) for an isolated filter with $Q_i \rightarrow \infty$.

A critical design consideration for a filter-bank is the distance between the through-line and the first coupler of each resonator. Although it may be convenient for a realistic filter implementation to separate the coupler from the through-line by a short transmission line, this is discouraged. The de-tuning introduced in each filter branch, which to first order causes an increase of the reflections, results in the degradation of the overall filter-bank performance. This is exemplified in Fig. 3.8 for a lossless filter-bank with a short through-coupler separation of $\lambda/20$, where the distortion of the channels becomes evident.

Another crucial consideration is the ordering of the different resonators within the filter-bank. Arranging the filter-bank to have the low-frequency channels lead at the antenna side results in a reduced performance for the high-frequency channels as can be seen in Fig. 3.9. The cause for the hampering, even in this idealized lossless filter-bank, is in the reflections in the proximity of the second harmonic of the low-frequency channels. These reflections heavily decrease the high-frequency power reaching the last resonators in the filter-bank, which in this case are the high-frequency channels. Instead, in the conventional arrangement with the high-frequency filters leading, those reflections were actually boosting the coupling to the detectors.

The idealized lossless scenario ($Q_i \rightarrow \infty$) in Fig. 3.7 represents the benchmark filter-bank response. Instead, Fig. 3.10 gives a more realistic scenario with losses, which can be characterized by $Q_i = 3300$ for an actual device [113] as we will see in Section 5.3.2. As evidenced in Fig. 3.10, the performance of the different channels

³We define ‘isolated filter’ as a single filter as opposed to a filter embedded in a filter-bank.

of the filter-bank with an inter-filter spacing of $\lambda_{\text{thru},i}/4$ is similar to that of an isolated filter with a few differences: firstly, the average peak transmission in Fig. 3.10 is $\langle |S_{11}(f_i)|^2 \rangle \approx -5.95 \text{ dB} \approx 25\%$ (instead of $-4.4 \text{ dB} \approx 36\%$ as expected from (3.14) for an isolated filter with $Q_i = 3300$) due to the overlapping pass-bands of the filters; and secondly, the leading filters of the filter-bank (higher frequencies) get more power due to the coherent addition of the reflections from the lower frequency filters in the proximity to their second harmonic. The reflection level at the input of the filter-bank ($|S_{11}|^2$) remains below $-6 \text{ dB} \approx 25\%$ until the second harmonics of the low-frequency resonators ring at frequencies higher than 440 GHz. The fraction of the input power transferred to the absorber terminating the through-line ($|S_{21}|^2$) is high for frequencies below the operational band of the filter-bank and reduces as the different filters extract power from the through-line. An indication of how much of the input power is extracted by all the filters combined can be calculated using $\sum_{i=3}^{N+2} |S_{i1}|^2$, which averages to $-3.49 \text{ dB} \approx 45\%$ in the band of operation in Fig. 3.10(a). The rest of the power is reflected at the entrance of the filter-bank, absorbed in its termination or associated to losses. The loaded quality factor averages 422 as seen from Fig. 3.10(d), which is lower than the intended value of 500 due to the interaction of the filters. Finally $\eta_{\text{filter},i}^{\text{FWHM}}$, which the ratio of power coupled within the half-power bandwidth of each filter to the available power at the entrance of the filter-bank over the same band is shown in Fig. 3.10(e). The average value is $\langle \eta_{\text{filter},i}^{\text{FWHM}} \rangle \approx -6.70 \text{ dB} \approx 21\%$, which is slightly lower than the $\eta_{\text{filter}}^{\text{FWHM}} \approx -5.49 \text{ dB} \approx 28\%$ for a single filter in isolation.

We shall now compare the response of the filter-bank with loss ($Q_i = 3300$) for three different inter-filter separations $L_{\text{thru},i}$: $\lambda_{\text{thru},i}/4$, $\lambda_{\text{thru},i}/2$ and $3\lambda_{\text{thru},i}/4$. The filter-bank with the $\lambda_{\text{thru},i}/4$ spacing shown in Fig. 3.10 performs well thanks to the constructive interference between the incoming signal and the reflections from the neighboring filters. When compared to the idealized lossless case in Fig. 3.7, the in-band coupling efficiency $\eta_{\text{filter},i}^{\text{FWHM}}$ is slightly degraded as evidenced in panel (e) due to the Q_i reduction, while the other panels remain quite similar. On the contrary, for a spacing of $\lambda_{\text{thru},i}/2$, panel (e) of Fig. 3.11 displays a strong reduction in the detector coupling due to the destructive interference between filters. From the $3\lambda_{\text{thru},i}/4$ case in Fig. 3.12 it is observed that a maximum inter-filter separation of $\lambda_{\text{thru},i}/4$ must be kept to prevent additional reflections from appearing within the octave band of a broadband filter-bank.

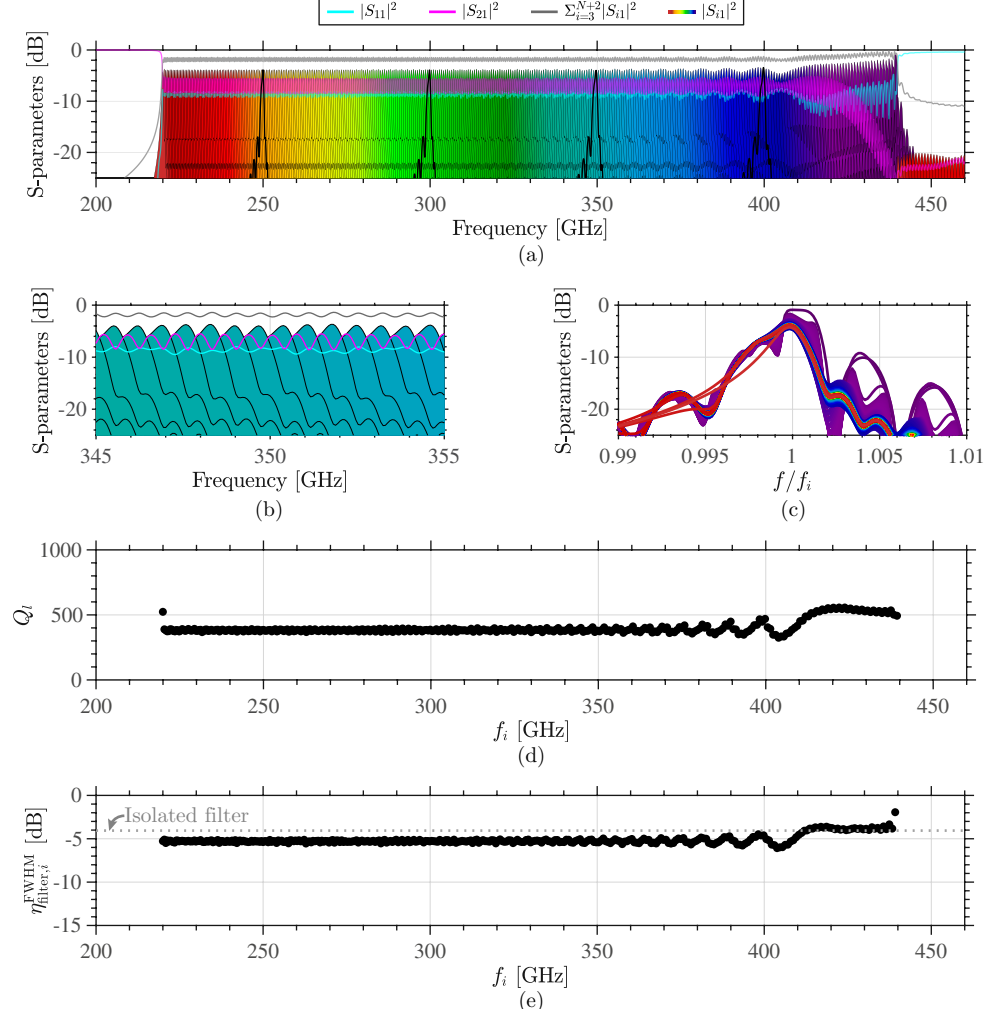


Figure 3.7: Simulated performance for a filter-bank circuit model fully sampling the 220–440 GHz band with $N = 347$ filters ordered $f_{\max} \rightarrow f_{\min}$, with a targeted spectral resolution of $R = Q_l = 500$, $Q_i \rightarrow \infty$, an inter-filter separation of $L_{\text{thru},i} = \lambda_{\text{thru},i}/4$ and no through-coupler separation. Panel (a) shows the S-parameters of the filter-bank, emphasizing some pass-bands for clarity. Panel (b) is a zoom-in of (a) around 350 GHz. Panel (c) overlays the response of the different filters around their resonance. Panel (d) shows the loaded quality factor of each filter, averaging $\langle Q_i \rangle \approx 398$. Panel (e) reports the in-band coupling efficiency for each channel, averaging $\langle \eta_{\text{filter},i}^{\text{FWHM}} \rangle \approx -5.10 \text{ dB} \approx 31\%$, and for an isolated filter, giving $\eta_{\text{filter}}^{\text{FWHM}} \approx -4.06 \text{ dB} \approx 39\%$.

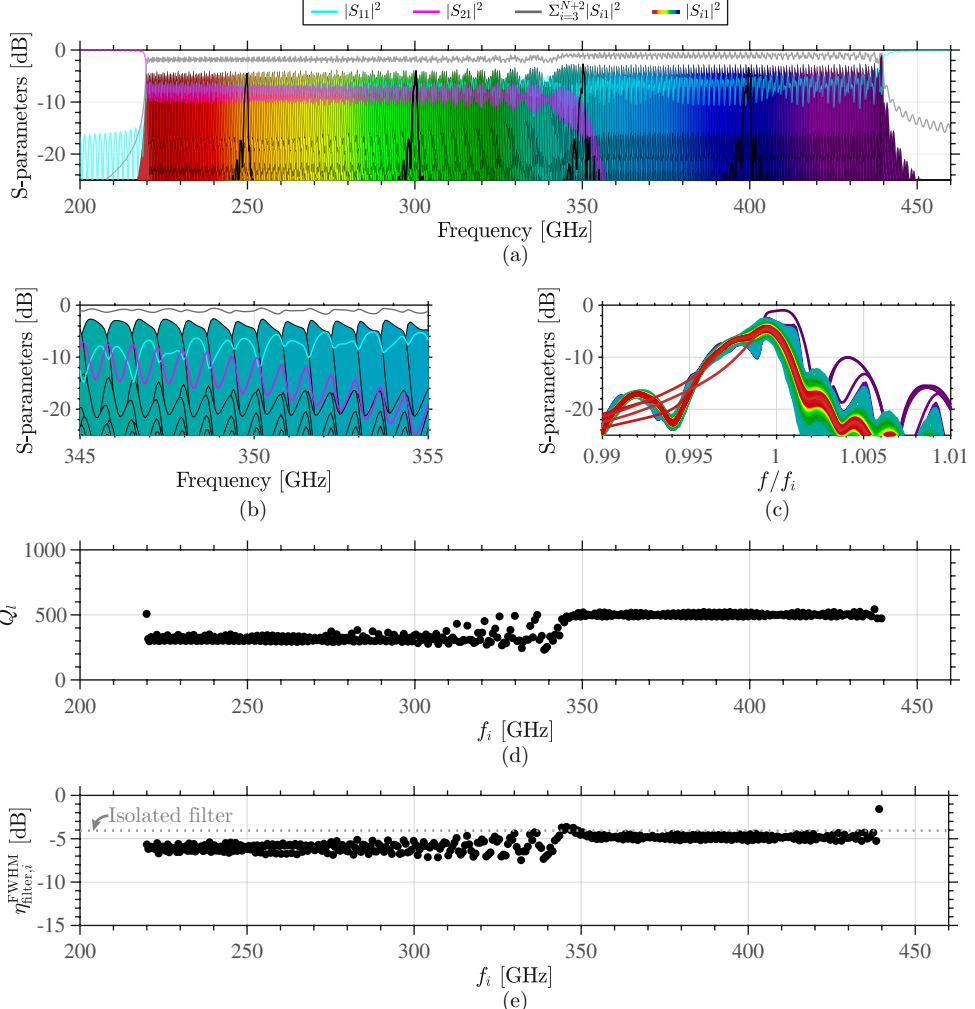


Figure 3.8: Simulated performance for a filter-bank circuit model fully sampling the 220–440 GHz band with $N = 347$ filters ordered $f_{\max} \rightarrow f_{\min}$, with a targeted spectral resolution of $R = Q_l = 500$, $Q_i \rightarrow \infty$, an inter-filter separation of $L_{\text{thru},i} = \lambda_{\text{thru},i}/4$ and a through-coupler separation of $\lambda/20$. Panel (a) shows the S-parameters of the filter-bank, emphasizing some pass-bands for clarity. Panel (b) is a zoom-in of (a) around 350 GHz. Panel (c) overlays the response of the different filters around their resonance. Panel (d) shows the loaded quality factor of each filter, averaging $\langle Q_l \rangle \approx 385$. Panel (e) reports the in-band coupling efficiency for each channel, averaging $\langle \eta_{\text{filter},i}^{\text{FWHM}} \rangle \approx -5.48 \text{ dB} \approx 28\%$, and for an isolated filter, giving $\eta_{\text{filter}}^{\text{FWHM}} \approx -4.06 \text{ dB} \approx 39\%$.

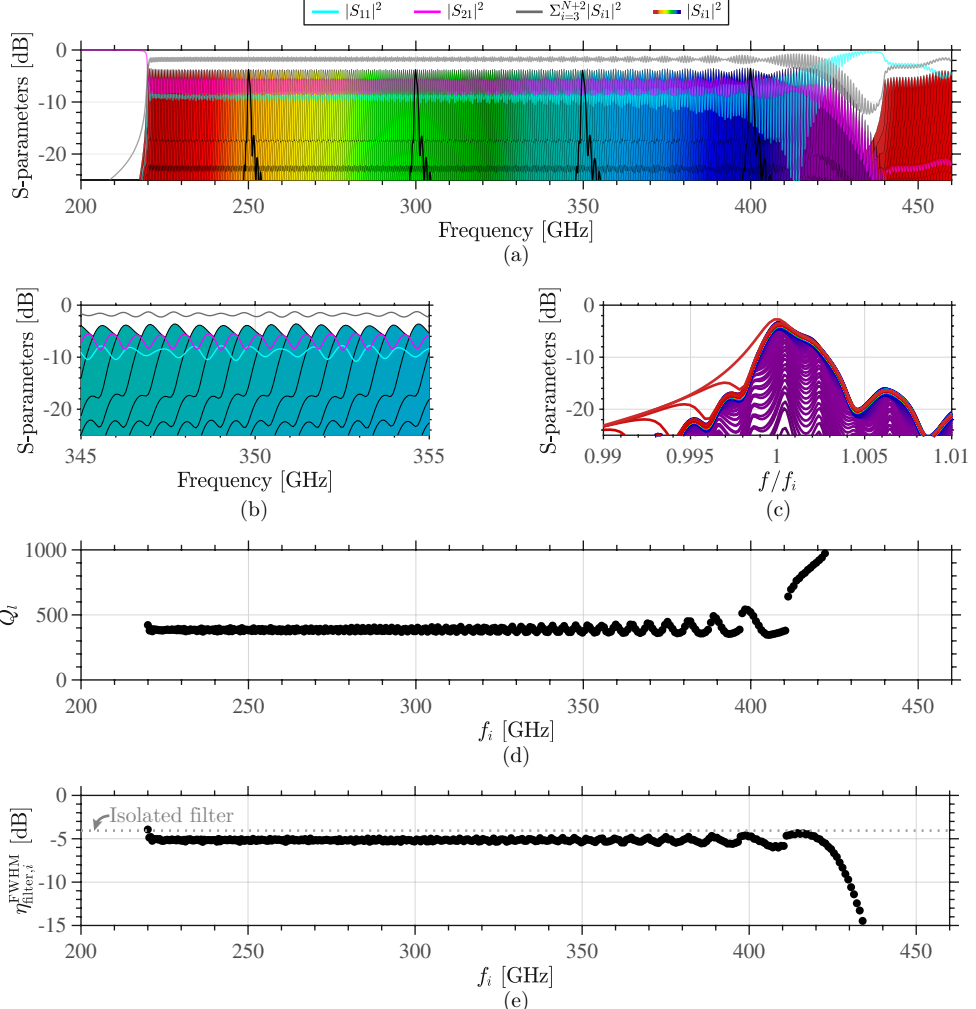


Figure 3.9: Simulated performance for a filter-bank circuit model fully sampling the 220–440 GHz band with $N = 347$ filters ordered $f_{\min} \rightarrow f_{\max}$, with a targeted spectral resolution of $R = Q_l = 500$, $Q_i \rightarrow \infty$, an inter-filter separation of $L_{\text{thru},i} = \lambda_{\text{thru},i}/4$ and no through-coupler separation. Panel (a) shows the S-parameters of the filter-bank, emphasizing some pass-bands for clarity. Panel (b) is a zoom-in of (a) around 350 GHz. Panel (c) overlays the response of the different filters around their resonance. Panel (d) shows the loaded quality factor of each filter, averaging $\langle Q_i \rangle \approx 455$. Panel (e) reports the in-band coupling efficiency for each channel, averaging $\langle \eta_{\text{filter},i}^{\text{FWHM}} \rangle \approx -5.31 \text{ dB} \approx 29\%$, and for an isolated filter, giving $\eta_{\text{filter}}^{\text{FWHM}} \approx -4.06 \text{ dB} \approx 39\%$.

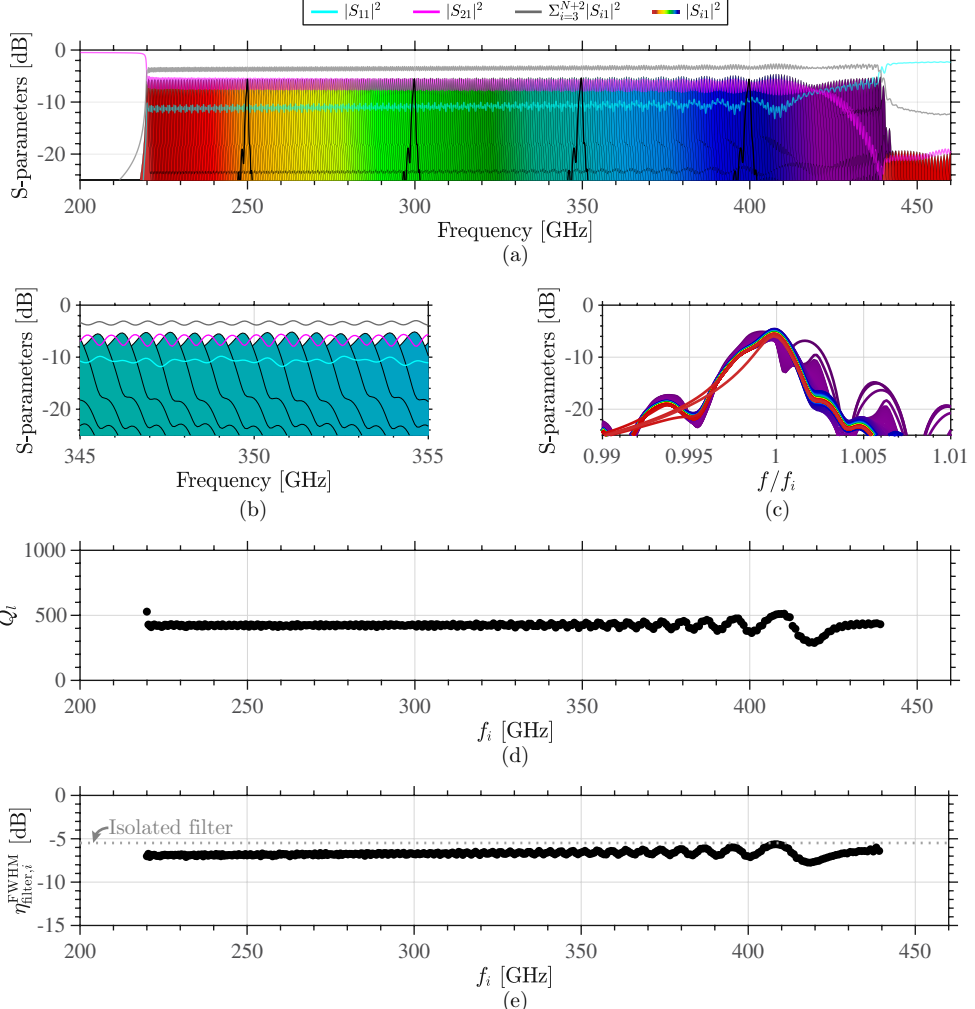


Figure 3.10: Simulated performance for a filter-bank circuit model fully sampling the 220–440 GHz band with $N = 347$ filters ordered $f_{\max} \rightarrow f_{\min}$, with a targeted spectral resolution of $R = Q_l = 500$, $Q_i = 3300$, an inter-filter separation of $L_{\text{thru},i} = \lambda_{\text{thru},i}/4$ and no through-coupler separation. Panel (a) shows the S-parameters of the filter-bank, emphasizing some pass-bands for clarity. Panel (b) is a zoom-in of (a) around 350 GHz. Panel (c) overlays the response of the different filters around their resonance. Panel (d) shows the loaded quality factor of each filter, averaging $\langle Q_l \rangle \approx 422$. Panel (e) reports the in-band coupling efficiency for each channel, averaging $\langle \eta_{\text{filter},i}^{\text{FWHM}} \rangle \approx -6.70 \text{ dB} \approx 21\%$, and for an isolated filter, giving $\eta_{\text{filter}}^{\text{FWHM}} \approx -5.49 \text{ dB} \approx 28\%$.

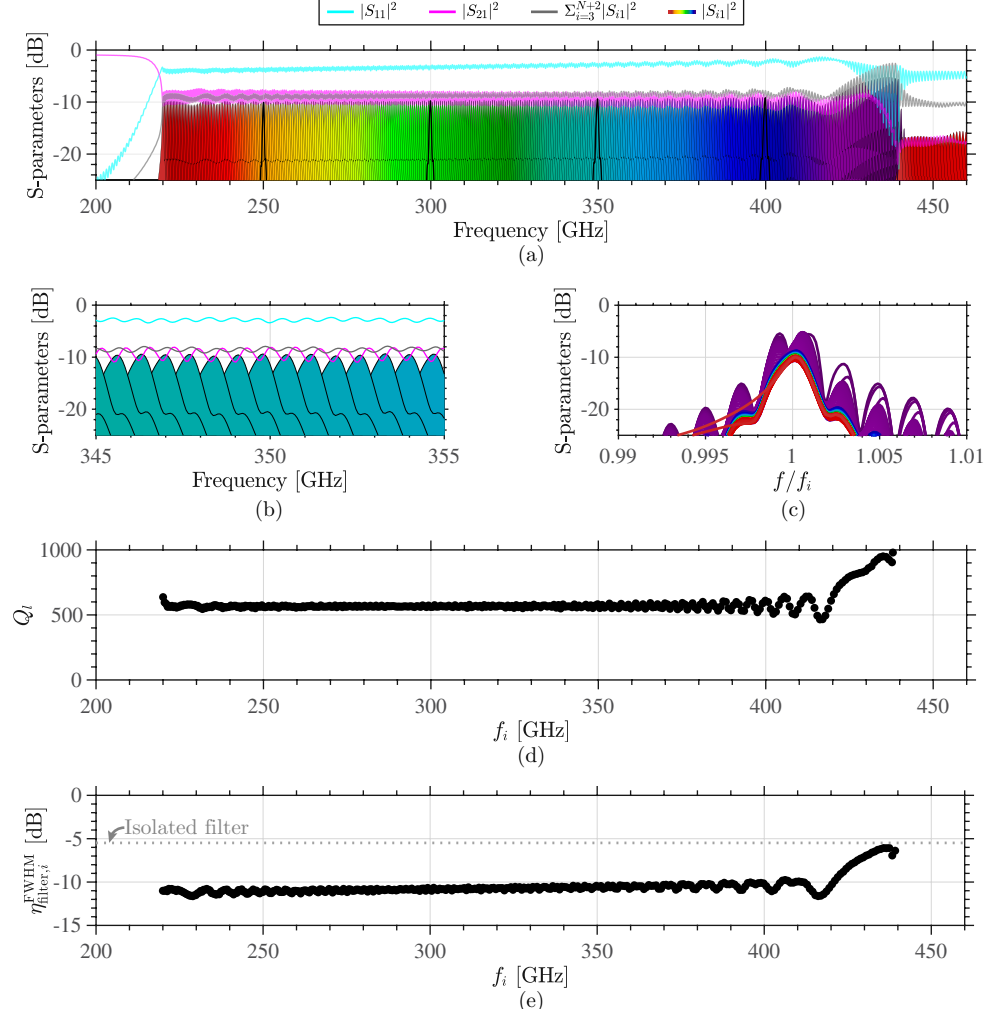


Figure 3.11: Simulated performance for a filter-bank circuit model fully sampling the 220–440 GHz band with $N = 347$ filters ordered $f_{\max} \rightarrow f_{\min}$, with a targeted spectral resolution of $R = Q_l = 500$, $Q_i = 3300$, an inter-filter separation of $L_{\text{thru},i} = \lambda_{\text{thru},i}/2$ and no through-coupler separation. Panel (a) shows the S-parameters of the filter-bank, emphasizing some pass-bands for clarity. Panel (b) is a zoom-in of (a) around 350 GHz. Panel (c) overlays the response of the different filters around their resonance. Panel (d) shows the loaded quality factor of each filter, averaging $\langle Q_i \rangle \approx 585$. Panel (e) reports the in-band coupling efficiency for each channel, averaging $\langle \eta_{\text{filter},i}^{\text{FWHM}} \rangle \approx -10.45 \text{ dB} \approx 9\%$, and for an isolated filter, giving $\eta_{\text{filter}}^{\text{FWHM}} \approx -5.49 \text{ dB} \approx 28\%$.

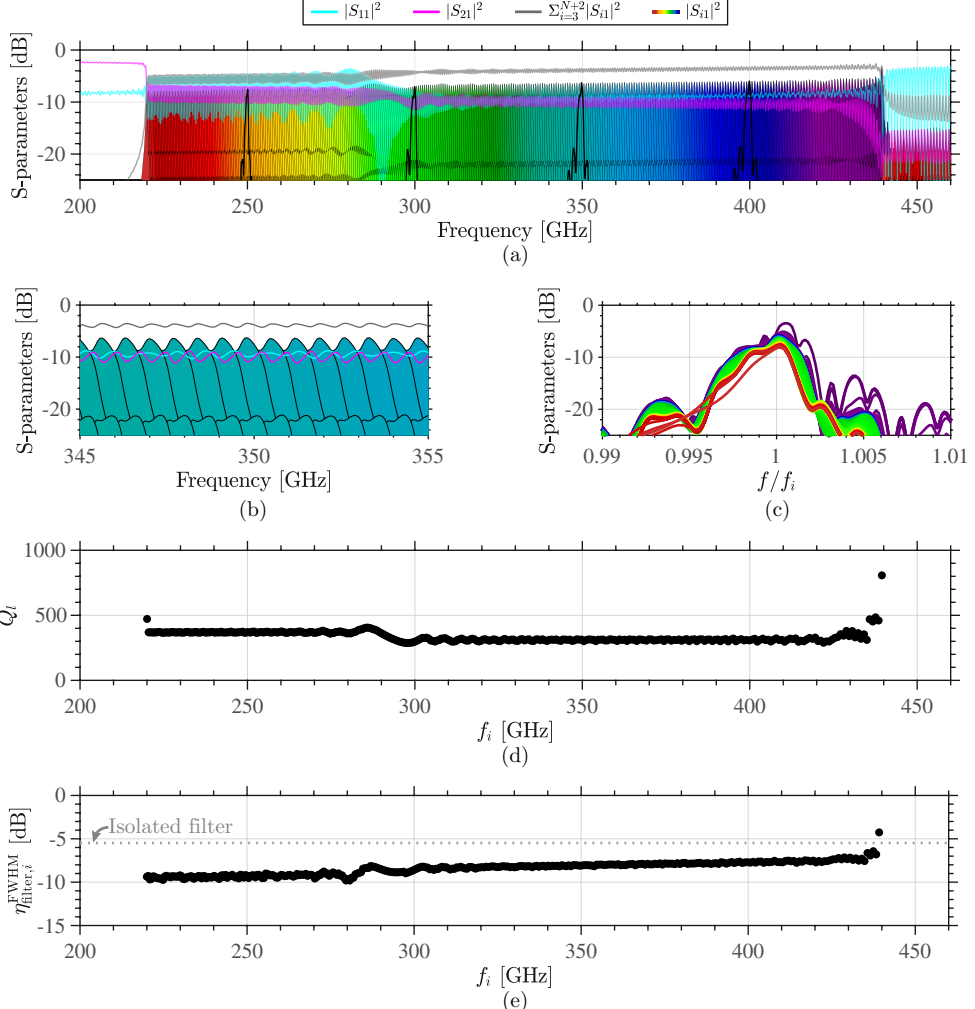


Figure 3.12: Simulated performance for a filter-bank circuit model fully sampling the 220–440 GHz band with $N = 347$ filters ordered $f_{\max} \rightarrow f_{\min}$, with a targeted spectral resolution of $R = Q_l = 500$, $Q_i = 3300$, an inter-filter separation of $L_{\text{thru},i} = 3\lambda_{\text{thru},i}/4$ and no through-coupler separation. Panel (a) shows the S-parameters of the filter-bank, emphasizing some pass-bands for clarity. Panel (b) is a zoom-in of (a) around 350 GHz. Panel (c) overlays the response of the different filters around their resonance. Panel (d) shows the loaded quality factor of each filter, averaging $\langle Q_l \rangle \approx 340$. Panel (e) reports the in-band coupling efficiency for each channel, averaging $\langle \eta_{\text{filter},i}^{\text{FWHM}} \rangle \approx -8.42 \text{ dB} \approx 14\%$, and for an isolated filter, giving $\eta_{\text{filter}}^{\text{FWHM}} \approx -5.49 \text{ dB} \approx 28\%$.

3.5. Conclusions

In this chapter we have investigated the theoretical foundations for the construction of a moderate spectral resolution fully-sampled octave-band filter-bank based on half-wavelength resonators acting as band-pass filters. Each of these filters has been analyzed from an energetic point of view, arriving to analytical expressions of its S-parameters in terms of the resonator quality factors and the resonance frequency. We have built a circuit model for a single band-pass filter that allows the arraying into a the filter-bank configuration with conventional microwave techniques. The filter-bank circuit model has given us insights on the effect of the different parameters involved. In particular, it has been shown that the separation between the through-line and the first coupler of each resonator must be minimized to avoid reflections that distort the response of neighboring channels. Furthermore, the ordering of the band-pass filters within the filter-bank needs to be from the high- to the low- frequency resonators to avoid hampering the response of the high-frequency channels due to losses and in-band reflections. We have also investigated the inter-filter separation and we have concluded that, in order to avoid reflections within an octave-band free spectral range, it has to be limited to $L_{\text{thru},i} < \lambda_{\text{thru},i}/4$. Lastly, it has become obvious that there is a need for high Q_i (low-loss) structures to achieve moderate spectral resolutions without compromising the coupling to the detectors.

Chapter 4

Co-planar THz Band-Pass Filters

Co-planar technology provides the easiest fabrication alternative for on-chip circuitry. In this light, superconducting co-planar THz filter-banks with moderate spectral resolution $R = f/\delta f$ have been investigated in the literature [133, 134]. This technology has been used for the first practical implementation of the THz on-chip filter-bank for astronomy in the DESHIMA 1.0 instrument [49, 74]. In this chapter we explain the performance of such filter-bank and the amendments that can be made in co-planar technology to improve its operation.

4.1. DESHIMA 1.0

The DESHIMA 1.0 instrument, which was developed outside of the scope of this thesis, was the first THz on-chip spectrometer to see first light at a telescope site [74], in particular at the ASTE telescope in Chile. As illustrated in Fig. 4.1, the chip consists of a superconducting filter-bank with 49 band-pass filters designed to probe the 332–377 GHz band (13% relative bandwidth) with a constant spectral sampling given by $R = 380$ as shown in Fig. 4.2. The on-chip circuitry is patterned on 100 nm-thick NbTiN layer ($L_k = 1 \text{ pH}/\square$) deposited on a c-plane Sapphire wafer. The THz radiation is coupled to the chip via a double-slot antenna placed at the focus of an $\varnothing 8 \text{ mm}$ extended-hemispherical Si lens. A superconducting 2–2–2 μm (slot-gap-slot width) CPW connects the antenna with the filter-bank. In the filter-bank, NbTiN-Al hybrid MKID detectors [108] couple power from different THz sub-bands with 49 meandered-slot filters parallel-coupled to the CPW through-line every $3\lambda/4$. Three wideband-coupled detectors, both at the entrance and at the back of the filter-bank,

Parts of this chapter have been published in *J. Astron. Telesc. Instrum. Syst.* [49].

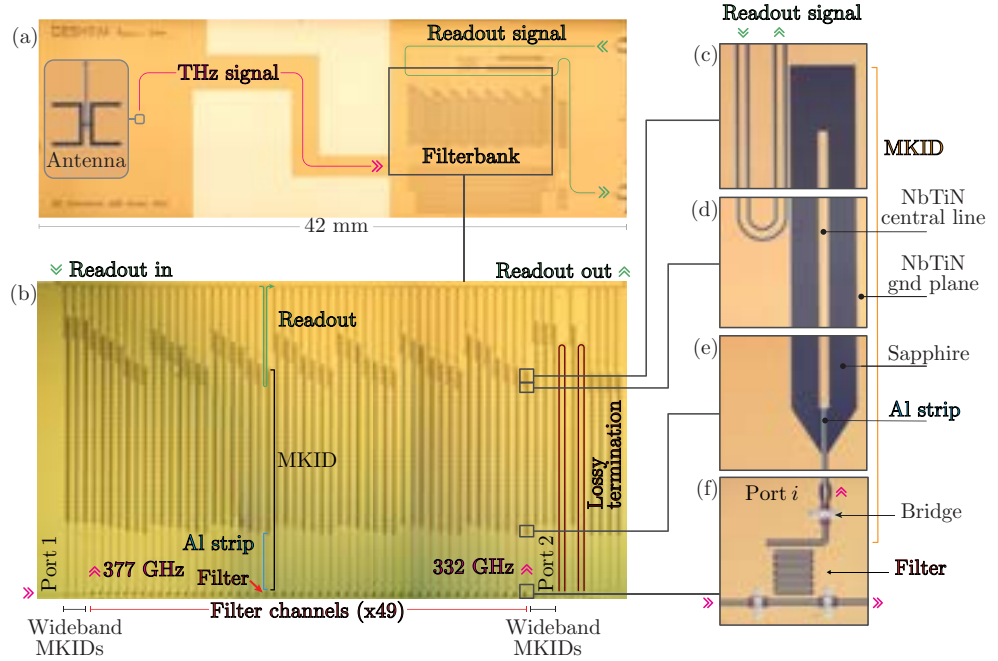


Figure 4.1: The DESHIMA 1.0 chip is shown in sub-figure (a). Panel (b) emphasizes the filter-bank and its parts; namely the entrance from the antenna, the termination, the THz filters, the wideband couplers, the MKIDs and the readout line. Sub-figures (c)–(f) highlight the different parts of a spectral channel including, from top to bottom, the readout line, the NbTiN-Al hybrid MKID, the meandered-slot THz band-pass filter and the THz through line. Figure adapted from [49].

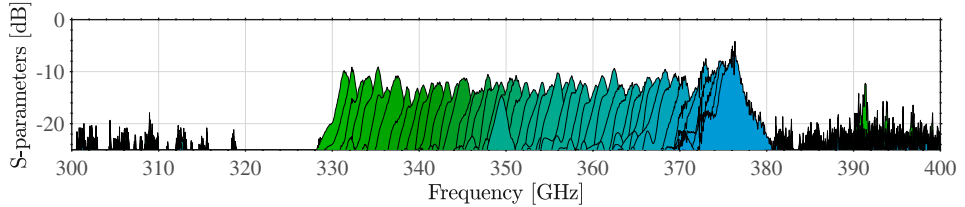


Figure 4.2: Measured frequency response of the filter-coupled detectors of the DESHIMA 1.0 chip with respect to the entrance of the filter-bank (see Fig. 4.1 for reference). The average peak coupling efficiency is -11 dB. The average loaded quality of the Lorentzian fits (following (3.7)) of these responses is $\langle Q_l \rangle \approx 300$, which is lower than the spectral sampling of $R = 380$ used, resulting in a slightly over-sampled filter-bank.

weakly couple THz power for diagnostic purposes. All these MKID detectors are sensed in parallel with a single frequency-multiplexed readout line.

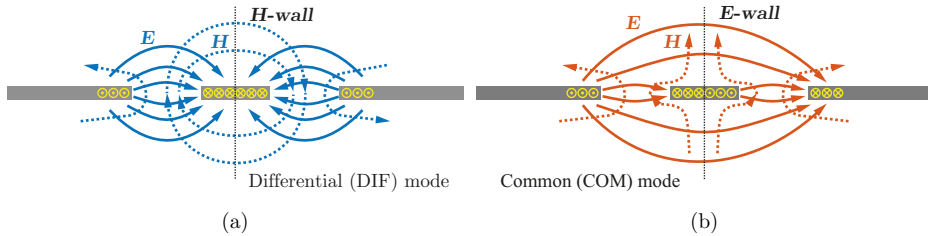


Figure 4.3: CPW line with its two fundamental modes: (a) the differential (DIF) mode and (b) the common (COM) mode. The continuous lines represent the electric field, the dotted lines the magnetic field and the yellow marks the electric currents.

The optical efficiency of the detectors of the DESHIMA 1.0 instrument averages to about $-17.79 \text{ dB} \approx 1.6\%$ measured from the opening of the cryostat. This efficiency includes the transmission through the cold optics ($\eta_{\text{opt}} \approx -0.97 \text{ dB} \approx 80\%$, simulated in GRASP [135]), the quasi-optical filter stack ($\eta_{\text{QOF}} \approx -3.98 \text{ dB} \approx 40\%$), the lens-antenna ($\eta_{\text{ant}} \approx -1.55 \text{ dB} \approx 70\%$, simulated in CST Microwave Studio [98]), the 30 bridges on the otherwise lossless (superconducting and radiation-free) CPW line [126] between the antenna and the filter-bank entrance ($\eta_{\text{tl}} \approx -0.32 \text{ dB} \approx 93\%$) and the efficiency of the filter-coupled detectors (port i in Fig. 4.1) with respect to the entrance of the filter-bank (port 1), which averages to $\langle |S_{i1}|^2 \rangle \approx -10.97 \text{ dB} \approx 8\%$, as shown in the frequency response in Fig. 4.2. We shall now investigate the cause for the low transmission through the bridges and the low coupling efficiency of the filters.

4.2. Bridges on a CPW Line

CPW lines support two fundamental modes: the differential (DIF) mode, for which the electric fields on the two slots have opposite directions (Fig. 4.3(a)), and the common (COM) mode, with electric fields in the two slots oriented in the same direction (Fig. 4.3(b)). The differential mode is the weakly-radiative fundamental transmission line mode of a CPW, whereas the common mode is mostly a broadband radiative mode associated to a leaky wave when the slots are placed between two media with different permittivity [136]. The excitation of the common mode incurs in radiation loss and thus should be avoided.

Bridges are routinely used in CPW lines to prevent the support of the spurious common mode [137–142]. At the THz frequencies of operation of the filter-bank, the excitation of the common mode introduces large radiation losses (as we will see in Section 4.5) and the materials of the bridges become lossy. In particular, the bridges used in DESHIMA 1.0 consist of a $1.1 \mu\text{m}$ -thick polyimide (Fujifilm LT9505, with $\epsilon_r \approx 2.9$

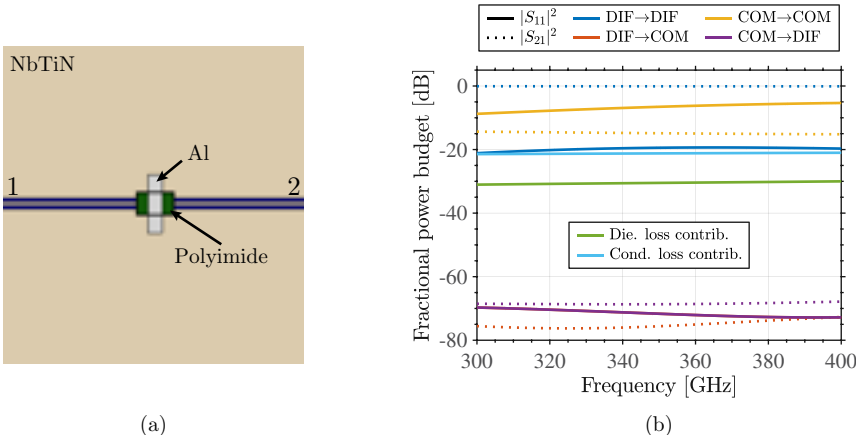


Figure 4.4: Polyimide-Al bridge balancing the grounds of a 2-2-2 μm CPW in (a) and its power budget in (b). The dielectric and conductor loss contributions are given for a differential excitation of the structure.

and $\tan \delta \approx 5 \times 10^{-3}$ [143]) dielectric support and a 40 nm-thick Al ($T_c = 1.25$ K, $R_s = 0.63 \Omega/\square$ ¹) strip connecting the NbTiN CPW grounds. As illustrated in Fig. 4.4, these bridges just partially reflect the common mode (-8.8 dB to -5.3 dB or 13–30%) but *do not transform it into a differential mode*. As a result, once the common mode is excited, its power is radiated unless it is asymmetrically re-coupled to a differential mode. Furthermore, the design of these bridges was not optimized and therefore affect the differential mode, yielding a reflection level of $|S_{11}|^2 \approx -20$ dB. The ohmic loss contributions in both the Al strip (used beyond its gap frequency at $f_{\text{gap}} = 90$ GHz) and the polyimide amount respectively to -21 dB and -30.5 dB. The resulting transmission for the differential mode is $\langle |S_{21}|^2 \rangle \approx -0.10$ dB $\approx 97.7\%$.

CPW bridges do not avoid the common mode, but they can still be valuable in co-planar circuitry for alleviating the effects of this mode by impeding its propagation or by confining it in a certain region. Given the usefulness of the bridges, we propose two amendments to improve their transparency to the differential mode. The bridges shown in Fig. 4.4 mostly suffer from conductor loss, due to the Al strip, and reflections, due to the parasitic capacitance between the strip and the CPW. Firstly, to avoid conductive dissipation, the strip connecting the CPW grounds could be made of a superconducting metal with a gap frequency exceeding the frequency of operation. NbTiN would be the obvious choice, with a gap frequency of $f_{\text{gap}}^{\text{NbTiN}} \approx 1.1$ THz. Sec-

¹This is slightly higher than the surface resistance of $R_s = 0.2 \Omega/\square$ obtained from the resistivity of $\rho_n = 0.8 \mu\Omega \text{cm}$ reported in [49] for the 40 nm-thick Al film directly grown on Sapphire instead of polyimide.

4.3. CPW Turns

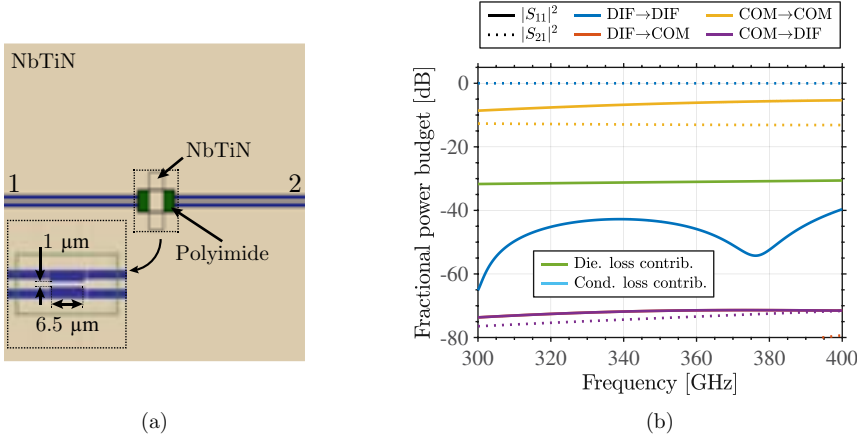


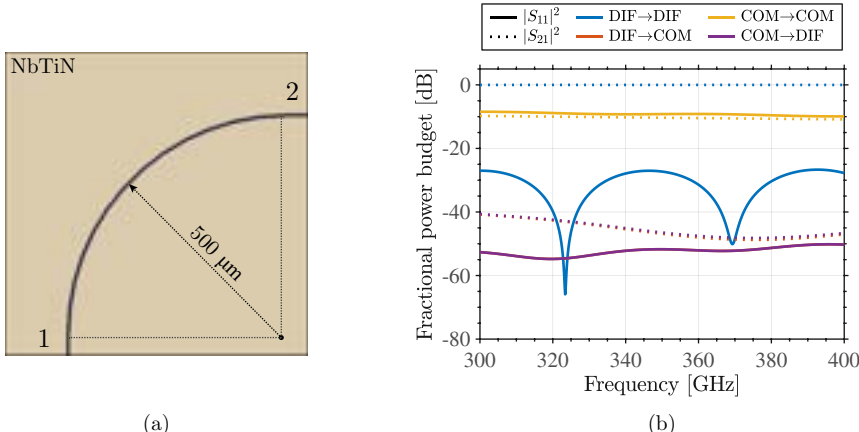
Figure 4.5: Polyimide-NbTiN reactively-tuned bridge. Sub-figure (a) shows the structure, with an inset displaying the narrowing of the CPW central conductor under the bridge. Sub-figure (b) exhibits the improved performance of this structure with no conductor loss and negligible reflections with respect to the normal bridge in Fig. 4.4. The dielectric and conductor loss contributions are given for a differential excitation of the structure.

ondly, to improve the reflection level of the differential mode, the central conductor of the CPW could be narrowed locally to tune out the capacitance with an inductive loading. These two measures result in the polyimide-NbTiN reactively-tuned bridge of Fig. 4.5. Compared to the nominal bridges of Fig. 4.4, the improved bridges show lower reflection level, no conductor loss and negligible dielectric loss, resulting in a transmission of the differential mode of $\langle |S_{21}|^2 \rangle \approx -0.015 \text{ dB} \approx 99.6\%$. The common mode rejection remains similar to the nominal bridges.

4.3. CPW Turns

At high frequencies, the delay between the electromagnetic fields in the two slots of a CPW starts to play a role in turns. This delay is caused by the path length difference between the two slots, and it is solely dependent on the width of the CPW, not on the radius of curvature of the turn. The phase difference between the fields in the two slots partially converts the differential mode into a common mode.

The 2-2-2 μm CPW connecting the antenna with the filter-bank makes three 90° turns while traversing the labyrinth structure of the chip holder for stray-light control. Despite the low mode conversion DIF \rightarrow COM in one of such turns with no bridges, as indicated in Fig. 4.6, to prevent the propagation of a common mode, 10 equispaced

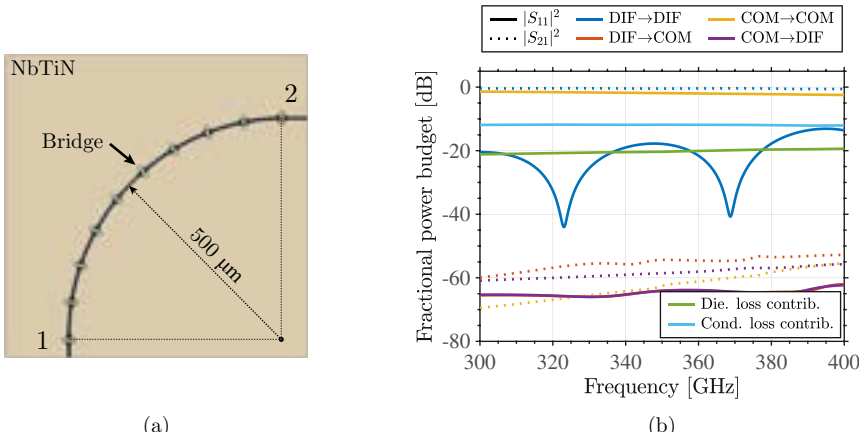


4

(a)

(b)

Figure 4.6: Turn of 90° and a radius of curvature of 500 μm for a 2-2-2 μm CPW with no bridges. Sub-figure (a) shows the structure and sub-figure (b) gives its frequency response for the different port mode combinations.



(a)

(b)

Figure 4.7: Turn of 90° and a radius of curvature of 500 μm for a 2-2-2 μm CPW with 10 equispaced bridges along the bend. Sub-figure (a) shows the structure and sub-figure (b) gives its frequency response for the different port mode combinations. The dielectric and conductor loss contributions are given for a differential excitation of the structure.

bridges were added on each turn as shown in Fig. 4.7. The inclusion of these bridges however incurs in a degraded differential mode transmission of $\langle |S_{21}|^2 \rangle \approx -0.44 \text{ dB} \approx 90\%$, due to the reflections and the ohmic losses anticipated in Fig. 4.4 for a bridge on a straight CPW.

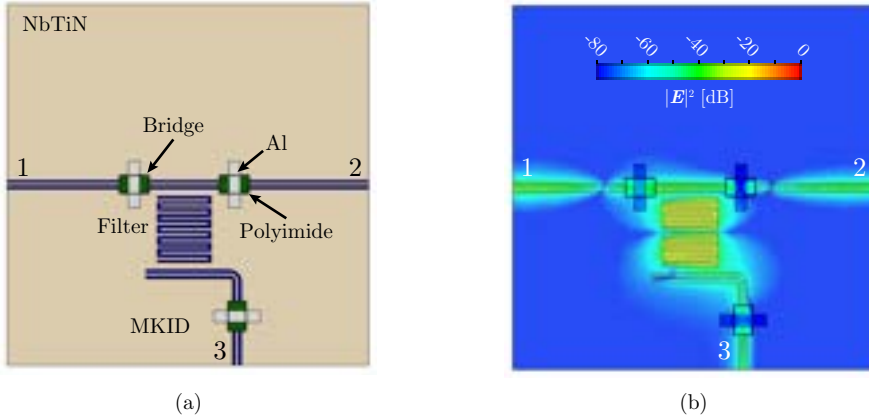


Figure 4.8: Sub-figure(a) shows a meandered-slot filter used in DESHIMA 1.0. Sub-figure (b) is a temporal snapshot of the normalized electric-field magnitude of the filter simulated at the resonance frequency of 374.6 GHz.

4.4. Meandered-Slot as a Band-Pass Filter

The THz band-pass filters used for DESHIMA 1.0 consist of a meandered slot as shown in Fig. 4.8. These co-planar filters couple THz power over a small pass-band from the 2-2-2 μm CPW through-line to a CPW MKID detector. By varying the length of the meandered sections, the resonant pass-band of these filters can be shifted over a moderate bandwidth while maintaining a similar loaded quality factor. The quality factor in turn is designed to a certain level by tuning the separation to the coupling CPW lines of the MKID and the through-line. In the neighborhood of every filter, these CPW lines are loaded asymmetrically, thereby inducing an unbalance in the potential of their grounds. To equalize the grounds on those CPWs, bridges are placed around the filters.

The frequency response of an isolated filter in the proximity of the filter-bank entrance (i. e. at the antenna end of the through-line) is shown in Fig. 4.9. Sub-figure (a) shows a large frequency span, where multiple harmonics of this filter can be seen. These multiple resonances effectively limit the operation of a filter-bank using these filters to a 21% bandwidth given by their free spectral range. Sub-figure (b) is a detailed view of the filter response around the resonance at ~ 374.6 GHz, which is the one used for filtering purposes due to its higher coupling strength. The simulated S-parameters of the isolated filter are compared with the measured frequency response of the corresponding channel of the filter-bank in Fig. 4.2. Despite the measured channel being embedded in the filter-bank, because it corresponds to one of the band-

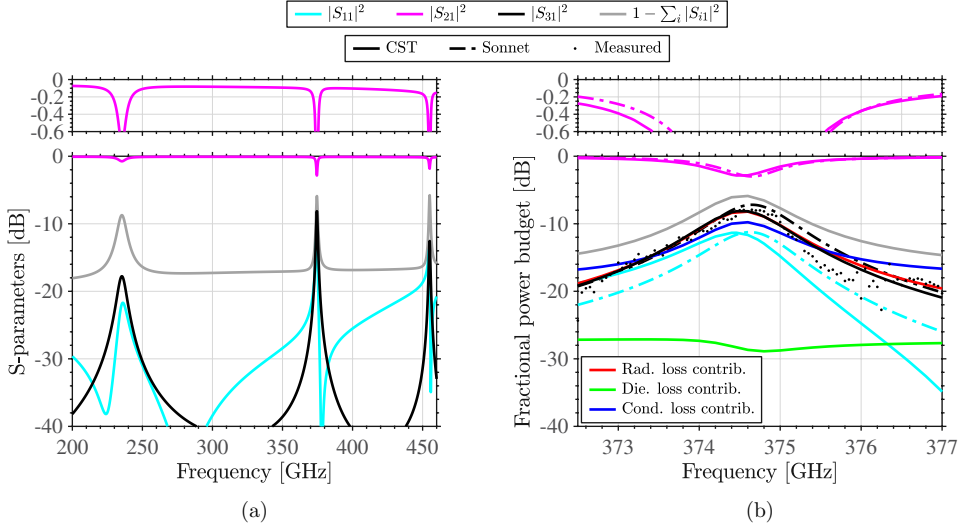


Figure 4.9: Frequency response of the filter in Fig. 4.8 as simulated with CST [98] (solid lines), Sonnet [99] (dashed-dotted lines), and measured (dots). The Sonnet simulations were originally used by Endo et al. to design this filter [144]. Sub-figure (a) shows the S-parameters over a moderate bandwidth, emphasizing the multiple resonances limiting the free spectral range of this filter and the low transmission off-resonance. Sub-figure (b) gives a detailed view of the power budget of the filter around the intended resonance at 374.6 GHz. The loss contributions are given for a differential excitation of the structure.

edge filters, its response is less affected by the neighboring channels. As a result, the agreement between the measured and simulated coupling efficiency $|S_{31}(f)|^2$ of the filter is found to be good², yielding a peak coupling efficiency of $|S_{31}|^2 \approx -8.1 \text{ dB} \approx 15.3\%$ and a moderate loaded quality factor of $Q_l \approx 361$. This performance, although higher than that of an average filter in Fig. 4.2 due to the diminished cross-talk between channels at the edge of the band, it is still low because of the high total loss (sum of conductor, dielectric and radiation losses) present in the system, which is associated to $Q_i \approx 826$ using (3.14). At the resonance frequency, the total power lost from the available power at port 1 amounts to $1 - \sum_i |S_{ii}|^2 \approx -5.9 \text{ dB} \approx 25.8\%$; comprising $-8.2 \text{ dB} \approx 15.2\%$ of power radiated, and $-9.8 \text{ dB} \approx 10.5\%$ and $-28.7 \text{ dB} \approx 0.1\%$ of power being respectively dissipated in the Al strips and the polyimide blocks of the bridges surrounding the filter. It can be noted that the contributions to the power budget ($|S_{ii}|^2$ and loss terms) add up to unity.

²The simulated kinetic inductance of the ground plane in CST had to be adjusted to $L_k = 0.71 \text{ pH}/\square$ to match the measured resonance location for a fabricated device with a $L_k = 1 \text{ pH}/\square$ NbTiN film. This discrepancy is not present in Sonnet [144]. See Appendix A.

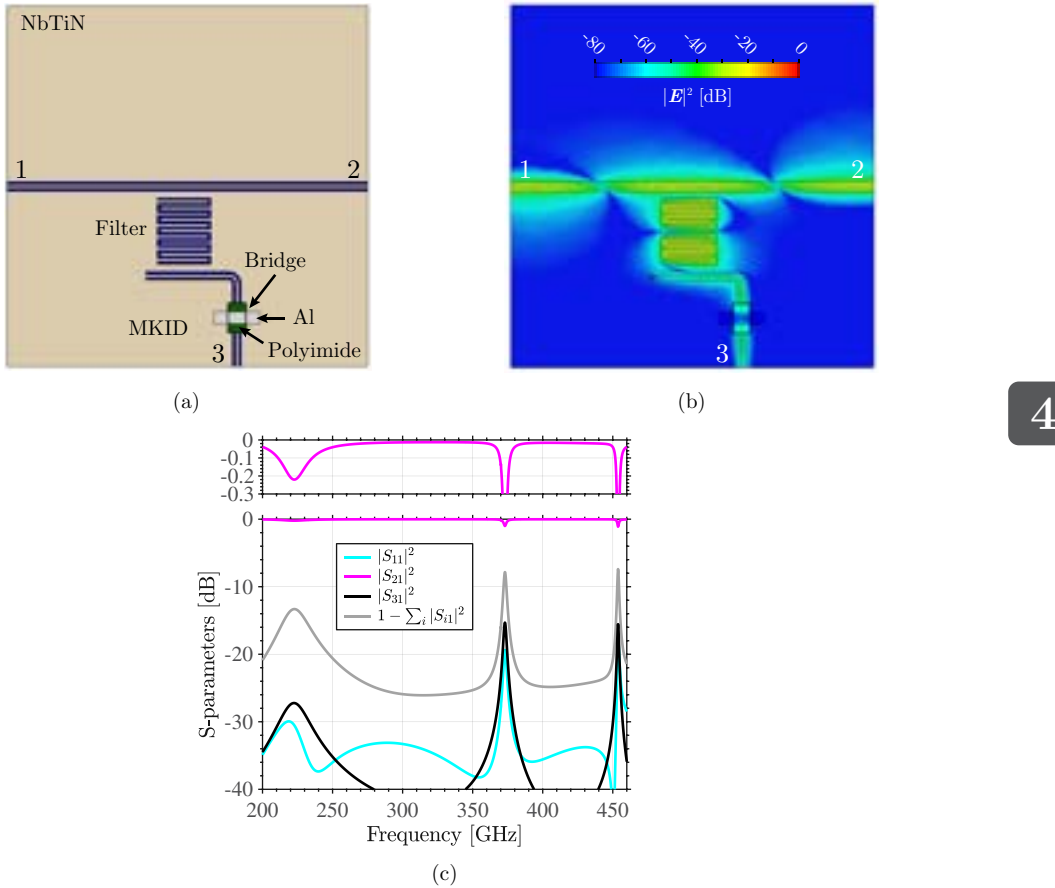


Figure 4.10: The band-pass filter in sub-figure (a) is the same as in Fig. 4.8 but without the bridges in the through-line. Sub-figure (b) shows a temporal snapshot of the normalized electric field magnitude at the resonance frequency of 374.6 GHz. The effect of the asymmetric loading on the through-line can be seen from the tilted wavefront. Sub-figure (c) shows the simulated S-parameters of the structure. The coupling to the detector ($|S_{31}|^2$) is severely degraded with respect to Fig. 4.9. Instead, the off-resonance transmission is improved due to the absence of bridges in the through-line, which dissipated power.

We now showcase the importance of the bridges surrounding each filter and how they help to boost the coupling to the detectors. The asymmetric loading of the through-line induces a common mode on it that is bounced between the surrounding bridges and it is eventually partially coupled COM \rightarrow DIF³ into the detector

³The COM \rightarrow DIF coupling can be stronger than the designed DIF \rightarrow DIF coupling, e. g. Fig. 4.13(a).

and partly radiated. Instead, if the bridges in the through-line are removed as shown in Fig. 4.10(a), a tilted wavefront appears in it as illustrated in sub-figure (b). This is an indication of the intertwining of the differential mode with the common mode, which are now both allowed to flow freely in the through-line, being the common mode radiated very fast. As a result, the coupling to the MKID drops to $|S_{31}|^2 \approx -15.4 \text{ dB} \approx 2.9\%$ as reported in panel (c).

4.5. Radiation Loss in Co-Planar THz Filter-Banks

We have already introduced in Section 4.2 that the two fundamental modes of a CPW are very different: while the differential mode is a transmission line mode, the common is mostly a radiative mode. Fig. 4.11 quantifies the radiation loss at 350 GHz of these fundamentally different modes as simulated using CST Microwave Studio [98] for a superconducting ($L_k = 1 \text{ pH}/\square$) CPW line on an infinitely thick⁴ Sapphire (modeled isotropic with $\epsilon_r \approx 10.34$) for different line widths. The differentially-excited 2-2-2 μm CPW yields a radiative attenuation rate of $5.8 \times 10^{-3} \text{ dB/mm}$, which is in agreement with the experimental value reported in [126]⁵. In this configuration, where the phase velocity of the differential mode of the CPW is slower than that of a plane-wave in Sapphire, the mode ceases to be leaky and the remnant radiation is a space wave from the slightly offset and opposite dipole moments in the two slots. The radiation of the common mode on the other hand is 3–4 orders of magnitude stronger than that of the differential mode, where the reported value is in agreement with the quasi-analytical tool of [145]. It is also apparent from Fig. 4.11 that the miniaturization of a CPW helps to reduce the radiation loss. In particular, the differential mode is seen to dramatically reduce its radiation by narrowing the CPW. On the contrary, the radiation from the COM mode is suppressed much less, preserving its strongly radiative nature for CPW line widths as narrow as $w_{\text{slot}} = w_{\text{cond}} = 0.3 \mu\text{m}$. Two experimental results qualitatively corroborate this discussion. Firstly, the support for these two modes and their intertwining in a co-planar filter are the cause for the low $Q_i \approx 2500$ reported at 350 GHz for the sub-micron-featured CPW resonators in [134]. Furthermore, the radiation loss is also noticeable from the slope in the optical efficiency measurements of the DESHIMA 1.0 filter-bank in Fig. 4.12 which, neglecting the standing waves, clearly shows a linear trend towards the end of the filter-bank at rate of 0.37 dB/mm. For the 2-2-2 μm CPW lines used in DESHIMA 1.0, this value sits between the DIF and COM mode attenuation rates in Fig. 4.11.

⁴This models well the environment of a superconducting line on an absorber-terminated wafer, as it is the case for the DESHIMA chips with a β -phase Ta mesh absorber at the Sapphire-air interface.

⁵This result also coincides with the Sonnet [99] simulations obtained in [126] following the prescriptions for a radiation-sensitive setup [144].

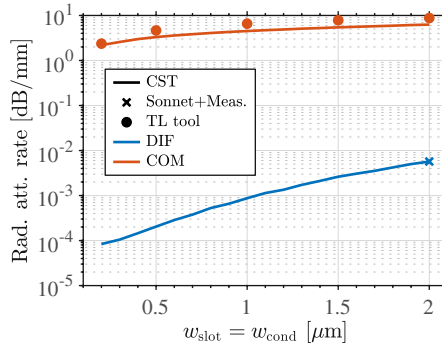


Figure 4.11: Radiative attenuation rate of a superconducting ($L_k = 1 \text{ pH}/\square$) CPW line on Sapphire (modeled isotropic with $\epsilon_r \approx 10.34$), with a slot width w_{slot} and a central conductor width w_{cond} , excited with either the differential mode or the common mode at 350 GHz. The continuous lines are the results calculated using CST Microwave Studio [98], the cross is the Sonnet [99] simulation and experimental result of [126], and the dot is the value obtained using the quasi-analytical transmission line tool of [145]. The width reduction largely decreases the radiation attenuation rate of the differential mode, whereas the common mode remains highly radiative.

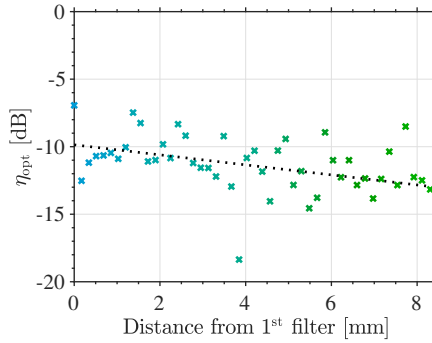


Figure 4.12: Optical efficiency measurement of the DESHIMA 1.0 filter-bank (calibrating out the quasi-optical band-pass filter) as a function of the distance with respect to the first filter (high frequency) of the filter-bank. A linear fit to the data gives an attenuation rate of 0.37 dB/mm. The optical efficiency measurements are further discussed in [49] and its principle is explained in detail in [137] and Section 5.3.3.

The excitation of the spurious common mode occurs with any asymmetry about a CPW line. This situation is of course ubiquitous throughout a co-planar filter-bank, where the shunted band-pass filters are parallel-coupled to the THz through-line and the ground planes get constantly interrupted. For the particular case of the filter in Fig. 4.8, the symmetry is broken around both the CPW through-line and the CPW of the detector attached to port 3. For the latter CPW, the common mode gets induced

in it due to the coupling with the meandered-slot filter, which asymmetrically loads the CPW, but also due to the unbalance of its ground planes caused by the directionality of the filter-bank excitation from port 1. The mode conversion in these two CPWs and the associated losses into radiation and ohmic dissipation in the bridges results in a broadband loss of power as evidenced in Fig. 4.9(a), which gives a degraded transmission for all the filters in the filter-bank.

To explicitly show the mode-conversion of a CPW-based tank circuit at high frequencies we simulate in CST Microwave Studio [98] the typical ‘elbow’ coupler, extensively used for MKID designs [146], as a THz half-wavelength resonator. The simulations consist of 2-2-2 μm CPW structures on an infinitely thin superconductor with a sheet inductance of $1\text{ pH}/\square$ on top of a Si substrate. In Fig. 4.13(a) we observe the mode conversion due to the asymmetric loading of the CPWs of the through-line and of the coupler. In particular we show that the differential mode in the through-line actually couples more strongly to the common mode than to the differential mode in the coupled line. Furthermore, the differential mode in the through-line is slightly converted into a common mode, which is in turn either coupled strongly to the ‘elbow’ coupler as COM \rightarrow DIF or radiated out fast (Fig. 4.11). Although the mode conversion in the through-line loaded with a single resonator is small, it can become significant for long filter-banks with many filters. Fig. 4.13(b) shows that a resonator excited with a common mode will have in comparison with a differentially-excited resonator: a much broader resonance, due to the stronger coupling and the larger energy leakage (as seen from (3.12)); and a shallower dip, due to the excess radiation losses (appreciated in (3.9)). Lastly, in Fig. 4.13(c) we observe the same two modes of Fig. 4.13(b) get intertwined in the response of a differentially-fed through-line with an ‘elbow’-coupled resonator. This is detrimental for both the intended differential mode resonance as well as for the performance of the next filters using the degraded transmission off-resonance. This low off-resonance transmission, which occurs also for the filter in Fig. 4.9 with bridges over the through-line, will make the filters down the line couple to a weaker input signal than the one at the entrance of the filter-bank. For large filter-banks operating over large bandwidths, hundreds of filters will be used, and a very high off-resonance transmission will become a crucial design parameter.

4.6. Conclusions

In this chapter we have explained the causes for the low performance of the co-planar filter-bank of the DESHIMA 1.0 spectrometer and we have proposed some minor amendments. First of all, each polyimide-Al bridge incurs in -21 dB of conductor loss, -30.5 dB of dielectric loss and -20 dB of reflections due to their parasitic capacitance. We have proposed the use of NbTiN instead of Al for the conductive strip of the

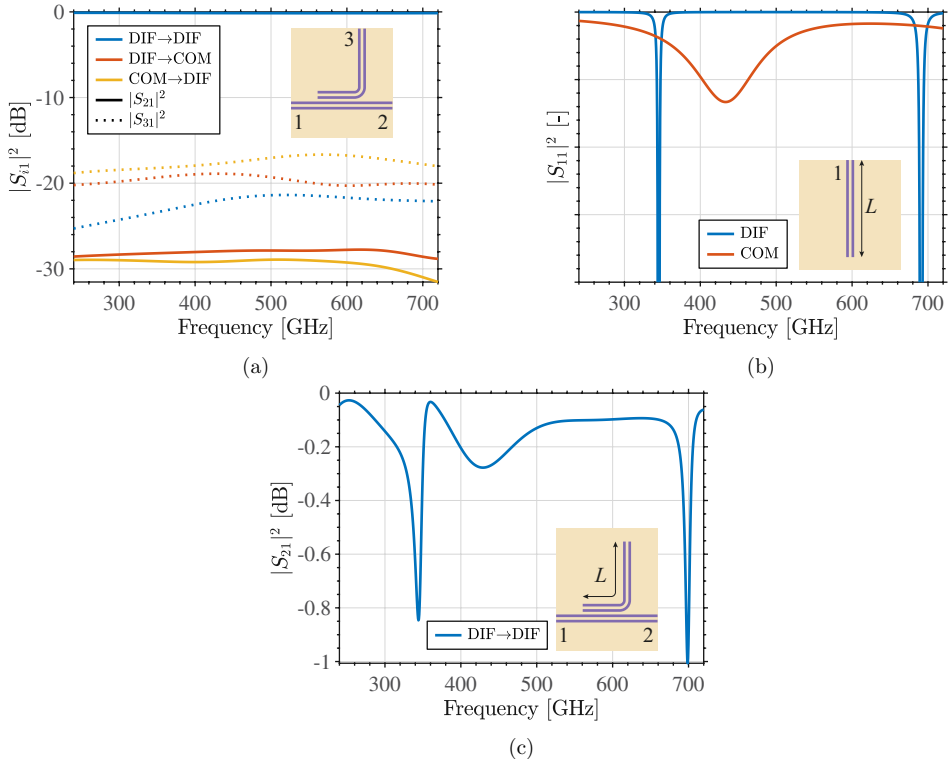


Figure 4.13: Simulations of 2-2-2 μm CPW structures on an infinitely thin superconductor with a sheet inductance of $1 \text{ pH}/\square$ on top of a Si substrate. Sub-figure (a) shows the mode conversion between a CPW through-line and an ‘elbow’-coupled CPW. Sub-figure (b) shows the large difference in the dips associated to a straight CPW half-wavelength resonator excited with DIF mode or COM mode at port 1 with an arbitrarily small port impedance to emulate a short-circuit. The COM mode shows a much broader and shallower resonance than the DIF mode, which is associated to higher losses (lower Q_i). Lastly, sub-figure (c) shows the response of a differentially-fed CPW structure consisting of a through-line and a resonator. We observe sharp and broad dips similar to the ones associated to the two different modes in sub-figure (b), which indicates that the CPW resonator allows both modes to be excited. The DIF resonance is largely deteriorated by the COM mode dip. Moreover, the COM mode spoils the transmission for subsequent filters in the through-line.

bridge and to tune out the parasitic capacitance with a localized narrowing of the central conductor of the CPW under the bridge. These losses are small for a single filter, but can add up to a non-negligible quantity when accounting for the large number of bridges employed. For straight and curved 2-2-2 μm CPWs, bridges are not needed and they should be removed to preserve an immaculate transmission. On the other hand, the bridges surrounding the filters should be kept as they serve to

confine the common mode and couple part of its energy into to detector. However, even more critical are the radiation losses, which stem from the filters on-resonance, contributing to up to $-8.2 \text{ dB} \approx 15.2\%$ of the input power on-resonance; but also from the unbalanced CPW through-line, which has part of the culprit for the attenuation along the filter-bank as shown in Fig. 4.12. Finally we have shown that the meandered-slot filter geometry used had several spurious harmonics that limit its free spectral range to a 21%, and thereby it is not suitable for a broadband filter-bank.

We have also qualitatively demonstrated the mode-related issues that arise in co-planar THz filter-banks, which necessitate from the asymmetric loading of CPW lines and the unbalancing of the CPW grounds to excite an array of shunt filter-coupled detectors. Although miniaturizing the CPW lines helps to reduce the radiation loss incurred by both the differential and common mode as illustrated in Fig. 4.11, the mere presence of the latter and its radiative nature renders impractical the use of co-planar technology for moderate spectral resolution THz filter-banks. It is worth noting that MKID detectors, which are operated on similarly-sized CPWs in the microwave regime, do not suffer from radiation loss due to the electrically thin dielectric stratification of a wafer; showing internal quality factors as high as $Q_i \sim 10^5\text{--}10^6$ [147, 148]. In this light, a membrane-based co-planar waveguide filter-bank might be worth investigating.

Despite the relatively easy fabrication of co-planar technology, the radiation loss issue and all the counter-measures to prevent it (bridges, miniaturizing CPWs) introduce more problems than solve. As a result, single-ended on-chip technology such as microstrip is required to design efficient filter-banks that can provide moderate spectral resolution and good coupling efficiency to the detectors.

Chapter 5

Microstrip THz Band-Pass Filters

The former version of the on-chip THz filter-bank spectrometer DESHIMA [49], described in Chapter 4, despite showing technological readiness for astronomy at a ground-based telescope [74], had several issues in its filter-bank as explained in Chapter 4. The reported performance of the 49 channels sampling the 332–377 GHz (13% relative bandwidth) spectrum averaged to a spectral resolution of $\langle R \rangle \approx 300$ and a coupling efficiency of 8% with respect to the signal entering the filter-bank. Both the low coupling efficiency and the low spectral resolution were caused by the radiative losses in its co-planar THz filters and the ohmic (conductive and dielectric) losses in the bridges balancing the potentials of the ground planes. Moreover, the filter design used was incompatible with broadband operation due to a free spectral range of 21%. In order to allow for truly wideband and highly-efficient filter-bank spectrometers a new band-pass filter design was required.

In this chapter, we propose a superconducting microstrip half-wavelength resonator as a suitable band-pass filter for broadband moderate spectral resolution spectroscopy for terahertz (THz) astronomy. The proposed filter geometry has a free spectral range of an octave of bandwidth without introducing spurious resonances, reaches a high coupling efficiency in the pass-band, and shows very high rejection in the stop-band to minimize reflections and cross-talk with other filters. A spectrally sparse prototype filter-bank in the band 300–400 GHz has been developed employing these microstrip filters as well as an equivalent circuit model to anticipate systematic errors. The fabricated chip has been characterized in terms of frequency response and optical efficiency, reporting an average peak coupling efficiency of $-5.7 \text{ dB} \approx 27\%$ with an average spectral resolution of 940. On the other hand, a spectrally dense microstrip filter-bank configuration, using the filters described in this chapter, currently provides $\langle |S_{11}|^2 \rangle \approx -7.74 \text{ dB} \approx 17\%$ and $\langle Q_l \rangle \approx 780$ (see Fig. 9.2).

Parts of this chapter have been published in *IEEE Trans. THz Sci. Tech.* [113].

5.1. On-Chip Technology: CPW vs. Microstrip

In this section we delve into the choice of on-chip technology, as this decision carries important consequences for the overall performance of the filter-bank. First of all, because the metals used are superconductors, conductor losses are negligible [91]. Dielectric losses, on the other hand, depend on whether the dielectrics in the proximity of the transmission lines are crystalline, e. g. crystalline Si, or amorphous, e. g. deposited dielectrics like a-Si [149]. Lastly, radiation losses largely depend on the technology choice (CPW or microstrip) and the overall size of the transmission line.

Despite the relatively easy manufacturing of CPW technology, this type of transmission line is problematic to work with at THz frequencies due to its support for two fundamentally different modes as introduced in Section 4.4: the differential and the common mode. As shown in Fig. 4.11, the common mode radiates much stronger than the differential mode. This has severe consequences because a combination of these two fundamental modes will exist with any asymmetry around a CPW, and will thereby incur excess radiation loss at high frequencies (resulting in a low Q_i) [49, 145, 150]. Balancing the potential of the grounds with bridges will only reflect the common mode as we have seen in Fig. 4.4, but it will not convert it to a differential mode. As a result, to minimize radiation loss in CPW structures at high frequencies, symmetry must be preserved. However, because the filter-bank concept requires to channelize the energy into shunt detectors, the symmetry will necessarily be broken in the through-line and the filters.

On the other hand, microstrip lines only support a single well-confined fundamental mode whose radiation losses are negligible [145]. However, practical microstrip devices require deposited dielectrics, which incur more losses than crystalline substrates as reported in [151] for microwave frequencies. At THz frequencies data on dielectric loss is very sparse: a CPW on crystalline Sapphire shows a Q_i in excess of 15000 [126], whereas microstrips fabricated from NbTiN and Plasma-Enhanced Chemical Vapor Deposition (PECVD) SiN report $Q_i \approx 1400$ at 200 GHz [152], and NbTiN microstrips on PECVD a-Si [149] show $Q_i \approx 4750$ at 350 GHz [153]. Despite the dielectric losses in deposited a-Si still being high for an ideal THz filter-bank, these are sufficient to design and build microstrip-based filters, thereby avoiding the mode-related issues of co-planar technology. In this light, we are going to investigate resonator geometries based on microstrip technology.

5.2. Band-Pass Filter Design

Several microstrip resonator geometries are investigated as candidates for the implementation of a THz superconducting band-pass filter. The geometries considered are an O-shaped, a C-shaped and a I-shaped microstrip resonator as shown in the insets of the sub-figures in Fig. 5.1. For all the three geometries, the microstrip layer is made of a thin NbTiN superconductor film with a sheet kinetic inductance of $L_k = 1 \text{ pH}/\square$. The microstrip sits on 300 nm of a-Si ($\epsilon_r = 10$) and it is backed by a NbTiN ground plane with $L_k = 0.448 \text{ pH}/\square$. The resonators are parallel-coupled to the surrounding microstrip lines through 300 nm gaps. The resonator microstrip lines are 450 nm wide, with the exception of the vertical bar of the 'I' resonator, which is 1.1 μm .

These three candidate geometries have been simulated in Sonnet [99] and their S-parameters in Fig. 5.1 show optimal on-resonance performance at 500 GHz as described in Section 3.3 and a loaded quality factor $Q_l \approx 500$. The second harmonic of the resonators rings at twice the frequency, at 1 THz. The O-shaped resonator resonates when its perimeter becomes one wavelength, but it also shows a spurious resonance at a slightly lower frequency than the intended one associated to a mode with current nodes in the middle of the coupling bars [154]. The spurious mode of the O-shaped resonator is in fact the fundamental resonant mode of the C-shaped half-wavelength resonator. This one, on the other hand, shows no spurious resonance and it has been successfully used for the filter-banks in [53, 131]. Lastly, the I-shaped resonator shows the best off-resonance performance with the lowest reflections ($|S_{11}|^2$) of the three resonators. Despite having a spurious resonance ($\sim 1030 \text{ GHz}$) associated to the resonance of the coupling bars, this could be tuned to fall beyond the intended octave free spectral range. Thereby we choose the I-shaped resonator option as it shows the best overall performance.

The actual implementation of the I-shaped resonator is depicted in Fig. 5.2, which deviates slightly from the inset of Fig. 5.1(c) with port 3 being terminated in a short-circuit to ground at $\lambda/4$ from the coupler and port 4 becoming port 3 in Fig. 5.2 as the only output to the detector. This filter comprises two couplers (horizontal bars of the 'I'), which are narrow microstrip lines (450 nm wide) coupling the resonator through a 300 nm gap to either the through-line or the detector line, controlling respectively Q_{c1} and Q_{c2} with their length. The 1.1 μm -wide microstrip connecting the two couplers (vertical bar of the 'I') was designed to have half the characteristic impedance of that of the coupler microstrip lines, resulting in an overall electrical length of the resonator of $\sim \lambda/2$, measured from one coupler extreme, through the vertical bar of the 'I', to another extreme of the other coupler. The microstrip line on the detector side is short-circuited to ground at roughly $\lambda/4$ from the coupler to coherently reflect the filtered THz signal to the MKID while providing a low electric field at the microwave frequencies of the readout to minimize TLS noise contributions [109].

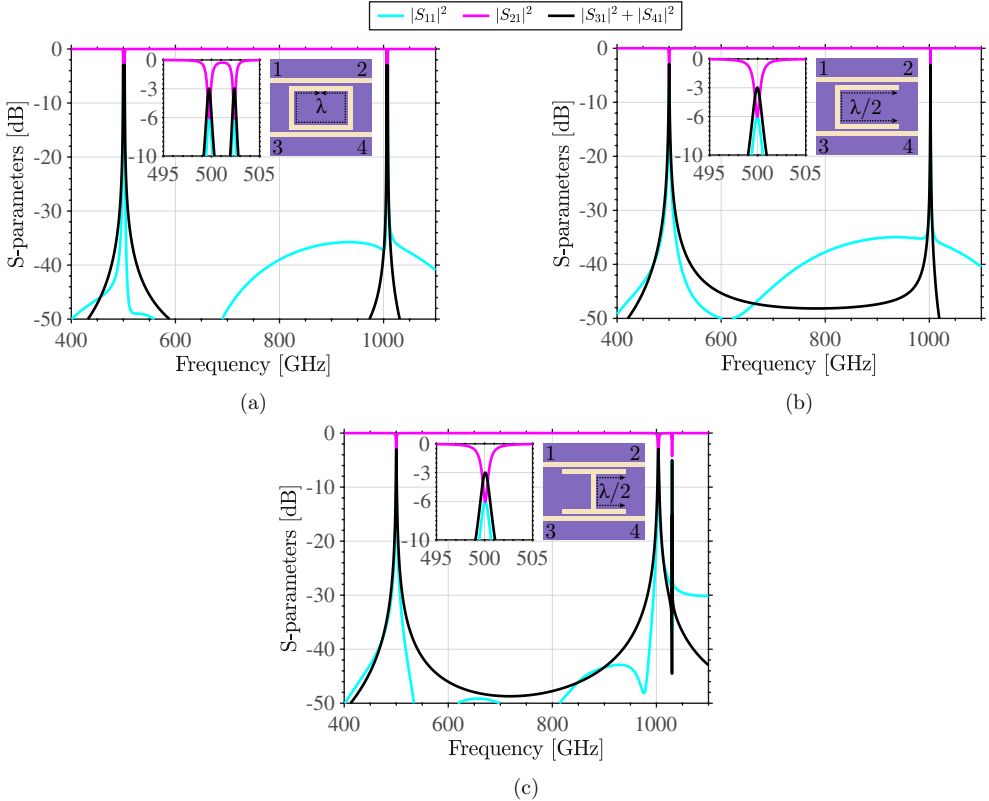


Figure 5.1: Comparison of the S-parameters simulated in Sonnet [99] of three microstrip resonator geometries: (a) an O-shaped resonator, (b) a C-shaped resonator and (c) an I-shaped resonator. The three geometries show optimal performance on-resonance with $Q_l = 500$, however, the O-shaped resonator shows a spurious resonance close to the intended one. The C-shaped resonator works well overall but the I-shaped resonator has a much better off-resonance performance. The I-shaped resonator has a high-Q spurious resonance associated to the coupling bar, but this falls beyond the octave band of interest.

The filter inside the dotted cyan box in Fig. 5.2 is simulated in Sonnet [99], and its performance is compared against the circuit model described in Section 3.3.2. The comparison in Fig. 5.3 shows an excellent agreement between the performance of an I-shaped filter in isolation and the circuit model, with a slight deviation for the reflections off-resonance. We then investigated the arraying of 4 contiguous filters with an inter-filter separation $L_{\text{thru},i} = \lambda_{\text{thru},i}/4$. The agreement between the model and the full-wave simulations was found to be excellent in Fig. 5.4; with a large difference in computation time between Sonnet [99], taking approximately 2 hours, and the model

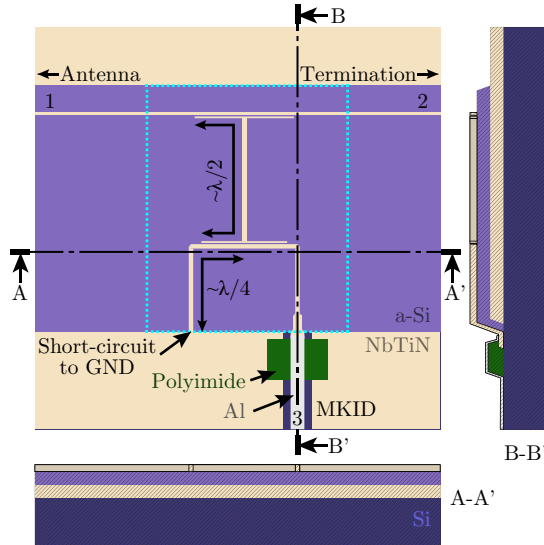


Figure 5.2: Views of the I-shaped microstrip band-pass filter. The thicknesses in the cross-sectional views A-A' and B-B' have been scaled by 150% to emphasize the layering (except for the Si wafer, which is not to scale). A slanted hatch is displayed over the parts cut.

coded in Matlab [155], lasting less than 0.5 seconds, using the same computer. This result is also relevant for claiming that our filters have a very low level of indirect cross-talk given that our circuit model can represent well their interactions with a transmission line model. With these results we were confident that we could use this code for predicting the behavior of a large filter-bank with hundreds of channels (like depicted in Fig. 3.10), which would be otherwise a prohibitively heavy simulation.

5.3. Sparse Filter-Bank Chip

In this section we describe and characterize a spectrally sparse filter-bank consisting of 11 I-shaped filters in the band 300–400 GHz as shown in Fig. 5.5. Each THz filter pass-band is separated from its neighboring channels by 10 GHz in order to disentangle their response and get a full spectral characterization of their performance in semi-isolation. Each spectral channel (each filter-MKID combination) is physically separated from the next down the through-line by $L_{\text{thru},i} = 7\lambda_{\text{thru},i}/4$. In order to minimize MKID cross-talk, their resonances have been shuffled with respect to the THz filters. The targeted spectral resolution of the 11 filters was $Q_l = 500$,

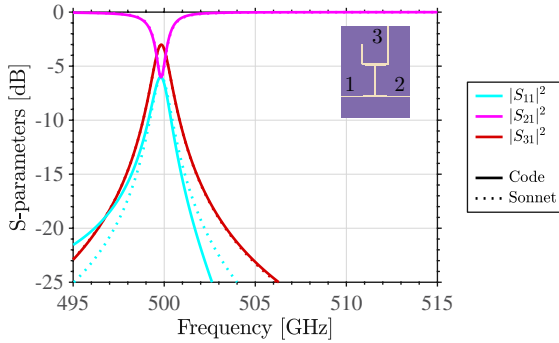


Figure 5.3: Comparison of the simulated S-parameters of 1 filter using Sonnet [99] (resonator of Fig. 5.1(c)) and the circuit model of Fig. 3.3(a).

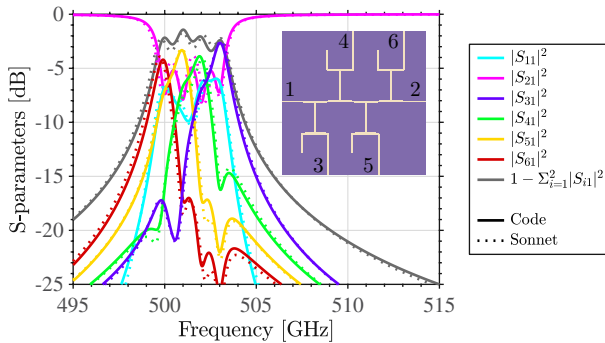


Figure 5.4: Comparison of the simulated S-parameters of 4 contiguous filters separated by $\lambda_{\text{thru},i}/4$ using Sonnet [99] and the circuit model of Fig. 3.3(a).

which would require $Q_c = Q_{c1} = Q_{c2} \approx 1179$ to maximize the coupling efficiency for $Q_i = 3300$ following (3.13). However, because previous experiments had consistently shown an increase of Q_c with respect to the design value (see Table 6.3), for this chip we took the ansatz of designing for a lower coupling quality factor of $Q_c = 500$. In order to decrease the Q_c of the filters, while preserving their dimensions and the location of their THz resonances, the a-Si dielectric thickness was increased from 300 nm to 370 nm and the sheet kinetic inductance L_k of the microstrip layer from $1 \text{ pH}/\square$ to $1.17 \text{ pH}/\square$. A more detailed description of the design procedure of these filters and the experimental feedback obtained from other iterations will be discussed in Chapter 6.

5.3.1. Fabrication

The fabrication route of this chip is similar to [153] and it is described in detail in Appendix B and [156]. It starts with a 260 nm-thick NbTiN layer ($T_c = 15\text{ K}$, $\rho_n = 90.0\text{ }\mu\Omega\text{ cm}$) being deposited on top of a Si wafer using reactive sputtering of a NbTi target in a Nitrogen-Argon atmosphere [157]. This layer is then patterned using photo-lithography with a positive resist and etched to define the microstrip filter-bank ground-plane and the central conductor of the CPW readout line. Afterwards, a 370 nm-thick a-Si layer is deposited at 250 °C using PECVD [149] and patterned to provide the dielectric support for the microstrips of the filter-bank. The microstrip lines are defined in a second NbTiN layer ($T_c = 15\text{ K}$, $R_s = 12.29\text{ }\Omega/\square^1$. on a-Si) 113 nm-thick using a mix-and-match recipe employing a negative resist with electron-beam lithography to accurately pattern the smallest parts of the chip (e.g. filter-bank) and photo-lithography to define the coarser parts (e.g. MKIDs, readout lines, antenna, etc.) in a single lithographic step. After the double exposure, the resist is developed and the pattern is etched into the NbTiN. Next, a 700 nm-thick layer of polyimide is spin-coated on the wafer, cured and patterned to provide the support for the bridges balancing the grounds of the CPW in the GHz readout and also to provide a good electrical contact between the Al and the NbTiN at the MKIDs. The 40 nm-thick Al ($T_c = 1.25\text{ K}$, $\rho_n = 1.9\text{ }\mu\Omega\text{ cm}$) layer is laid next, defining the central conductor of the narrow CPW section of MKIDs. Lastly, a 40 nm-thick layer of β -phase Ta ($T_c = 0.95\text{ K}$, $\rho_n = 239\text{ }\mu\Omega\text{ cm}$) is deposited on the backside as an absorbing mesh for stray-light control [158]. Fig. 5.6 shows the fabricated chip and Fig. 5.7 is a colored scanning electron microscope (SEM) micrograph showcasing a THz filter.

5.3.2. Frequency Response Measurements

To characterize the frequency response of the fabricated device, the chip is placed inside a modified commercial Bluefors dilution refrigerator, where it is cooled to 120 mK. As illustrated in Fig. 5.8, the chip is placed directly facing the cryostat window through an infrared filter stack with approximately 60% transmission in the band 100–700 GHz to limit the thermal loading [159]. We also employed a wire-grid polarizer and a cryogenic quasi-optical band-pass filter stack (with a 338–373 GHz half-maximum pass-band) inside the cryostat to minimize stray radiation on the chip. From the outside, a continuous-wave photo-mixing source (Toptica Terabeam 1550) illuminates the chip with a tunable single THz frequency. By sweeping the frequency of the source while recording the phase response of the microwave tones probing the MKIDs, the THz frequency response is obtained with a spectral resolution of 50 MHz.

¹Estimate using a four-probe resistance measurement at the edge of the wafer and the typical spatial variations of a film deposited with a small NbTi target in a Nordiko 2000 sputtering machine [157]

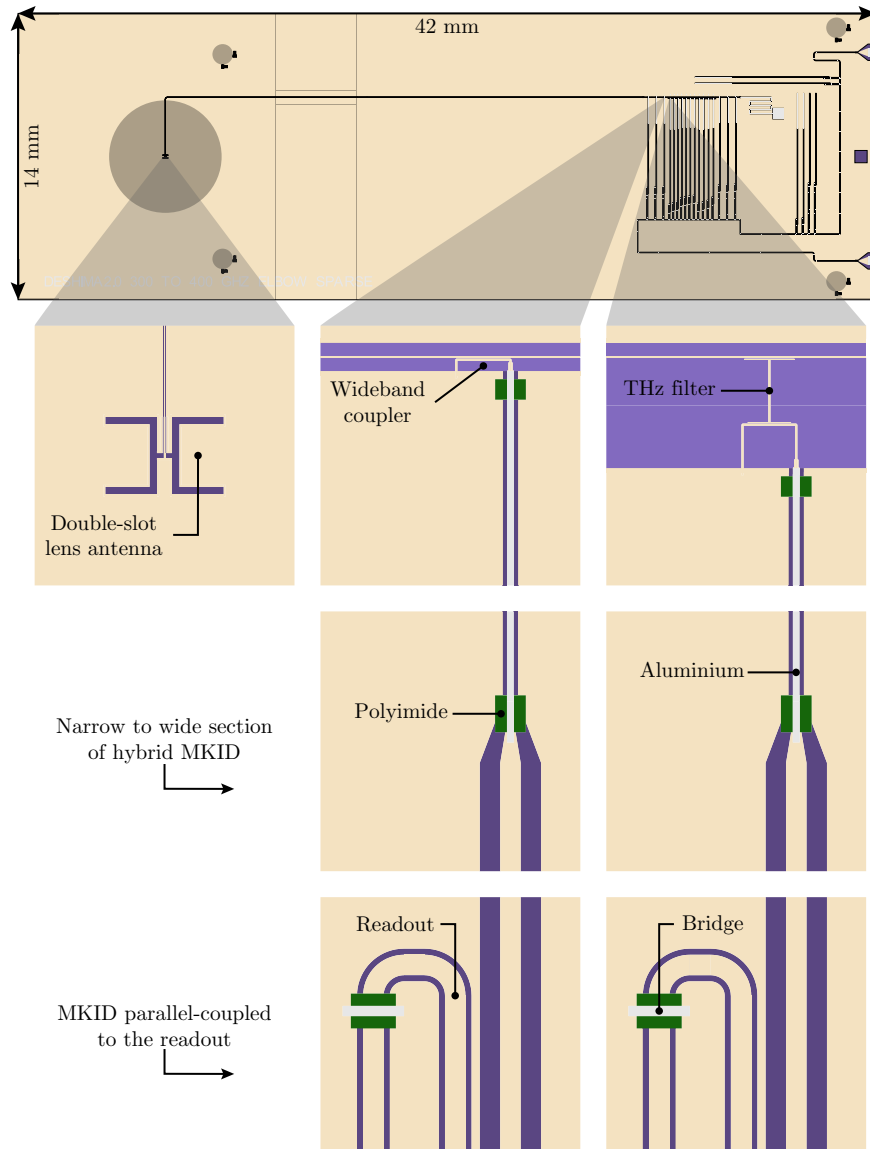
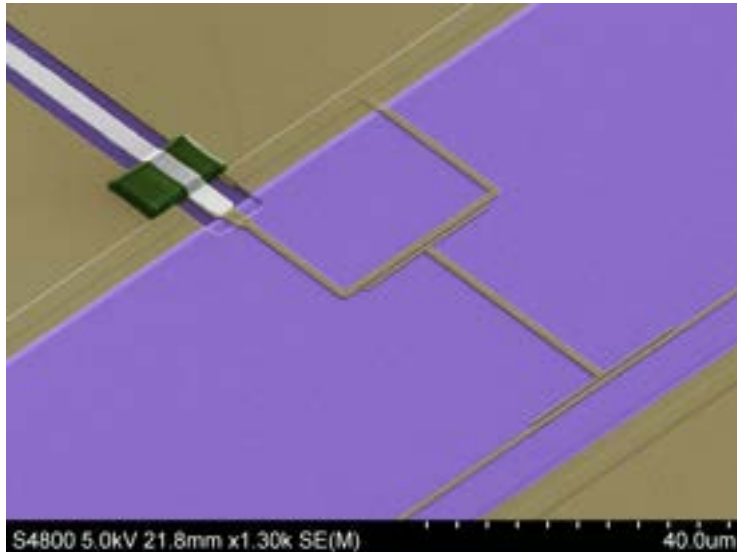


Figure 5.5: Mask set of the 300–400 GHz sparse filter-bank prototype chip with close-up views of the double-slot lens antenna, a microstrip wideband coupler, a microstrip THz filter, the narrow and the wide sections of the hybrid CPW MKIDs and the CPW readout with its bridges.



Figure 5.6: Sparse filter-bank chip for the band 300–400 GHz fabricated in the batch LT194.



5

Figure 5.7: Colored SEM micrograph of a fabricated THz filter with an MKID on the top left of the image and the through-line in the bottom right.

In the forthcoming study we will experimentally evaluate all the relevant filter parameters, anticipating that the coupling strength of the wideband couplers η_{wb} , which is needed to normalize the coupling efficiency of the filters ($|S_{i1}(f)|^2$), is not known with high accuracy due to fabrication tolerances and three-dimensional effects which are difficult to simulate. Therefore, we use the strategy of freeing the parameter η_{wb} and combining the peak and dip analyses to get the best consistent estimate in terms of coupling efficiency of the filters.

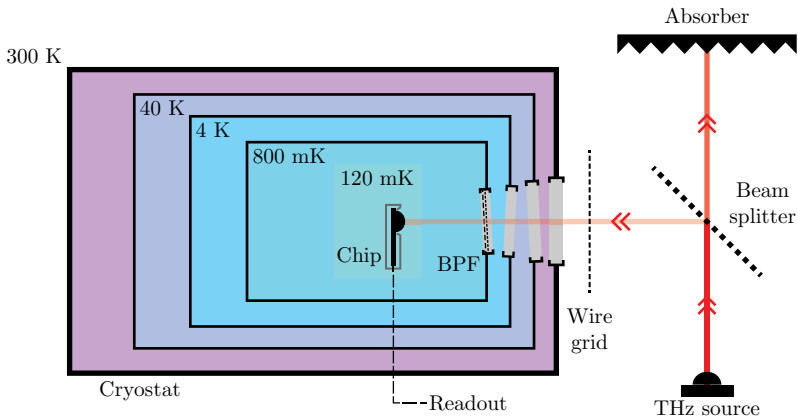


Figure 5.8: Frequency response measurement setup of the filter-bank chip. A continuous-wave photo-mixing source launches a single THz frequency onto the chip inside the cryostat.

5

In the first analysis we measure the transmission through the filter-bank, $|S_{21}(f)|^2$, which may be estimated from the ratio between the averaged phase response of the three wideband-coupled MKIDs after and before the filter-bank (respectively $\langle R_{\text{wb}}^{\text{af}}(f) \rangle$ and $\langle R_{\text{wb}}^{\text{bf}}(f) \rangle$) as

$$|S_{21}(f)|^2 \approx \frac{\langle R_{\text{wb}}^{\text{af}}(f) \rangle}{\langle R_{\text{wb}}^{\text{bf}}(f) \rangle}. \quad (5.1)$$

The dips emerging in Fig. 5.9 correspond to the filters extracting power from the through-line. Both the resonance frequency f_0 and the loaded quality factor Q_l may be directly obtained by fitting the resonances of the pseudo transmission coefficient in Fig. 5.9 using a skewed Lorentzian function

$$L(f) = A_1 \left(1 + A_2(f - f_0) + \frac{A_3 + A_4(f - f_0)}{1 + 4Q_l^2 \frac{f - f_0}{f_0}} \right), \quad (5.2)$$

which follows from (3.6). From the estimation of the resonance frequency f_0 , the loaded quality factor Q_l and the transmission dip depth $|S_{21}(f_0)| = \sqrt{L(f_0)/A_1}$, (3.9) allows the retrieval of q_i . Then, by means of (3.12), Q_{c1} can be retrieved. An estimate of the coupling strength of the filters $|S_{i1}(f_i)|^2$ may be obtained at this point assuming $Q_c = Q_{c1} = Q_{c2}$ in (3.10) and (3.11), which simplifies (3.10) to

$$|S_{31}(f_0)|^2 = \frac{2}{\left(2 + \frac{Q_c - q_i}{q_i} \right)^2} \approx |S_{i1}(f_i)|^2. \quad (5.3)$$

5.3. Sparse Filter-Bank Chip

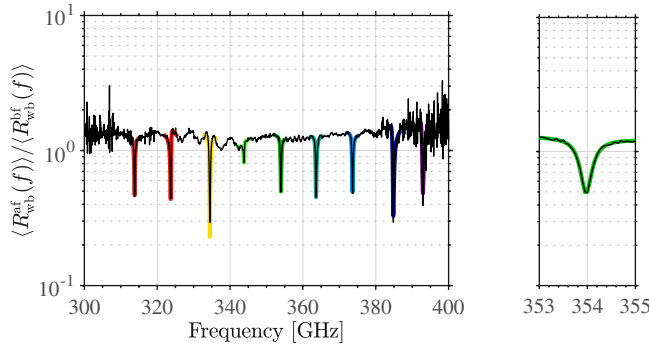


Figure 5.9: Pseudo transmission coefficient through the filter-bank estimated from (5.1), which is the averaged frequency response of the three wideband-coupled MKIDs trailing the filter-bank divided by that of the three leading it. The right-hand side panel emphasizes one of the skewed Lorentzian fits to the data with (5.2).

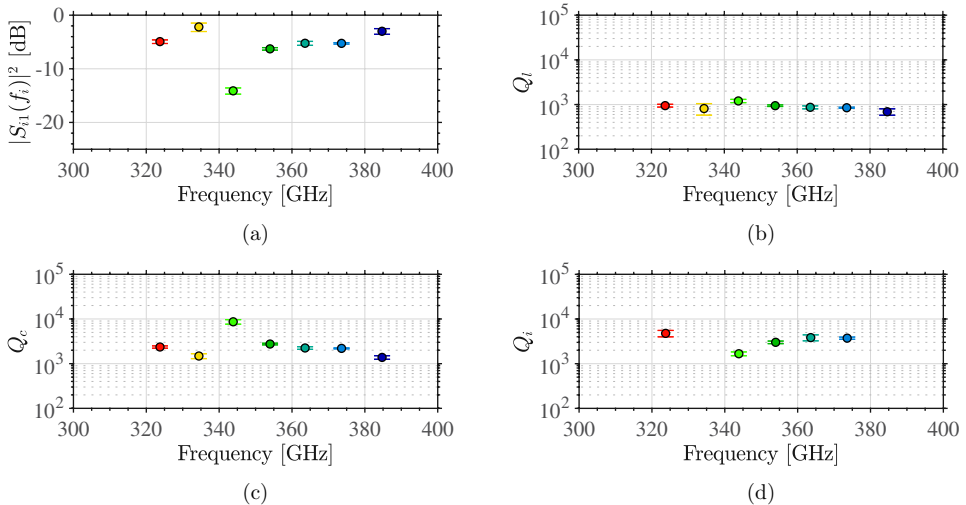


Figure 5.10: Measured values of the filters using only the dip analysis. Sub-figure (a) shows the coupling efficiency $|S_{11}(f_i)|^2$, sub-figure (b) the loaded quality factor Q_l , sub-figure (c) the coupling quality factor $Q_c = Q_{c1} = Q_{c2}$ and sub-figure (d) the internal quality factor Q_i .

Using the assumption $Q_{c1} = Q_{c2}$, Q_i may be calculated from (3.11). This analysis on the dips of the $|S_{21}(f)|^2$ estimate of Fig. 5.9 results in the values reported in Fig. 5.10; which average to $\langle |S_{11}(f_i)|^2 \rangle \approx -5.7 \text{ dB} \approx 27\%$, $\langle Q_l \rangle \approx 960$, $\langle Q_c \rangle \approx 2860$ and $\langle Q_i \rangle \approx 2890$.

In the next analysis we measure the coupling efficiency of each filter $|S_{i1}(f)|^2$, which may be estimated with

$$|S_{i1}(f)|^2 \approx \frac{R_{\text{filter},i}(f)}{\langle R_{\text{wb}}^{\text{bf}}(f) \rangle} \eta_{\text{wb}}, \quad (5.4)$$

where $R_{\text{filter},i}(f)$ is the phase response of the MKID attached to the i^{th} filter. The underlying assumptions for these estimates are that all the MKIDs have the same responsivity and that the filter-bank does not reflect a lot of power in-band. By fitting the peaks with the prototype function of (3.7), the peak efficiency and the loaded quality factor can also be obtained. Subsequently using the knowledge of Q_l , q_i , Q_{c1} from the dip analysis and the peak coupling efficiency of the filters $|S_{i1}(f_i)|^2$, the parameter Q_{c2} may be obtained from (3.10) as

$$Q_{c2} = \frac{2Q_{c1}}{(1 + Q_{c1}/Q_i)^2 |S_{i1}(f_i)|^2}. \quad (5.5)$$

The three-port network internal quality factor Q_i can be obtained henceforth by means of (3.11).

The problem with the peak analysis (using (5.4)) is that, although we can directly measure the MKID responses $R_{\text{filter},i}(f)$ and $R_{\text{wb}}^{\text{bf}}(f)$, the strength of the wideband couplers η_{wb} cannot be directly obtained. Hence we perform a consistency check between the dip and peak analyses. To do so, we overlay in Fig. 5.11(a) the mean value of the coupling efficiencies $\langle |S_{i1}(f_i)|^2 \rangle$, obtained from the dip analysis with (5.3), and the one obtained from the peak analysis by letting η_{wb} change in (5.4). In order to avoid data from low signal-to-noise ratio (SNR) measurements, the filters analyzed are well-within the 320–370 GHz quasi-optical pass-band, which is determined by the lens antenna in combination with the quasi-optical band-pass filter stack. It is apparent that the value that makes these experiments consistent is $\eta_{\text{wb}} \approx -24$ dB, which is also in agreement with the design value simulated in Sonnet for this structure. With this congruent combination between the peak and dip analyses, based on the uncertainty of the strength of the wideband coupler, the filters can now be fully and unequivocally characterized.

Fig. 5.12 depicts the coupling efficiency of the different band-pass filters as a function of frequency when estimated using (5.4) with a coupling strength for the wideband-coupled MKID of $\eta_{\text{wb}} \approx -24$ dB as inferred previously. By fitting the peaks with the prototype function of (3.7), an average peak efficiency of $\langle |S_{i1}(f_i)|^2 \rangle \approx -5.7$ dB $\approx 27\%$ can be obtained for those filters well-within the quasi-optical pass-band. Fig. 5.13 collects the different quality factors of these filters, whose average values are: $\langle Q_l \rangle \approx 940$, which may be obtained from either the peak or the dip analyses; and $\langle Q_{c1} \rangle \approx 2860$, $\langle Q_{c2} \rangle \approx 2680$, and $\langle Q_i \rangle \approx 3300$ which are acquired by combining the dip and the peak analyses.

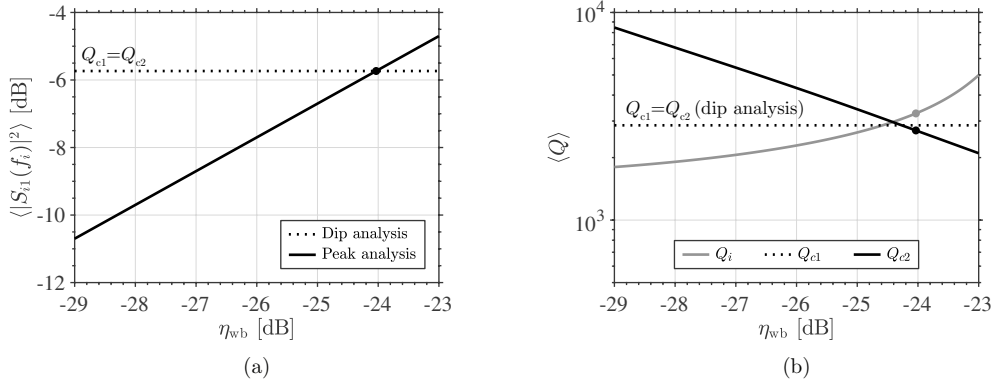


Figure 5.11: Sub-figure (a) is a consistency check between the peak and dip analyses for the average fitted coupling efficiency of the filters $\langle |S_{i1}(f_i)|^2 \rangle$ using the strength of the wideband couplers η_{wb} as a free parameter. The value of $\eta_{wb} \approx -24$ dB (dot) makes the peak and dip analyses agree. Sub-figure (b) shows the quality factors Q_i , Q_{c1} and Q_{c2} as a function of the strength of the wideband coupler.

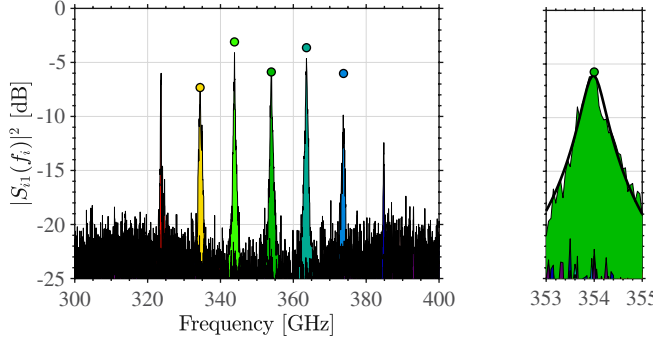


Figure 5.12: Frequency response measurement of the pseudo coupling efficiency of the different filters (estimated with (5.4)) overlaid with the optical efficiency measurements (represented with dots and calculated with (5.13)). The right-hand side panel emphasizes one of the Lorentzian fits to the data. Only 7 out of 11 filters are visible above the noise floor due to the narrow quasi-optical pass-band determined by the antenna and the quasi-optical filter stack used.

5.3.3. Optical Efficiency Measurements

To absolutely quantify the efficiency of the filter-bank we follow the same procedure as explained in [137], where the measured noise-equivalent power NEP_{exp} of each background-limited detector is compared with the expected background-limited NEP . To do so we employ the setup of Fig. 5.14 consisting of a closed cryostat with a

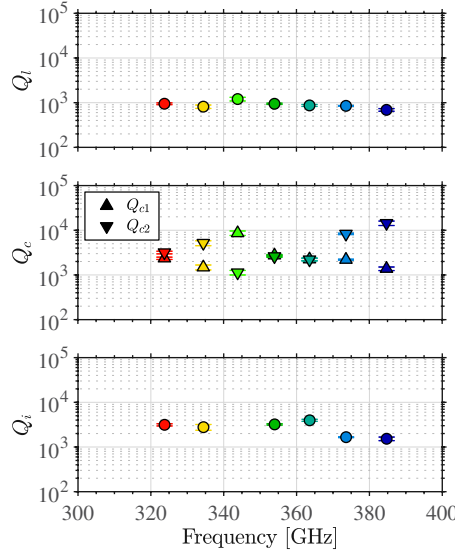


Figure 5.13: Measured quality factors of the filters using the peak and dip analyses.

calibrated² black body radiator shining power onto the lens of the filter-bank chip through some quasi-optical filters. At a temperature T of the black body source, the optical efficiency can be calculated with

$$\eta_{\text{opt}} = \frac{\int 2P_s(f, T)hfdf + \int 4\Delta P_s(f, T)/\eta_{\text{pb}}df}{\text{NEP}_{\text{exp}}^2 - \int 2P_s(f, T)hff(f)O(f)df}, \quad (5.6)$$

where h is the Planck constant, $O(f) = (e^{hf/(k_B T)} - 1)^{-1}$ is the mean Bose-Einstein occupation number, 2Δ is the gap energy of the absorbing superconductor (Al in this case), η_{pb} is the pair-breaking efficiency (for thin Al films $\eta_{\text{pb}} \approx 0.4$ [160]) and $F(f)$ is the frequency response of the quasi-optical band-pass filters between the black body radiator and the lens antenna on the chip. The maximum power reaching the singly-polarized lens antenna emanating from the black body radiator is given by $P_s(f, T) = (1/2)B_s(f)\lambda^2F(f)$, where λ is the wavelength at frequency f and $B_s(f, T)$ is the black body spectral brightness, which is in turn given by

$$B_s(f, T) = \frac{1}{\lambda^2}2hfo(f) = \frac{1}{\lambda^2} \frac{2hf}{e^{\frac{hf}{k_B T}} - 1}, \quad (5.7)$$

being k_B the Boltzmann constant. The experimental NEP can be calculated from the responsivity $\delta x/\delta P_s$ and the measured noise power spectral density level S_x at

²A control system regulates the temperature of a high-emissivity stycast-coated corner reflector.

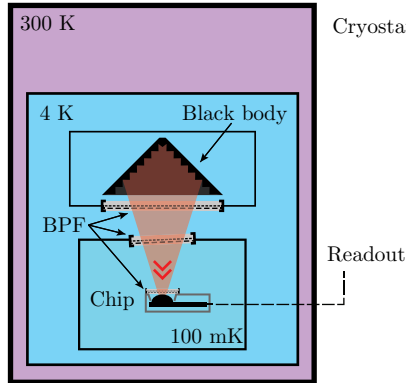


Figure 5.14: Optical efficiency measurement setup. A calibrated black body radiates THz power onto the lens-antenna of the chip inside a closed cryostat.

the flat part of the Lorentzian profile as (e.g. central panel of Fig. 15 in [137])

$$\text{NEP}_{\text{exp}} = \sqrt{S_x} \left(\frac{\delta x}{\delta P_s} \right)^{-1}. \quad (5.8)$$

The responsivity $\delta x / \delta s$ is obtained by monitoring the response change δx of the MKID³ to a small change in the power level δP_s due to a small temperature δT variation around 30 K. The noise power spectral density level S_x of the MKID response is obtained for a black body temperature T , at a frequency high enough to avoid $1/f$ noise but low enough to avoid the Lorentzian roll-off due to the finite quasi-particle lifetime, typically of the order of 10^1 – 10^2 Hz [137].

Although the optical efficiency η_{opt} of each detector can be calculated as just explained, we are interested in the coupling efficiency of the i^{th} filter with respect to the entrance of the filter-bank, $\eta_{\text{filter},i}$. To calibrate out the efficiency contributions of all the components before the filter-bank⁴, η_{bfFB} , we employ once again the a-priori knowledge of the strength of the wideband couplers η_{wb} . As a result, the measured optical efficiency of the wideband-coupled detectors can be written as

$$\eta_{\text{opt}}^{\text{wb}} = \eta_{\text{bfFB}} \eta_{\text{wb}}, \quad (5.9)$$

and approximated for the filter-coupled detectors in the Rayleigh-Jeans limit ($hf \ll k_B T$) as

$$\eta_{\text{opt}}^{\text{filter},i} \approx \eta_{\text{bfFB}} \eta_{\text{filter},i} \frac{\Delta f_{\text{filter},i}}{\Delta f_{\text{BPF}}}, \quad (5.10)$$

³The MKID observable x is commonly the phase or the amplitude response.

⁴The efficiency of the components before the filter-bank refers namely to the antenna efficiencies (including spill-over, internal reflections and impedance mismatches), as the response of the quasi-optical filters $F(f)$ is already accounted for in (5.6).

where $\Delta f_{\text{filter},i}$ and Δf_{BPF} respectively represent the normalized equivalent bandwidth of the i^{th} filter and of the quasi-optical band-pass filter. These equivalent bandwidths are given by

$$\Delta f_{\text{filter},i} = \int_{-\infty}^{\infty} \frac{|S_{i1}(f)|^2}{|S_{i1}(f_i)|^2} df \approx \frac{\pi}{2} \frac{f_i}{Q_i} = \frac{\pi}{2} \delta f_i, \quad (5.11)$$

$$\Delta f_{\text{BPF}} = \int_{-\infty}^{\infty} \frac{F(f)}{\max\{F(f)\}} df \approx 35 \text{ GHz}. \quad (5.12)$$

By combining (5.9) and (5.10) and solving for $\eta_{\text{filter},i}$, the coupling efficiency of the filter-coupled detectors can be estimated from

$$\eta_{\text{filter},i} \approx \eta_{\text{opt}}^{\text{filter},i} \frac{\eta_{\text{wb}}}{\eta_{\text{opt}}^{\text{wb}}} \frac{\Delta f_{\text{BPF}}}{\Delta f_{\text{filter},i}}. \quad (5.13)$$

The results of applying (5.13) can be directly overlaid and compared to the frequency response peaks⁵ in Fig. 5.12. The error-weighted average coupling efficiency, calculated for the experimentally inferred $\eta_{\text{wb}} = -24 \text{ dB}$ (see Fig. 5.11), is $\langle \eta_{\text{filter},i} \rangle \approx -5.5 \text{ dB} \approx 28\%$, which is in good agreement with the $-5.7 \text{ dB} \approx 27\%$ average value obtained from the frequency response measurements as can be seen from Fig. 5.12. This result implies that the coupling efficiency between the blackbody and the entrance of the filter-bank averages $\langle \eta_{\text{bfFB}} \rangle \approx -7.5 \text{ dB} \approx 18\%$. This value is lower than the expected transmission through the lens antenna of $-2.5 \text{ dB} \approx 56\%$ and it can be partly understood from the limited lens-antenna alignment accuracy in the experimental setup and the absence of an anti-reflection (AR) coating on the lens, resulting in standing waves that will reduce the coupling at specific frequencies. An experiment with an AR-coated lens and good control over the alignment needs to be performed to further investigate if there are unknown losses between the lens surface and filter bank entrance. Furthermore, it is worth noting here that the coupling efficiency, calculated either from the frequency response with (5.4) or from the optical efficiency with (5.13), is proportional to the strength of the wideband coupler η_{wb} and thus these two measurements scale together. As a result, a precise knowledge of η_{wb} is key to properly calibrate our measurements.

⁵The optical efficiency measurements can be compared to the peaks of the frequency response measurements because the normalized equivalent bandwidth gives a commensurate boxcar shape whose area is the same as the original response and has a constant unity height. In other words, the effective bandwidth leaves the coupling efficiency as the height-scaling parameter of the equivalent box-car filter response.

5.3.4. Discussion

The yield of this chip has been 100%, with 11 detectors observing 11 different THz pass-bands. The central frequencies of the filters have been observed to shift upwards by $\sim 4\%$ from their designated values. This frequency up-shift is likely due to the sheet kinetic inductance reduction in the top NbTiN layer caused by a lower resistivity than expected [157].

The measured data for those filters well-within the quasi-optical pass-band show a modest peak coupling efficiency of $\langle |S_{i1}(f_i)|^2 \rangle \approx -5.7 \text{ dB} \approx 27\%$ and a loaded quality factor of $\langle Q_l \rangle \approx 940$, which is higher than the targeted spectral resolution of 500. Both these results may be explained from the moderate internal quality factor $\langle Q_i \rangle \approx 3300$ (which is slightly lower than the dielectric Q_i reported in [153]), and the high coupling quality factors $\langle Q_{c1} \rangle \approx 2860$ and $\langle Q_{c2} \rangle \approx 2680$ of the couplers surrounding the resonators.

In order to understand why Q_c was too high with respect to the design value⁶ $Q_c^{\text{des}} = 500$, we carefully inspected the filters using SEM. As can be seen in the inset of Fig. 5.15, the a-Si was over-etched around 100 nm after patterning the top NbTiN layer. The rest of the dimensions from the fabricated filters were altered by at most 5%. These fabrication tolerances have been analyzed in CST Microwave Studio [98] for a coupler in the through-line side of a filter nominally designed to operate at 350 GHz. Q_c was found to strongly vary as a function of the dielectric over-etch as illustrated in Fig. 5.15. With the 100 nm over-etch measured we expect a threefold increase in Q_c with respect to the design value, i.e. $Q_c \approx 3 \cdot Q_c^{\text{des}} = 1500$. This qualitatively agrees with the observed increased quality factor, but is still quantitatively underestimating the measured Q_c . Note that, in this experiment, the coupling efficiency before the filter-bank improved from $\eta_{\text{bfFB}} \approx -7.5 \text{ dB} \approx 18\%$ to $\eta_{\text{bfFB}} \approx -6 \text{ dB} \approx 25\%$ thanks to the re-alignment of the lens.

To partially compensate the impact of this fabrication tolerance, as well as for that of the thickness of the microstrips, we investigated the effect of re-depositing 35 nm of a-Si on top of the filter-bank to reduce Q_c by a factor 1.8 as simulated in CST Microwave Studio [98]. This addition has partially compensated the effect of these three-dimensional features, yielding $\langle Q_{c1} \rangle \approx 1790$ and $\langle Q_{c2} \rangle \approx 2010$, resulting in $\langle Q_l \rangle \approx 640$ and a peak coupling strength $\langle |S_{i1}(f_i)|^2 \rangle \approx -5.8 \text{ dB} \approx 26\%$. The loaded quality factor has been reduced as intended, however the coupling efficiency has not increased due to a lower $\langle Q_i \rangle \approx 2140$, which is likely caused by higher dielectric losses in this 35 nm a-Si layer (deposited at 100 °C) [149], which is also sensed by the microstrip fields.

⁶We already aimed for this lower Q_c of 500 by design thanks to the observations from a previous batch (LT184). Note that, according to (3.13), one would target $Q_c > 10^3$ for a finite Q_i .

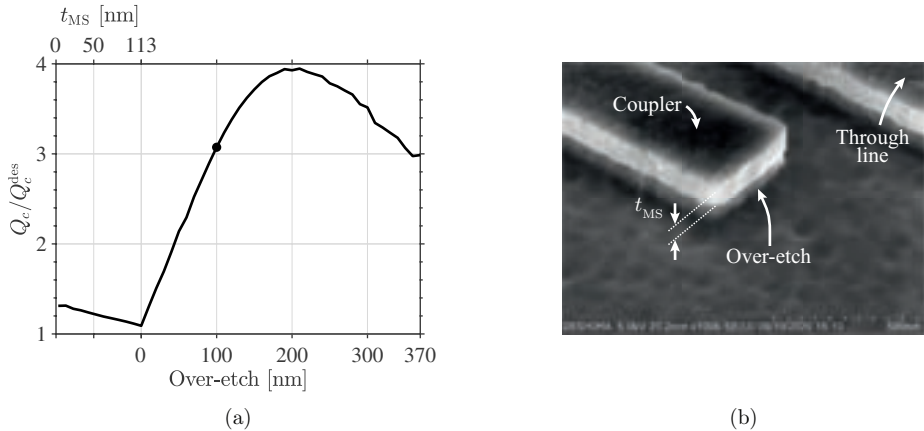


Figure 5.15: Simulated coupling quality factor variation as function of the microstrip metal thickness (t_{MS}) and the a-Si over-etch using the fabricated dimensions of the filters, the measured electrical properties of the superconductors and the dielectric loss reported in [153]. Instead Q_c^{des} is the design performance of the fully planar coupler using nominal dimensions and electrical properties on a lossless dielectric. The dot is the simulation with the closest approximation to the fabricated coupler shown in the micrograph of the inset.

5

5.4. Conclusions and Outlook

In this chapter we propose a band-pass filter design suitable for mid-resolution broad-band THz spectroscopy. The proposed filter geometry consists of an I-shaped microstrip half-wavelength resonator that couples energy with a spectral resolution $R = Q_l = f_0/\delta f$ from the through-line to the MKID sensing the spectral channel. From simulations, this resonator achieves on-resonance the optimal -3 dB coupling efficiency with a loaded quality factor of $Q_l \approx 500$. Off-resonance, an extremely low disturbance is incurred by the filter to the through-line signal over a free spectral range of an octave, thus allowing for the arraying of many resonators in a large filter-bank configuration.

A filter-bank chip sparsely sampling the 300–400 GHz spectrum with these I-shaped resonators has been fabricated in-house following a newly-developed micro-fabrication recipe. This fabrication route has shown a great level of reproducibility and accuracy, yielding a 100% channel yield and achieving all the filter dimensions within 5% error from their nominal values. The frequency response measurements of this chip showcases filters with a moderate spectral resolution of $\langle R \rangle = \langle Q_l \rangle \approx 940$ with no spurious resonances in the band 300–400 GHz. The measured peak coupling efficiency averages $\langle |S_{11}(f_i)|^2 \rangle - 5.7 \text{ dB} \approx 27\%$, which is in agreement with the opti-

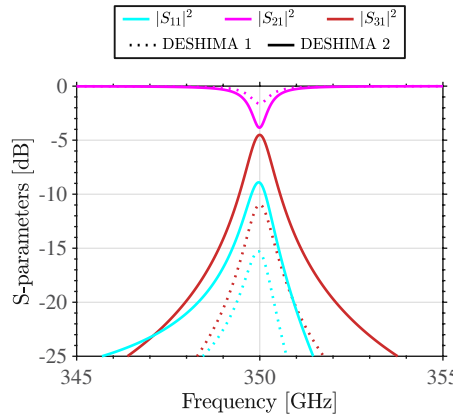


Figure 5.16: Simulated circuit response of a single band-pass filter tweaked to achieve $Q_l = 500$ when using the measured internal quality factor of filters in semi-isolation of DESHIMA 1 ($Q_i \approx 826$) and DESHIMA 2 ($Q_i \approx 3300$).

cal efficiency measurements $\langle \eta_{\text{filter},i} \rangle \approx -5.5 \text{ dB} \approx 28\%$. The current limitations are caused by dielectric losses and amendable errors in the micro-fabrication such as the over-etch of the a-Si dielectric due to the patterning of the top NbTiN layer. This fabrication error has largely increased the coupling quality factors Q_{c1} and Q_{c2} of the filters, which in turn has given rise to an exceedingly large average loaded quality factor at the cost of a moderate coupling efficiency. To amend the performance of the filters from this fabrication tolerance, a dielectric patch has been re-deposited on top of the filters to attempt the recovery of the intended coupling quality factor.

By properly tuning the coupling strength of these microstrip filters of DESHIMA 2 to $Q_{c1} = Q_{c2} \approx 1179$, a loaded quality factor of $Q_l \approx 500$ and a peak coupling efficiency of $\langle |S_{11}(f_i)|^2 \rangle \approx -4.4 \text{ dB} \approx 36\%$ should be within reach with the measured $\langle Q_i \rangle \approx 3300$. When compared to the co-planar waveguide filter of DESHIMA 1 (described in Chapter 4), which has a measured internal quality factor of $Q_i \approx 826$, the peak coupling efficiency would reach $-11 \text{ dB} \approx 8\%$ when tweaked to achieve $Q_l = 500$. This is illustrated in Fig. 5.16. Apart from the higher peak coupling efficiency achievable with the lower loss of the microstrip filters, a wideband filter-bank configuration is made possible with the higher off-resonance transmission (thanks to the avoidance of the losses associated to the common mode in CPW technology) and the larger free-spectral range of the microstrip filters.

Further improvement of the performance of the microstrip filters requires the development of low-loss and low-stress deposited dielectrics such as SiC. Moreover, to enhance the coupling efficiency beyond -3 dB , the spectrum could be over-sampled with more filters as described in [124], however this would require an engineering effort

to coherently or incoherently add the filtered signals at the detector level. Furthermore, sharper response tails could be achieved by adding extra filtering structures [124, 127, 128], which can be beneficial to reduce cross-talk between neighboring channels.

Chapter 6

Design and Optimization of the I-Shaped Microstrip Resonator

In this chapter we detail the design procedure for the THz microstrip band-pass filters (I-shaped resonators) described in Chapter 5 and illustrated with the defining geometrical parameters in Fig. 6.1. Since these filters are half-wavelength resonators, their overall electrical length is determined by the designated resonance frequency and the phase velocity of the lines comprising them. To control their spectral resolution R , and thus their loaded quality factor $Q_l = R$, the coupling quality factor of the coupler at the through-line side (coupler 1), Q_{c1} , and that of the coupler at the detector side (coupler 2), Q_{c2} , are tuned for a given internal quality factor Q_i according to (3.13). For a particular configuration of the microstrips involved, i. e. fixed widths and stratification, the coupling strength can be tuned with the coupling bar length and/or the separation between the parallel-coupled microstrips involved. Since this co-planar capacitive coupling mostly makes use of the fringing fields of the microstrips, tuning the coupling strength with the separation between the lines can be too sensitive to fabrication tolerances. Instead, tuning the coupling strength with the length of the couplers provides more control and granularity with current fabrication capabilities [156].

Each THz band-pass filter extracts power from the through-line, connecting ports 1 and 2, to the detector attached to port 3. The loading posed by the hybrid MKID detector at port 3 is the characteristic impedance of its THz-absorbing Al-NbTiN CPW section. To avoid reflections at this interface, the microstrip attached to port 3 must be impedance-matched. Furthermore, because the quarter-wavelength¹ hy-

¹In view for compactness and a large free spectral range at microwave frequencies, the MKIDs used are quarter-wavelength resonators, where their open-end is capacitively coupled to the readout line and their shorted-end is galvanically connected to ground.

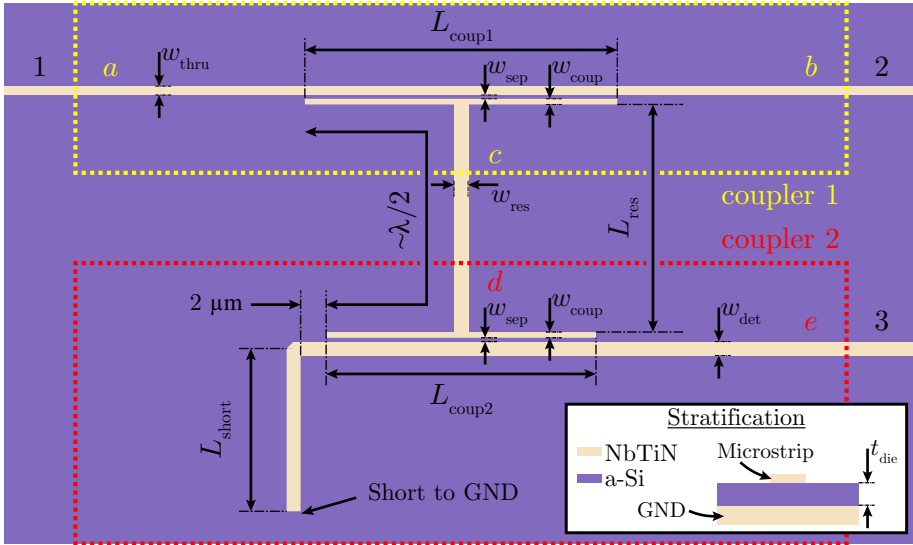


Figure 6.1: I-shaped half-wavelength resonator microstrip band-pass filter with the defining geometrical parameters and the simulation boxes used in Sonnet [99] for each coupler: coup1 and coup2.

6

w_{res}	w_{coup}	w_{sep}	w_{thru}	w_{det}	t_{die}
1.1 μm	450 nm	300 nm	700 nm	1.1 μm	300 nm

Table 6.1: Geometrical parameters common to all the filters as in Fig. 6.1.

L_k^{top}	L_k^{bottom}	ε_r
1 pH/□	0.448 pH/□	10

Table 6.2: Electrical parameters of the filters.

brid MKIDs used need to be connected to ground in the proximity of the radiation absorption location [109], there must be a short-circuit close to the THz filter. To enhance the already weak coupling strength of the filter couplers, the short-circuit was separated from coupler 2 by $L_{\text{short}} \approx \lambda/4$ at THz frequencies.

The general dimensions and electrical properties for these filters are collected in Tables 6.1 and 6.2 and motivated henceforth. The deposited dielectric layer available for the microstrip support when this project started was a PECVD film of a-Si outsourced from Philips, with a relative permittivity of $\varepsilon_r \approx 10$. This dielectric film

had a high tensile stress ($\sim 1 \text{ GPa}$)² and as a result, its thickness was limited to $t_{\text{die}} = 300 \text{ nm}$ to avoid adhesion loss of this layer during the rest of the fabrication process of the microstrip structures (see Appendix B for more details on the fabrication procedure). The top superconducting NbTiN film (which is shared by the microstrip top layer, the antenna, the MKIDs and the readout lines) was tuned to give the metal of the antenna CPW line a large kinetic inductance so that radiation loss is highly suppressed [126]. A kinetic inductance of $L_k^{\text{top}} = 1 \text{ pH}/\square$ was targeted for the superconducting film grown on a-Si, which results in a slightly lower kinetic inductance value for the CPW structures due to the film properties when grown directly on the crystalline Si. A larger kinetic inductance value was not considered for two reasons. Firstly, a higher kinetic inductance would make the resonances too sensitive to thickness variations in the fabrication process. Secondly, a higher kinetic inductance would excessively slow down the waves in the through-line, bringing too close together the different channels (THz filter and MKID), and thereby incurring in problems such as increasing the cross-talk [141, 161] and the TLS noise level [109] when enforcing the inter-filter distance of $L_{\text{thru},i} = \lambda_{\text{thru},i}/4$ as seen from Section 3.3. On the other hand, the ground plane beneath the microstrip filters did not need a high kinetic inductance and thus a moderate value of $L_k^{\text{bottom}} = 0.448 \text{ pH}/\square$ was employed to make use of a thicker metal, which provides a better resilience against the over-etch occurring at the contact points between the top and bottom NbTiN layers (i.e. filter and ground plane connections)³.

With the 300 nm a-Si dielectric layer, we found from simulations that we require to use coupling gaps as narrow as $w_{\text{sep}} \leq 300 \text{ nm}$ to reach a moderate coupling quality factor of $Q_c \geq 10^3$ for coupling bar lengths $L_{\text{coup}1,2}$ less than $\lambda/2$. We chose $w_{\text{sep}} = 300 \text{ nm}$ to limit the fabrication complexity. Also as a result of the thickness of the deposited dielectric, the width of the THz microstrip through-line was fixed to $w_{\text{thru}} = 700 \text{ nm}$ to provide a good impedance match to the 2-2-2 μm -wide CPW line connecting the antenna to the filter-bank with very low radiative losses thanks to the use of a high kinetic inductance NbTiN film [126]. Although a narrower through-line would have given an even better impedance match, this option was discarded since narrower lines are much harder to fabricate reliably, especially over the long lengths needed for a fully sampled octave-band filter-bank (approximately 15 mm). The width of the coupling bars was instead chosen as narrow as $w_{\text{coup}} = 450 \text{ nm}$ to render a compact and strong coupler, thereby pushing its self-resonance beyond the intended octave free spectral range of the filters. To ease the tuning of the resonance of the filter, the characteristic impedance of the vertical bar in the I-shaped resonator

²Currently we grow hydrogenated a-Si in-house with a PECVD process that yields very low mechanical stress ($\sim 3.0 \text{ MPa}$ of tensile stress) [149] and dielectric losses at 350 GHz in the order of $Q_i \approx 4700 \pm 300$ [153]. This is the dielectric film used in the chip discussed in Chapter 5.

³When etching the a-Si layer, the etching process will have to be done always a bit longer than needed to ensure a complete removal of a-Si everywhere. The result is an over-etch into the NbTiN ground plane, which is also etched by the plasma used to etch the a-Si.

is half the one of the couplers. In this way there is no mismatch at the junctions of the couplers with the vertical bar, resulting in a straightforward relation between the resonator overall length and its resonance as we shall see. Finally, the width of the microstrip MKID section is $w_{\text{det}} = 1.1 \mu\text{m}$ to match the impedance of the absorbing CPW section of the Al-NbTiN hybrid MKID.

To relate the intended coupling quality factor Q_c of each coupler to an observable S-parameter, an energetic approach as in [96] is employed. The energy leakage through each coupler is associated to the transmission T through it, which allows to make explicit its contribution to (3.3) with

$$Q_c = 2\pi f_0 \frac{\langle E_{\text{stored}} \rangle}{P_{\text{lost}}} = 2\pi f_0 \frac{\langle E_{\text{stored}} \rangle}{T \alpha \langle E_{\text{stored}} \rangle f_0} = \frac{2\pi}{T}, \quad (6.1)$$

where α is the number of times a wave inside the resonator encounters the coupler per cycle, which is equal to 1 for the half-wavelength resonator case.

In the following sections we shall introduce a procedure to parameterize the design of the microstrip resonator depicted in Fig. 6.1 so that large filter-banks can be scripted without requiring the design of each instance. The geometrical and electrical parameters common to all the filters are respectively given in Tables 6.1 and 6.2. The software employed to simulate the structures is Sonnet [99], which accurately models the superconductors with a sheet inductance.

6.1. Coupler at the Through-Line Side

The coupler at the through-line side of the half-wave microstrip resonator can be seen as a three-port network with ports a , b , c as depicted in the yellow box in Fig. 6.1. Ports a and b are on the through-line and port c is inside the THz resonator. The associated coupling quality factor Q_{c1} can be related to the S-parameters of the yellow box using (6.1), which can be rewritten as

$$Q_{c1} = \frac{2\pi}{|S_{ac}|^2 + |S_{bc}|^2} = \frac{\pi}{|S_{ac}|^2} = \frac{\pi}{|S_{bc}|^2}, \quad (6.2)$$

where $S_{ac} = S_{bc}$ by the symmetry of the structure.

To parameterize this coupler, the length L_{coup1} is swept between the values that meet the previous equation at the lowest and highest operational resonant frequencies as depicted in Fig. 6.2(a). Subsequently, for each length L_{coup1} , a frequency is found that meets the condition in (6.2). Finally, to obtain more granularity, each of these lengths are fitted against the frequency as shown in Fig. 6.2(b), resulting in a lookup table that fully parameterizes coupler 1 for a particular Q_{c1} value over the operational band.

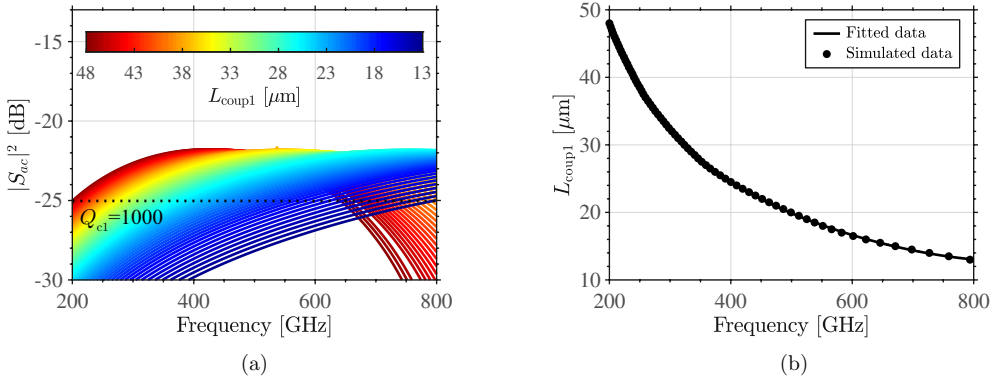


Figure 6.2: Parameterization of the coupler 1, the coupler in the through-line side. Sub-figure (a) shows the frequency response of the transmission through the coupler for a parameter sweep of the coupling bar length L_{coup1} . Sub-figure (b) is the resulting look-up table when fitting in frequency the points intersecting the line $Q_{c1} = 1000$ in sub-figure (a) for each L_{coup1} .

6.2. Coupler at the MKID Side

The coupler at the detector side of the half-wave microstrip resonator can be seen as a two-port network with ports d, e as depicted in the red box in Fig. 6.1. Port d is inside the THz resonator and port e is on the microstrip section of the MKID. The associated coupling quality factor Q_{c2} can be related to the S-parameters of the red box using (6.1), which can be rewritten as

$$Q_{c1} = \frac{2\pi}{|S_{ed}|^2}. \quad (6.3)$$

There are two main geometrical parameters that define the coupling strength of this resonant coupler: the length of the coupling bar L_{coup2} and the vertical distance L_{short} at which the microstrip section of the MKID is short-circuited to ground. To avoid hampering the coupling strength of this capacitive coupler, the distance between the short-circuit and the parallel-coupled lines is kept at a distance of about $\sim \lambda/4$.

The first step is to analyze this coupler in frequency for a sweep of both parameters L_{coup2} and L_{short} between the values that make the first maximum of the resonant coupling strength satisfy (6.3) at the lowest and highest frequency of operation as depicted in Fig. 6.3(a). Subsequently, for all the combinations of the parameters L_{coup2} and L_{short} , the lowest frequency maximum of the coupling strength $|S_{ed}|^2$ is found. Then, for each value of L_{coup2} , the peak values of $|S_{ed}|^2$ are fitted against L_{short} , as depicted in Fig. 6.3(b), and against frequency, as shown in Fig. 6.3(c). Using these fits for each realization of L_{coup2} , a tuple $(f_0, L_{\text{coup2}}, L_{\text{short}})$ can be found

that meets (6.3). From these tuples, each of the parameters can be fitted against frequency to have more granularity in the look-up tables shown in Fig. 6.3(d,e).

6.3. Tuning the Resonance Frequency

Having designed the couplers at a specific frequency for a particular coupling quality factor $Q_c = Q_{c1} = Q_{c2}$ following (3.13), the next step is to tune the resonator to actually ring at the intended frequency. With the geometry of the couplers being fixed, the only free parameter to tune the resonance of the half-wavelength resonator is the length of the vertical bar L_{res} of the 'T' shape. Because the characteristic impedances of the coupling bars have been chosen to be twice the one of the vertical bar of the resonator, there is no mismatch between those sections and thus the overall length of the resonant structure is $\lambda/2$ measured from a tip of one of the couplers through the vertical bar of the 'T' shape and until a tip of the other coupler. As a result, to calculate L_{res} the following equation must be satisfied:

$$\frac{1}{2} = \frac{L_{\text{coup1}}/2 - w_{\text{res}}/2}{\lambda_{\text{eff,coup}}} + \frac{L_{\text{coup2}}/2 - w_{\text{res}}/2}{\lambda_{\text{eff,coup}}} + \frac{L_{\text{res}} + w_{\text{coup}}}{\lambda_{\text{eff,res}}}, \quad (6.4)$$

where $\lambda_{\text{eff,coup}}$ and $\lambda_{\text{eff,res}}$ are respectively the effective wavelength at the design frequency of the microstrips of the coupling bars and of the central part of the resonator.

6.4. Blind Design of a THz Filter at 350 GHz

To validate the procedure explained in this chapter, we are going to blindly design an I-shaped resonator to ring at 350 GHz by making use of the equation in (6.4) and the look-up tables in Fig. 6.2(b), 6.3(d) and 6.3(e). The particular design is depicted in Fig. 6.4(a) together with the defining geometrical parameters. The S-parameters of this filter, simulated in Sonnet [99], are reported in Fig. 6.4(b) and around the resonance in Fig. 6.4(c). The performance of this blindly designed filter at 350 GHz filter deviates very slightly from the nominal performance: the resonance is located at 350.9 GHz (shifted upwards by 0.26% with respect to the nominal location at 350 GHz) and the loaded quality factor is $Q_l \approx 495$, instead of 500.

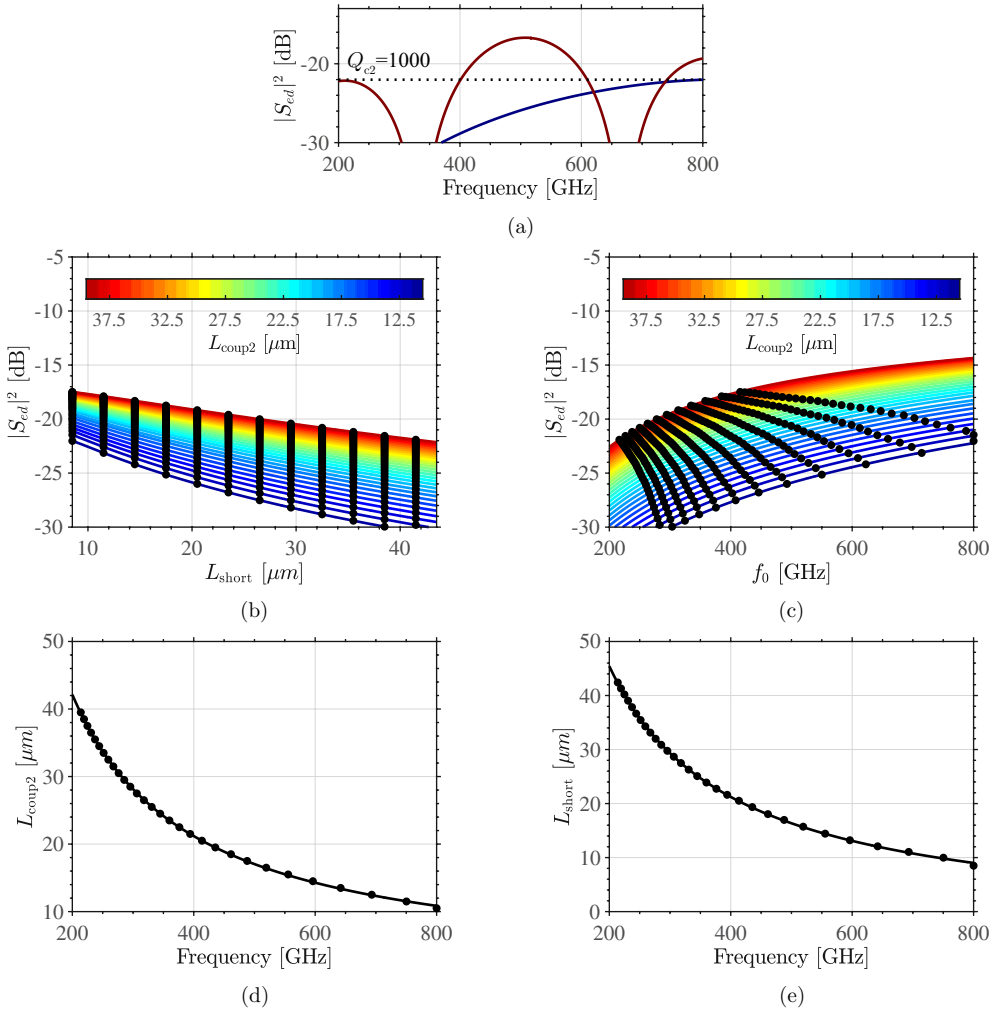


Figure 6.3: Parameterization of the coupler 2, the coupler in the detector side. Sub-figure (a) shows the two parameter realizations that achieve the peak value of $|S_{ed}|^2$ corresponding to $Q_{c2} = 1000$ at the edges of the band. All the intermediate values of L_{coup2} and L_{short} are swept. Sub-figure (b) shows the value of the first $|S_{ed}|^2$ peak for every parameter tuple (L_{coup2}, L_{short}) and the fit against L_{short} for every L_{coup2} . Sub-figure (c) plots the value of the first $|S_{ed}|^2$ peak for every L_{coup2} realization at the resonance location and their fit against frequency. Sub-figures (d) and (e) show respectively the resulting look-up tables for L_{coup2} and L_{short} in terms of the intended resonance frequency for the particular value of $Q_{c2} = 1000$.

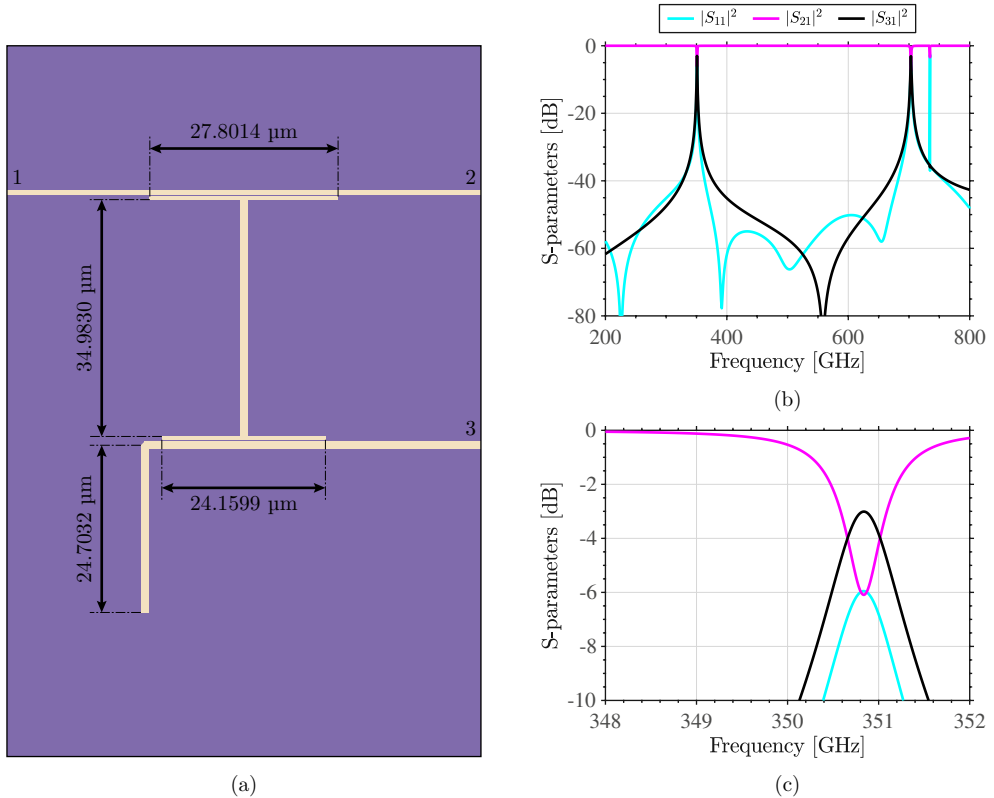


Figure 6.4: Blind design of a THz filter at 350 GHz for $Q_l = 500$. Sub-figure (a) shows the resonator geometry as simulated in Sonnet (cell size of 50 nm), sub-figure (b) shows the S-parameters of the filter and sub-figure (c) a close-up view around the resonance. The resulting filter resonates at 350.8 GHz with $Q_l \approx 495$.

6.5. Empirical Design Optimization

Using the filter design procedure explained earlier in this chapter, we fabricated several batches of filter-bank chips. Each of these different iterations included some small differential changes in their design to investigate possible improvements with respect to the previous batches. We focus our discussion here on the sparse filter-bank chips because they allow to fully characterize the response of their filters with a minimal influence from the neighboring channels. These sparse chips contain 11 filters sampling every 10 GHz the 300–400 GHz spectrum with a targeted loaded quality factor of $Q_l^{\text{des}} = 500$. The relevant design values and the measurement results of the dif-

ferent sparse chip iterations are compiled in Table 6.3 and are discussed next. The explanation of the data analysis procedure is detailed in Chapter 5.

	LT184 (Ch. 5)	LT194 (patched [*])	LT194 (a-Si 350 °C)	LT195 (a-Si 350 °C)	LT207 (buried MS)
Design values					
t_{patch} [nm]	—	—	35	—	—
L_k^{top} [pH/□]	1.00	1.17	1.17	1.17	0.821
t_{die} [nm]	300	370	370	370	300
L_k^{bottom} [pH/□]	0.448	0.448	0.448	0.448	0.723
Q_l^{target}	500	500	500	500	500
$Q_{c1} = Q_{c2}$	1000	1000/2	1000/2 [†]	1000/2	880
η_{wb} [dB]	−26	−24	−24	−24	−26
η_{bfFB} [dB]	−2.5	−2.5	−2.5	−2.5	−2.5
Measurement values					
Peak = Dip	✗	✓	✓	✗	✓
η_{wb} [dB]	−26 [‡]	−24	−25	−26 [‡]	−24
$\langle Q_i^{\text{peak}} \rangle$	450	940	580	570	240
$\langle Q_i^{\text{dip}} \rangle$	700	910	640	560	270
$\langle Q_{c1} \rangle$	2600	2860	1790	1350	1450
$\langle Q_{c2} \rangle$	3500	2680	2010	4500	1450
$\langle Q_i \rangle$	1400	3300	2140	1300	440
$\langle S_{i1}^{\text{peak}}(f_i) ^2 \rangle$ [dB]	−10.0	−5.7	−5.8	−9.5	−11.4
$\langle S_{i1}^{\text{dip}}(f_i) ^2 \rangle$ [dB]	−8.4	−5.7	−5.8	−4.3	−11.3
$\langle \eta_{\text{filter}} \rangle^{\$}$ [dB]	—	−5.5	−6.0	—	—
η_{bfFB} [dB]	—	−7.5	−6	—	—

^{*} Patch of PECVD a-Si grown at 100 °C on top of the filter-bank.

[†] Simulated in CST to include the NbTiN thickness and a-Si over-etch.

[‡] Assumed values.

[§] Using the measured optical efficiency of the filters $\eta_{\text{opt}}^{\text{filter}} = \eta_{\text{bfFB}} \eta_{\text{filter}} \frac{\Delta f_{\text{filter}}}{\Delta f_{\text{BPF}}}$, with η_{bfFB} being the optical efficiency attributed to everything before the filter-bank by means of the calibration with the wideband coupler as $\eta_{\text{bfFB}} = \frac{\eta_{\text{opt}}^{\text{wb}}}{\eta_{\text{wb}}}$.

Table 6.3: Comparison of the different sparse filter-bank batches with the design parameters changing among them and the averaged measured results in terms of quality factors and coupling efficiency.

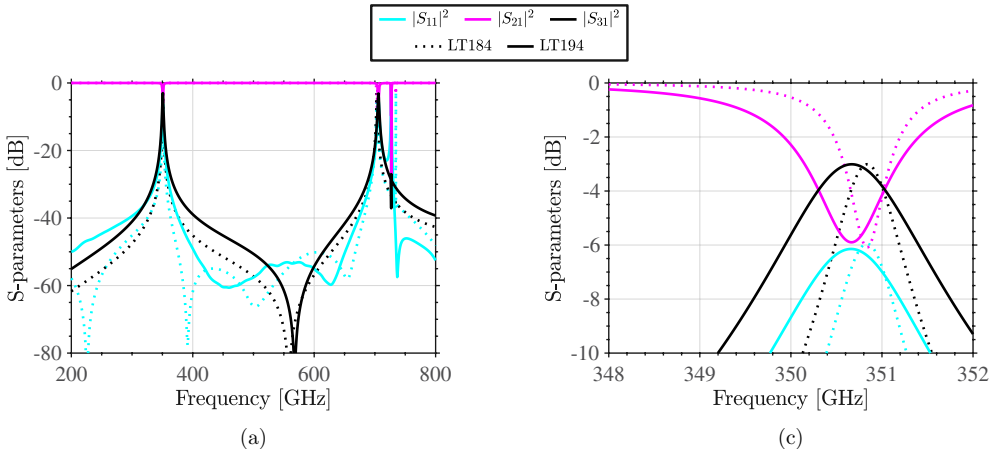


Figure 6.5: Comparison between the simulations in Sonnet of a filter blindly designed to resonate at 350 GHz with a loaded of $Q_l \approx 500$ for LT184 and $Q_l \approx 250$ for LT194. The intention is to obtain filters with $Q_l = 500$ for both batches, but LT194 attempts to preemptively account for the increase in Q_c with a thicker a-Si film.

6

The sparse chip of the first batch (LT184) yielded 2.6–3.5 times too high coupling quality factors with respect to the design value of 1000, resulting in a high loaded quality factor of about 450–700 but also a low coupling efficiency in the order of -10 to -8.4 dB (10–14.4%) due to the limited internal quality factor of about 1400. The probable cause for this coupling strength mistune is some over-etch of the a-Si layer as shown in Fig. 5.15.

The next batch was LT194, which is discussed in detail in Chapter 5. For this batch, we attempted to decrease by a factor 2 the coupling quality factor of the filters in LT184, while reusing the same mask plates. To obtain $Q_c = 500$, we thickened the a-Si dielectric layer t_{die} from 300 nm to 370 nm, which was possible thanks to the low mechanical stress of the a-Si films deposited in the Kavli Institute of Nanoscience Delft [149]. This increase in t_{die} by itself would cause a faster phase velocity on the microstrip lines, resulting in an up-shift of the filter resonances. To reestablish the nominal location of these resonances, the kinetic inductance of the top NbTiN film L_k^{top} was increased from $1 \text{ pH}/\square$ to $1.17 \text{ pH}/\square$ by reducing its thickness. These two changes together effectively resulted in a simulated value of $Q_l \approx 250$ as shown in Fig. 6.5 when compared against the $Q_l \approx 500$ of a filter of LT184. Despite the designed strengthening of the couplers for LT194, these adjustments did not suffice and the measurements of this batch still gave yield to 5.36–5.72 too high coupling quality factors ($\langle Q_{c1} \rangle \approx 2860$ and $\langle Q_{c2} \rangle \approx 2680$), thereby resulting in a high loaded quality factor of 910–940 and a moderate coupling efficiency of the filters of -5.7 dB $\approx 27\%$.

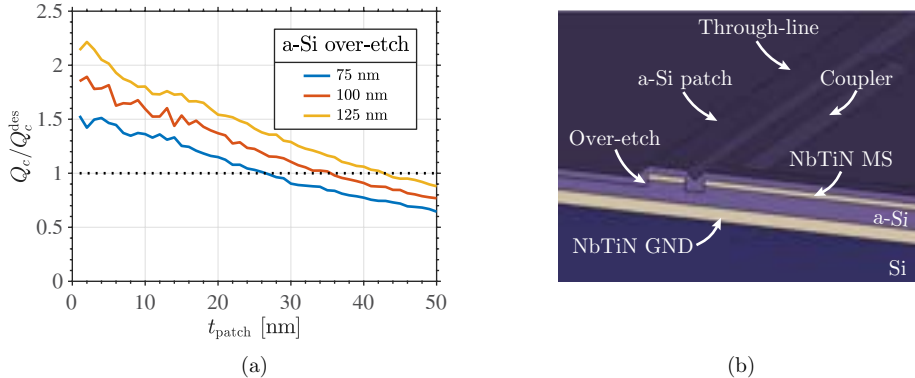


Figure 6.6: Inclusion of a thin a-Si patch of thickness t_{patch} atop of the filters whose couplers were nominally designed as all-planar structures giving a coupling quality factor of Q_c^{des} . Sub-figure (a) shows the effect on the coupling quality factor Q_c with respect to the nominal value of Q_c^{des} when varying the patch thickness for different over-etch depths. Sub-figure (b) shows a cross-sectional view of the 3D coupler structure as simulated in CST Microwave Studio [98].

In parallel with LT194, the batch LT195 was also fabricated following exactly the same recipe and differing only in the use of a higher-temperature grown a-Si film (350 °C instead of 250 °C). The higher substrate temperature in the PECVD process resulted in a dielectric film with high compressive mechanical stress of the order of 379 MPa, causing fabrication issues. The performance of this batch resulted in higher losses than those in LT194, evidenced by a lower Q_i .

To attempt amending the sub-optimal performance of the filters in the sparse chip of LT194, a 35 nm layer of a-Si was deposited atop of the stack-up in order to compensate for both the three-dimensional effects on the couplers as well as the over-etch effects. As illustrated in Fig. 6.6, the idea was to recover the nominal coupling quality factor Q_c^{nom} by choosing the appropriate a-Si patch thickness that decreased Q_c by the same amount the metal thickness and the over-etch into a-Si had introduced. The measured results indicate a moderate (but insufficient) decrease in Q_c to about 1800–2000 but also a reduced Q_i of roughly 2100, which is likely caused by the extra layer of a-Si grown at 100 °C [149]. As a result, the coupling efficiency remained around –6.0 and –5.8 dB (25–26%), which is quite comparable with to the uncovered filters of LT194.

As a follow-up, seeking a coupling quality factor resilient against dielectric over-etch, we investigated a buried microstrip design, where the signal and the ground layers of conventional microstrips are interchanged, making the signal layer interface both a-Si and Si as shown in Fig. 6.7. We used CST Microwave Studio [98] to obtain a differential correction to be applied in the all-planar design simulations using Sonnet

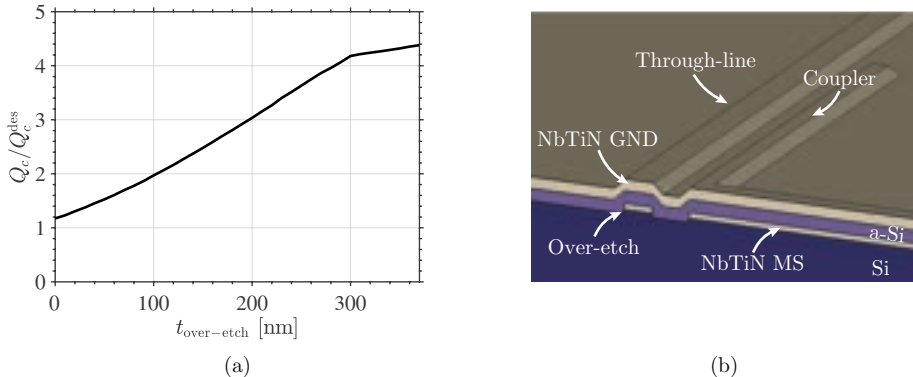


Figure 6.7: Buried microstrip version of the filters whose couplers were nominally designed as all-planar structures giving a coupling quality factor of Q_c^{des} . Sub-figure (a) shows the effect on the coupling quality factor Q_c with respect to the nominal value of Q_c^{des} for different over-etch depths into Si. Sub-figure (b) shows a cross-sectional view of the 3D coupler structure as simulated in CST Microwave Studio [98].

[99], which accounts for the three-dimensional features of the structures and a possible over-etch into Si of ~ 80 – 100 nm. The caveat of this design is that it is prone to suffer from the excitation of surface waves, which can be observed from the spurious box resonances in the Sonnet simulations of Fig. 6.8. For this device we measured an internal quality factor of $\langle Q_i \rangle \approx 440$, which is significantly lower than that of the regular microstrip designs. Since the fabrication steps for both devices are identical, excess radiation losses are a likely candidate for the observed Q_i reduction in the buried microstrip design. As a result of the diminished Q_i , this chip also yielded a low loaded quality factor $\langle Q_l \rangle$ of 240–270 and a very weak coupling strength $\langle |S_{11}(f_i)|^2 \rangle$ of -11.4 to -11.3 dB (7.2–7.4%).

6.6. Conclusions

In this chapter we have discussed the procedure to design band-pass filters as I-shaped half-wavelength resonators for broadband THz filter-banks. In this discussion we have included fabrication trade-offs that drive the designs. Further we have designed, fabricated and measured several sparse filter-bank chips that have allowed us to perform statistics on several semi-isolated filters. After the characterization of several sparse filter-bank chips we have a number of recommendations for the future developments of broadband THz filter-banks:

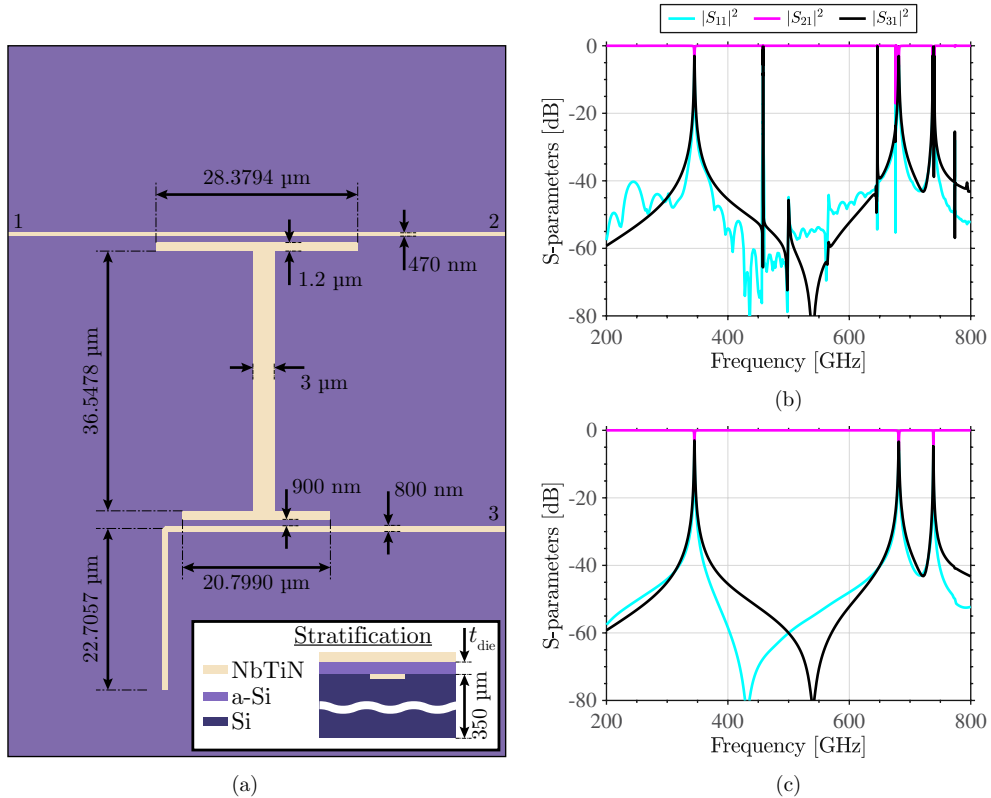


Figure 6.8: Buried microstrip THz filter design at 350 GHz for $Q_l = 500$. Sub-figure (a) shows the resonator geometry as simulated in Sonnet whose S-parameters are given for (b) the nominal stratification and (c) for the stratification with an absorbing layer below Si, following [144]. The resulting filter resonates at 344.90 GHz with $Q_l \approx 428$.

- Use conventional microstrip technology and not co-planar technology or buried microstrips because they can respectively excite leaky and surface wave modes, which effectively amount to radiation loss.
- Lay the microstrip filters on low-stress and low-loss dielectric films such as a-Si [149] or SiC.
- Increase the dielectric film thickness to alleviate the effects on the performance of the filters that the micro-fabrication tolerances may have.

- Fine-tune the etching rate in the micro-fabrication of the different layers, and in particular for those patterned after the dielectric support of the microstrip structures has been laid down, because it can get over-etched and thus hamper the performance of the filters. When needed, a thin low-loss dielectric film patch may be used to tweak a-posteriori a design.

II

Towards a Broadband THz Superconducting On-Chip Beam-Steering Antenna

Chapter 7

Focused Connected Array Antenna

This chapter proposes a broadband and efficient integrated focal plane array solution for terahertz (THz) space observation based on a superconducting near-field focused connected array of slots on a membrane. The focused aperture provides (1) broadband and highly efficient illumination of the quasi-optical system, and (2) scanning capabilities within a focusing system. The connected array antenna in turn allows for a fully integrated solution that can synthesize a focused aperture while providing broadband impedance matching. Focused connected array antennas enable the coupling to a reflector system over bandwidths in excess of one octave and with aperture efficiencies in excess of 60%. To demonstrate the concept we present two scaled printed circuit board (PCB) prototypes operating in the band 3–6 GHz and yielding more than 60% reflector aperture efficiency under broadside illumination and allowing to scan one beamwidth at the lowest frequency with a frequency-averaged scan loss of 0.2 dB (5% attenuation). The feasibility of scaling this concept to THz frequencies, based on superconducting microstrips, is also discussed.

7.1. Introduction

Broadband moderate spectral resolution THz spectroscopy for astronomy is crucial for the understanding of the underlying physics of star-formation [27]. The key instruments to this end are broadband imaging spectrometers like the integral field units, fully-sampling the image plane, and the multi-object spectrometers, sparsely-sampling the image plane with (steerable) pixels. These instruments do not exist yet in the THz regime despite their very successful optical counterparts [54]. To

Parts of this chapter are published in *IEEE Trans. Antennas Propag.* [162].

At this end, single-pixel superconducting on-chip spectrometers based on Microwave Kinetic Inductance Detectors (MKIDs) [104] are being developed [49, 52, 53, 113] as the comprising units for future THz imaging spectrometers. The antennas on these spectrometer chips are coupled to the MKIDs with superconducting lines. In order to ensure a broadband and efficient operation of these instruments, the on-chip antennas need to be co-designed with the quasi-optical system that focuses the THz radiation impinging on the primary reflector of a telescope.

Proper illumination of the telescope quasi-optical chain is key for the signal-to-noise ratio of the instrument. On the one hand, spillover losses cannot only weaken the already faint astronomical signal, but also contribute to noise and thus to an overall increase in the exposure time. On the other hand, over-dimensioning the quasi-optics typically incurs in higher costs and the under-utilization of the resolution capabilities. As a result, broadband instruments require both frequency-stable feed radiation patterns and low spillover in the quasi-optical chain. The former ensures an efficient and wideband utilization of the quasi-optical system, while the latter minimizes the loss and noise contributions. The figure of merit is thereby the aperture efficiency, which should be as high and independent of frequency as possible.

Reflector feeds synthesizing frequency-stable beams have been demonstrated in the literature, specially in the microwave regime. In the realm of lens antennas there exist a waveguide-fed double-shell lens [163], achieving an aperture efficiency of 78% over a 3:1 band (excluding dielectric loss in the lens); a connected array of slots under an extended hemispherical lens [164], reporting more than 70% aperture efficiency over a 3:1 bandwidth (excluding dielectric and reflection losses in the lens); and a sinuous antenna under a quasi hyper-hemispherical lens [165] and a pair of leaky-slots feeding an elliptical cone lens [166], which both obtain largely frequency-independent beamwidths in a 4:1 band. There are also log-periodic antenna solutions synthesizing low-dispersive beams such as the Eleven antenna [167], providing an aperture efficiency greater than 66% over a decade bandwidth; and a non-planar quasi-self-complementary antenna [168], presenting an aperture efficiency larger than 50% over a 5.5:1 band. In the context of horn antennas with frequency-stable beams we emphasize the quadruple-ridged flared horn in [169], averaging an aperture efficiency of 69% in a 6:1 band; the smooth-walled spline-profile horn in [170], attaining an aperture efficiency greater than 60% over a 3:1 band; the bullet-horn in [171], yielding an aperture efficiency better than 60% in a 3.5:1 band; and the corrugated horns in [172] and [173], realizing low-dispersive beams over bandwidths of 1.8:1 and 2.5:1 respectively.

In the THz regime there are fewer examples in the literature for frequency-independent feeds. The predominant technology in this regime is the corrugated horn, achieving aperture efficiencies in excess of 80% over a 1.8:1 band [174, 175]. Recently, an integrated hyper-hemispherical leaky lens antenna fed by a bow-tie has been proposed as an on-chip antenna solution with a predicted average aperture efficiency of 65% over a 3:1 band [176, 177] assuming a broadband anti-reflection (AR)

coating for the silicon lens. However, such broadband AR-coatings are difficult to fabricate with stable mechanical properties at cryogenic temperatures [178–182].

To provide directive beams, without requiring the use of integrated lenses, antenna arrays based on superconducting corporate feeding networks (operated below the gap frequency to avoid conductor losses) have been demonstrated over operational relative bandwidths of 20–30% [37, 183, 184] and up to two octaves [185]. In this work we propose a broadband antenna array concept as a reflector feed than can operate over bands larger than one octave and with scanning capabilities. The antenna consists of a connected array of slots on a membrane focusing in the near field [186], which is an out-of-focus phased-array configuration in a reflector system such as [187, 188]. To enable electronic beam-steering from a superconducting array, phase-shifters based on the non-linear behavior of the kinetic inductance of superconductors with a bias current are being investigated as tunable-delay lines [189–192]. This contribution demonstrates the focused connected array concept with two downscaled prototype antennas based on printed circuit board (PCB) technology in the band 3–6 GHz, one scanning broadside and another scanning one beam at the lowest frequency. Scaling to THz frequencies is now within reach with the technology developed for [113, 153, 193].

This chapter is organized as follows. In Section 7.2 we investigate the properties of focused apertures as quasi-optical feeders with broadband and scanning capabilities. In Section 7.3 we present a scaled PCB prototype design of a connected array of slots synthesizing a focused aperture. In Section 7.4 we present the measurements of the fabricated prototypes and discuss the scalability to a THz device.

7.2. Near-Field Focused Aperture

A circular aperture of diameter D with uniform amplitude and phase, henceforth called unfocused¹ aperture following Sherman [194], produces far fields proportional to the Airy pattern. The far-field half-power beamwidth of this aperture is dispersive and it is given by λ/D radians, where λ is the wavelength. A focused aperture, as illustrated in Fig. 7.1, exhibits similar properties such as frequency dispersion of the beamwidth, but in the near field instead of the far field [194–196]. In this section we will investigate these properties and how they can be exploited to render a broadband, efficient and steerable feeder for a focusing system.

¹An unfocused aperture is actually focused at infinity.

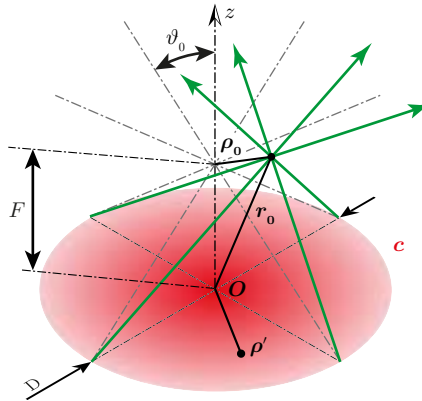


Figure 7.1: A focused circular aperture of diameter D . ϑ_0 is the de-focusing angle subtended between the normal of the aperture and the ray emerging from the edge of the aperture and passing through the focus at a focal distance F .

7.2.1. Focusing Currents

Let us consider a current distribution on a circular aperture of diameter D , whose center coincides with the origin of the reference system as sketched in Fig. 7.1. The currents are such that radiation focuses at the point $\mathbf{r}_0 = (x_0, y_0, F)$ in the plane $z = F$. Their expression is written out in terms of their location $\rho' = (x', y', 0)$ as

$$\mathbf{c}(\rho') = e^{jk|\mathbf{r}_0 - \rho'|} e^{-\frac{1}{w_0^2} \rho'^2} \text{circ}(\rho'; D/2) \hat{\mathbf{c}}, \quad (7.1)$$

where $\rho' = |\rho'| = (x'^2 + y'^2)^{1/2}$ is the radial component of the position of the currents in cylindrical coordinates, k is the free-space propagation constant, F is the focal distance measured orthogonally from the aperture, $\hat{\mathbf{c}}$ is the polarization unit vector and $\text{circ}(\rho'; D/2)$ equals 1 for $\rho' \leq D/2$ and 0 elsewhere. The first exponential term provides the complex-conjugated phase of the free-space Green's function that point sources in the aperture would radiate in \mathbf{r}_0 . The second exponential term provides a Gaussian amplitude taper, whose waist w_0 is fixed for certain edge taper in dB $T_{\text{edge}}|_{\text{dB}}$ (defined negative) as $w_0 = (-5D^2 \log_{10}(e)/T_{\text{edge}}|_{\text{dB}})^{1/2}$. The current in (7.1) can then be approximated for flash points \mathbf{r}_0 in the proximity of $(0, 0, F)$ as

$$\mathbf{c}(\rho') \approx e^{j\frac{k}{2F} \rho'^2} e^{-j\frac{k}{F} (x_0 x' + y_0 y')} e^{-\frac{1}{w_0^2} \rho'^2} \text{circ}(\rho'; D/2) \hat{\mathbf{c}}, \quad (7.2)$$

when $|\rho_0 - \rho'| \ll F$, being $\rho_0 = (x_0, y_0, 0)$ the radial vector to the flash point in the focal plane [194]. The first exponential term in (7.2) is a quadratic phase shift providing the focusing and the second a linear phase shift to scan the flash point \mathbf{r}_0 in

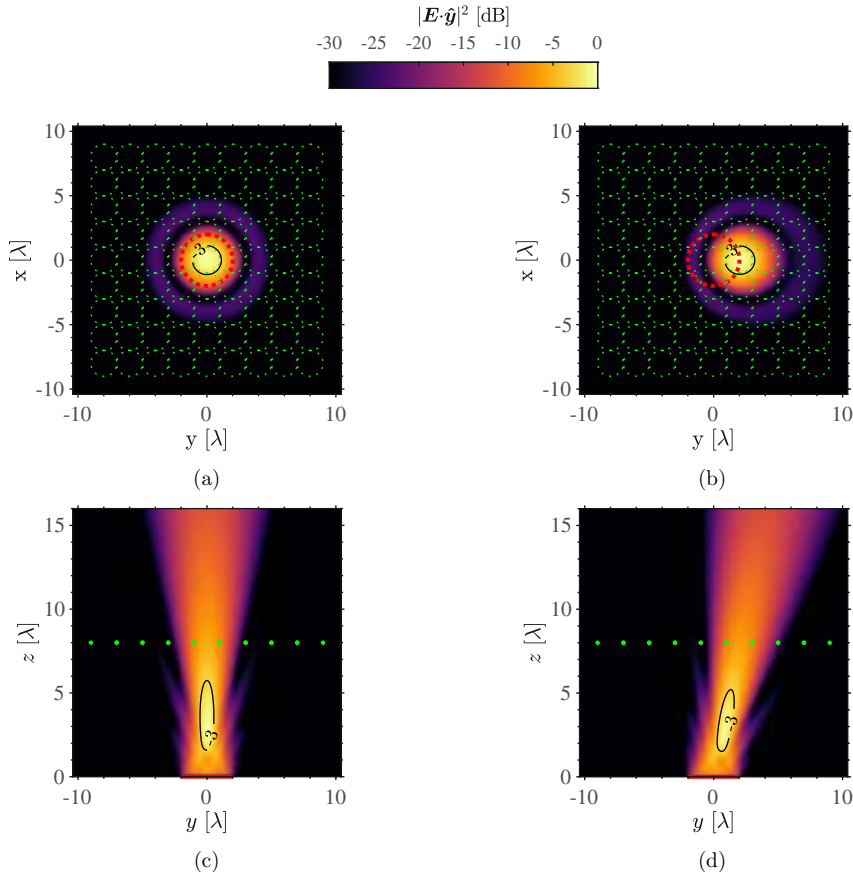


Figure 7.2: Co-polarized component (y -component) of the radiative near-fields in the focal plane generated by an x -polarized magnetic focusing current as in (7.2) when scanning to (a) $\mathbf{r}_0 = (0, 0, F)$ (broadside) and (b) $\mathbf{r}_0 = (0, \lambda f_{\#}, F)$ (one half-power beamwidth in the E-plane). Similarly, sub-figures (c) and (d) show the E-plane of the broadside and scanning scenario, respectively. The focusing current synthesizes a focal ratio $f_{\#} = 2$ and a Gaussian amplitude taper characterized by $T_{\text{edge}}|_{\text{dB}} = -7$. A focal shift is apparent in the axial displacement of the field maximum with respect to the focal plane as noted in [194–197]. The green contours represent the half-power beamwidths ($\lambda f_{\#}$) in the focal plane and the red contours the radiating focusing aperture.

the focal plane. Fig. 7.2 shows two near-field vertical cuts generated by the focusing currents in (7.2) for a focal length $F = 8\lambda$, an aperture diameter $D = 4\lambda$ and a Gaussian amplitude taper with $T_{\text{edge}}|_{\text{dB}} = -7$.

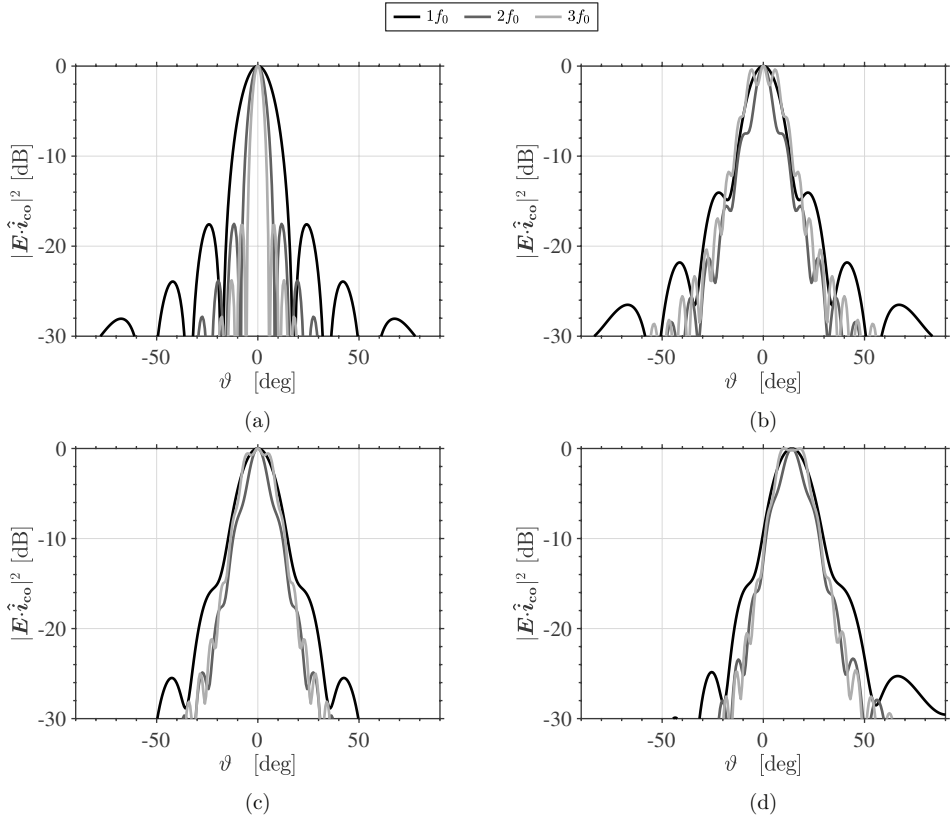


Figure 7.3: Normalized co-polarized component (according to Ludwig's third definition [198]) of the E-plane electric far-field patterns of a circular aperture with $D = 4\lambda_0$, where λ_0 is the wavelength at the lowest frequency f_0 . We compare the frequency dispersion of several current distributions over the aperture, namely: (a) a conventional unfocused aperture; and an $f_\# = 2$ focused aperture (b) with a uniform amplitude, (c) with a Gaussian amplitude taper characterized by $T_{\text{edge}}|_{\text{dB}} = -7$, and (d) with the same taper while scanning one half-power beamwidth ($\lambda f_\#$) in the focal plane, or equivalently to $\vartheta \approx 14.3^\circ$ in the far field.

Thanks to the beamwidth dispersion in the near field, the far fields of focused apertures have fairly frequency-independent beam-widths when compared to unfocused apertures as can be seen from Fig. 7.3(a) and 7.3(b). Furthermore, the diffraction given by the finite size of the focused aperture also causes side-lobes in the near-field that get transformed into far-field ripples, and which need to be attenuated with an amplitude taper as exemplified in Fig. 7.3(c). Lastly, Fig. 7.3(d) shows a steered far-field beam due to the displacement of the flash-point in the focal plane as depicted in

Fig. 7.2(b), which is rendered by the linear phase shift in (7.2). From the ray-tracing of Fig. 7.1, it is apparent that a focused aperture broadens the far-field beamwidth due to the diverging rays beyond the focus. As a result, the beamwidth is proportional to the de-focusing angle $\vartheta_0 = \text{atan}(1/(2f_\#))$, which in turn is given by the focal ratio $f_\# = F/D$. The phase center of the focused aperture far fields is at the flash-point (\mathbf{r}_0), whereas the uniform unfocused aperture far fields are centered in the aperture plane ($z = 0$).

7.2.2. Broadband and Highly-Efficient Quasi-Optical Coupling

To quantify how efficiently a focused aperture can illuminate a quasi-optical system like the Dragonian reflector system of [49], the simplified set-up in Fig. 7.4 is investigated. For a non-scanning scenario, it chiefly consists of a confocal parabolic reflector sharing the focal ratio $f_\#$ with the aperture under investigation. The magnification of such a system is given by the ratio $M = F_{\text{refl}}/F = D_{\text{refl}}/D$, where F_{refl} and D_{refl} are respectively the focal distance and the diameter of the parabolic reflector. For this analysis, the current in (7.2) is propagated to the near-field focal plane with the free-space radiation integral, and subsequently propagated with GRASP [135] to a parabolic reflector using Physical Optics. In this procedure, the spillover efficiency η_{so} is calculated by the software, quantifying how much power misses the reflector. The taper efficiency η_{tap} is calculated from the ratio between the achieved directivity, obtained from integrating the far field of the reflector, and the maximum achievable directivity $D_{\text{max}} = 4\pi A/\lambda^2$, obtained for the ideal uniform illumination of the cross-sectional area A of the reflector. We define the reflector aperture efficiency as $\eta_{\text{ap}} = \eta_{\text{tap}} \cdot \eta_{\text{so}}$.

As illustrated in Fig. 7.5, the aperture efficiency η_{ap} of a reflector illuminated by the far fields of a focused aperture with diameter D is relatively flat for large values of $D/(\lambda f_\#)$. Thereby, focused apertures with $D \geq 2\lambda f_\#$ at the lowest frequency of operation achieve high and fairly frequency-independent reflector aperture efficiencies. On the contrary, the aperture efficiency of a reflector illuminated by an unfocused aperture from its focus peaks around $D = 2\lambda f_\#$; where the angle subtended by the optical axis and the reflector from its focus, $\vartheta_{\text{rim}} \approx \text{atan}(1/(2f_\#))$, matches half the half-power beamwidth of the feed. For focused apertures this angle coincides with the de-focusing angle ϑ_0 as indicated in Fig. 7.1. Furthermore, three different amplitude tapers are also shown in Fig. 7.5. The effect of the amplitude taper on the efficiency quickly saturates, and thus a compromise value of $T_{\text{edge}}|_{\text{dB}} = -7$ is chosen.

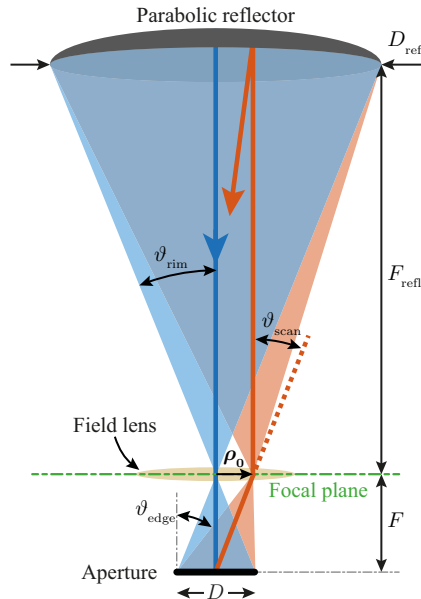


Figure 7.4: Focused aperture illuminating a reflector system. A field lens is placed at the focal plane to collimate the scanned beams.

7

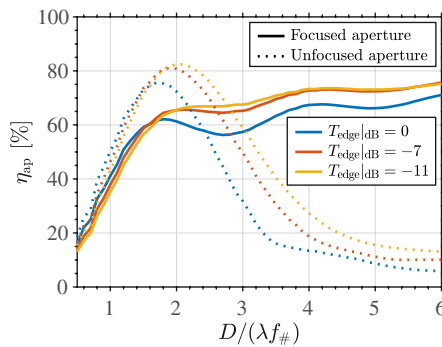


Figure 7.5: Reflector aperture efficiency as a function of the feeding aperture size for focused and unfocused circular apertures and for different aperture tapers.

7.2.3. Scanning Capabilities Inside a Focusing System

To enable scanning inside a focusing system, a small off-focus shift has to be introduced in the focal plane, which corresponds to a linear phase-shift in the primary fields illuminating a quasi-optical system, and eventually a beam tilt in the secondary fields radiated by the reflector [199, 200]. By controlling the linear phase shift term on the aperture current of (7.2), a flash-point displacement on the focal plane can be synthesized. This is illustrated in the simplified quasi-optical system of Fig. 7.4. To minimize the spillover losses, a field lens [201] at the focal plane is required to achieve a telecentric system, where the central ray for each scanned beam comes out parallel to the optical axis.

To assess the performance of this scanning scenario, a similar procedure as described in the previous subsection for the non-scanning illumination is used, differing only in the need to straighten the scanned beams towards the reflector as shown in Fig. 7.4. As a preliminary study, the ideal field lens tilting effect on the beams is incorporated by linearly phase-shifting the focal fields around the flash point \mathbf{r}_0 with the term $e^{-jk\sin(-\vartheta_{\text{scan}})((x-x_0)\cos(\varphi_{\text{scan}})+(y-y_0)\sin(\varphi_{\text{scan}}))}$, where $\vartheta_{\text{scan}} = \text{atan}(\rho_0/F)$ and $\varphi_{\text{scan}} = \text{atan}(y_0/x_0)$. Fig. 7.6(a) showcases the scanning capabilities for both the currents in (7.1) and (7.2) for $f_{\#} = 2$ and $D = 4\lambda_0$, where λ_0 is the wavelength at f_0 . As expected, the approximated phase in (7.2) hampers the scanning performance. Nonetheless, the reflector aperture efficiency is in excess of 60% for at least an octave bandwidth when pointing broadside and scanning one half-power beamwidth at the lowest frequency ($\rho_0 = 1\lambda_0 f_{\#}$) as reported in Fig. 7.6(b).

7.2.4. Prototype Dimensioning

As seen in Fig. 7.5, a focused aperture with $D \geq 2\lambda f_{\#}$ illuminates a reflector system with an aperture efficiency in excess of 60%. However, for the same aperture size D , a smaller focal ratio $f_{\#}$ is beneficial for the reflector aperture efficiency due to the shrinkage of the depth of focus (-3 dB axial beamwidth), where the fields are dominated by the diffraction of the aperture and not the geometrical optics picture. This is exemplified in Fig. 7.7 for $D = 4\lambda$. Moreover, a smaller $f_{\#}$ is advantageous in that it makes a more compact quasi-optical system. On the other hand, a smaller $f_{\#}$ enforces a larger scanning angle from the aperture edge, which is given by $\vartheta_{\text{edge}} = \text{atan}((D/2 + \rho_0)/F)$. As we shall see in the next section, a practical implementation of the focused aperture using flat phased-array antennas limits this angle to about 30° , and thereby sets a lower bound for the focal ratio of $f_{\#}^{\min} = (D/2 + \rho_0)/(D \tan(\vartheta_{\text{edge}}))$. To demonstrate the concept of a beam-steering focused aperture we investigate the scanning of one half-power beamwidth ($\rho_0 = 1\lambda f_{\#}$), for which $f_{\#}^{\min} \approx 1.527$. Although a larger aperture would allow scanning further and with a better illumination of the reflector

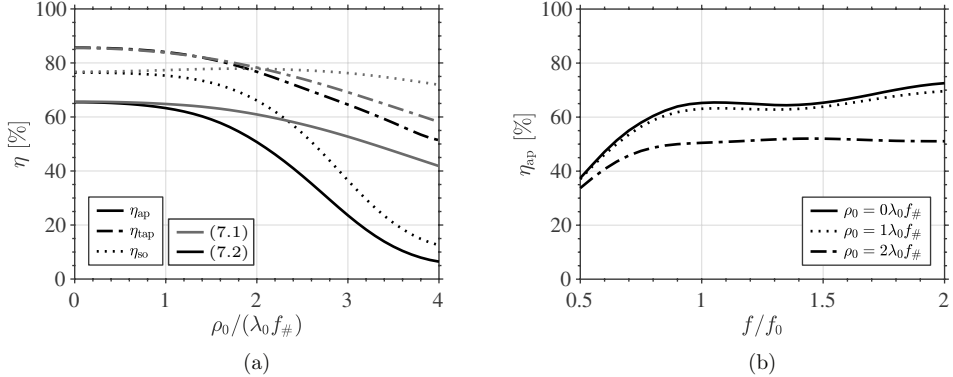


Figure 7.6: Quasi-optical efficiencies for scanning scenarios using a focused aperture with a diameter $D = 4\lambda_0$ and $f_\# = 2$. Sub-figure (a) shows the scanning capabilities at f_0 for the currents in (7.1) and (7.2) as a function of the radial scanning ρ_0 in the focal plane. Sub-figure (b) shows a reflector aperture efficiency in excess of 60% beyond f_0 when scanning broadside or one half-power beamwidth at f_0 using the currents in (7.2).

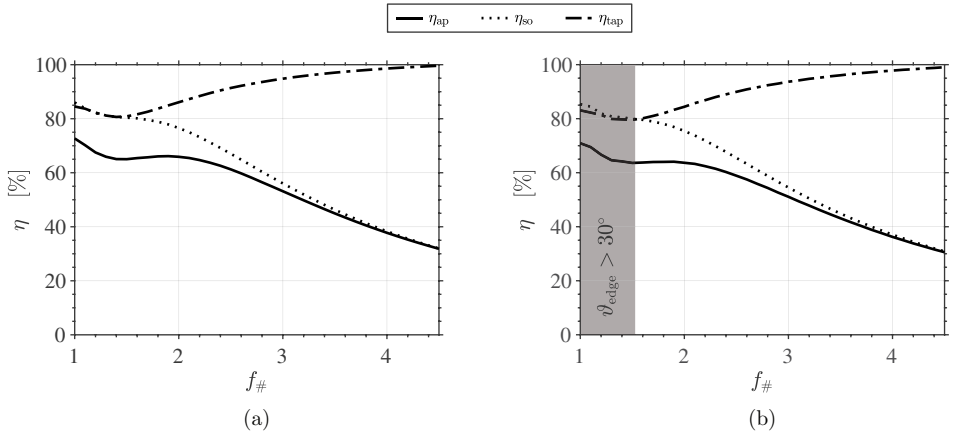


Figure 7.7: Efficiencies of the quasi-optical system in Fig. 7.4 as a function the focal ratio $f_\#$ for a feeding focused aperture with a diameter of $D = 4\lambda$ when (a) pointing broadside and (b) scanning to $\rho_0 = 1\lambda f_\#$.

system, to ease the fabrication of a scaled prototype in standard PCB technology we have fixed $f_\# = 2$ and $D = 4\lambda_0$.

7.3. Focused Connected Array of Slots

Antenna arrays can approximate the currents in (7.2) by providing different amplitudes and phases to each element. Connected arrays are a fully-planar and broadband antenna array solution with low cross-polarization levels [202] that can exploit the broadband properties of the focused apertures. Among the two complementary structures, the slot-type array is preferred over the dipole version because the former is much easier to feed since microstrip technology can be used, thereby avoiding the need for baluns. Moreover, a microstrip feeding network can be shielded from stray radiation by the slot plane, which also serves as the ground plane for the strips.

7.3.1. Array Unit Cell

Fig. 7.8 depicts a unit cell of an array of connected slots radiating in the presence of a thin dielectric slab to minimize the excitation of surface waves while providing the support for a microstrip feeding network. To emulate a future on-chip implementation of the antenna array, the dielectric membrane is made with Rogers RT/duroid® 5880 ($\epsilon_r \approx 2.2$) because it has a reported dielectric loss as low as $\tan \delta \approx 9 \cdot 10^{-4}$ at 10 GHz, which is comparable to the dielectric loss of $\tan \delta \approx 2 \cdot 10^{-4}$ of PECVD (Plasma-Enhanced Chemical Vapor Deposition) a-Si at 350 GHz [149, 153]. Furthermore, a metal plane is located at a distance behind the antenna plane to ensure unidirectional radiation. To counteract the inductive effect on the input impedance of the back reflector, a series capacitor at the end of the feeding point is added as in [203].

The main geometrical parameters are depicted in Fig. 7.8 and their values (nominal and normalized to λ_{\min} , the wavelength at the highest frequency) are compiled in Table 7.1 for a design tuned in the band 3–6 GHz, and scanning up to $\vartheta = 30^\circ$ in all azimuthal planes. This maximum scan angle is the one that an element at the edge of the array would need to scan in order to steer $1\lambda_0 f_{\#}$ in the focal plane in the opposite direction. The active input impedance and matching of the infinite antenna array with the described dimensions and fed from a 100 μm -wide microstrip have been simulated in CST Microwave Studio [98]. The results in Fig. 7.9 show good performance over an octave band. The bandwidth has been compromised against the number of array elements in order to allow the routing of the feeding network in the tight inter-slot spacing $d_y - w_s$ while providing an aperture diameter of $D \approx 4\lambda_0$ at the lowest frequency to ensure a good reflector illumination.

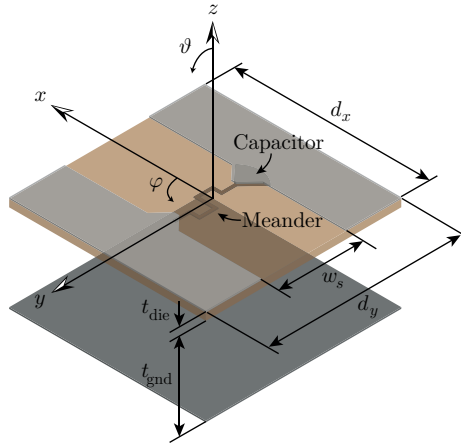


Figure 7.8: Unit cell of a y-polarized connected array of slots with its main geometrical parameters.

Table 7.1: Unit cell parameters and their values.

$d_x = d_y$	w_s	t_{die}	t_{gnd}
21.98 mm $0.44\lambda_{\min}$	9.49 mm $0.19\lambda_{\min}$	0.381 mm $0.007\lambda_{\min}$	12.24 mm $0.27\lambda_{\min}$

— $(\vartheta, \varphi) = (0^\circ, 0^\circ)$ — $(\vartheta, \varphi) = (30^\circ, 0^\circ)$ — $(\vartheta, \varphi) = (30^\circ, 90^\circ)$

7

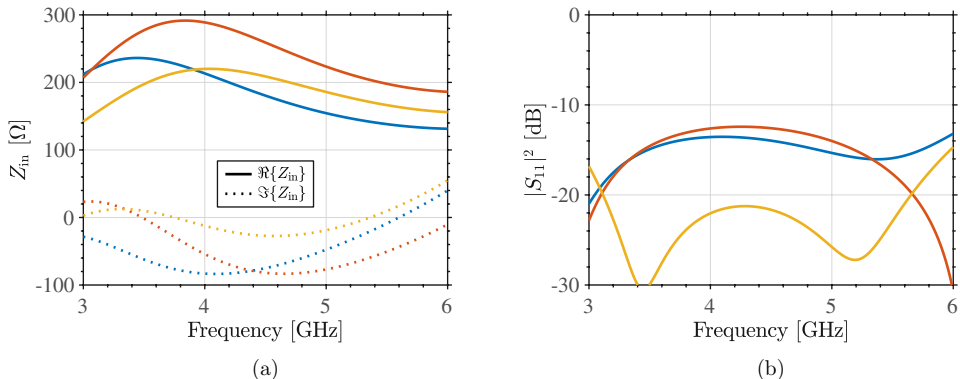


Figure 7.9: Simulated (a) active input impedance and (b) active reflection coefficient of the unit cell in Fig. 7.8 for a normalization impedance of 190Ω and different angles of scanning.

7.3.2. Corporate Feeding Network

The corporate feeding network of this connected array of slots, depicted in Fig. 7.10, approximates the currents in (7.2) for $f_{\#} = 2$, $D \approx 4\lambda_0$ and $T_{\text{edge}}|_{\text{dB}} = -7$ in the band 3–6 GHz with 256 feeds distributed on a square lattice over a circular aperture. To investigate the broadside and the scanning scenarios, two feeding networks have been designed hardwired for each scanning scenario. The quadratic and linear phase shifts have been distributed with true-time delay lines in the different stages of the feeding network (inset on the left in Fig. 7.10) and the Gaussian amplitude taper has been implemented by means of unbalanced T-junctions (inset on the right in Fig. 7.10). Moreover, several tapered lines and quarter-wavelength transformers have been used to achieve the required power splitting ratios in the T-junctions while keeping the impedance high enough throughout the network to avoid very wide microstrips. Fig. 7.11 shows a comparison between the targeted and the designed amplitude and phase distributions at the output of the feeding network. The simulation results are obtained from the S-parameters of the feeding network simulated in Ansys HFSS [204] from the 50Ω input microstrip to the different feeding points loaded with the broadside infinite array active input impedance of Fig. 7.9.

Following the same methodology as in Section 7.2, the reflector aperture efficiency can be calculated for an approximation of the current (7.2) assuming an array of x -polarized elementary magnetic currents using the sampling of the actual array as described in Section 7.3.1. The amplitude and phase distribution over the array aperture are given by the transmission coefficients of the simulated feeding network when loaded with the infinite array active input impedance pointing broadside as exemplified in Fig. 7.11. The aperture efficiencies achieved with the simulated feeding network and with the nominal weights following (7.2) for $f_{\#} = 2$ and $T_{\text{edge}}|_{\text{dB}} = -7$ show a good agreement in Fig. 7.12, thereby showcasing an adequate design.

7.3.3. Finite Array Simulations

The finite dimensions of any antenna array will degrade the performance estimated with the infinite array approximation. This applies especially for tightly-coupled arrays such as connected arrays, whose broadband operation relies on the high mutual coupling between the elements. To quantify this degradation, we compare the active reflection coefficients of an infinite array with those of the finite array defined as

$$\Gamma_i^{\text{act}} = \left. \frac{V_i^-}{V_i^+} \right|_{V_j^+ \neq 0 \forall j} = \frac{\sum_j S_{ij} V_j^+}{V_i^+} \quad (7.3)$$

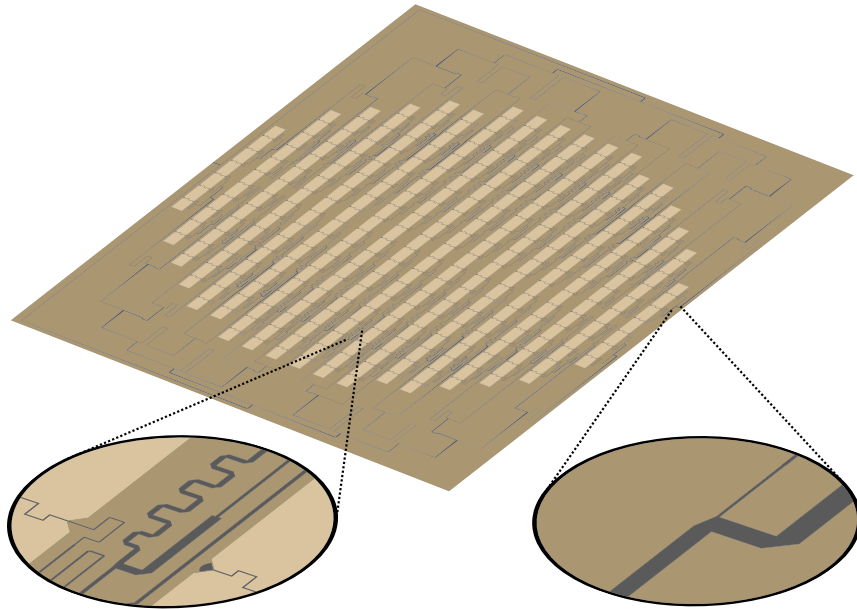


Figure 7.10: Circular connected array of slots fed with a corporate feeding network. The inset on the left emphasizes the implementation of the true-time delay lines for the quadratic and linear phase shifts. The inset on the right-hand side shows an unbalanced T-junction for the amplitude taper.

for the i^{th} port, where V_i^+ and V_i^- are respectively the weights of the forward and backward propagating voltage waves in that port. As can be seen from Fig. 7.13(a), the active reflection coefficient of the different elements of the finite array, fed with the simulated weights of the feeding network V_i^+ , vary around the one of the infinite case.

Despite the high active reflection coefficient of some elements, because the aperture taper sends less power to the feeds on the edges of the array, the figure of merit to investigate is the total mismatch efficiency, defined as

$$\eta_\Gamma = \frac{P_{\text{in}} - P_{\text{ref}}}{P_{\text{in}}}; \quad (7.4)$$

where P_{in} is the total incident power, which is given by

$$P_{\text{in}} = \sum_i \frac{|V_i^+|^2}{2Z_0}, \quad (7.5)$$

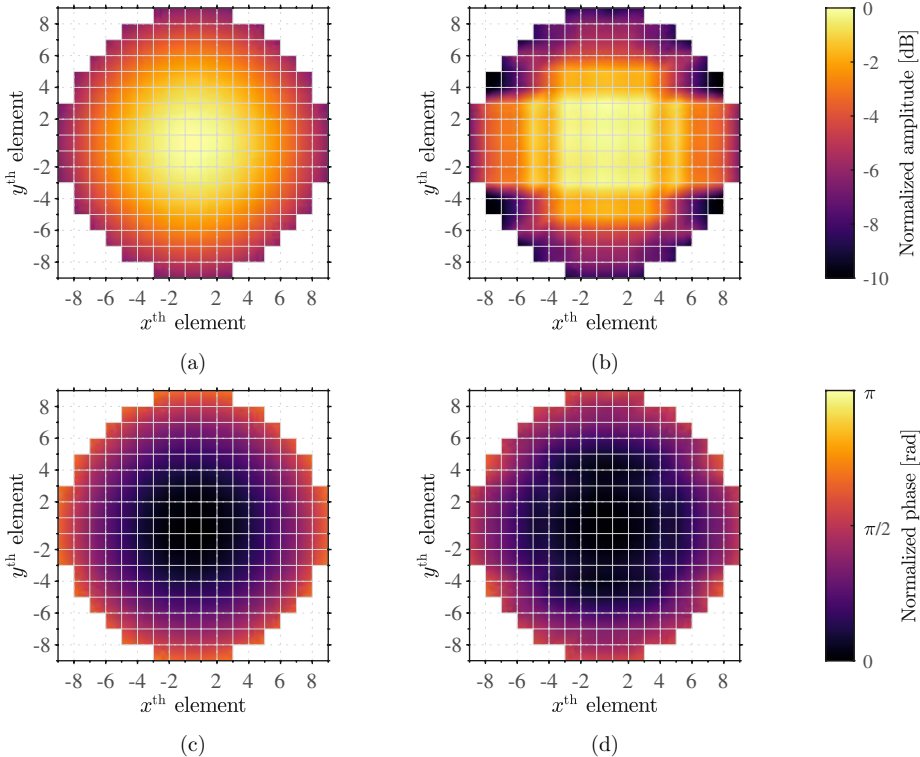


Figure 7.11: Feeding network ideal weights, in amplitude (a) and phase (c), using equation (7.2) and the simulated results from the actual design, in amplitude (b) and phase (d), at 4.5 GHz for broadside pointing.

and P_{ref} is the total reflected power, which is given by

$$P_{\text{ref}} = \sum_i \frac{|\Gamma_i^{\text{act}} V_i^+|^2}{2Z_0}. \quad (7.6)$$

Since the elements that receive less power in the edges are also the ones that typically get more mismatched, the obtained efficiency remains high as reported in Fig. 7.13(b).

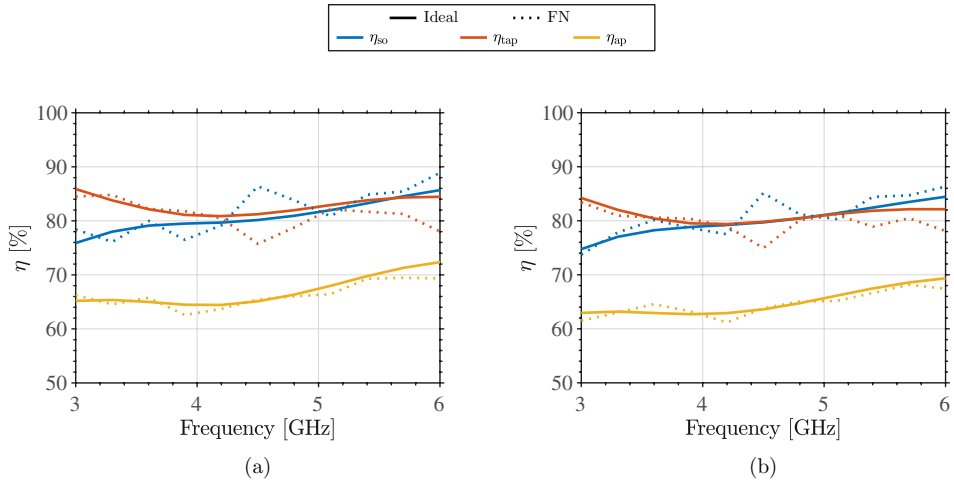


Figure 7.12: Comparison of the quasi-optical efficiencies (spillover, taper and aperture) of a parabolic reflector fed with the aperture currents in (7.2) for the (a) broadside and (b) scanning scenarios, with $T_{edge}|_{dB} = -7$ and a focal ratio $f_{\#} = 2$, using either the ideal sampling weights or the simulated weights obtained from the transmission of the feeding network (FN) loaded with the unit cell impedance shown in Fig. 7.9.

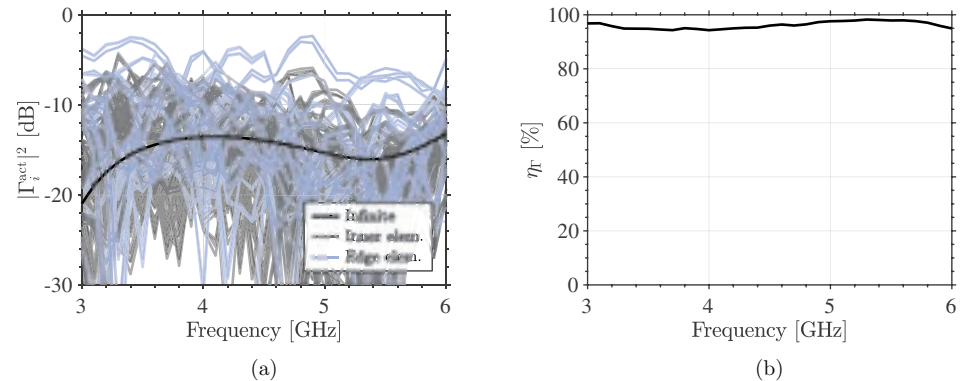


Figure 7.13: Simulated (a) active reflection coefficient (using (7.3)) and (b) reflection efficiency (using (7.4)) of the 256 elements of the finite connected array when fed with the simulated weights of the broadside-pointing feeding network and using a normalization impedance of $Z_0 = 190 \Omega$. Each unit cell of the array is as depicted in Fig. 7.8.

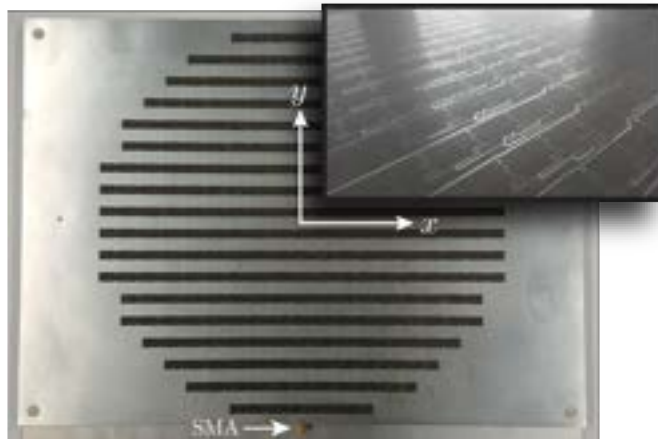


Figure 7.14: One of the fabricated prototypes. The inset is a zoom-in of the backside of the array with the microstrip feeding network.

7.4. Measurements

Following the designs in the previous section, two prototypes of the same antenna array have been fabricated (Fig. 7.14), differing only in their feeding network: one pointing broadside and another scanning to $1\lambda_0 f_{\#}$ in the focal plane along the E-plane. The E-plane represents the worst scenario for scanning as it is the plane where the TM_0 parallel-plate waveguide mode propagates between the back reflector and the slot plane.

Both measured antennas are well matched at the SMA input of the feeding network with a reflection level below -15 dB for the 3–6 GHz band as reported in Fig. 7.15. Fig. 7.16 compares the measured near-field patterns in the focal plane with the calculated ones using the equivalent current in (7.2) with the simulated weights of the feeding network as exemplified in Fig. 7.11(b–d). The simulated beams are in agreement with the measured ones in terms of beamwidth and pointing, however we do observe some differences, chiefly for the scanned array. Firstly, the side-lobe level is higher in the measurements than in the simulations, which we attribute to the edge effects of the connected slots as well as of the TM_0 surface wave propagating between the slot plane and the back reflector. Secondly, the cross-polarization level struck as relatively high compared to simulations, in particular at the lower frequencies.

The high cross-polarized fields were observed to be caused by the low polarization purity of the ultra wideband near-field probe used for the measurements, as seen in Fig. 7.17. To counteract the effect of the probe antenna, we applied a probe-

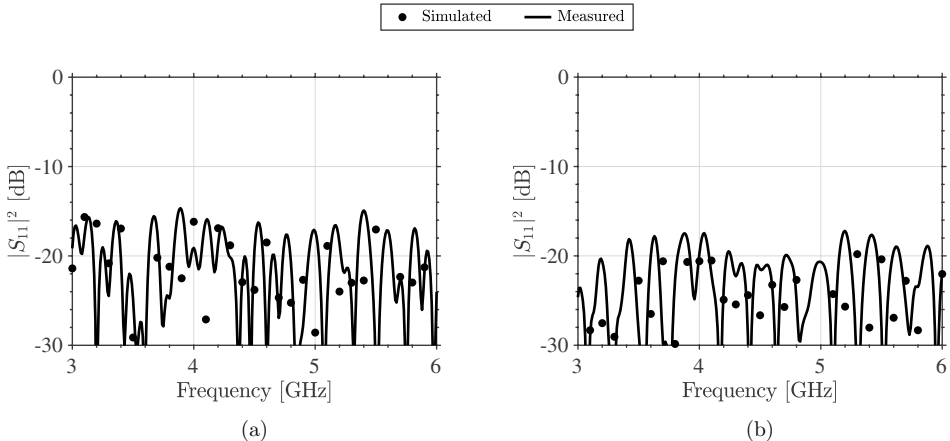


Figure 7.15: Measured reflection coefficient from the SMA of Fig. 7.14 compared against the reflection coefficient of the feeding network loaded with the broadside active input impedance of the unit cell of Fig. 7.8. Sub-figure (a) is for the broadside pointing antenna and (b) for the scanning prototype.

compensation algorithm in the near-field measurement plane as described in [205]. The resulting probe-compensated fields are compared against the un-calibrated ones in the E-plane in Fig. 7.18, which showcases the low cross-polarization level of the proposed antenna array.

The fields in Fig. 7.16 are locally a plane wave around the focus, and thus the near-field directivity can be calculated as described in [206]. The near-field directivities depicted in Fig. 7.19 as a function of frequency agree well with the simulations and show a typical far-field dispersion in the near field. The measured near-field scan-loss for the steering antenna averages to 0.6 dB (13% attenuation) in the operational band.

The gain of the array pointing broadside, reported in Fig. 7.19(a), highlights a large loss, which is detailed separately in Fig. 7.19(b). Surface waves as well as the finiteness effects on the impedance matching of the array amount to a small loss contribution, denoted by ‘Others’ in the plot. The feeding network has been simulated with the specifications of the dielectric material Rogers RT/duroid® 5880 ($\epsilon_r = 2.2$, $\tan \delta = 9 \cdot 10^{-4}$), and with conductors with a typical roughness of $1.3 \mu\text{m}$ and an effective conductivity of $\sigma \sim 2.6 \times 10^7 \text{ S/m}$, as inferred from a four-probe measurement of the dc resistance of a tin-finished $9 \mu\text{m}$ -thick copper strip. From these simulations, it appears that the largest loss contribution arises from the feeding network, which incurs in approximately 3.43–5.51 dB (52–75% attenuation) of conductor loss and 0.28–0.63 dB (6–14% attenuation) of dielectric loss in the band 3–6 GHz. The feed-line length from the SMA to the different feeding points of the array averages $13.4\lambda_{\text{eff,max}}$, where $\lambda_{\text{eff,max}}$ is the effective wavelength at the lowest frequency of an average-width

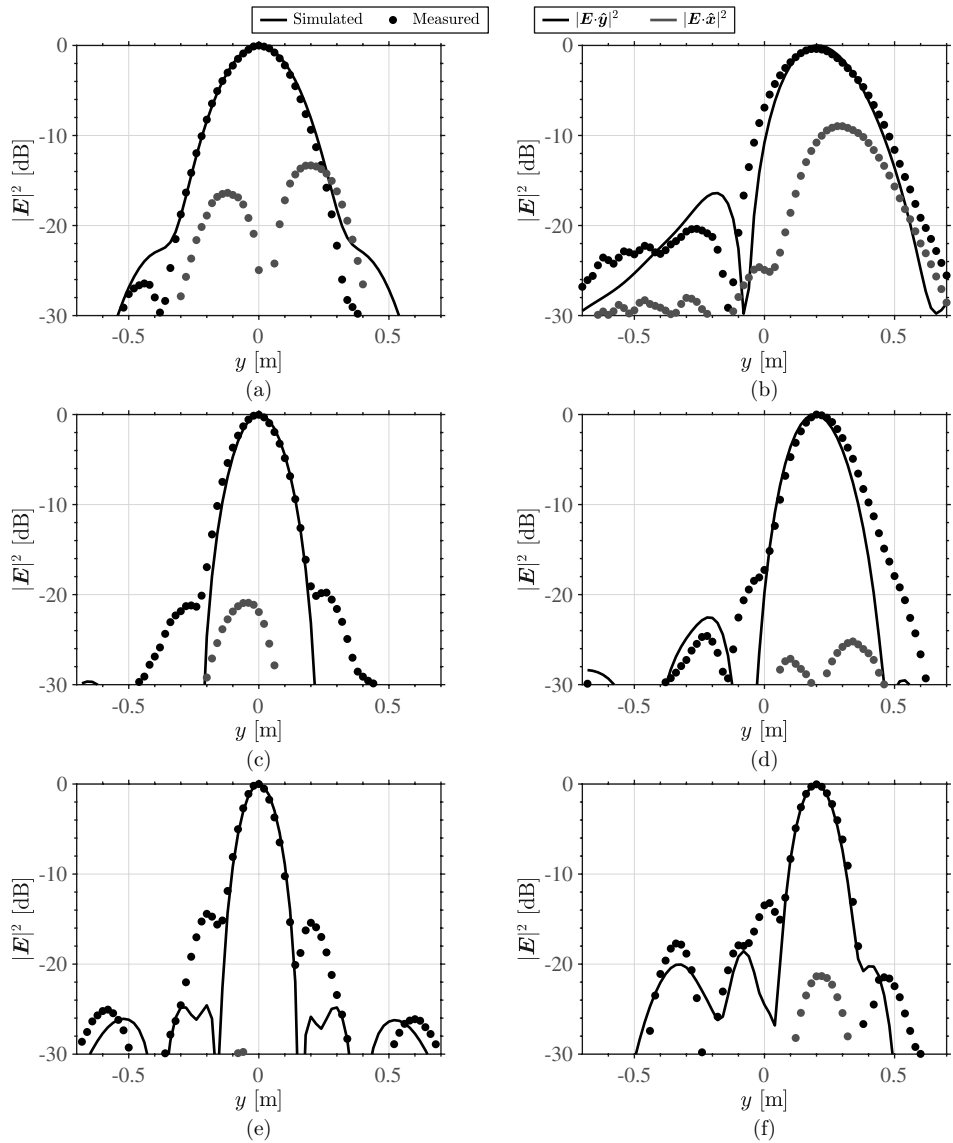


Figure 7.16: Normalized E-plane near fields simulated and measured (un-calibrated) near the focal plane for the array pointing broadside (a, c, e) and for that scanning one 3 GHz half-power beamwidth in the E-plane (b, d, f). Panels (a, b) are for 3 GHz, (c, d) for 4.5 GHz and (e, f) for 6 GHz.

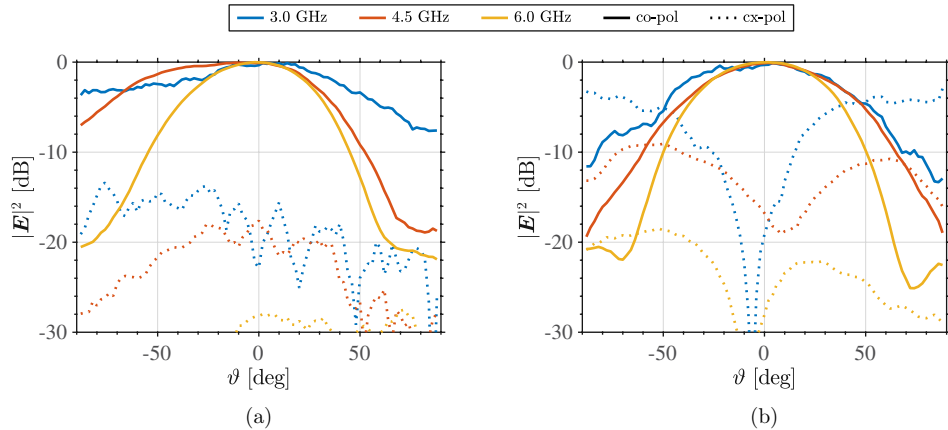


Figure 7.17: Normalized far-field patterns at several frequencies in (a) the E-plane and (b) the H-plane of the probe used to measure the antenna array.

microstrip line. This average line has an attenuation constant of $\alpha \approx 0.27 \text{ dB}/\lambda_{\text{eff,max}}$, from which conductor and dielectric contributions can be distinguished to be $\alpha_{\text{cond}} \approx 0.25 \text{ dB}/\lambda_{\text{eff,max}}$ and $\alpha_{\text{die}} \approx 0.02 \text{ dB}/\lambda_{\text{eff,max}}$ respectively.

On the other hand, a superconducting THz antenna would have negligible conductor loss and would be dominated by the dielectric loss in the feeding network. A separate THz experiment has reported an attenuation constant of $\alpha \approx 0.007 \text{ dB}/\lambda_{\text{eff}}$ for a superconducting NbTiN microstrip on a-Si, where λ_{eff} is the effective wavelength at 350 GHz [153]. As a result, assuming the same electrical length of the feeding network of $13.4\lambda_{\text{eff}}$, we can expect a dielectric loss of 0.09 dB (2% attenuation) for the THz superconducting device. Moreover, the combination of the very narrow features achievable with electron-beam lithography [156] and the high kinetic inductance of the superconducting films [157] can significantly increase the characteristic impedance of the microstrips, making them more suitable for the input impedance of an almost free-standing antenna.

Lastly, the coupling to a prospective quasi-optical system is characterized with the measured fields as explained in Section 7.2. Fig. 7.20 compares the aperture efficiency of the equivalent reflector in Fig. 7.4 achieved when fed by the probe de-embedded fields of the measured prototypes and the simulated fields of an array of elementary magnetic currents following (7.2) for an amplitude taper of $T_{\text{edge}}|_{\text{dB}} = -7$ and a focal ratio $f_{\#} = 2$ using the simulated weights of the designed feeding network loaded with the broadside active input impedance of the infinite array as shown in Fig. 7.11. The efficiency achieved with the calibrated measured fields for the prototype pointing broadside reaches $\eta_{\text{ap}} \geq 60\%$ over the octave band. The prototype scanning one

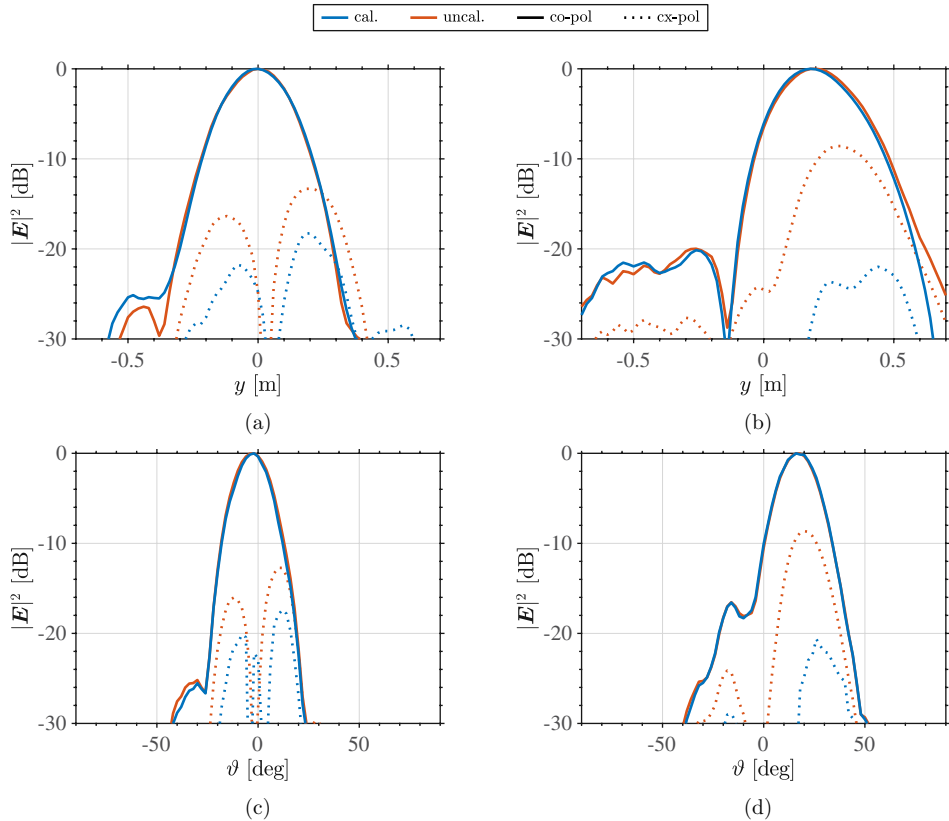


Figure 7.18: Normalized probe-compensated (cal.) and raw (uncal.) E-plane near-field patterns at 3 GHz of the antenna array (a) pointing broadside and (b) scanning one half-power beamwidth ($\rho_0 = 1\lambda_0 f_\# \approx 0.2$ m). Similarly for the far-field patterns (c) pointing broadside and (d) scanning one half-power beamwidth (corresponding to $\vartheta_{\text{scan}} \approx 14^\circ$).

half-power beamwidth illuminates the reflector with an efficiency $\eta_{\text{ap}} \geq 55\%$ for the whole band. The results are in good agreement with the simulations and only slightly deviate from the simulated results due to the edge effects of the array and a small beam-tilt at the lower frequencies as shown in Fig. 7.18(c, d).

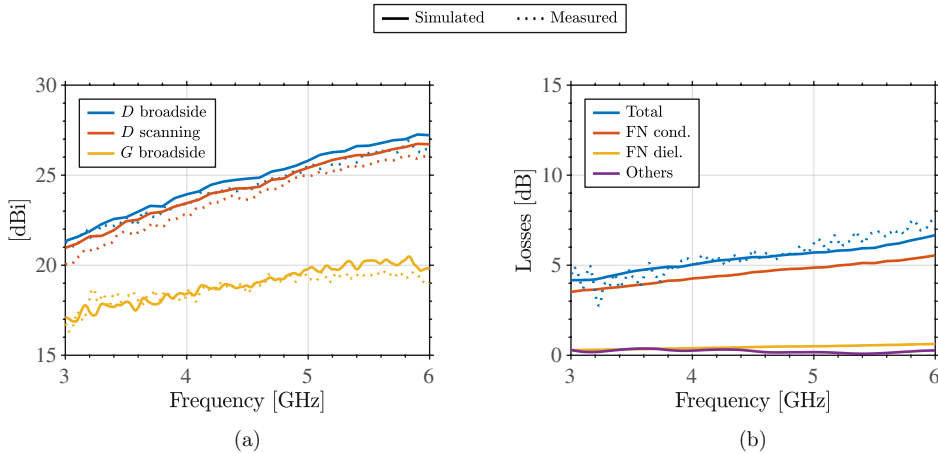


Figure 7.19: Sub-figure (a) compiles the simulated and measured (calibrated) near-field directivity and gain for the antennas pointing broadside and scanning. Sub-figure (b) compares the measured and simulated loss. From the simulated loss terms it appears that the largest loss contribution is the conductor loss in the feeding network (FN).

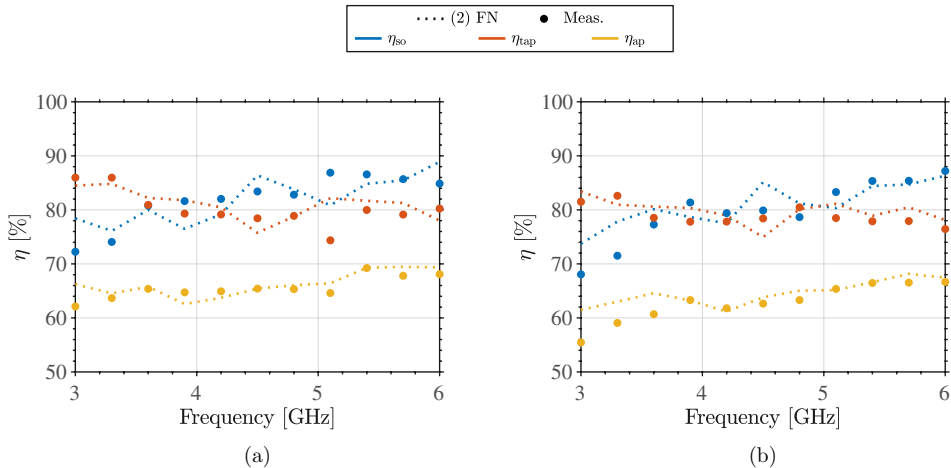


Figure 7.20: Comparison of the reflector aperture efficiency, for the (a) broadside and (b) scanning scenarios, when the reflector is fed with the calibrated measured near-field patterns or when fed with the aperture currents in (7.2) using the simulated weights obtained with the feeding networks loaded with the unit cell impedance in Fig. 7.9.

7.5. Conclusions and Outlook

A study has been carried out on the potential of reflector feeds based on focused connected arrays of slots for efficient and broadband illumination of quasi-optical systems including scanning capabilities with application in future broadband superconducting on-chip THz imaging spectrometers. The feeding network of the connected array synthesizes a near-field focused aperture, approximated by a quadratic phase profile, providing with frequency-stable far fields and thus almost frequency-independent aperture efficiency. Moreover, a Gaussian amplitude taper has been implemented to remove the ripples in the far fields. Lastly, a linear phase shift has been added to shift the flash point in the focal plane, and thereby enabling beam-steering from within a focusing system.

We have designed and characterized two low frequency prototype antennas to demonstrate the concept of a focused connected array as an steerable and broadband reflector feed. The coupling to a prospective quasi-optical system has been investigated by propagating the measured near fields to an equivalent parabolic reflector with a focal ratio $f_{\#} = 2$, yielding aperture efficiencies in excess of 60% for the whole 3–6 GHz band and allowing to scan one half-power beamwidth at the lowest frequency with an average scan loss of 0.2 dB (5% attenuation).

The overall efficiency and bandwidth of these focused connected array antenna PCB prototypes are currently limited by the technology in a twofold manner. First and foremost, the conductor loss for such long feeding networks dominates in PCB technology. Secondly, the requirement for a large aperture ($> 4\lambda_0$) from the standpoint of the quasi-optics together with the tight spatial sampling of the array feeds ($\lesssim \lambda_{\min}/2$) confronts the PCB technological limits, namely the maximum board size and the minimum trace width. These limitations will be overcome in a future superconducting THz implementation of this antenna concept thanks to the negligible conductor loss and the electrically narrower trace widths achievable with current micro-fabrication techniques [156].

Chapter 8

On-Chip Superconducting Phase-Shifters at THz Frequencies

8.1. Introduction

The negligible dissipation incurred by superconductors up to their gap frequency [91] has enabled efficient electrically-long circuitry, with clear manifestations in superconducting delay lines [208–210], on-chip spectrometers [49, 50, 52, 53, 113] and phased-arrays [37]. Furthermore, due to the high kinetic inductance of superconducting thin films, electromagnetic waves are slowed down. This results in the suppression of radiation losses in co-planar waveguides (CPW) at terahertz (THz) frequencies [126] and allows superconducting circuits to become very compact, yet electrically long.

Interestingly, the kinetic inductance not only depends on the temperature and frequency, as explained in Chapter 2, but it is also a non-linear function of a bias current I through the superconducting line due to the increased momentum of the Cooper pairs [211]. This can be parameterized in a phenomenological expression as [212]

$$L_k(I) \approx L_k(0) \left(1 + \left(\frac{I}{I^*} \right)^2 \right) \quad (8.1)$$

for $I \ll I^*$; where I^* is proportional to the critical current I_c , and $L_k(0)$ is the kinetic inductance in the unbiased state. As a consequence, the phase velocity in a

Parts of this chapter have been published in [207].

superconducting transmission line depends on a bias current I as

$$v(I) \approx \frac{v(0)}{\sqrt{1 + \alpha_k \left(\frac{I}{I^*}\right)^2}} \approx \frac{v(0)}{1 + \frac{\alpha_k}{2} \left(\frac{I}{I^*}\right)^2} \approx v(0) \left(1 - \frac{\alpha_k}{2} \left(\frac{I}{I^*}\right)^2\right), \quad (8.2)$$

where $v(0)$ is the unbiased phase velocity and α_k is the kinetic inductance fraction of the superconducting transmission line, which is defined as

$$\alpha_k = \frac{L_k}{L} = \frac{L_k}{L_g + L_k}. \quad (8.3)$$

In this equation L is the total inductance of the line, which is the combination of the geometrical inductance L_g and the kinetic inductance L_k . As a consequence, the phase introduced in a biased superconducting transmission line of length l_{bias} can be tuned by altering its propagation constant $\beta(I)$ with a bias current as

$$\phi(I) = -\beta(I)l_{\text{bias}} \approx -\beta(0)l_{\text{bias}} \left(1 + \frac{\alpha_k}{2} \left(\frac{I}{I^*}\right)^2\right), \quad (8.4)$$

yielding a variable phase shift with respect to the unbiased scenario of

$$d\phi(I) = \phi(I) - \phi(0) \approx -\beta(0)l_{\text{bias}} \frac{\alpha_k}{2} \left(\frac{I}{I^*}\right)^2. \quad (8.5)$$

Hence, the phase shift dependence on bias current increases for a superconducting line with a high unbiased propagation constant $\beta(0)$ (or low unbiased phase velocity $v(0)$), a high kinetic inductance fraction α_k and a long biased length l_{bias} driven with a high current I (well below I^*).

Current-biased superconducting devices operating at microwave frequencies have been reported in the literature for various applications: parametric amplifiers [191, 192, 213–216], current sensors [217, 218], tunable resonators [219–222], on-chip interferometers [223, 224] and phase shifters [189–191]. The tuning range of these devices can be given in terms of a relative phase shift $d\phi/\phi$ in the case of a superconducting line or as a relative resonance frequency shift df/f in a biased superconducting resonator. Since the underlying principle is the same, i. e. (8.1), the tuning range expressions are related as follows

$$\frac{df}{f} = -\frac{d\phi}{\phi} \approx -\frac{\alpha_k}{2} \left(\frac{I}{I^*}\right)^2. \quad (8.6)$$

The state of the art tunability is $d\phi/\phi \approx 0.7\%$ for the CPW parametric amplifier in [192], $df/f \approx -1.3\%$ for the strip current sensor in [217], $df/f \approx -2.6\%$ for the

microstrip resonator in [220], $df/f \approx -4\%$ for both the microstrip resonator in [216] and the CPW resonator in [219], and $df/f \approx -5\%$ for the lumped-element MKID using a biased nanowire in [218]. The tuning range of these devices is limited by how large the bias current I can become with respect to I^* . The maximum value of I before the superconducting state is lost is typically much smaller than I^* in practice and it is given by the experimental critical current I_c : under a current bias, even the smallest resistive fluctuations tend to result in a thermal run-away that breaks the superconducting state. This principle is in fact used in superconducting nanowire single photon detectors (SNSPD's) [225].

In principle, the possibility to modify the kinetic inductance of a superconducting line by means of a bias current should be applicable up to the gap frequency, where the phase-shifting capabilities cease. Hence, NbTiN lines should enable the creation of transmission lines with a tunable phase velocity up to a fraction of the unbiased gap frequency of NbTiN (1.1 THz) due to the energy gap reduction with current. Such lines could be used as feedlines for THz superconducting phased-array antennas [37, 162] which, by tuning their electrical length, could potentially enable electronic beam-steering. In this context, evaluating the phase-shifting capabilities at THz frequencies with current microfabrication techniques is key. In this chapter we address this by proposing an on-chip platform based on a dc-biased Fabry-Pérot resonator, whose sharp resonances serve as proxies for quantifying the phase-shifting range and also allow a very precise measurement of possible additional losses due to the biasing.

The rest of this chapter is organized as follows. In Section 8.2 we introduce the electronic beam-steering concept of a THz phased-array antenna using biased superconducting delay lines. In Section 8.3 we discuss the on-chip platform we have designed to quantify the phase-shifting capabilities at THz frequencies: a dc-biased Fabry-Pérot resonator. In Section 8.4 we explain the fabrication of the actual device. Section 8.4.2 compiles the simulation results of the biased Fabry-Pérot. Lastly, Section 8.5 concludes the chapter with a summary and an outlook.

8.2. Electronic Beam-Steering of a Superconducting Phased-Array Antenna

Scanning a phased-array requires a linear phase progression among the array elements. To dynamically change the pointing angle, the phase shift of the elements would need to be varied. To achieve the different phase shift required for each array element with superconducting delay lines, either each feeding line is biased with a different current or all the lines are biased with the same current but their lengths vary progressively across the array according to the required phase profile. The later option is a simpler solution that only requires two bias lines to achieve two-dimensional beam-steering.

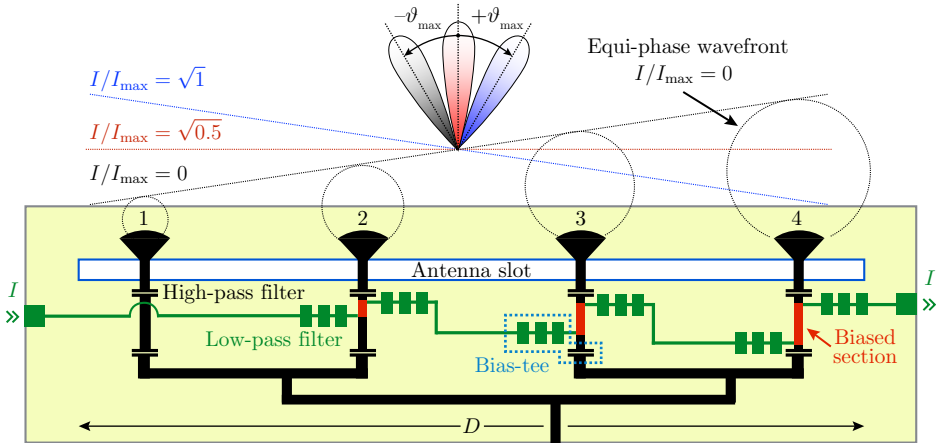


Figure 8.1: Schematic representation of a one-dimensional phase-shifting network for a superconducting phased-array antenna with a maximum aperture dimension D . The feeding of each element of the slot antenna array has a dc-biased section (red) and two bias-tees (blue dotted box), which comprise a dc-block (high-pass filter) and an RF-choke (low-pass filter). These bias-tees avoid the leakage of THz power into the dc network (green) and also constrain the dc-currents to a certain well-delimited section. A hardwired phase in the antenna feedlines is implemented to have a beam pointing towards $-\vartheta_{\max}$ when no extra phase shift due to the bias current is applied. Scanning is achieved by increasing the bias current I .

An impression of a superconducting feeding network exploiting this electronic phase-shifting concept is illustrated in Fig. 8.1 for one-dimensional scanning. In this figure, the corporate feeding network of the antenna (black lines) distributes the power to each array element and a dc network (green lines) bias them to enable electronic beam-steering. The biased sections (red lines) of each element are linearly longer along the array so that the same current can introduce a progressive phase shift. Bias-tees (blue dotted box in the figure) are used to constrain the dc current into a certain transmission line section and also to avoid the leakage of THz power into the dc network. These components comprise a dc-block (high-pass filter) and an RF-choke (low-pass filter). Due to the monotonic dependence of the phase with a current bias in (8.5), the maximum scanning should be hardwired with true-time delay lines. This can be noted in the asymmetric branching of the feeding network in Fig. 8.1. When no bias current is applied, the array points to the maximum scanning direction $-\vartheta_{\max}$. By increasing the bias current as $I = I^*(2\alpha_k^{-1}d\phi/\phi)^{1/2}$, linear beam-steering is achieved in the opposite direction up to $+\vartheta_{\max}$. To extend this scenario to the two-dimensional scanning, a second dc-bias line should introduce, in a similar manner, a phase shift among several slots in the orthogonal dimension.

The two bias-tees used per biased transmission line section allow the separation of the high- and low- frequency paths. The low-pass filter of the bias-tees should reject as much as possible the THz frequencies to avoid any energy leakage. Due to the high frequency of operation, distributed-element solutions such as the stepped-impedance filter can provide good low-pass filtering responses as we will see in Section 8.3.4. The high-pass filter of the bias-tee instead can be simply realized in a lumped-element fashion with a parallel-plate capacitor of about 1 pF with just $\sim 50\mu\text{m}^2$ thanks to the use of thin dielectrics such as a 10 nm-thick layer of a-Si or a-SiC, deposited using Plasma Enhanced Chemical Vapor Deposition (PECVD) [153, 226].

8.2.1. Scanning a 1-D Conventional Phased-Array

A one-dimensional phased-array with an aperture of length D produces a diffraction-limited half-power beamwidth in the plane of the array of $\vartheta_{\text{HPBW}} = \lambda/D$, where λ is the wavelength of operation in free-space. In order to scan such an array to ϑ_{scan} in a reference system centered in its aperture, the array element located at x' must sample the linear phase profile given by $-k \sin(\vartheta_{\text{scan}})x'$, where k is the free-space wavenumber. To scan a maximum angle of ϑ_{max} , comprising N half-power beamwidths, the phase required at each location x' in the array aperture is

$$\phi_{\text{max}}(x') = -k \sin(\vartheta_{\text{max}})x' = -k \sin(N\lambda/D)x'. \quad (8.7)$$

To enable dynamic beam-steering up to $+\vartheta_{\text{max}}$ from the hardwired scanning angle $-\vartheta_{\text{max}}$, the feedline of the array element in x' needs to be biased over a length

$$l_{\text{bias}}(x') \approx \frac{v(0)}{c} \frac{\sin(2\vartheta_{\text{max}})(x' + \frac{D}{2})}{\frac{\alpha_k}{2} \left(\frac{I_{\text{max}}}{I^*} \right)^2} = \frac{v(0)}{c} \frac{\sin(2N\frac{\lambda}{D})(x' + \frac{D}{2})}{\frac{\alpha_k}{2} \left(\frac{I_{\text{max}}}{I^*} \right)^2}, \quad (8.8)$$

which is depicted in red in Fig. 8.1. The current I_{max} is an experimentally determined maximum bias. The longest biased line section for a small scan angle ϑ_{max} can be approximated by

$$l_{\text{bias}}(D/2) \approx \frac{v(0)}{c} \frac{2N\lambda}{\frac{\alpha_k}{2} \left(\frac{I_{\text{max}}}{I^*} \right)^2} = \frac{v(0)}{c} \frac{2N\lambda}{\frac{d\phi}{\phi}}, \quad (8.9)$$

where we have used (8.6) in the last equality. Using maximum relative phase shift $d\phi/\phi \approx 0.7\%$ achieved in [192] and a realistic¹ unbiased phase velocity of a feedline of $v(0) \approx c/\sqrt{50}$, we estimate a maximum biased line length of $l_{\text{bias}}(D/2) \approx 80.8\lambda \approx 55.06\text{ mm}$ for scanning $N = 2$ beams at 440 GHz.

¹This is the phase velocity of the through-line used in the filter-banks of Chapters 5 and 6, which is a reliable microstrip line: not too narrow (700 nm), not from a too thin NbTiN film (113 nm) and on a low-loss dielectric such as a-Si.

8.2.2. Scanning a Focused Connected Array

A conventional phased-array as just investigated cannot be used to scan from the focus of a quasi-optical system. Instead, imaging within a focusing system typically requires off-setting the focal plane pixels [162, 199]. To provide broadband imaging capabilities within a focusing quasi-optical system we proposed in Chapter 7 a phased-array solution: the focused connected array of slots fed by a microstrip feeding network, which is illustrated in Fig. 7.10. Such an array focuses its steerable beam in a focal plane shared with the quasi-optical system. For the particular case of this antenna, the dynamic beam-steering requires a variable linear phase shift among the array elements given by $-\frac{k}{F}(x'x_0 + y'y_0)$ (see Section 7.2 and Fig. 7.1 for reference); where k is the propagation constant in free-space, (x', y') are the cartesian coordinates of the elements of the array, (x_0, y_0) are the cartesian coordinates of the scanned point in the focal plane and F is the focal distance from the array aperture. To scan a maximum of $\pm N$ beams overlapping at -3 dB over a square lattice, i.e. a focal plane sampling of $\lambda f_{\#}$ (with $f_{\#}$ the f-number), the phase shift required on a circular focused aperture of diameter D is

$$\phi_{\max}(x', y') = -\frac{k}{F}(N\lambda f_{\#})(x' + y'). \quad (8.10)$$

We hardwire the maximum scanning scenario of $x_0 = y_0 = -N\lambda f_{\#}$ by adjusting the length of the feedlines of the different array elements by

$$\Delta l_{\max}(x', y') \approx \frac{v(0)}{c} \frac{(-N\lambda f_{\#})(x' + y')}{F \frac{\alpha_k}{2} \left(\frac{I_{\max}}{I^*}\right)^2} \quad (8.11)$$

where we have used (8.5) for a maximum bias current I_{\max} . On the other hand, to enable dynamic beam-steering, the feedline of each array element needs to be biased over a length of

$$l_{\text{bias}}(x', y') \approx \frac{v(0)}{c} \frac{(2N\lambda f_{\#})(x' + y' + \frac{D}{\sqrt{2}})}{F \frac{\alpha_k}{2} \left(\frac{I_{\max}}{I^*}\right)^2}. \quad (8.12)$$

By varying the bias current intensity run over these biased sections of superconducting line of length l_{bias} , the focal spot is displaced and thus beam-steering is achieved.

To exemplify a realistic phase-shifting microstrip feeding network for the electronic beam-steering of a superconducting focused connected array implementation we give preliminary calculations for the biased lines. The antenna fed by this network would have the following specifications by simply scaling the design in Chapter 7: a circular aperture with 18 elements in its diameter D , an octave bandwidth, a highest operating frequency of $f_{\max} = 440$ GHz, a focal ratio $f_{\#} = 2$ and an array period of $d = 0.44\lambda_{\min}$ (λ_{\min} is the free-space wavelength at f_{\max}), a scanning range

of $\pm 2\lambda_{\min} f_{\#}$ (i.e. $N = 2$). Assuming a tunability of $d\phi/\phi = 0.7\%$ as in [192] and a realistic¹ unbiased phase velocity of $v(0) = c/\sqrt{50}$ in the tunable superconducting microstrip lines of the feeding network, the longest biased section for this preliminary estimate would be about $785\lambda_{\text{eff,min}} \approx 75.64$ mm long ($\lambda_{\text{eff,min}}$ is the effective wavelength at f_{\max}). The required linear increase of biased line length among co-linear neighboring array elements is about $31.75\lambda_{\text{eff,min}} \approx 3.06$ mm. This is calculated using

$$\delta l_{\text{bias}} = d \frac{v(0)}{c} \frac{(2N\lambda f_{\#})}{F \frac{\alpha_k}{2} \left(\frac{I_{\max}}{I^*} \right)^2} = \frac{d}{D} \frac{v(0)}{c} \frac{(2N\lambda)}{\frac{\alpha_k}{2} \left(\frac{I_{\max}}{I^*} \right)^2} = \frac{d}{D} \frac{v(0)}{c} \frac{(2N\lambda)}{\frac{d\phi}{\phi}}, \quad (8.13)$$

where we have used (8.6) in the last equality.

8.3. Current-Biased Fabry-Pérot Resonator

From the bias length estimates in the previous section it is clear that a practical implementation of an electrically-steered superconducting phased-array requires long tunable delay lines. The experimental values of the maximum obtainable phase shift are wildly varying (see Section 8.1) and are only available at microwave frequencies. Therefore, an investigation on the phase shifting capabilities of superconducting transmission lines at THz frequencies must be carried out first.

Characterizing the achievable phase shift of a tunable superconducting delay line requires a phase-sensitive system. At THz frequencies, phase-locked commercial systems for cryogenics are very expensive or require ad-hoc solutions which are too involved for the accuracy required [227]. Instead, we propose a very accurate on-chip solution using an antenna-coupled frequency-tunable Fabry-Pérot resonator coupled to a power detector, which in this case is an MKID [104]. This principle has been used recently by our group to measure the loss and phase velocity in superconducting NbTiN co-planar waveguide lines [126] and microstrip lines fabricated from NbTiN and PECVD deposited a-Si [153].

A current-biased Fabry-Pérot resonator is schematically shown in Fig. 8.2(a) and compared to an unbiased equivalent in (b). The resonator consists of an electrically-long transmission line with length L_{FP} , weakly coupled at its two ends to a transmission line. On one side this line leads to the antenna (port 1) with coupler 1, and in the other side to the MKID detector (port 2) with coupler 2. To allow the tuning of its resonance a dc bias current is passed through its length, whose injection points are galvanically connected in shunt in close proximity of the couplers at a distance L_{sep} . The advantage of this technique is that the Fabry-Pérot structure creates narrow resonance peaks, which allow a precise measurement of the absolute phase and phase changes, as well as the losses in the system.

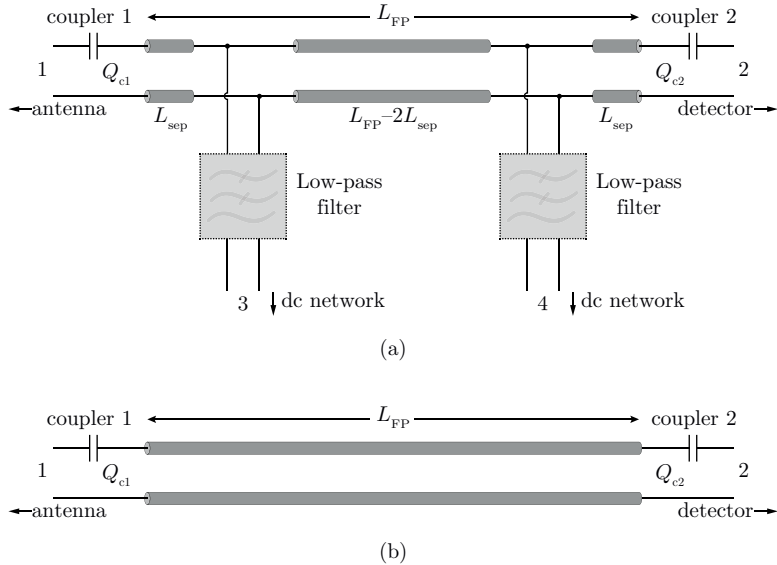


Figure 8.2: Circuit model of Fabry-Pérot resonator. Sub-figure (a) shows a dc-biased resonator and sub-figure(b) an unbiased resonator.

8.3.1. Fabry-Pérot Resonator

The loaded quality factor Q_l of the Fabry-Pérot at a certain resonance is given by

$$Q_l^{-1} = Q_{c1}^{-1} + Q_{c2}^{-1} + Q_i^{-1}, \quad (8.14)$$

which includes all its energy-leaking mechanisms: coupler 1 at the antenna side, with a coupling quality factor Q_{c1} ; coupler 2 at the detector side, with a coupling quality factor Q_{c2} ; and the internal quality factor Q_i , associated to losses. The Fabry-Pérot under consideration is an over-moded resonator defined by capacitive couplers at either side. The fundamental mode of such resonator corresponds to a length $\lambda_0/2$, where λ_0 is the wavelength at the lowest resonance frequency f_0 . By driving the resonator at higher frequencies, harmonics appear at

$$f_n = n f_0, \quad (8.15)$$

where n represents the mode number. Hence, the resonator length can be written as

$$L_{FP} = \frac{\lambda_0}{2} = n \frac{\lambda_n}{2}, \quad (8.16)$$

where λ_n is the wavelength at f_n . The quality factor of the two couplers surrounding the resonator must be equal to maximize the on-resonance transmission and their

value for the n^{th} resonance f_n is given by

$$Q_c = Q_{c1} = Q_{c2} = \frac{2\pi n}{|S_{21}^{\text{coup}}(f_n)|^2}, \quad (8.17)$$

where $|S_{21}^{\text{coup}}(f_n)|^2$ is the transmission at f_n through either coupler in isolation.

8.3.2. Fabry-Pérot Design

In this section we investigate the design of Fabry-Pérot resonators in order to allow an experimental characterization of the phase-shifting capabilities in the 300–400 GHz range. For simplicity we consider the circuit model of the resonator with no bias shown in Fig. 8.2(b). We will show later that the dc network does not heavily distort the response of the resonators if properly designed.

The higher the loaded quality factor Q_l of a Fabry-Pérot resonator, the easier to discern the frequency shift introduced with a bias current. In our current investigation we aim at being able to shift the resonances by at least a full-width half-maximum bandwidth, i. e. $|df/f| \geq Q_l^{-1}$. Assuming that we can reach the tuning range of 0.7–5% found in the literature discussed in Section 8.1 [192, 216–220], this requirement on Q_l would in practice be satisfied for $Q_l \gtrsim 10^1\text{--}10^2$. In order to allow some experimental margin, we aim for $Q_l \sim 10^3$. Although a higher Q_l could be experimentally resolved with our equipment², this is undesirable for two reasons.

First, an exceedingly large Q_l would require stronger rejection from the low-pass filters of the dc-bias network to minimize the distortion to the Fabry-Pérot response and to avoid the leakage of THz power from the resonator into the dc network. To do so, the low-pass filters should be associated to a quality factor much larger than that of the Fabry-Pérot resonator, i. e. $Q_{\text{LPF}} \gg Q_l$, or equivalently a much weaker energy leakage through the filters than energy lost and transmitted through the couplers in the band of operation of the Fabry-Pérot resonator. This makes the filter design harder and it is therefore avoided.

Second, an exceedingly large Q_l would reduce the on-resonance peak transmission through the Fabry-Pérot as

$$|S_{21}(f_n)| = \frac{2Q_l}{Q_c} = \frac{Q_i}{\frac{Q_c}{2} + Q_i} \quad (8.18)$$

due to the internal losses (Q_i). From the equation it is clear that this starts to happen when Q_i becomes comparable to or smaller than Q_c . This could result in the peak

²For the spectral characterization of this device we will use a continuous-wave THz photo-mixing source (Toptica Terabeam 1550), which has a minimum spectral step size of 10 MHz, allowing to distinguish quality factors up to about 4×10^4 in our frequency range of interest.

	Q_l	Q_c	Q_i	$ S_{21}^{\text{coup}}(f_n) ^2$ [dB]	f_n [GHz]	f_0 [GHz]	n	n_{vis}
FP-A	3058	17500	4700	-12	350	1.99	175.73	50
FP-B	1684	5250	440	-12	350	6.64	52.72	15

Table 8.1: Two Fabry-Pérot designs for the band 300–400 GHz. FP-A serves for a low-loss scenario and FP-B for a high-loss scenario.

transmission sinking below the -30 dB noise floor expected from the measurements in [126, 158, 228]. As a result, designs targeting a high Q_l with $Q_i \ll Q_c$ should be avoided. For the particular case of microstrip technology, the internal quality factor can be expected to be in the order of $Q_i \approx 440$ –4700 from the experiments in [153] and those compiled in Table 6.3.

The two design parameters of a Fabry-Pérot resonator are the length L_{FP} and the transmission of the couplers $|S_{21}^{\text{coup}}(f_n)|^2$. In the following sections we shall investigate the influence these parameters have on the spectral response of a Fabry-Pérot resonator and we shall provide designs that enable the observation of both the frequency shift of the resonances, which acts as a proxy of the phase shift by means of (8.6); and the loaded quality factor, which probes the losses when $Q_c \ll Q_i$. Since the expected values of Q_i differ by an order of magnitude, we have designed two Fabry-Pérot resonators for exploring the band 300–400 GHz with the highest possible value of Q_l combined with a significantly large peak transmission. The first design (FP-A) is meant for $Q_i = 4700$ (as measured in [153]) and the second design (FP-B) is meant for $Q_i = 440$ (see Table 6.3). The parameters of these designs are compiled in Table 8.1 and their expected transmission response from the circuit model in Fig. 8.2(b) is shown for two realistic loss scenarios in Fig. 8.3(a) for $Q_i = 4700$ and Fig. 8.3(b) for $Q_i = 440$. The designs only differ in the length of the resonator L_{FP} (and the dependent parameters thereof), but both employ the same coupler with a coupling strength of $|S_{21}^{\text{coup}}|^2 = -12$ dB, as this results in a good compromise for a high loaded quality factor Q_l and high transmission $|S_{21}|^2$.

Resonator length (L_{FP})

Designing Fabry-Pérot resonators with different lengths L_{FP} but identical couplers, i. e. identical values of $|S_{21}^{\text{coup}}(f_n)|^2$, results in resonators with different values of the fundamental frequency (and resonance separation) f_0 , giving thus different values of the mode number n (from (8.15)). As a direct consequence, also the coupling quality factor Q_c (8.17) and the loaded quality factor Q_l (8.14) change, together with the

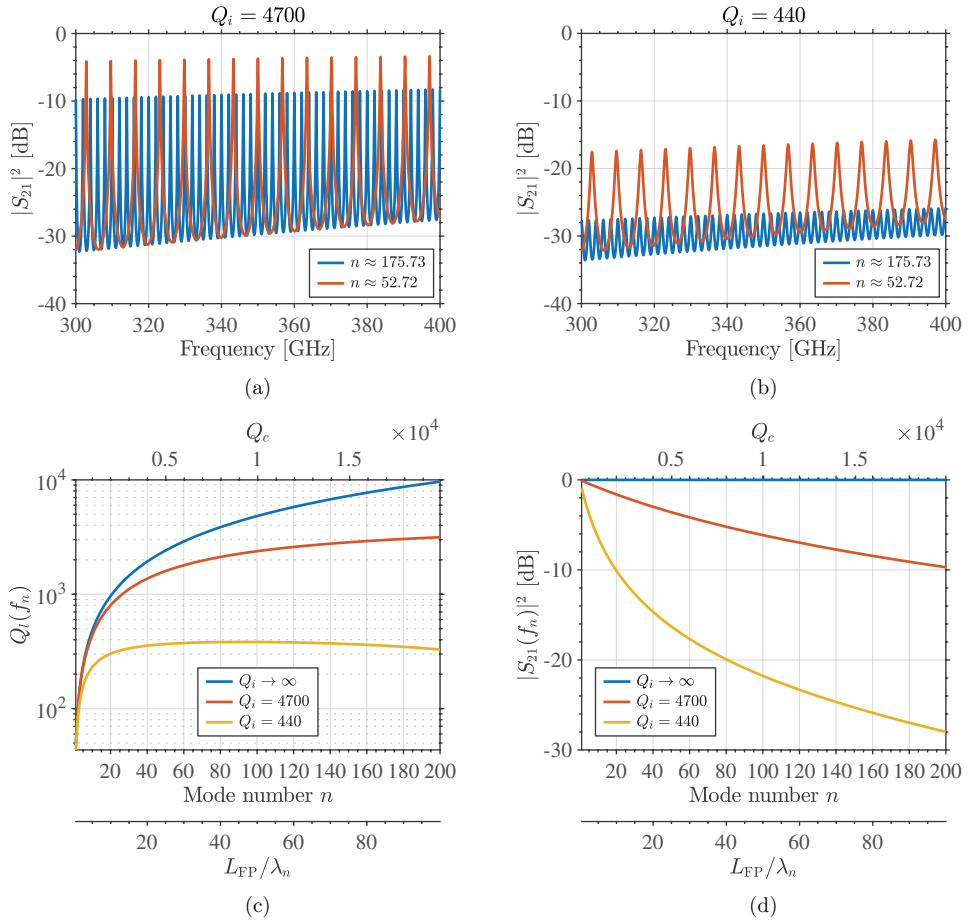


Figure 8.3: Fabry-Pérot resonator (as in Fig. 8.2(b)) operated at $f_n = 350$ GHz for different number of modes n (varying length L_{FP}) but using the same coupling strength $|S_{21}^{\text{coup}}(f_n)|^2 = -12$ dB. To allow an easy comparison among the cases shown, we make every resonator ring at exactly $f_n = 350$ GHz by calculating the L_{FP} value that satisfies the resonance condition $\Im\{Z_{\text{in,FP}}\} = 0$. Panel (a) shows the transmission frequency response $|S_{21}(f)|^2$ through a $Q_i = 4700$ Fabry-Pérot for different mode numbers n . Panel (b) shows the transmission through the same resonator but with $Q_i = 440$. Panels (c) and (d) show respectively the loaded quality factor Q_l and the peak transmission $|S_{21}(f_n)|^2$ for the resonance at f_n as a function of the number of modes n , for various loss configurations in terms of Q_i .

number of visible peaks in the observation bandwidth $f_{\min} : f_{\max}$, which is given by

$$n_{\text{vis}} = \left\lfloor \frac{f_{\max} - f_{\min}}{f_0} \right\rfloor. \quad (8.19)$$

Consequently, a longer resonator with a larger mode number n (i. e. smaller f_0) gives access to more visible peaks with higher quality factors in the observation bandwidth as shown in panel (a) of Fig. 8.3, where we present the simulated data for two different values of L_{FP} using $|S_{21}^{\text{coup}}(f_n)|^2 = -12 \text{ dB}$ and $Q_i = 4700$. This allows for more statistics and thus better resilience against systematic errors caused by, for instance, standing waves in the measurement setup. In panel (b) we consider the same resonator but now with the highest expected loss, associated to $Q_i = 440$ (measured for a buried microstrip filter-bank reported in Table 6.3), which shows how the transmission is strongly suppressed with respect to the $Q_i = 4700$ resonator in (a), especially for the longer resonator (high mode number). Note that the peak transmission, even for the high mode number simulation, is higher than the -30 dB noise floor, as required. Lastly, panels (c) and (d) show respectively the loaded quality factor Q_l and the peak transmission $|S_{21}(f_n)|^2$ for the resonance at $f_n = 350 \text{ GHz}$ as a function of the mode number, for various loss conditions in terms of Q_i . It becomes apparent that a higher mode number (longer resonator) results in a higher loaded quality factor (asymptotically converging to Q_i) in detriment of a lower transmission, especially for low Q_i . In the very high mode number regime with low Q_i , even Q_l will start to deteriorate due to the very shallow resonances in close proximity, which can be appreciated in both panels (b) and (c).

Coupling strength ($|S_{21}^{\text{coup}}(f_n)|^2$)

We have chosen $|S_{21}^{\text{coup}}(f_n)|^2 = -12 \text{ dB}$ in the previous section as this results in a good design as shown in Fig. 8.3. In this section we present the effect of changing this value by $\pm 2 \text{ dB}$ and what the measured data would look like for the two extreme values of Q_i expected from the previous measurements in [153] and Table 6.3. Weakening the couplers increases Q_c and thus Q_l , but causes the reduction of the transmission as illustrated in Fig. 8.4 for two resonator mode numbers and two realistic loss scenarios. This deterioration of the transmission is similar to the cases illustrated in Fig. 8.3 for resonators with equal couplers ($|S_{21}^{\text{coup}}(f_n)|^2$) but different lengths L_{FP} (or mode number n). However, increasing Q_c by weakening the couplers instead of elongating the resonators differs in that the resonator mode number and length are kept, reducing the resonator transmission according to the power allowed by the couplers, even for a lossless scenario.

Following [153], both Fabry-Pérot designs in Table 8.1 employ the same coupler in order to enable the characterization of the internal quality factor Q_i by fitting a curve of the measured loaded quality factors Q_l as a function of the mode number n , which may be experimentally determined by dividing the measured resonance frequency with the measured resonance separation as $n = f_n/f_0$.

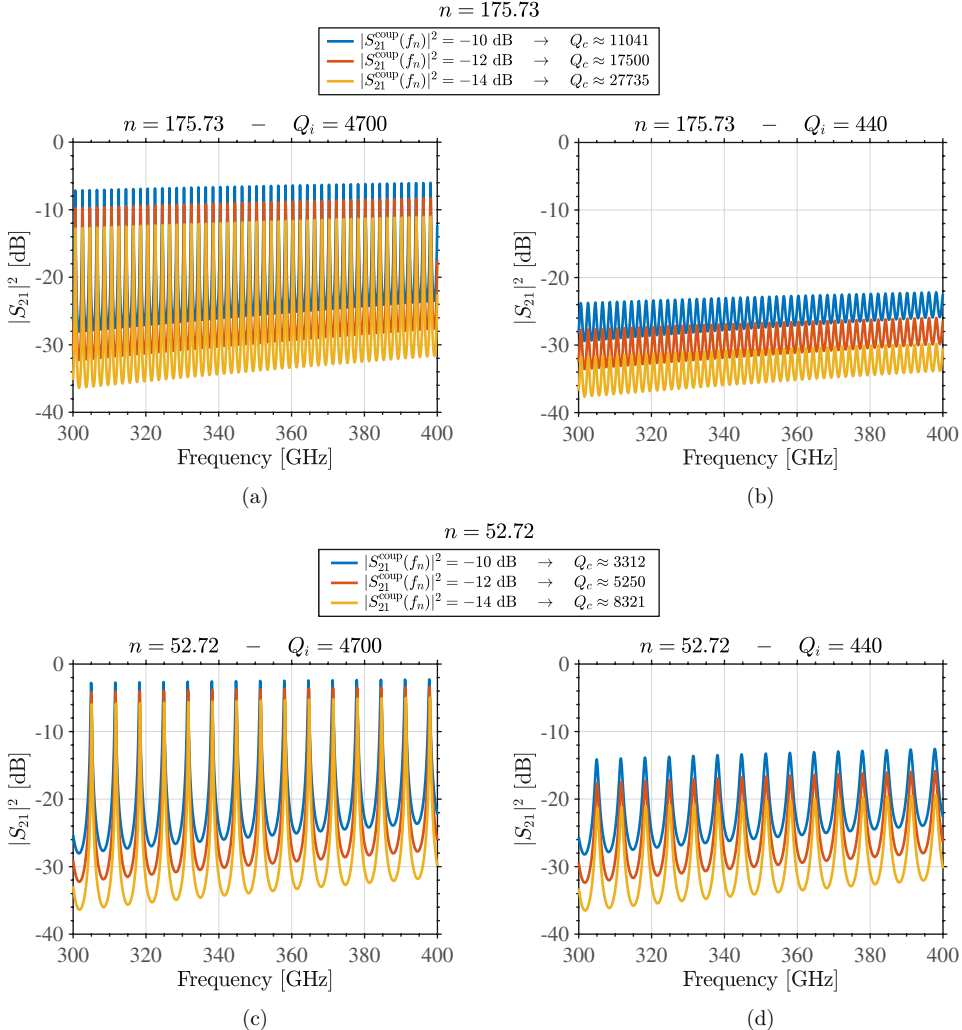


Figure 8.4: Frequency response of the Fabry-Pérot resonator circuit model of Fig. 8.2(b) operated at $f_n = 350 \text{ GHz}$ with $n = 52.72$ (panels (a) and (b)) and $n = 175.73$ (panels (c) and (d)) for different coupling strengths $|S_{21}^{\text{coup}}(f_n)|^2$ and the loss scenarios of $Q_i = 4700$ and $Q_i = 440$. It is apparent that increasing the loaded quality factor Q_i by means of a weaker coupling strength $|S_{21}^{\text{coup}}(f_n)|^2$ comes at the expense of a degraded transmission: on-resonance, due to (8.18), and off-resonance, due to the weaker couplers. This degradation is accentuated for low Q_i scenarios, as can be noted comparing panels (a) and (c) with panels (b) and (d), respectively.

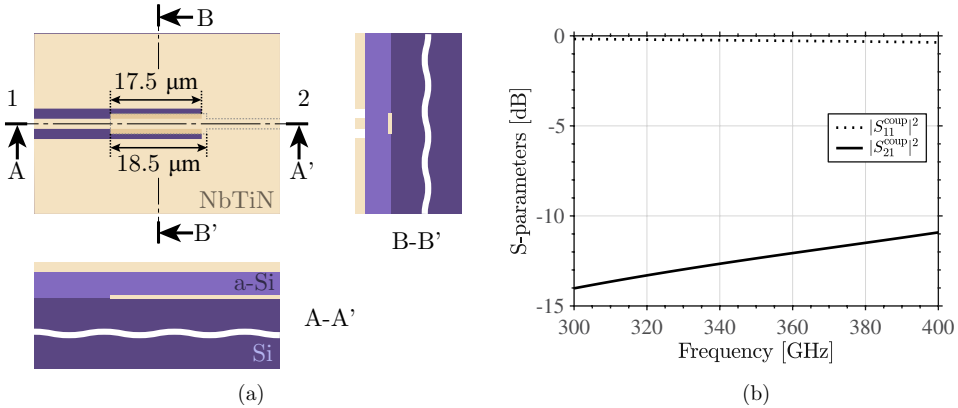


Figure 8.5: CPW-microstrip coupler, in this case a buried microstrip. Sub-figure (a) shows the structure with two cross-sectional views (the Si wafer sub-figure (b) displays its S-parameters.

8.3.3. Fabry-Pérot Implementation

The implementation of the resonators is done with buried microstrip technology with the ground plane on top of the microstrip line. This stratification provides the best thermal contact between the line and the substrate, reducing the impact of the heating due to the bias current. The stack-up of the resonator consists of a 350 μm-thick Si ($\epsilon_r = 11.44$) wafer, a NbTiN layer with a kinetic inductance $L_k = 4 \text{ pH}/\square$ for the resonator, a 300 nm-thick a-Si ($\epsilon_r = 10$) layer as the microstrip dielectric and lastly a NbTiN ground plane layer with $L_k = 0.926 \text{ pH}/\square$. This arrangement is potentially prone to the excitation of radiative modes into the thick substrate, similarly to the buried microstrip filter design presented in Section 6.5. We however deem the advantage of a well-thermalized line to be more important to achieve a greater phase-shift tunability thanks to a higher expected maximum bias current.

In both designs the buried microstrip Fabry-Pérot resonator is connected to 2-2-2 μm wide CPW lines in the top NbTiN layer. The couplers at each end of the resonator line are designed using Sonnet [99] as CPW-microstrip couplers, whose actual geometry is shown in Fig. 8.5. The design consists of a microstrip overlayed for 17.5 μm over a short-circuited CPW, providing a moderate transmission of $|S_{21}^{\text{coup}}(f_n)|^2 \approx -12 \text{ dB}$ at $f_n = 350 \text{ GHz}$ and good resilience against a possible misalignment between the CPW and microstrip layers [228].

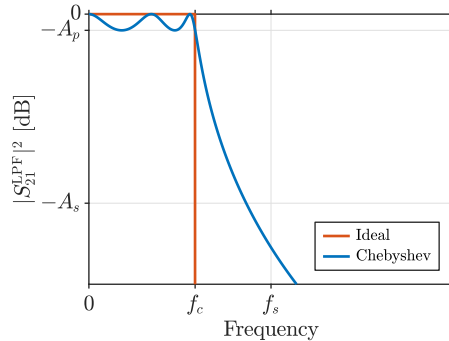


Figure 8.6: Ideal box-car filter compared against a realistic low-pass filter, in this case a Chebyshev.

8.3.4. Low-Pass Filter Design Procedure

The injection of the dc biasing currents into the Fabry-Pérot resonator is done through the low pass-filters in Fig. 8.2(a). The ideal boxcar response of such filter transmits perfectly all the power up to the cut-off frequency f_c , after which all the power is rejected. This response is not realistic and some compromises need to be done to arrive to a practical filter (see comparison in Fig. 8.6). The pass-band will have an attenuation maximum of A_p (in dB) up to the cut-off frequency f_c , the stop-band will have a minimum attenuation of A_s (in dB) from the stop frequency f_s and there will exist a transition-band separating the previous two between the frequencies f_c and f_s .

The pass-band for our low-pass filters does not have any stringent requirements on the insertion loss other than at dc, where a good galvanic connection between the filters and the Fabry-Pérot is absolutely essential to eliminate dissipation due to the dc bias current. On the other hand, the stop-band of these filters need to be highly rejecting in the operational band of the Fabry-Pérot (300–400 GHz) so that its response is not distorted by the loading of the dc network. This requires that the stop-band transmission of the low-pass filter should be much weaker than that of the Fabry-Pérot couplers, i. e. $|S_{21}^{\text{LPF}}|^2 \ll |S_{21}^{\text{coup}}|^2$.

Chebyshev Low-Pass Filter

A suitable low-pass filtering response for these requirements allows a small ripple in the pass-band to benefit from a faster roll-off into the stop-band. Such response can be obtained with Chebyshev filters, whose transmission is illustrated in Fig. 8.6 and

given by [100]

$$|S_{21}^{\text{LPF}}(f)|^2 = \frac{1}{1 + \varepsilon^2 T_N^2 \left(\frac{f}{f_c} \right)}, \quad (8.20)$$

where the filtering function is given by the homonymous Chebyshev polynomials of the first kind and order N

$$T_N(f/f_c) = \begin{cases} \cos(N \cos^{-1}(f/f_c)) & f/f_c < 1 \\ \cosh(N \cosh^{-1}(f/f_c)) & f/f_c \geq 1. \end{cases} \quad (8.21)$$

The ripple constant ε fixes a maximum wiggle of $1 + \varepsilon^2$ in the pass-band, which is typically given as a maximum attenuation in the pass-band of A_p (in dB), as shown in Fig. 8.6. The cut-off frequency f_c is defined as the frequency at the edge of the pass-band for which the transmission has been attenuated by A_p (in dB), i.e. $|S_{21}^{\text{LPF}}(f_c)|^2 = 10^{-A_p/10} = (1 + \varepsilon^2)^{-1}$. The filter order N to achieve a maximum attenuation of A_p in the pass-band and a minimum of A_s in the stop-band is given by [229]

$$N \geq \left\lceil \frac{\cosh^{-1} \left(\sqrt{\frac{10^{A_s/10} - 1}{10^{A_p/10} - 1}} \right)}{\cosh^{-1} \left(\frac{f_s}{f_c} \right)} \right\rceil, \quad (8.22)$$

which determines the number of reactive elements in the prototype ladder circuit in Fig. 8.7. The values of the circuit elements are given by

$$L_i = \frac{g_i Z_0}{2\pi f_c}, \quad (8.23)$$

$$C_i = \frac{g_i}{Z_0 2\pi f_c}, \quad (8.24)$$

$$Z_{\text{src}} = g_0 Z_0, \quad (8.25)$$

$$Z_{\text{load}} = g_{N+1} Z_0; \quad (8.26)$$

where the reactive elements of the frequency- and impedance- normalized circuit, g_i , are computed as [230]

$$g_1 = \frac{2}{\gamma} \sin \left(\frac{\pi}{2N} \right), \quad (8.27)$$

$$g_i = \frac{1}{g_{i-1}} \frac{4 \sin \left(\frac{(2i-1)\pi}{2N} \right) \sin \left(\frac{(2i-3)\pi}{2N} \right)}{\gamma^2 + \sin^2 \left(\frac{(i-1)\pi}{N} \right)} \quad \text{for } i = 2, 3, \dots, N; \quad (8.28)$$

with $\gamma = \sinh(\xi/2N)$ and $\xi = \ln(\coth(A_p/17.37))$. The normalized source impedance is $g_0 = 1$ and the normalized load impedance $g_{N+1} = 1$ for odd N , and $g_{N+1} = \coth^2(\xi/4)$ for even N .

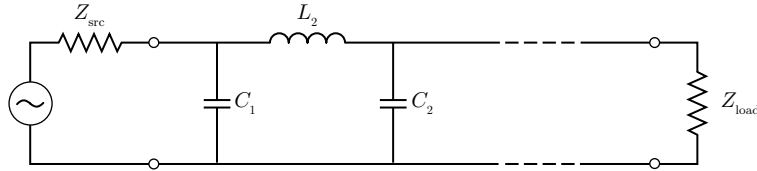


Figure 8.7: Ladder circuit of a low-pass filter prototype starting with a shunt element.

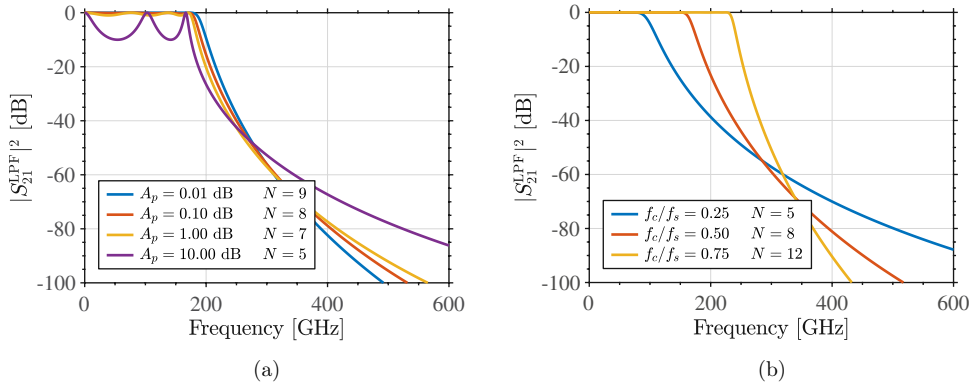


Figure 8.8: Simulated response of lumped-component Chebyshev low-pass filters for $A_s = 50$ dB and $f_s = 300$ GHz. In sub-figure (a), the cut-off frequency is fixed to $f_c = 150$ GHz and the maximum attenuation in the pass-band A_p is varied. In sub-figure (b), $A_p = 0.01$ dB is fixed and f_c is varied. The smaller the ripple in the pass-band and the larger the ratio f_c/f_s , the higher the filter order and thus the faster roll-off.

Different parameters participate of the tuning of the Chebyshev low-pass filter frequency response; namely the cut-off frequency f_c , the stop frequency f_s , the maximum pass-band attenuation A_p and the minimum stop-band attenuation A_s . To meet the specifications given by these parameters, the filter order N will change. The examples given in Fig. 8.8 illustrate the effect of the parameters A_p and f_c for lumped-element Chebyshev filters with a stop-band starting at $f_s = 300$ GHz with a minimum attenuation of $A_s = 50$ dB. From (8.22) it can be seen that a smaller ripple in the pass-band, a higher attenuation in the stop-band and a narrower transition-band will all require a higher filter order N (more reactive elements), resulting in a faster roll-off into the stop-band.

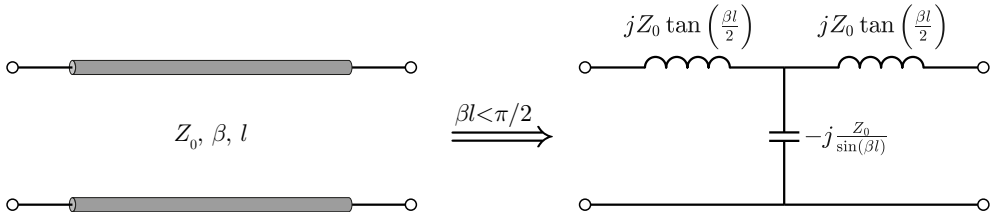


Figure 8.9: T-network representation for a transmission line shorter than $\beta l < \pi/2$.

Stepped Impedance Filter Implementation

So far we have only considered a lumped-component implementation of the low-pass filter. However, at sub-mm wave frequencies ($f > 300$ GHz) this is very difficult and a distributed-element approach must be used. A possible way is to use electrically-short ($\beta l \ll 1$) transmission line sections to approximate the behavior of the ladder lumped circuits elements in (3.11) and (8.27). An equivalent representation of a short transmission line is given in Fig. 8.9 [100], where the series loads are inductive and the shunt load capacitive if the line has a phase length of $\beta l < \pi/2$. Furthermore, if the characteristic impedance of the line is high (high-Z), a short section (typically $\beta l < \pi/4$) of it would render a series inductor with an inductance

$$L = \frac{Z_0 \beta l}{\omega} = \frac{Z_0 l}{v}. \quad (8.29)$$

Instead, if the characteristic impedance is low (low-Z), the line would resemble a shunt capacitor whose capacitance is given by

$$C = \frac{\beta l}{Z_0 \omega} = \frac{l}{Z_0 v}. \quad (8.30)$$

Since the line sections need to be electrically-short ($\beta l < \pi/4$) to approximate a lumped element behavior, but the particular filter under consideration may operate at very high frequencies and may require from high values of L and C , the only resort is to have a large contrast between the high characteristic impedance of the inductive line $Z_{0,L}$ and the low characteristic impedance of the capacitive line $Z_{0,C}$, i.e. $Z_{0,L}/Z_{0,C} \gg 1$. The resulting structure (illustrated in Fig. 8.10) is a stepped-impedance filter (or an RF choke as typically referred to in the SIS community [231]).

The elements of the Chebyshev filter ladder circuit discussed previously can now be approximated by the sections of a stepped-impedance filter. To this end, the first step is to re-scale the frequency- and impedance- normalized values in (8.27) and (8.28) with the actual cut-off frequency f_c and port impedance Z_0 using (8.23) and (8.24). The lengths of the stepped-impedance filter sections are then calculated by equating

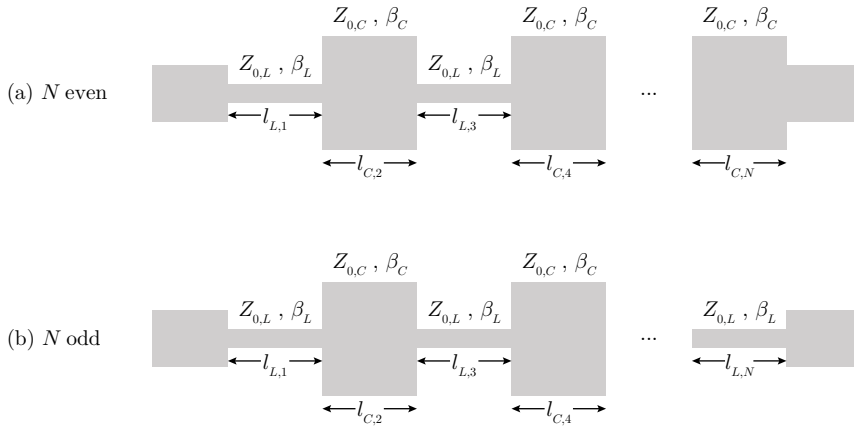


Figure 8.10: Schematic representation of a stepped-impedance filter with (a) an even and (b) an odd number of sections N .

(8.23) and (8.24) with (8.29) and (8.30) evaluated at the cut-off frequency f_c . This results in the following expressions for the lengths of the high-Z and low-Z sections:

$$l_{L,i} = \frac{g_i Z_0}{Z_{0,L} \beta_L}, \quad (8.31)$$

$$l_{C,i} = \frac{g_i Z_{0,C}}{Z_0 \beta_C}; \quad (8.32)$$

where β_L and β_C are respectively the propagation constant of the inductive and capacitive lines, and similarly for their characteristic impedance $Z_{0,L}$ and $Z_{0,C}$.

8.3.5. Filter Design for the Tunable Fabry-Pérot Resonator

To preserve the spectral response of the two Fabry-Pérot resonators in Table 8.1 when adding the biasing network, a very high isolation in the band 300–400 GHz is sought between the dc network and the resonator. Furthermore, to avoid spurious resonances in the stop-band caused by electrically-long sections of the stepped-impedance implementation of the low-pass filter, we design for a relatively high cut-off frequency. A Chebyshev low-pass filter satisfying these requirements can be characterized with $A_p = 0.01$ dB, $A_s = 50$ dB, $f_s = 300$ GHz and $f_c = 175$ GHz. This set of requirements results in a filter order $N = 9$ using (8.22).

To allow the stepped-impedance microstrip implementation of the prototype filter response, the capacitive (low-Z) sections need to be as wide as 10 μm and the inductive (high-Z) sections as narrow as 500 nm to avoid electrically-long filter sections.

	w [μm]	L_k^{MS} [pH/□]	L_k^{GND} [pH/□]	Z_0 [Ω]	$(c/v)^2$
Inductive filter section	0.5	1	0.926	90.6	78.9
Capacitive filter section	10	1	0.926	6.6	59.5
Fabry-Pérot line	2	4	0.926	52.8	169.2

Table 8.2: Parameters of the buried microstrip lines on a 300 nm-thick a-Si ($\epsilon_r = 10$) dielectric layer used to define the Fabry-Pérot resonator and the stepped-impedance low-pass filter. The characteristic impedances and phase velocities are calculated using [99].

Section number	1	2	3	4	5	6	7	8	9
Width [μm]	0.5	10	0.5	10	0.5	10	0.5	10	0.5
Length [μm]	14.57	6.28	32.28	7.54	34.10	7.54	32.28	6.28	14.57
βl [rad]	0.47	0.18	1.05	0.21	1.11	0.21	1.05	0.18	0.47

Table 8.3: Dimensions of a buried microstrip 9th-order stepped-impedance Chebyshev low-pass filter with $A_p = 0.01$ dB, $A_s = 50$ dB, $f_c = 175$ GHz and $f_s = 300$ GHz. Sections 3, 5 and 7 are not electrically-short at f_c , i. e. $\beta l > \pi/4$ due to an insufficient contrast $Z_{0,L}/Z_{0,C}$ for the required filter response.

The properties of these microstrip lines are listed in Table 8.2, showcasing a large contrast $Z_{0,L}/Z_{0,C} \gg 1$. The lengths of the nine sections of the stepped-impedance Chebyshev low-pass filter are listed in Table 8.3, which have been calculated using (8.31) and (8.32). Fig. 8.11 shows the filter and its simulated response using both Sonnet and a transmission line circuit model, and compared against the lumped element equivalent. The rejection in the stop band is higher than 40 dB and the dc transmission is perfect. The stepped-impedance implementation approximates well the lumped component circuit response up to the cut-off frequency, after which the response starts to deviate due to the non-compliance with the short electrical length requirement on the filters sections, becoming eventually resonant as can be noticed at the high frequencies.

8.3.6. DC Current Injection Point

In the previous discussion we have designed a highly-rejecting low-pass filter for the insertion of dc bias currents into the Fabry-Pérot resonator. We have found excellent in-band rejection for the filter designed in the previous section. The next step is to verify how the position of the filter on the Fabry-Pérot resonator affects its performance. Due to the resonant nature of the Fabry-Pérot, the impedance will depend on the location along its length: current minima are high impedance points and current maxima are low impedance points. In order to preserve the high isolation at THz

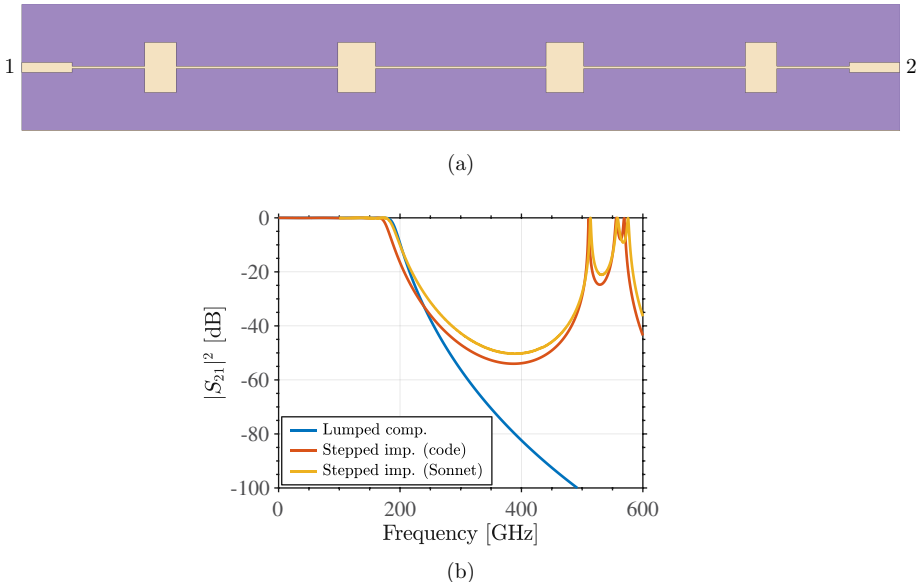


Figure 8.11: Chebyshev low-pass filter response for $A_p = 0.01$ dB, $A_s = 50$ dB, $f_c = 175$ GHz and $f_s = 300$ GHz. The resulting filter order is $N = 9$ and the dimensions of its geometry in (a) are given in Table 8.3. Panel (b) compares the transmission response of the stepped-impedance filter geometry in (a) simulated using Sonnet [99], that of a transmission-line equivalent model and the one from a lumped-element circuit ladder model. Each port is terminated with a load of 52.8Ω for all cases.

8

frequencies between the dc network and the resonator, the input impedance of the filter should dominate, making a low impedance point along the resonator a proper current injection position. These impedance locations are frequency-dependent and thus can only be used over a narrow band. However, the combination of the high rejection of the low-pass filter designed and its connection to low-impedance points at the central frequency of operation should allow for a relatively broad operational band for the Fabry-Pérot resonator.

In Fig. 8.12 we report the normalized current density in the middle of the main conductor of a buried microstrip Fabry-Pérot resonator with mode number $n = 6$ at $f_n = 350$ GHz, which is the central frequency in our band of interest. The first high-impedance point occurs at the coupler edge, where the current cannot flow. The first low-impedance point at f_n occurs at $\lambda_n/4$ from the resonator edges, at $20.1\mu\text{m}$, which almost coincides with the $18.5\mu\text{m}$ -long coupler. The second low-impedance point at occurs at $51.7\mu\text{m}$ ($3\lambda_n/4$ from the edges). The second high-impedance point is located at $35.4\mu\text{m}$ ($\lambda_n/2$ from the edges). An insertion point further within the resonator is not sensible as it diminishes the section of the resonator that can be biased. The

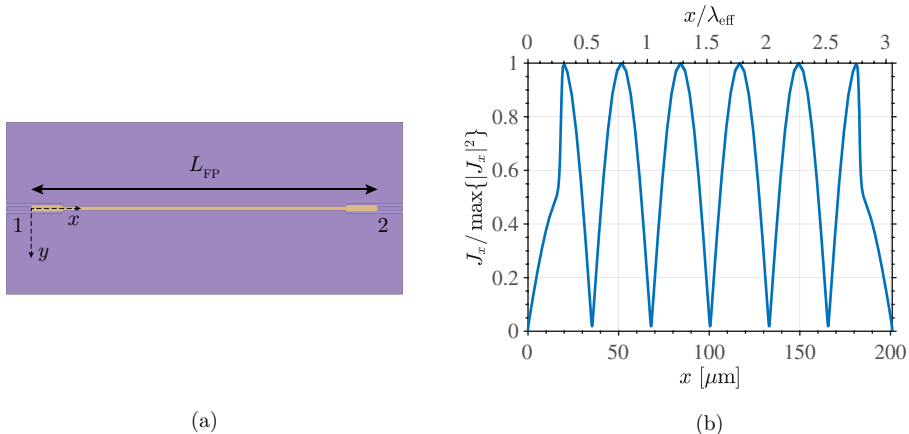


Figure 8.12: Fabry-Pérot resonator (a) geometry and (b) its normalized current density profile simulated with Sonnet [99] for a resonator length L_{FP} corresponding to $f_n = 350$ GHz at $n = 6$. The simulation frequency is f_n . The loci of the current maxima (minima) are the low-impedance (high-impedance) points.

S-parameters of the Fabry-Pérot, including the stepped-impedance low-pass filters, were simulated in Sonnet [99] using the geometry in Fig. 8.13(a). The simulated responses are compiled in panels (b) through (e) for the four previously mentioned bias-current injection points L_{sep} with respect to the far edge of the couplers. Despite the expected shift of the impedance minima and maxima with frequency, it appears from Fig. 8.13 that all the investigated dc-current injection points would actually be suitable places for the connection of the low-pass filters since the transmission through the Fabry-Pérot is largely unaltered, in the resonance peak height and the quality factor, with respect to the resonator without the loading of the low-pass filters. Nevertheless, the isolation of the dc network is worse for connections made at high-impedance points, as expected, yielding about -40 dB on-resonance (c. f. -60 dB for the low-impedance connections). Furthermore, all the insertion points investigated have shifted the nominal resonance at $f_n = 350$ GHz by less than a 6.5%. This shift is slightly larger for the connection at the first low-impedance point ($\lambda_n/4$) in Fig. 8.12(c), which is likely caused by the interaction with the nearby CPW short-circuit in the CPW-microstrip coupler.

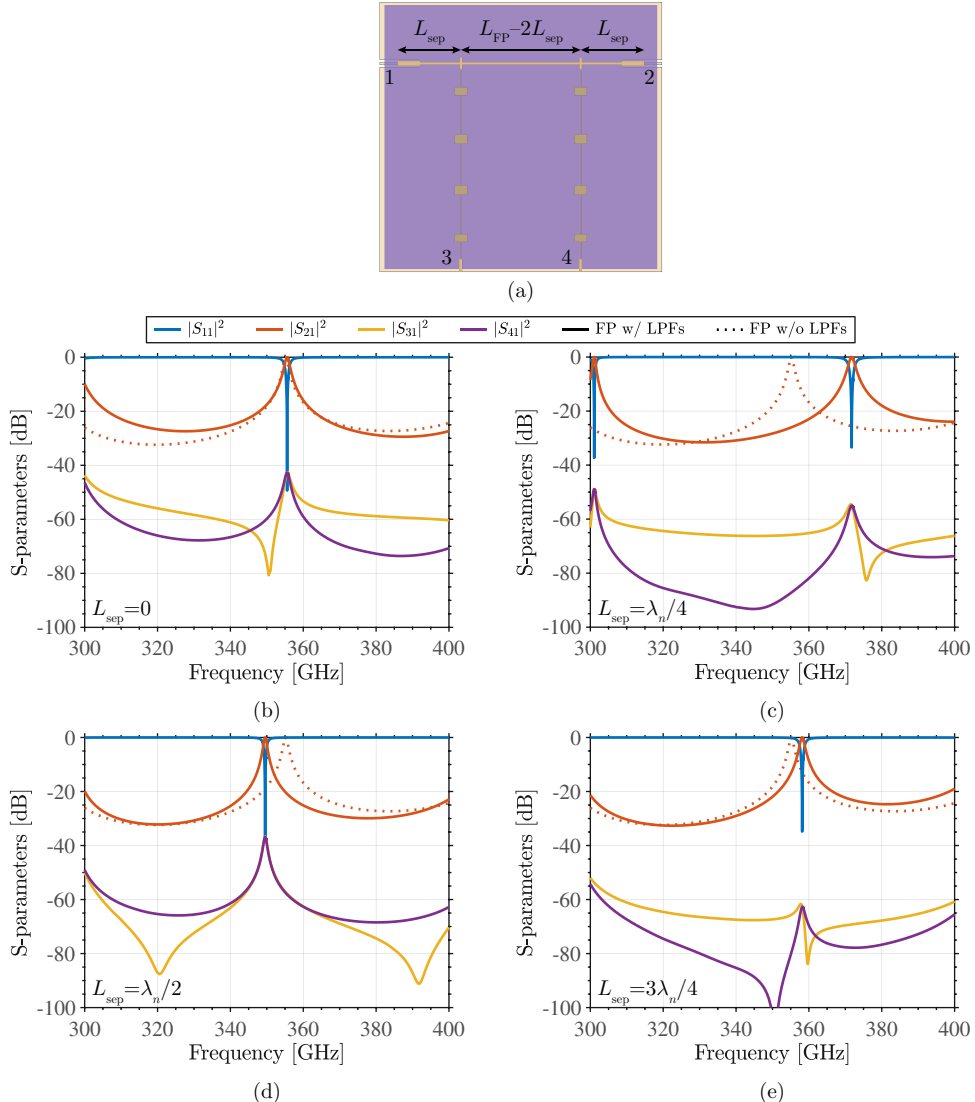


Figure 8.13: Buried microstrip Fabry-Pérot resonator $n = 6$ tapped with the stepped-impedance low-pass filter of Fig. 8.11 attached at L_{sep} from each resonator edge as shown in (a). The other panels show the S-parameters obtained in Sonnet [99] for the different filter locations: (b) $L_{\text{sep}} = 0$, (c) $L_{\text{sep}} = \lambda_n/4$, (d) $L_{\text{sep}} = \lambda_n/2$ and (e) $L_{\text{sep}} = 3\lambda_n/4$. We overlay the simulated transmission through the Fabry-Pérot without the low-pass filters for comparison.

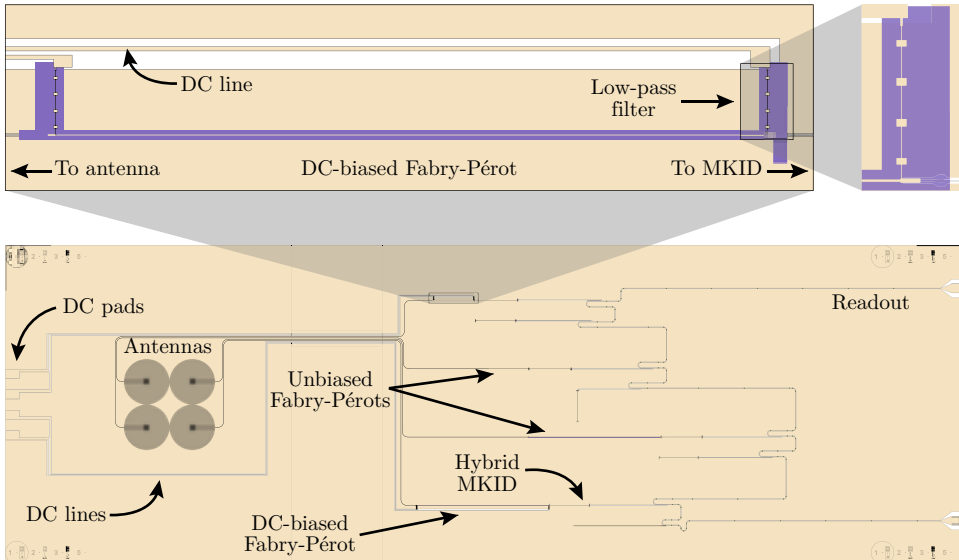


Figure 8.14: Illustration of a Fabry-Pérot chip from the mask-set see through the Si wafer (not shown). We also show a detailed view of a dc-biased Fabry-Pérot.

8.4. Chip Design

To characterize experimentally the phase-shifting capabilities at THz frequencies with the kinetic inductance non-linearity we have designed several dc-biased Fabry-Pérot chips. An illustration is given in Fig. 8.14. In every chip we place four antenna-coupled Fabry-Pérot resonators operating in the 300–400 GHz band: two of the FP-A design and two of the FP-B design (see Table 8.1). For each design, one resonator is dc-biased and the other not, for reference. Furthermore we are fabricating four variations of this chip: one with the current-injection at the first low-impedance point ($\lambda_n/4$) from the resonator edges, one at the second high-impedance point ($\lambda_n/2$), one at the second low-impedance point ($3\lambda_n/4$) and lastly a fourth one where the resonators revert to CPW technology after the CPW-microstrip couplers and the current-injection points at $\lambda_n/4$ from the edges.

The fabrication route of these chips will be very similar to the procedure described in Appendix B and in [126, 228], with the main differences being the use of buried microstrip technology and the use of an extra NbTiN layer with very high kinetic inductance ($4 \text{ pH/}\square$) for the Fabry-Pérot resonator in order to maximize the non-linear response of the line and thus improve the phase-shifting tunability of the Fabry-Pérot resonator. The properties of the three superconducting films to be used for

	L_k [pH/◻]	T_c [K]	ρ_n [$\mu\Omega\text{cm}$]	t [nm]
GND layer	0.926	15	100	107
Low-pass filter layer	1	14.3	120	115
Fabry-Pérot layer	4	13	125	35

Table 8.4: Superconducting film properties for the Fabry-Pérot resonators. The critical temperature T_c and the normal state resistivity ρ_n are estimates.

the different structures are compiled in Table 8.4. At the writing of this thesis the fabrication of the devices has not started, but the masks were produced.

8.4.1. Critical Current Avoidance

The maximum current that can be run on a particular superconducting line before it becomes resistive is given by the critical current I_c , whose value is geometry and material dependent. Apart from the critical current limit, the reduction of the energy gap due to the bias current will decrease the gap frequency down to the operational band, setting a bias limit. Furthermore, although the kinetic inductance dispersion in the proximity of the gap frequency (see Fig. 2.3(b)) would reduce the current required to achieve the same phase shift, it would have a detrimental effect on the wideband performance of the phase shifters. In particular, the wideband properties of the beam-steerable focused connected antenna concept presented in Section 8.2.2 would be deteriorated due to the different feeding lines being biased over different lengths, allowing the dispersion in $L_k(0)$ to introduce an error in the phase profile over the antenna aperture, eventually resulting in an undesired de-focusing and beam-squinting.

At the moment the maximum dc current that can be inserted in our superconducting films is unknown and needs to be investigated with our proposed experiment. We can however estimate their value extrapolating from the data found in the literature for similar NbTiN films. The closest case are the 35 nm-thick and 250 nm-wide NbTiN lines in [216, 223], which showed a critical current of 0.8 mA and a non-linearity current factor (I^*) of 3 mA. Since dc currents are approximately uniformly distributed within a superconductor with a thickness smaller than the penetration depth ($\lambda \approx 300$ nm for NbTiN) and since the current density scales as $J \propto \rho_n^{-1/2}$ for the same superconducting material [232], we can scale the currents measured in the NbTiN devices of [216, 223] (denoted by I') for the different line dimensions in our device with

$$I \approx I' \left(\frac{t}{35 \text{ nm}} \right) \left(\frac{w}{250 \text{ nm}} \right) \left(\frac{200 \mu\Omega\text{cm}}{\rho_n} \right)^{1/2}. \quad (8.33)$$

	w [μm]	t [nm]	ρ_n [μΩ cm]	I_c [mA]	I^* [mA]
Fabry-Pérot line	2	35	125	8.09	30.36
LPF inductive sections	0.5	92	120	6.79	25.45
LPF capacitive sections	10	92	120	135.74	509.02

Table 8.5: Estimated values for the critical currents (I_c) and non-linearity factors (I^*) of the lines of the biased Fabry-Pérot device. The values have been calculated scaling the measured values in [216, 223] by means of (8.33).

In this equation we have used the fact that the resistivity of the NbTiN films of [216, 223] is $200 \mu\Omega \text{ cm}$. The resulting critical currents (I_c) and non-linearity current factors (I^*) for the different lines in our devices are compiled in Table 8.5.

Because the non-linearity current factor (I^*) is of the same order of the critical current (I_c) [192], reducing the latter results in an improved tuning range by means of (8.1). Thereby, the current limitation should stem from the resonator line rather than in any other dc-biased superconducting line in the Fabry-Pérot device. From the expected critical currents in Table 8.5 it can be seen that the tuning range may be limited by the critical current in the inductive sections of the stepped-impedance low-pass filters. With the kinetic inductance fraction of the Fabry-Pérot line $\alpha_k = 94.02\%$ and the currents in Table 8.5, the expected tuning range can be calculated with (8.6) to be $df/f \approx -2.35\%$, that is $83.93\% (\approx 6.79/8.09)$ of the theoretical maximum achievable for this line, which is still adequate for our purpose as it will be discussed in the next section.

Another potential issue which can also result in a reduced critical current is the current crowding in bends and sudden linewidth changes [233]. To avoid reaching the critical current in such transitions, the inner corners of the structures were rounded with a radius of 700 nm .

8.4.2. Expected Performance

The two dc-biased Fabry-Pérot designs of Table 8.1 have been simulated using the circuit model in Fig. 8.2(a) with the different transmission line parameters simulated in Sonnet [99] for a kinetic inductance variation governed by (8.1) and the current values of Table 8.5. The design FP-A assumes a loss characterized by $Q_i = 4700$ and the design FP-B a loss given by $Q_i = 440$. The resulting transmission through the resonator and the loaded quality factor associated to the visible peaks are illustrated in Fig. 8.15 and 8.16, color-coded according to the bias-current level, for both designs FP-A and FP-B with current injection points at $\lambda_n/4$ from the couplers. As the bias current increases, the resonance peaks shift to lower frequencies as expected from an electrically longer line whose phase velocity decreases with the current as

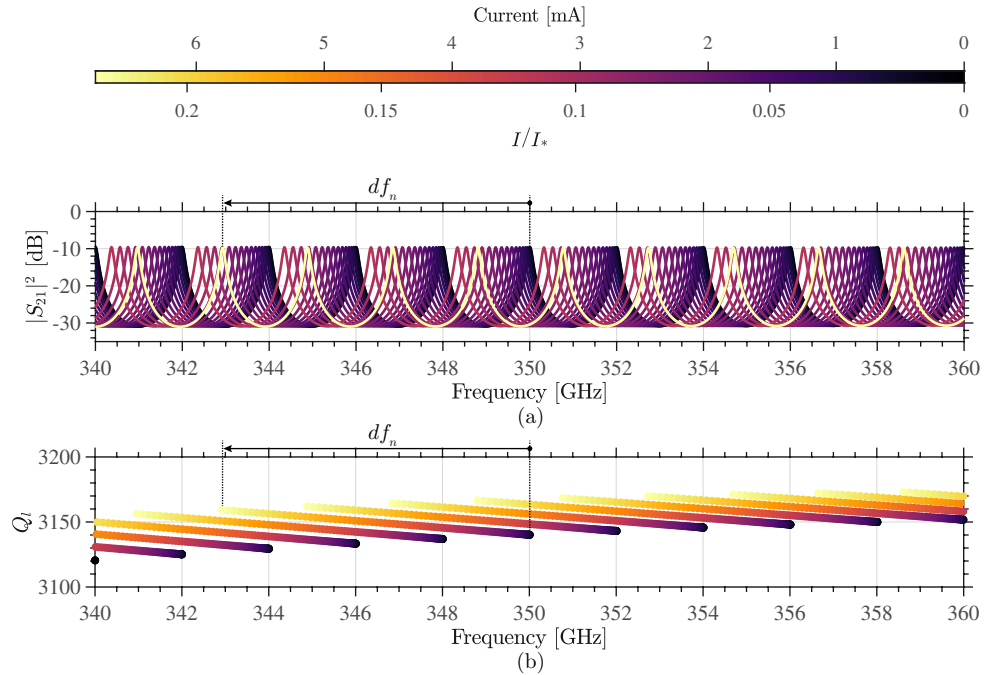


Figure 8.15: Simulated performance of the circuit model in Fig. 8.2(a) of the biased Fabry-Pérot FP-A of Table 8.1, which targets a low loss scenario characterized by $Q_i = 4700$. The low-pass filters are connected at $L_{\text{sep}} = \lambda_n/4$ from the resonator edges. Sub-figure (a) shows the transmission through the resonator and sub-figure (b) the realized loaded quality factors, both for different biasing currents. The simulated tuning range is $df_n \approx -7.07 \text{ GHz}$ around the peak at $f_n = 350 \text{ GHz}$ or $df_n/f_n \approx -2.02\%$.

(8.2). For the particular case of the resonance at $f_n = 350 \text{ GHz}$ this shift is df_n , as indicated in the figures. The simulated tuning range achieved up to the estimated critical current of the system of $I_c = 6.79 \text{ mA}$ (limited here by the inductive section of low-pass filters) is $df_n/f_n = -2.02\%$ for THz frequencies, which is on-par with the state of the art tunability at microwave frequencies. With this tunability, using (8.5) and (8.6), we would require a biased-line length of about $-0.1269 \text{ rad}/\lambda$, where λ is the effective wavelength in the superconducting line. As an example, a 12.38λ -long biased line would be required to achieve a phase shift of $-\pi/2 \text{ rad}$ at the maximum biasing point.

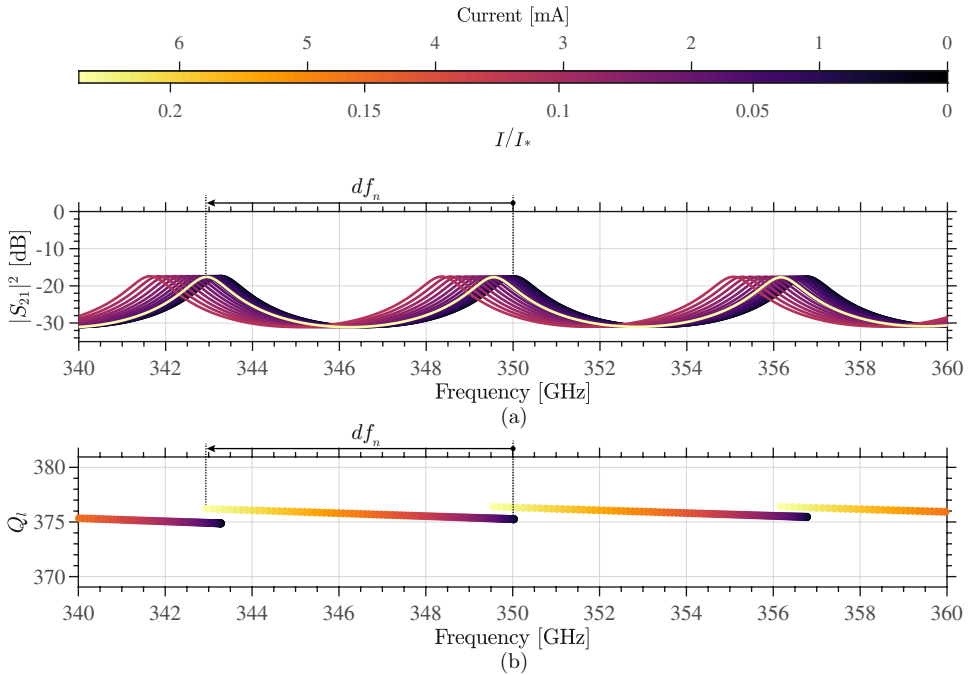


Figure 8.16: Simulated performance of the circuit model in Fig. 8.2(a) of the biased Fabry-Pérot FP-B of Table 8.1, which targets a high loss scenario characterized by $Q_i = 440$. The low-pass filters are connected at $L_{\text{sep}} = \lambda_n/4$ from the resonator edges. Sub-figure (a) shows the transmission through the resonator and sub-figure (b) the realized loaded quality factors, both for different biasing currents. The simulated tuning range is $df_n \approx -7.05$ GHz around the peak at $f_n = 350$ GHz or $df_n/f_n \approx -2.02\%$.

8.5. Conclusions

In this chapter we have investigated the application of the non-linear behavior kinetic inductance with a bias current of superconductors to the concept of electronic beam-steering a superconducting THz phased-array antenna. As a preliminary estimation of the requirements for the microstrip feeding network of such antenna we have used the available data from the state of the art in the microwave regime. This has yielded the need for biased lines of hundreds of microns to a few millimeters long. However, although there are contributions in the literature that have already demonstrated the phase-shifting capabilities of superconducting lines at microwave frequencies, in this work we aim to quantify the possibilities for THz applications using microstrips.

To this end, we have designed an on-chip platform based on a buried-microstrip current-biased Fabry-Pérot resonator coupled to an MKID detector. This highly-sensitive setup comes however at the cost of stringent requirements for the connection of its biasing network, as it has to appear almost transparent to the THz frequencies of interest. For that we have designed highly-rejecting Chebyshev low-pass filters implemented with stepped-impedance sections. The high stop-band rejection ensures a low distortion of the transmission through the Fabry-Pérot as well as the possibility to place the current-injection points anywhere along the standing wave pattern in the resonator with just a small frequency shift of the resonances but practically no detriment for the loaded quality factor.

With the simulations of a biased Fabry-Pérot circuit model and the realistic assumptions of I_c and I^* extrapolated from the state of the art in the microwave regime, we expect to very easily see the resonance shift with the two resonator designs. We have estimated the phase-shifting capabilities at THz frequencies to be around $d\phi/\phi = -df/f = 2.02\%$ or $-0.1269 \text{ rad}/\lambda$, where λ is the effective wavelength in the biased superconducting line.

Chapter 9

Conclusions and Outlook

This dissertation focuses on the design of several solutions for future broadband terahertz (THz) on-chip imaging spectrometers as described in Chapter 1. Such devices are nonexistent in the THz regime but represent a crucial instrument type toward the investigation of the early Universe. This work contributes to this endeavor with the development of three fundamental building-blocks of broadband imaging spectrometers at THz frequencies: (1) a superconducting on-chip filter-bank design enabling octave-band moderate spectral resolution spectroscopy; (2) an antenna concept suitable for on-chip integration facilitating broadband operation of a reflector system with beam-steering capabilities; and (3) an electronic phase-shifting concept based on biased superconducting lines, allowing among others the electronic beam-steering of a superconducting phased-array antenna. The study and the design of these enabling technologies have been carried out with the aid of newly-developed ad-hoc numerical tools based on transmission line theory, filter theory and Green's functions; as well as full-wave electromagnetic solvers [98, 99, 135, 204]. Several prototypes have been fabricated and characterized to validate the designs and the modeling strategies, showing good agreement overall.

In this chapter we summarize the conclusions and the most significant results of this dissertation. Furthermore, we discuss recommendations regarding possible future research.

9.1. High-Frequency Superconducting Circuits

Prior to delving into the actual contributions of this dissertation, Chapter 2 set the framework on which the superconducting circuits in this thesis build. In this chapter it was discussed how the pairing of electrons in a superconductor cooled below its

critical temperature is responsible for both a lossless charge transport and the opening of a meV-wide energy band gap. The first results in the enabling of high quality factor resonators and efficient electrically-long circuitry at high frequencies. The second provides the means for high-frequency radiation detection using pair-breaking detectors. One such detector is the MKID, which is a high quality factor microwave resonator very well suited for large arrays. This is the detector of choice for the designs in this thesis.

As illustrated in that chapter, the superconducting NbTiN films employed in this thesis are virtually lossless conductors with an electrical behavior that should be modeled with an inductive surface impedance up to the gap frequency at 1.1 THz. Because the band of operation of the devices described in this thesis is in the proximity of the gap frequency of NbTiN, the low-frequency approximations cannot be used, requiring the evaluation of the surface impedance employing the complex conductivity calculated numerically from the Mattis-Bardeen expressions (2.3) and (2.4). Furthermore, the kinetic inductance will show a dispersive behaviour in the proximity of the gap (see Fig. 2.3(b)) that needs to be taken into account.

9.2. Superconducting On-Chip Filter-Bank Spectrometers

The first part of this dissertation investigated the design of a broadband THz superconducting frequency-demultiplexing filter-bank to build, in conjunction with MKID detectors, the next generation on-chip spectrometers suitable for single-pixel instruments like DESHIMA and future multi-pixel imaging spectrometers.

9.2.1. Filter-Bank of Half-Wavelength Resonators

Chapter 3 explained the working principle of the on-chip filter-bank spectrometer and how it accomplishes a footprint reduction of several orders of magnitude when compared to other dispersion technologies such as quasi-optical gratings and interferometers. Prior to any specific technological considerations, a fundamental study was carried out on the performance of a shunted half-wavelength resonator acting as a band-pass filter. To do so, the resonator was investigated from an energetic point of view as well as from a circuit standpoint; allowing thereby to write approximate S-parameter expressions in terms of quality-factors, which are useful estimators for the experimental characterization of semi-isolated filters (e.g. sparse filter-banks). It was found that, for a lossless isolated shunted resonator, the optimum on-resonance performance is limited to -3 dB of the input power coupling through the filter, while

the remaining -3 dB are equally split in power reflected and power transmitted past the filter. To preserve an adequate coupling efficiency to the detectors with a high quality factor, the losses should be small ($Q_i \gg Q_l$).

The circuit model of the isolated shunt resonator band-pass filter was then extended into a full filter-bank resorting to ABCD matrices. This circuit model allowed to evaluate the performance of a large and frequency-dense filter-banks in terms of S-parameters, which would have been otherwise prohibitively time-consuming to arrange in a commercial circuit simulator or to simulate with full-wave simulators. The filter-bank analysis with the circuit model simulations gave valuable insights such as the expected degradation of the different channels with respect to the isolated filter response; as well as information about a proper filter-bank configuration, whose channels should be ordered with respect to its input monotonically from the highest to the lowest frequency and with a maximum tolerable inter-filter spacing of $\lambda/4$ in order to minimize reflections within an octave-band free spectral range and losses. Actual filter-bank implementations and the choice of the on-chip technology were subsequently discussed in Chapters 4 to 6.

9.2.2. Co-Planar Filter-Bank

Chapter 4 motivated why co-planar technology should be avoided in THz filter-banks. This stems from the support of CPW technology for two fundamental modes: the differential mode, which is a transmission line mode, and the common mode, which is a highly radiative mode. The inherent asymmetry of a channelizing filter-bank makes inevitable that a combination of these two modes is excited, resulting in a degraded performance due to radiation losses. We exemplified this with the measured performance of the DESHIMA 1.0 spectrometer [49], which was designed outside the scope of this thesis. This 49 channel filter-bank in the 332–377 GHz band (13%) showed an average channel peak coupling efficiency of $\langle |S_{i1}(f_i)|^2 \rangle \approx -11$ dB $\approx 8\%$ and an average loaded quality factor of $\langle Q_l \rangle \approx 300$. To understand the cause for this low performance, several structures along the on-chip electrical path of the THz signal were evaluated in isolation with full-wave simulations: straight CPWs, 90° CPW turns and a filter in the proximity of the filter-bank entrance, all with and without bridges balancing the potential of the grounds.

The findings were that narrow ($\leq 2-2-2$ μm) differentially-excited CPWs, both when following a straight path or in a turn, show a negligible radiation rate of less than 6×10^{-3} dB/mm and no mode conversion. Instead, when CPWs are excited with a common mode, the radiation rate is much faster, about 3–4 orders of magnitude more than with a differential mode. On the other hand, the simulations of the bridges indicated that a small fraction of the input power is dissipated by the materials used (Al strip and polyimide support) and that bridges do not restore the differential mode

from a common mode excitation, but rather strongly reflect the latter, allowing to confine this mode before it radiates out. Lastly, the simulation of the meandered-slot filter indicated that, apart from the limited free-spectral range of 21% due to spurious resonances, the common mode is induced due to various asymmetries in the structure, incurring in radiation losses. As a result, the coupling efficiency in the pass-band to the filter-coupled detector and its quality factor were low.

It was also argued that the issue of mode conversion and subsequent radiative loss of all the power converted into the common mode is a fundamental issue with co-planar filter-banks at THz frequencies. The power loss originates from the progressive radiation along the filter-bank through-line as well as from the filters themselves, reducing thereby the power coupled to the detectors and in particular for those situated at the far end of the filter-bank.

9.2.3. Microstrip Filter-Bank

Chapter 5 discussed the microstrip implementation of a channelizing filter-bank. Microstrip technology, as opposed to co-planar technology, does not suffer from mode-related issues and it is thereby better suited for the construction of efficient, broadband and moderate spectral resolution on-chip filter-banks. The caveat of this technology however is the need for deposited dielectrics¹, whose amorphous atomic structure make them be more dissipative, noisy and brittle than crystalline dielectrics. A parallel development to this work enabled the PECVD deposition of low-stress thin films (~ 300 – 400 nm) of a-Si. With this technology we investigated various resonators geometries to act as band-pass filters: an O-shaped resonator, a C-shaped resonator and an I-shaped resonator. Among the three geometries, the latter was found to provide with the best overall performance: an octave-band free-spectral range, an optimum on-resonance performance and a high transparency off-resonance. Subsequently, a practical implementation of the I-shaped filter was given for its use in combination with quarter-wavelength hybrid MKID detectors.

To test this band-pass filter in a semi-isolated environment we developed a sparse filter-bank chip. The design was aided by the filter-bank circuit model introduced in Chapter 3, which showed excellent agreement with full-wave simulations of an isolated filter as well as four contiguous filters. The experimental characterization of this filter-bank used two procedures: a frequency response measurement and a optical efficiency characterization, both in good agreement. Both experiments rely on the knowledge of the strength of the wideband-coupled detectors, which could be estimated directly from the frequency response measurements using a new analysis technique combining the peaks of $|S_{11}(f_i)|$ and the dips in $|S_{21}(f_i)|$ of semi-isolated filters by means of the

¹Crystalline dielectrics could also be employed but the fabrication would become exceedingly hard.

analytical S-parameters expressions in Chapter 3. The measurements of this device indicated an average channel peak coupling efficiency of $\langle |S_{i1}(f_i)|^2 \rangle \approx -5.7 \text{ dB} \approx 27\%$ and an average loaded quality factor of $\langle Q_l \rangle \approx 940$; which showcase a much improved performance of the filters with respect to the co-planar meandered-slots discussed in Chapter 4. The performance improvement of the new microstrip band-pass filters mainly stems from their lower losses with respect to the co-planar meandered-slot filters, which are respectively characterized by $Q_i = 3000$ and $Q_i = 826$. In spite of this, the value of the loaded quality factor Q_l was found to be larger than designed due to a too weak coupling (too high Q_c) of the filters. This could be partially explained by the over-etch in the a-Si layer when patterning the filters and it will be mitigated in a next design-fabrication iteration.

Chapter 6 discussed the design details of the chosen filter geometry: the I-shaped resonator. The design was based on full-wave simulations using Sonnet [99] following the prescriptions of the fabrication constraints. CST Microwave Studio [98] was also used to accurately model the three-dimensional features of the filters. Given the novelty of the development, both in terms of design and fabrication, several slightly different prototypes were built based upon the findings of previous batches. In summary it was found that, currently, the moderate coupling efficiency of the filters is limited by the too high coupling quality factor, which in turn is partly caused by the over-etch into the a-Si dielectric layer during the fabrication of the last layers. Covering the chip with a second layer of thin a-Si dielectric to compensate the effect the over-etch helped to reduce the quality factor but did not succeed in increasing the coupling efficiency due to the lower internal quality factor of that layer. Furthermore, a buried microstrip configuration for the filter-bank was also investigated as an alternative to avoid the over-etch of the a-Si layer, but the presence of the electrically-thick Si wafer caused a further degradation of the performance due to the excitation of surface wave modes. From this empirical design optimization it was concluded that a thicker dielectric will be of use to lessen the effect of the over-etch and avoid sub-micron features.

9.3. Broadband Beam-Steering Reflector Feed

The second part of this thesis dealt with the development of telescope reflector feed concept easy to integrate on a chip and enabling on-sky beam-steering over a wide bandwidth. Chapter 7 investigated an antenna array concept suited for the task and Chapter 8 an electronic phase-shifting network based on the tunable superconducting delay lines.

9.3.1. Focused Connected Array

Chapter 7 proposed an all-planar antenna array concept easy to integrate on a chip and providing broadband coupling to the quasi-optics of a reflector system while allowing beam-steering. The concept of the focused connected array antenna was based on the combination of the so-called focused apertures, which focus their energy in the near field giving it far-field properties, and connected arrays, which are non-resonant antenna arrays using tightly-coupled elements. On the one hand, near-field focused apertures achieve relatively frequency-independent beams in the far field and thereby allow a broadband illumination of a quasi-optical system with a moderate aperture efficiency. On the other hand, connected arrays provide wideband impedance matching.

The analysis was carried out using an array of elementary sources, whose amplitude and phase follow respectively a Gaussian taper and a combination of quadratic and a linear phase-shift. Such phase profile enforces the focusing in the near field with a movable flash-point, while the amplitude profile ensured a moderate side-lobe level in the near field and consequently a low-ripple in the far-field. The illumination quality of a reflector sharing the focal plane and focal ratio $f_{\#}$ with a focused aperture was subsequently analyzed in terms of the reflector aperture efficiency, which includes both spillover and taper. From this analysis it was found that a focused aperture requires a diameter of $D \geq 2\lambda f_{\#}$ with a Gaussian amplitude taper profile to illuminate a parabolic reflector with an aperture efficiency in excess of 60%. The telecentric system required to enable the scanning scenarios was obtained by tilting the scanned beams in the focal plane, which can be practically obtained with a field lens. As a preliminary study, the field lens effect was emulated with an artificial focal plane linear phase shift. From the study of a moderate aperture size of $D = 4\lambda$ and with a focal ratio $f_{\#} = 2$ it was found that scanning up one half-power beamwidth (i. e. focal plane scanning up to the rim of the aperture) is feasible with a negligible scan-loss, and thereby retaining an aperture efficiency of more than 60%.

Low frequency (3–6 GHz) prototypes were built in PCB technology to demonstrate the concept of the focused connected array for two fixed scanning scenarios: broadside and scanning one half-power beamwidth at the lowest frequency in the antenna E-plane. Each prototype consisted of a circular array with 18 slots printed on a 9 μm -thick copper film deposited atop of a 381 μm -thick dielectric membrane of Rogers RT/duroid® 5880. On the other side of the dielectric, a microstrip corporate feeding network is patterned on another 9 μm -thick cooper film, which implements the Gaussian amplitude taper with unbalanced power splitters and the quadratic/linear phase profile hardwired with true-time delay lines. Finally a planar back-reflector ensures unidirectional radiation. The beam patterns of the antennas were measured in the near-field focal plane by means of an ultra-wideband probe on a XY-scanner. The measured fields showed a good agreement (upon probe compensation) with the

expected fields using the simplified array of elementary sources. As a result the (near-field) directivity was also in good agreement with the expectations. From the gain measurements it was found that there was a large loss in the antenna chiefly originating from the conductor dissipation of the tin-finished cooper microstrip feeding network. This finding was key to claim the feasibility of a future superconducting antenna, whose conductor loss would be negligible and whose only attenuation would be given by a small dielectric loss at a rate of approximately $0.007 \text{ dB}/\lambda$ (c. f. $0.02 \text{ dB}/\lambda$ in the PCB prototypes). Lastly, the measured fields were propagated to a reflector in the far field of the antenna to obtain an aperture efficiency in excess of 55% over the whole octave bandwidth and for both investigated pointing scenarios. This design can in principle be scaled to frequencies up to almost 1.1 THz using a NbTiN-based feeding network. This will make the fabrication compatible with the filter-bank spectrometer discussed in the previous chapters and, very importantly, will eliminate conductor losses.

9.3.2. Superconducting Phase-Shifters

Chapter 8 proposes an electronic phase-shifting concept to allow the dynamic beam-steering of the superconducting THz antenna envisioned in Chapter 7. The operating principle relies on the non-linear response of the kinetic inductance to a bias current, which modifies the phase velocity of a superconducting line and hence achieves a variable phase shift. To allow an easy separation of the THz signal from the bias, a dc current, injected through a bias-tee, would be used to bias the superconducting line. The linear phase profile over the aperture of a scanning phased-array would be obtained by biasing with the same current linearly longer sections for each array element feed line. To allow bidirectional beam-steering, the maximum scanning scenario must be hardwired with true-time delay lines. Finally, to achieve two-dimensional scanning, a second bias line should be employed.

Prior to the development of the proposed electronic beam-steering superconducting phased-array antenna, we have designed an on-chip dc-biased Fabry-Pérot resonator to quantify the phase-shifting capabilities at THz frequencies. The highly-resonant transmission of the Fabry-Pérot provides the dispersion necessary to allow, in a phase-insensitive setup, an accurate quantization of the achievable phase shift by means of an observable frequency shift. Similarly to the antenna phase-shifting concept, this device is biased with a dc current, which is injected and extracted through low-pass filters to avoid the leakage of THz power. Since the quality factor of the resonances of the Fabry-Pérot resonator were tuned to be high to allow an easy detection of a frequency-shift, the low-pass filter disturbance to the resonator at THz frequencies should be minimal, thereby requiring a very high rejection in its stop-band.

Two dc-biased Fabry-Pérot resonators were designed in buried microstrip technology for the band 300–400 GHz. In one side, the resonators were coupled to a lens antenna and in the other side to an MKID detector. Chebyshev stepped-impedance low-pass filters of 9th order were designed to allow the insertion of the dc bias current while providing with at least 40 dB of rejection over the whole THz band of interest, relaxing therein the influence of injection point on the Fabry-Pérot response. A circuit model for the biased Fabry-Pérot resonator was built to anticipate the response at THz frequencies of the device. This model included the resonator as well as the low-pass filters, and it accounts for the simulated transmission line properties of the buried microstrips involved using a non-linearity current factor and a critical current scaled from state of the art values for NbTiN films. The achieved phase shift is estimated to be in the order of $d\phi/\phi \approx 2.02\% (-0.1269 \text{ rad}/\lambda)$ with a maximum bias current of 6.79 mA, possibly limited by the inductive section of the low-pass filters.

9.4. Outlook

In this thesis the electromagnetic design and verification of on-chip filter-banks have been carried out. Using these designs we are now making the first broadband single-pixel on-chip spectrometer. This single pixel on-chip spectrometer uses a leaky-wave antenna and dedicated optics [234] for efficient octave-band radiation coupling. From here, the design and fabrication of full-scale Integral Field Units (IFU's) is in principle only requiring the combination of multiple lens-antenna filter-bank elements on a single chip, which can be done with the work developed in the first part of this thesis. Additionally, creating similar filter-banks with a spectral resolution smaller than 500 is a possible adaptation using the design concepts presented in this thesis. Hence, all the imaging spectrometers proposed in Chapter 1 can now be designed and fabricated. Further improvements to the channelizing filter-bank technology as presented in this thesis are possible, the most interesting directions would be the following:

- The in-band filter coupling efficiency between the THz through-line and the filter-coupled detectors is currently limited by the losses in the dielectrics ($Q_i \sim 3000$). Better dielectrics such as a-SiC [226] can be used to improve the in-band power coupling of the filters.
- With the current filter-bank design, the maximum peak coupling efficiency between the THz through-line and an isolated filter-coupled detector is 50%. Additionally, the pass-band roll-offs of the current band-pass filters follow a Lorentzian profile, affecting thereby neighboring spectral channels. Novel filter designs and filter-bank concepts could be investigated to create an on-chip filter-bank with spectral channels approaching more closely the ideal box-car-shaped 100% filter coupling.

Apart from the IFU's, the Multi-Object Spectrometer (MOS), whose spatial pixels are independently beam-steered, is another very promising instrument concept for THz astronomy. In this line, this dissertation has also laid down the foundations for a superconducting beam-steering phased-array antenna: fixed-pointing low-frequency PCB prototypes were designed and verified, and an on-chip experiment was prepared to evaluate the phase-shifting capabilities of superconducting lines at THz frequencies. This experiment needs to be performed, after which a superconducting beam-steering THz antenna can be designed using the framework described in the second part of this thesis, enabling thereby MOS's in the THz band. To make these a reality, the following research projects are needed:

- The maximum phase-shift tuning range, the losses and the experimental critical current need to be evaluated for our films, both in a buried microstrip configuration as well as in conventional microstrip technology arrangement. The chips to do this experiment are designed, only fabrication and evaluation is needed.
- From the proof-of-concept PCB prototypes of the focused connected array antenna presented in this thesis, a superconducting version needs to be designed and fabricated using the heritage on on-chip membranes [193, 235], low-loss low-stress deposited dielectrics [153, 226] and sub-micron NbTiN patterns with electron-beam lithography [156]. Testing the performance of such device will require the measurement of the complex beam-patterns [227] and the characterization of the optical efficiency [137].
- The scanning scenarios of the focused connected array concept require the placement of a field lens in the focal plane in order to achieve a telecentric quasi-optical system. This is currently emulated in the simulations with an artificial beam-straightening correction from the focal plane. In reality this field lens needs to be designed along with the whole quasi-optical system, which needs checking for scanning scenarios.

9.5. Impact of the Research

The work described in this dissertation has led to a number of journal and conference publications (see List of Publications in page 199). In total 5 peer-reviewed journal articles and 18 conference contributions have been published.

Following the prescriptions in this work, full octave-band filter-banks are currently being developed for the on-chip spectrometer DESHIMA 2.0. The first chips have been fabricated (see Fig. 9.1) and tested (see Fig. 9.2) in preparation for the imminent deployment in the ASTE telescope (Chile) next year. Furthermore, THz imaging spectrometers in the form of IFU's or MOS's are now technologically within reach.



Figure 9.1: A prototype chip for the DESHIMA 2.0 on-chip spectrometer. This device features a microstrip filter-bank employing the designs of this dissertation and an anti-reflection-coated lens hyper-hemispherical lens according to [176, 177]. This filter-bank has 319 spectral channels with a targeted spectral resolution of $R = 500$ spanning over the band 230–430 GHz. Four extra semi-isolated filters have been added at 220, 224.9, 434.8 and 439.2 GHz to allow the use of the peak and dip analyses in Section 5.3.2.

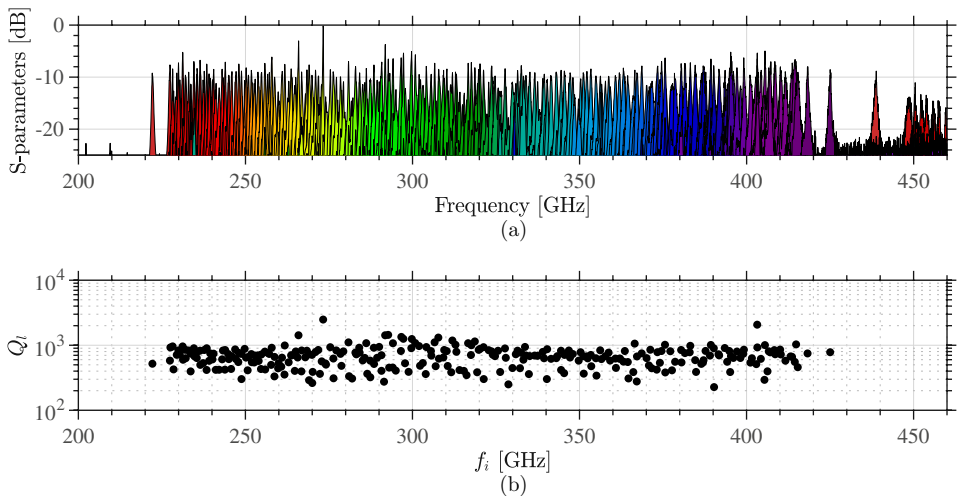


Figure 9.2: Measured performance of the octave-band chip in Fig. 9.1. Sub-figure (a) shows the frequency response of the different channels, estimated using (5.4) with a wideband coupling strength of $\eta_{wb} \approx -31.2$ dB (-27 dB designed). The peak coupling efficiency averages $\langle |S_{11}(f_i)| \rangle \approx -7.74$ dB $\approx 17\%$. Sub-figure (b) shows the loaded quality factor of the different channels, averaging $\langle Q_l \rangle \approx 780$.

Appendix A

Modeling Superconducting Films

In this appendix we describe how we modeled the superconducting films in the electromagnetic solvers used in this work: CST Microwave Studio [98] and Sonnet [99].

In CST, the superconducting films are modeled with opaque¹ (fields in each side of the surface are decoupled) tabulated surface impedance sheets with zero surface resistance and a surface reactance equal to ωL , where ω is the angular frequency. The surface inductance L is slightly different from the actual kinetic inductance L_k (calculated as $L_k = X_s/\omega$, where X_s is the imaginary part of the surface impedance in (2.8)) for two reasons. Firstly, because we want to excite the structures with well-established transmission line modes, we use waveguide ports which in turn require opaque impedance sheets to compute the port eigenvector. When modeling films as infinitely thin impedance sheets, the overlapping mesh cells in each side of the sheet effectively places two surface impedances in shunt, thus requiring the doubling of the inductance implemented (see Fig. 6 in [94]). Secondly, because the frequency-domain solver of CST uses a Finite Element Method, which meshes all the simulation volume, it will differ from the results computed from the Method of Moments solver of Sonnet, which only meshes the metal and thus accurately calculates the currents. For this reason we allowed the manual tweaking of the simulated inductance with a pre-factor K . As a result, CST simulations were performed with $L = 2KL_k$.

In Sonnet, the superconducting films are modeled as sheet impedances which can be directly given a kinetic inductance value. The simulated kinetic inductance typically agrees well with the measured one in contrast with the simulated inductance in CST [144]. As result, Sonnet simulations were performed with $L = L_k$.

We compare the results from CST and Sonnet simulations computed for the I-shaped microstrip resonator in Fig. 6.4. Given the high quality factor of this resonator,

¹The superconducting films used in this thesis are thin with respect to the penetration depth λ , thereby they should actually appear quasi-transparent to the alternating fields impinging on them.

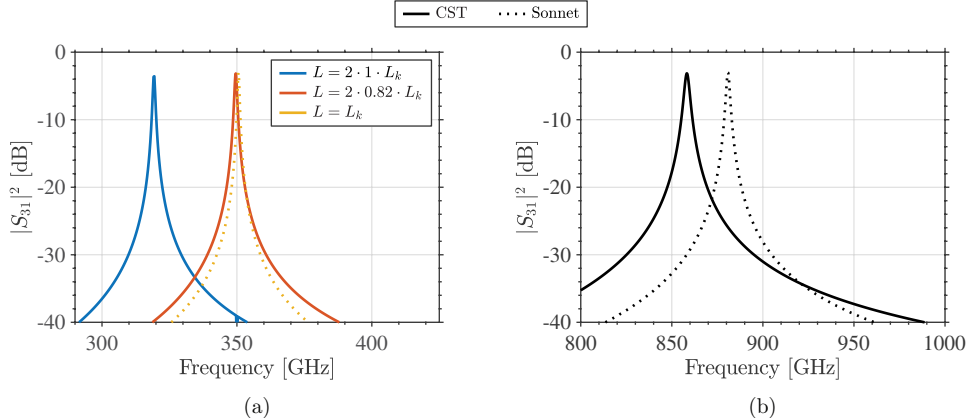


Figure A.1: Frequency response of the microstrip filter in Fig. 6.4 as simulated with CST [98] (solid lines) and Sonnet [99] (dotted lines) for: (a) superconducting metals ($L_k = 1 \text{ pH}/\square$ for the top layer and $L_k = 0.448 \text{ pH}/\square$ for the ground) and (b) perfectly conducting metals.

this type of simulation is very well suited to compare the simulators. As can be seen from Fig. A.1, there exists a disagreement in the location of the resonances between the results obtained in CST and Sonnet for the exact same geometry of the superconducting resonator (a). It should be noted that this discrepancy is also present for the case of a perfectly conducting resonator in panel (b), thereby implying a fundamental difference between these simulators, namely the solver type.

Appendix B

Fabrication of a Microstrip Filter-Bank On-Chip Spectrometer

In this appendix we describe the micro-fabrication route followed to manufacture the microstrip filter-banks of batch number LT194, whose results are discussed in Chapter 5. In the following we compile the seven layers stacked in this device and how they are processed to render the different structures on the chip.

Layer 1: Si wafer

We use a $\varnothing 100$ mm $350\text{ }\mu\text{m}$ -thick float-zone high-resistivity ($\rho > 10\text{ k}\Omega\text{ cm}$) Si wafer as a substrate.

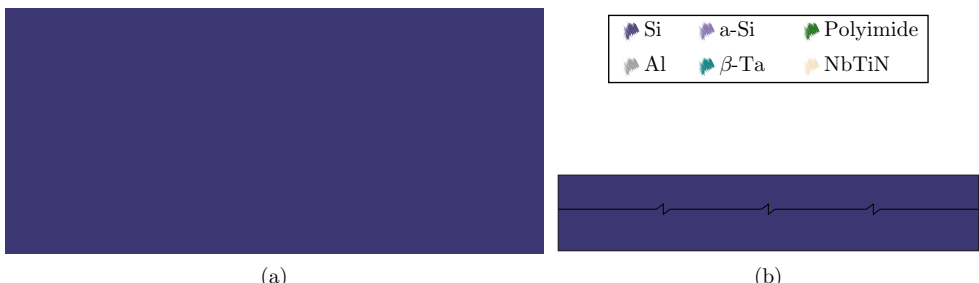


Figure B.1: Layer 1 - Si wafer. Schematic top-view in (a) and cross-section in (b).

Layer 2: bottom NbTiN

The structures in this layer make up the ground plane of the microstrips and the central conductor of the readout CPW. Procedure:

Preparation We perform a cleaning process as follows: (1) RCA1 organic clean ($\text{NH}_4\text{OH}:\text{H}_2\text{O}_2:\text{H}_2\text{O}$, 1:1:5) at 70°C for 10', (2) oxide removal and surface passivation with 10% HF in DI water for 10", (3) RCA2 metal clean ($\text{HCl}:\text{H}_2\text{O}_2:\text{H}_2\text{O}$, 1:1:5) at 70°C for 10', (4) second dip in 10% HF in DI water for 10", and (5) HDMS vapor coating to promote adhesion of the following layers.

Deposition We deposit a 260 nm-thick layer of NbTiN ($T_c = 15\text{ K}$, $\rho_n = 90.0\text{ }\mu\Omega\text{ cm}$) using a Nordiko 2000 reactive magnetron sputter system with NbTi target in a Nitrogen-Argon atmosphere.

Lithography The NbTiN layer is subsequently spin-coated with a positive photoresist (AZ ECI 3027) and soft baked for 90" at 110°C . Using UV contact lithography, the patterns of the ground plane are exposed with a dose of 160 mJ/cm^2 into the resist. Then the resist is developed in AZ 351B (5:1 dilution ratio in water) for 60".

Etching The NbTiN is patterned with a slightly sloped profile using a reactive ion etching (RIE) with a combined flow of 25 sccm O_2 and 13.5 sccm SF_6 at 5 mTorr for 12' under 50 W of RF power. Next, a plasma descum is done using a 100 sccm O_2 flow at 100 mTorr for 90" under 50 W of RF power. After etching, the resist is removed in AZ100 remover at 60°C , followed by an optional O_2 plasma clean if there are resist residues left.

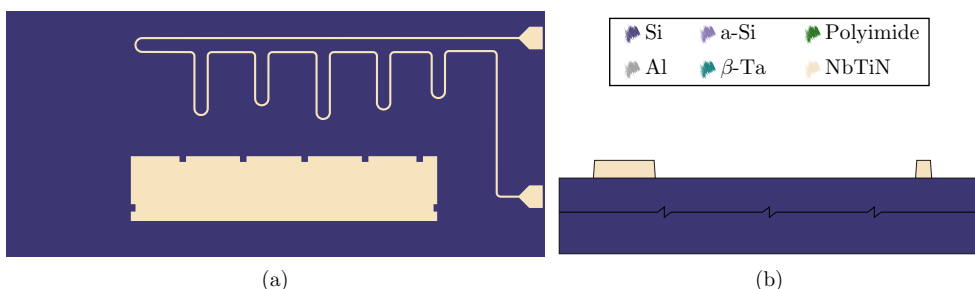


Figure B.2: Layer 2 - bottom NbTiN. Schematic top-view in (a) and cross-section in (b).

Layer 3: a-Si

This layer makes up the dielectric support for the microstrips in the filter-bank. Procedure:

Preparation The wafer is dipped for 10" in room temperature 10% water-diluted HF to remove surface oxides and to passivate the Si.

Deposition A 370 nm-thick a-Si layer is deposited using a Plasma-Enhanced Chemical Vapor Deposition (PECVD) in an Oxford Instruments Plasmapro 80. The deposition chamber is brought to a pressure of 1 Torr, the substrate is heated at 250 °C and a gas inflow of SiH₄ at 25 sccm and Ar at 475 sccm is activated with an RF power of 15 W for 10'35".

Lithography Prior to any further processing, the wafer is coated with HDMS vapors to promote the adhesion of the resist. A photoresist (AZ ECI 3027) is subsequently spin-coated and soft baked for 120" at 110 °C. Using UV contact lithography, the patterns of the dielectric are exposed for 8" with a dose of 160 mJ/cm² into the resist. Then the resist is developed in AZ 351B (5:1 dilution ratio in water) for 60". The a-Si is then baked for 60" at 120 °C.

Etching The a-Si is patterned with a sloped profile using two steps of RIE: first, using a combined flow of 25 sccm O₂ and 13.5 sccm SF₆ at 5 mTorr for 6' under 50 W of RF power; and second, using a 100 sccm O₂ flow at 100 mTorr for 90" under 50 W of RF power. After etching, the resist is removed in acetone first and then with AZ100 remover at 80 °C, followed by an optional O₂ plasma-clean if there are resist residues left.

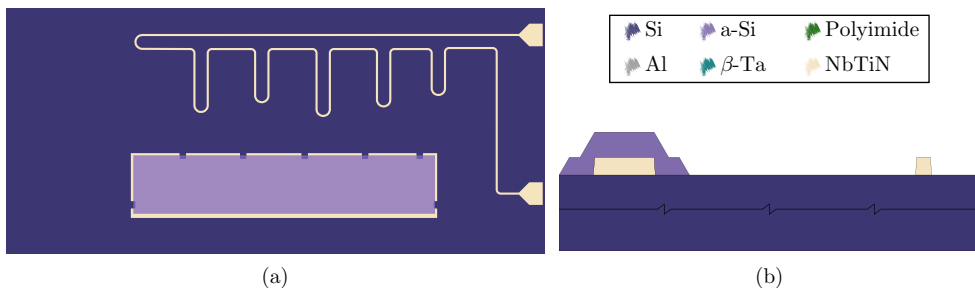


Figure B.3: Layer 3 - a-Si. Schematic top-view in (a) and cross-section in (b).

Layer 4: top NbTiN

The structures in this layer make up the filter-bank, the antenna, the MKIDs, the CPW connecting the antenna and the filter-bank, the CPW readout ground planes and the filter-bank termination. This is an advanced newly-developed processing step that combines UV and electron beam exposures on a single negative resist, which is then developed and used as an etch mask [156]. Procedure:

Preparation The wafer is dipped for 10" in room temperature 5% water-diluted HF to remove surface oxides that may cause a suboptimal galvanic connection in the contact points with the NbTiN of Layer 1 and to passivate the Si and a-Si. An HMDS coating is then applied and the wafer is baked at 150 °C for 45".

Deposition We deposit a 113 nm-thick layer of NbTiN ($T_c = 15$ K, $\rho_n = 135 \mu\Omega \text{ cm}$) using a Nordiko 2000 reactive magnetron sputter system with NbTi target in a Nitrogen-Argon atmosphere.

Lithography A negative (cross-linked resist remains) photoresist (maN1405), sensitive to both UV- and electron-beam lithography, is subsequently spin-coated and soft baked for 3' at 100 °C. First, the coarser structures of this layer are exposed using UV contact lithography for 15" with a dose of 300 mJ/cm² into the resist. Second, an electron-beam exposure is done in an Raith EBPG-5000+. Then the resist is developed in maD533/S for 45".

Etching The NbTiN is patterned with a sloped profile using two steps of RIE: first, using a combined flow of 25 sccm O₂ and 13.5 sccm SF₆ at 5 mTorr for 6' under 50 W of RF power; and second, using a 100 sccm O₂ flow at 100 mTorr for 90" under 50 W of RF power. After etching, the resist is removed in AZ100 remover at 70 °C.

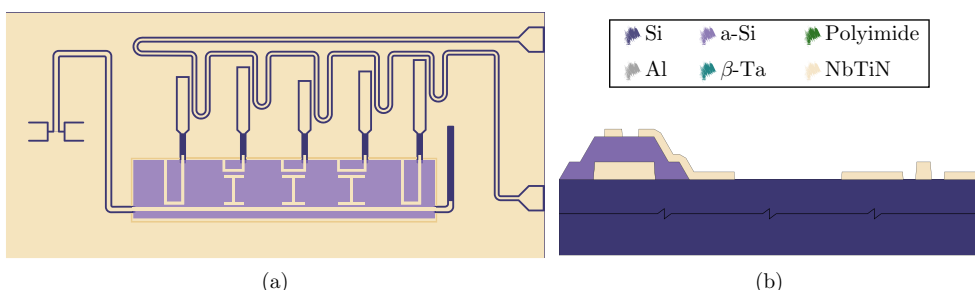


Figure B.4: Layer 4 - top NbTiN

Layer 5: polyimide

The structures in this layer make up the dielectric supports for the CPW bridges in the readout and for the NbTiN-Al interfaces to ensure a good galvanic connection despite the trenching that can occur due to the over-etch into the Si wafer. Procedure:

Preparation None.

Deposition A 700 nm-thick polyimide (Fujifilm LTC9305 [143]) layer is spin-coated on the wafer and subsequently cured at 100 °C.

Lithography The polyimide is exposed using UV contact lithography for 10.5" with a dose of 210 mJ/cm² and then let to rest for 1 h. The cross-linked polyimide is developed in three sequential baths: first in HTRD2 for 70", second in HTRD2:RER600 (1:1 solution ratio) for 60" and third in RER600 for 30". Then we plasma-clean with RIE using 100 sccm O₂ flow at 100 mTorr for 30" under 50 W of RF power.

Curing The polyimide is cured at 250 °C for 3 h and finally cleaned using RIE with an O₂ flow of 100 sccm at 100 mTorr for 30" under 50 W of RF power.

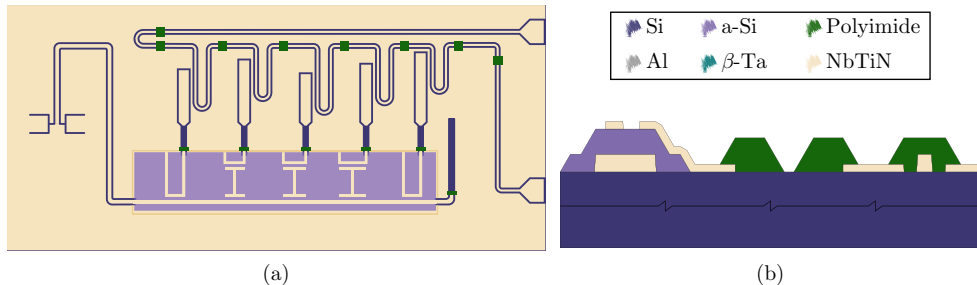


Figure B.5: Layer 5 - Polyimide. Schematic top-view in (a) and cross-section in (b).

Layer 6: Aluminium

The structures in this layer make up the bridges in the CPW readout and the absorbing metal for the hybrid MKIDs and the filter-bank termination. Procedure:

Preparation The wafer is dipped for 10" in room temperature 10% water-diluted HF to remove surface oxides and to passivate the Si and a-Si.

Deposition We deposit a 40 nm-thick layer of Al ($T_c = 1.25$ K, $\rho_n = 1.9 \mu\Omega \text{ cm}$) using DC magnetron sputtering in an Evatec LLS801 system with an Al target in a 5 mTorr Argon atmosphere under 876 W of DC power for 132".

Lithography We start with a soft bake at 100 °C for 120" to remove any liquid remnant. We then spin-coat the AZ1518 resist and cure it for 90" at 100 °C. We apply HDMS on the mask plate. The patterns of this layer are exposed using UV contact lithography with an 5.5" exposure of 110 mJ/cm² on the resist. The resist is then developed in a 1:1 water-diluted AZ100 developer for 50". Then a RIE O₂ plasma-clean is used to remove any resist residues left to ensure proper etching. The resist is then hard-baked at 125 °C for 1'30". The wafer is cleaned again using RIE with a 100 sccm O₂ flow at 100 mTorr and 50 W of RF power.

Etching The Al is wet-etched at 25 °C for 1'45". The resist is removed afterwards using acetone at room temperature for 30".

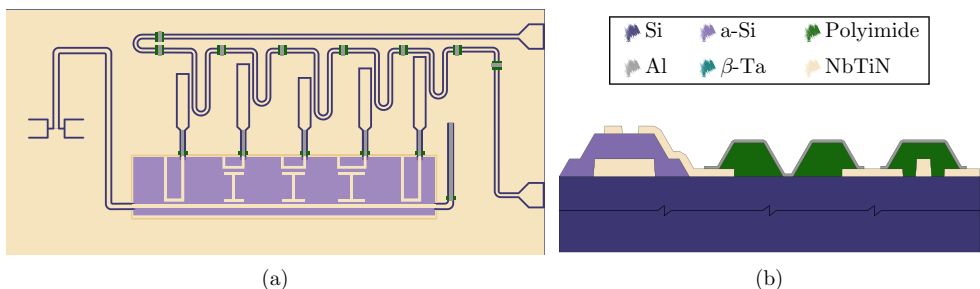


Figure B.6: Layer 6 - aluminium. Schematic top-view in (a) and cross-section in (b).

Layer 7: β -phase Tantalum

The structures of this layer make up a stray light patch absorber in the back side of the Si wafer. Procedure:

Preparation To protect the front side of the wafer, where we have processed so-far, we spin-coat AZ6632 (positive resist) at 4000 rpm for 30" and bake it at 110 °C for 120". Afterwards, the back side of the wafer is cleaned by firstly spinning it at 4000 rpm and spraying acetone and then IPA for 30", and secondly applying RIE with a 100 sccm O₂ flow at 100 mTorr for 4".

Deposition We deposit a 40 nm-thick layer of β -phase Ta ($T_c = 0.95$ K, $\rho_n = 239 \mu\Omega \text{ cm}$) is DC magnetron sputtered Evatec LLS801 system with a Ta target in a 5 mTorr Ar atmosphere under 876 W of DC power for 56".

Lithography We spin-coat ECI3012 (positive resist) at 4000 rpm for 30" and cure it for 60" at 110 °C. The patterns of this layer are exposed using UV contact lithography with an 3.7" exposure of 70 mJ/cm² on the resist. The resist is then developed in a 1:1 water-diluted AZ100 developer for 45". An optional RIE O₂ plasma-clean is used to remove any resist residues left. The resist is then hard baked at 125 °C for 1'30".

Etching The Ta is patterned with a sloped profile using three steps of RIE: first, using a combined flow of 30 sccm Ar and 25 sccm SF₆ at 10 mTorr for 2'30" under 60 W of RF power; second, using a combined flow of 100 sccm O₂ and 15 sccm CHF₃ at 100 mTorr for 60" under 50 W of RF power; and third, using a 100 sccm O₂ flow at 100 mTorr for 90" under 50 W of RF power. After etching, the resist is removed by spinning the wafer at 4000 rpm and spraying acetone and then IPA for 30".

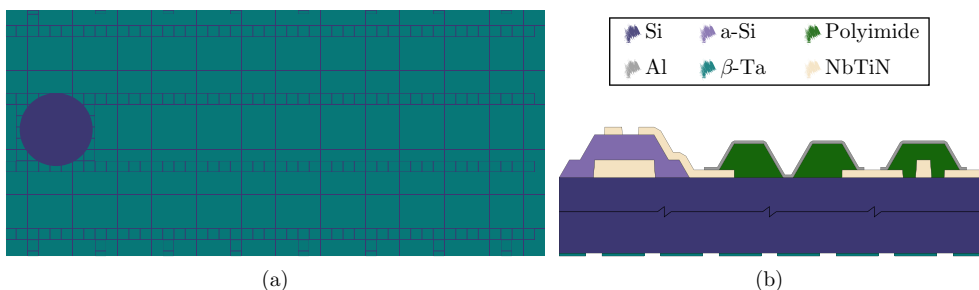


Figure B.7: Layer 7 - β -phase tantalum. Schematic bottom-view in (a) and cross-section in (b).

Dicing the wafer into chips

To protect the devices during the dicing process, we coat the front and the back of the wafer with resist: first we spin-coat at 4000 rpm and for 30" the front side of the wafer with ECI3027, which we cure at 110 °C for 120"; and afterwards we spin-coat at 4000 rpm and for 30" with ECI3012 on the back side of the wafer, which we cure at 110 °C for 60". Finally the wafer is diced into chips.

Mounting a Si lens

For each chip, a Si lens is carefully aligned to the double-slot antenna and glued to the back of the chip.

Appendix C

S-parameters of a shunt resonator in terms of its quality factors

In this appendix, the relations between the S-parameters and the quality factors of a half-wavelength resonator acting as a band-pass filter are derived. Fig. C.1 depicts both a three port network shunt half-wave resonator and a two-port network shunt quarter-wave resonator; both as circuit model and an energy model. We shall first establish the analytical expressions of the S-parameters for the two-port network of a shunt quarter-wavelength resonator (blue boxes in Fig. C.1) and then extend to the three-port network of a shunt half-wavelength resonator (yellow boxes in Fig. C.1).

C.1. Two-port network of a quarter-wavelength resonator in shunt

The S-parameters of the shunt load two-port network are given by

$$S_{11}(f) = \frac{-Z_0}{2Z(f) + Z_0}, \quad (C.1)$$

$$S_{21}(f) = \frac{2Z(f)}{2Z(f) + Z_0}, \quad (C.2)$$

where Z represents the impedance of the shunt load and Z_0 the normalization impedance at the ports. For the particular loading of a capacitively-coupled quarter-wavelength resonator (shown in the blue boxes in Fig. C.1), the expression of the

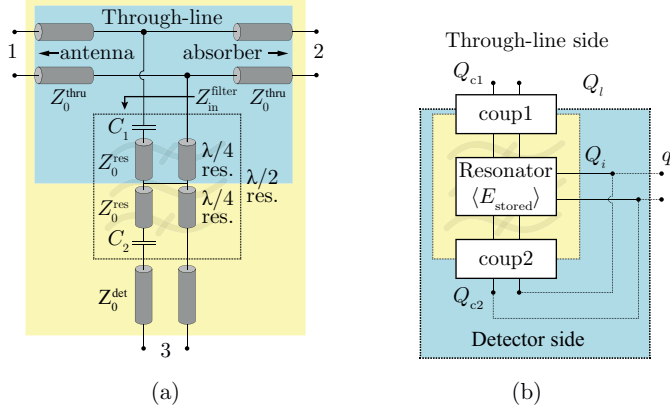


Figure C.1: Sub-figure (a): shunt half-wave resonator circuit as a band-pass filter emphasizing the almost virtual ground in its center and thereby its resemblance to two series quarter-wave resonators. Sub-figure (b) puts the manifest the energy resonator and its main energy-leaking mechanisms. The blue boxes represent the two-port network of a shunt quarter-wave resonator and the yellow boxes the three-port network of a shunt half-wave resonator acting as a band-pass filter.

input impedance can be approximated by [96, 107]

$$Z(f) \approx Z_0 \frac{Q_{c1}}{2q_i} \left(1 + j2q_i \frac{f - f_0}{f_0} \right), \quad (\text{C.3})$$

where f is the frequency around the resonance f_0 , Q_{c1} represents the coupling quality factor of the capacitor C_1 and q_i the internal quality factor of the resonator. Substituting (C.3) in (C.1) and (C.2) gives the expression of the two-port network S-parameters of the shunt capacitively-coupled quarter-wavelength resonator around its natural frequency f_0 , which can be written as

$$S_{11}(f) \approx \frac{S_{11}(f_0)}{1 + j2Q_l \frac{f - f_0}{f_0}}, \quad (\text{C.4})$$

$$S_{21}(f) \approx \frac{S_{21}(f_0) + j2Q_l \frac{f - f_0}{f_0}}{1 + j2Q_l \frac{f - f_0}{f_0}}, \quad (\text{C.5})$$

where the values on-resonance are

$$S_{11}(f_0) = \frac{-q_i}{Q_{c1} + q_i} = \frac{-Q_l}{Q_{c1}}, \quad (\text{C.6})$$

$$S_{21}(f_0) = \frac{Q_{c1}}{Q_{c1} + q_i} = \frac{Q_l}{q_i}. \quad (\text{C.7})$$

From an energy conservation argument, and using (C.4) and (C.5), the total loss of the two-port network resonator system on resonance is given by

$$\begin{aligned} L_{2\text{port}}(f_0) &= 1 - (|S_{11}(f_0)|^2 + |S_{21}(f_0)|^2) \\ &= \frac{2Q_{c1}q_i}{(Q_{c1} + q_i)^2}. \end{aligned} \quad (\text{C.8})$$

Similarly, the loaded quality factor of this network relates the energy stored in it to the power lost per cycle, which may be expressed in terms of its contributing energy-leaking mechanisms as

$$Q_l^{-1} = Q_{c1}^{-1} + q_i^{-1}. \quad (\text{C.9})$$

C.2. Three-port network of a half-wavelength resonator in shunt

The extension to the three-port network of a shunt half-wavelength resonator relies on the symmetry about the center of the half-wavelength resonator, where an approximate virtual ground exists, resembling two quarter-wavelength resonators connected in series as illustrated in Fig. C.1. Furthermore, the energy leakage through coupler 2 to port 3 (detector) can be accounted for as a “loss” term in the two-port network by means of (C.8) as

$$L_{2\text{port}}(f_0) = L_{3\text{port}}(f_0) + |S_{31}(f_0)|^2 = \frac{2Q_{c1}q_i}{(Q_{c1} + q_i)^2}, \quad (\text{C.10})$$

where $L_{3\text{port}}(f_0)$ represents the actual loss of the three-port network. In a similar fashion as we have redefined the loss in (C.10), we can expand the loaded quality factor of the three-port network from (C.9) as

$$Q_l^{-1} = Q_{c1}^{-1} + Q_{c2}^{-1} + Q_i^{-1}, \quad (\text{C.11})$$

where we have used

$$q_i^{-1} = Q_{c2}^{-1} + Q_i^{-1}. \quad (\text{C.12})$$

The loss of the three-port network can then be expressed in terms of its associated internal quality factor as

$$Q_i = \frac{2\pi f_0 \langle E_{\text{stored}} \rangle}{P_1 L_{3\text{port}}(f_0)}, \quad (\text{C.13})$$

where P_1 is the power injected from port 1. Similarly, the energy leakage to the detector can be modeled with its pertinent coupling quality factor as

$$Q_{c2} = \frac{2\pi f_0 \langle E_{\text{stored}} \rangle}{P_1 |S_{31}(f_0)|^2}. \quad (\text{C.14})$$

By combining (C.13) and (C.14) we can obtain the relation

$$\frac{Q_i}{Q_{c2}} = \frac{|S_{31}(f_0)|^2}{L_{3\text{port}}(f_0)}. \quad (\text{C.15})$$

From (C.10) and (C.15) one may obtain the transmission on-resonance from port 1 to port 3, which can be formulated as

$$|S_{31}(f_0)|^2 = \frac{2Q_{c1}q_i}{(Q_{c1} + q_i)^2} \frac{Q_i}{Q_i + Q_{c2}}. \quad (\text{C.16})$$

Using (C.12) on (C.16) allows to express the transmission coefficient $|S_{31}(f_0)|^2$ with only genuine three-port network parameters as

$$|S_{31}(f_0)|^2 = \frac{2Q_{c1}Q_{c2}}{\left(Q_{c2} + Q_{c1} \left(1 + \frac{Q_{c2}}{Q_i}\right)\right)^2} = \frac{2Q_l(-Q_lQ_i + Q_{c2}(Q_i - Q_l))}{Q_{c2}^2Q_i}, \quad (\text{C.17})$$

where we have used (C.11) to get to the last equality. The expression of the transmission around its resonance can be written out as

$$S_{31}(f) \approx \frac{S_{31}(f_0)}{1 + 2jQ_l \frac{f-f_0}{f_0}}. \quad (\text{C.18})$$

C.3. Maximum power transfer to the detector

To optimize the power transfer on-resonance from the input (port 1) to the detector (port 3) of the shunt half-wave resonator band-pass filter, the maximum of the function $|S_{31}(f_0)|^2$ needs to be found for a fixed $\{Q_l, Q_i\}$ pair. To do so, we shall equate to zero the derivative with respect to Q_{c2} of the last term in (C.17). After some algebraic steps this results in

$$Q_{c2} = \frac{2Q_iQ_l}{Q_i - Q_l} = 2(Q_l^{-1} - Q_i^{-1})^{-1} = 2(Q_{c1}^{-1} + Q_{c2}^{-1})^{-1}, \quad (\text{C.19})$$

where (C.11) has been used to arrive to the last equality. It becomes apparent from the last expression that the condition

$$Q_{c1} = Q_{c2} = \frac{2Q_iQ_l}{Q_i - Q_l} \quad (\text{C.20})$$

is the one giving the maximum transmission

$$|S_{31}^{\max}(f_0)|^2 = \frac{(Q_i - Q_l)^2}{2Q_i^2} = \frac{2Q_l^2}{Q_c^2}. \quad (\text{C.21})$$

Bibliography

- [1] W. Herschel, “XIV. Experiments on the refrangibility of the invisible rays of the Sun,” *Philos. Trans. R. Soc. Lond.*, vol. 90, pp. 284–292, 1800.
- [2] J. C. Maxwell, “VIII. A dynamical theory of the electromagnetic field,” *Philos. Trans. R. Soc. Lond.*, vol. 155, pp. 459–512, 1865.
- [3] J. Stefan, *Über die Beziehung zwischen der Wärmestrahlung und der Temperatur*, ser. Sitzungsberichte der Kaiserlichen Akademie der Wissenschaften in Wien. Kaiserlich-Königliche Hof-und Staatsdruckerei, 1879.
- [4] L. Boltzmann, “Derivation of Stefan’s law regarding the dependence of thermal radiation on temperature from electromagnetic light theory,” *Ann. Phys.*, vol. 258, no. 6, pp. 291–294, 1884.
- [5] M. Planck, *The theory of heat radiation*. P. Blakiston’s Son & Co., 1914.
- [6] R. A. Alpher and R. C. Herman, “Remarks on the evolution of the expanding Universe,” *Phys. Rev.*, vol. 75, no. 7, pp. 1089–1095, Apr. 1949.
- [7] R. H. Dicke, P. J. E. Peebles, P. G. Roll, and D. T. Wilkinson, “Cosmic black-body radiation,” *Astrophys. J.*, vol. 142, pp. 414–419, Jul. 1965.
- [8] A. A. Penzias and R. W. Wilson, “A measurement of excess antenna temperature at 4080 Mc/s.” *Astrophys. J.*, vol. 142, pp. 419–421, Jul. 1965.
- [9] R. Hill, K. W. Masui, and D. Scott, “The spectrum of the Universe,” *Appl. Spectrosc.*, vol. 72, no. 5, pp. 663–688, May 2018.
- [10] G. Lagache, J.-L. Puget, and H. Dole, “Dusty infrared galaxies: Sources of the Cosmic Infrared Background,” *Annu. Rev. Astron. Astrophys.*, vol. 43, no. 1, pp. 727–768, 2005.
- [11] G. Lemaître, “Un Univers homogène de masse constante et de rayon croissant rendant compte de la vitesse radiale des nébuleuses extra-galactiques,” *Annales de la Société Scientifique de Bruxelles*, vol. 47, pp. 49–59, Jan. 1927.

- [12] E. Hubble, “The law of red-shifts,” *Mon. Not. R. Astron. Soc.*, vol. 113, no. 6, pp. 658–666, Dec. 1953.
- [13] S. W. Hawking and G. F. R. Ellis, “The cosmic black-body radiation and the existence of singularities in our Universe,” *Astrophys. J.*, vol. 152, p. 25, Apr. 1968.
- [14] A. G. Riess *et al.*, “Observational evidence from supernovae for an accelerating universe and a cosmological constant,” *Astron. J.*, vol. 116, no. 3, pp. 1009–1038, Sep. 1998.
- [15] A. Friedman, “On the curvature of space,” *Gen. Relativ. Gravit.*, vol. 31, no. 12, pp. 1991–2000, Dec. 1999.
- [16] P. A. Oesch *et al.*, “A remarkably luminous galaxy at $z=11.1$ measured with Hubble Space Telescope GRISM spectroscopy,” *Astrophys. J.*, vol. 819, no. 2, p. 129, Mar. 2016.
- [17] L. Jiang *et al.*, “Evidence for GN-z11 as a luminous galaxy at redshift 10.957,” *Nat. Astron.*, vol. 5, no. 3, pp. 256–261, Mar. 2021.
- [18] S. C. Glover, J. Chluba, S. R. Furlanetto, J. R. Pritchard, and D. W. Savin, “Chapter three - Atomic, molecular, and optical physics in the early Universe: From Recombination to Reionization,” ser. Advances in Atomic, Molecular, and Optical Physics, E. Arimondo, P. R. Berman, and C. C. Lin, Eds. Academic Press, 2014, vol. 63, pp. 135–270.
- [19] C. M. Casey, D. Narayanan, and A. Cooray, “Dusty star-forming galaxies at high redshift,” *Phys. Rep.*, vol. 541, no. 2, pp. 45–161, Aug. 2014.
- [20] C. Casey *et al.*, “Taking census of massive, star-forming galaxies formed <1 Gyr after the Big Bang,” *Bull. Am. Astron. Soc.*, vol. 51, no. 3, May 2019.
- [21] C. Carilli and F. Walter, “Cool gas in high-redshift galaxies,” *Annu. Rev. Astron. Astrophys.*, vol. 51, no. 1, pp. 105–161, Aug. 2013.
- [22] A. W. Blain, I. Smail, R. Ivison, J.-P. Kneib, and D. T. Frayer, “Submillimeter galaxies,” *Phys. Rep.*, vol. 369, no. 2, pp. 111–176, Oct. 2002.
- [23] C. Kulesa, “Terahertz spectroscopy for astronomy: From comets to cosmology,” *IEEE Trans. Terahertz Sci. Technol.*, vol. 1, no. 1, pp. 232–240, Sep. 2011.
- [24] D. J. Fixsen, “The temperature of the Cosmic Microwave Background,” *Astrophys. J.*, vol. 707, no. 2, pp. 916–920, Nov. 2009.

- [25] Planck Collaboration, “Planck 2013 results. XII. Diffuse component separation,” *Astron. Astrophys.*, vol. 571, p. A12, 2014.
- [26] European Southern Observatory (ESO). ALMA deep view of part of the Hubble Ultra Deep Field. [Online]. Available: <https://www.eso.org/public/images/eso1633e/>
- [27] G. J. Stacey, “THz low resolution spectroscopy for astronomy,” *IEEE Trans. Terahertz Sci. Technol.*, vol. 1, no. 1, pp. 241–255, Sep. 2011.
- [28] J. A. Hodge and E. da Cunha, “High-redshift star formation in the Atacama large millimetre/submillimetre array era,” *R. Soc. Open Sci.*, vol. 7, no. 12, p. 200556, Dec. 2020.
- [29] J. Glenn *et al.*, “Bolocam: a millimeter-wave bolometric camera,” in *Proc. SPIE, Advanced Technology MMW, Radio, and Terahertz Telescopes*, T. G. Phillips, Ed., vol. 3357, Int. Soc. Opt. Photon. SPIE, 1998, pp. 326–334.
- [30] G. W. Wilson *et al.*, “The AzTEC mm-wavelength camera,” *Mon. Not. R. Astron. Soc.*, vol. 386, no. 2, pp. 807–818, Apr. 2008.
- [31] Siringo, G. *et al.*, “The Large APEX BOlometer CAmera LABOCA,” *Astron. Astrophys.*, vol. 497, no. 3, pp. 945–962, Apr. 2009.
- [32] B. Reichborn-Kjennerud *et al.*, “EBEX: a balloon-borne CMB polarization experiment,” in *Proc. SPIE, Millimeter, Submillimeter, and Far-Infrared Detectors and Instrumentation for Astronomy V*, W. S. Holland and J. Zmuidzinas, Eds., vol. 7741, Int. Soc. Opt. Photon. SPIE, 2010, pp. 381–392.
- [33] M. D. Niemack *et al.*, “ACTPol: a polarization-sensitive receiver for the Atacama Cosmology Telescope,” in *Proc. SPIE, Millimeter, Submillimeter, and Far-Infrared Detectors and Instrumentation for Astronomy V*, W. S. Holland and J. Zmuidzinas, Eds., vol. 7741, Int. Soc. Opt. Photon. SPIE, 2010, pp. 537–557.
- [34] J. E. Austermann *et al.*, “SPTpol: an instrument for CMB polarization measurements with the South Pole Telescope,” in *Proc. SPIE, Millimeter, Submillimeter, and Far-Infrared Detectors and Instrumentation for Astronomy VI*, W. S. Holland, Ed., vol. 8452, Int. Soc. Opt. Photon. SPIE, 2012, pp. 393–410.
- [35] W. S. Holland *et al.*, “SCUBA-2: the 10000 pixel bolometer camera on the James Clerk Maxwell Telescope,” *Mon. Not. R. Astron. Soc.*, vol. 430, no. 4, pp. 2513–2533, Mar. 2013.

- [36] P. A. R. Ade *et al.*, “BICEP2/KECK Array. IV. Optical characterization and performance of the BICEP2 and KECK Array experiments,” *Astrophys. J.*, vol. 806, no. 2, p. 206, Jun. 2015.
- [37] ——, “Antenna-coupled TES bolometers used in BICEP2, Keck Array, and SPIDER,” *Astrophys. J.*, vol. 812, no. 2, pp. 176–182, Oct. 2015.
- [38] J. A. Grayson *et al.*, “BICEP3 performance overview and planned Keck Array upgrade,” in *Proc. SPIE, Millimeter, Submillimeter, and Far-Infrared Detectors and Instrumentation for Astronomy VIII*, W. S. Holland and J. Zmuidzinas, Eds., vol. 9914, Int. Soc. Opt. Photon. SPIE, 2016, pp. 157–173.
- [39] R. Adam *et al.*, “The NIKA2 large-field-of-view millimetre continuum camera for the 30 m IRAM telescope,” *Astron. Astrophys.*, vol. 609, p. A115, Jan. 2018.
- [40] Y. Inoue *et al.*, “POLARBEAR-2: an instrument for CMB polarization measurements,” in *Proc. SPIE, Millimeter, Submillimeter, and Far-Infrared Detectors and Instrumentation for Astronomy VIII*, W. S. Holland and J. Zmuidzinas, Eds., vol. 9914, Int. Soc. Opt. Photon. SPIE, 2016, pp. 372–380.
- [41] J. J. A. Baselmans *et al.*, “A kilo-pixel imaging system for future space based far-infrared observatories using microwave kinetic inductance detectors,” *Astron. Astrophys.*, vol. 601, p. A89, May 2017.
- [42] A. Suzuki *et al.*, “The LiteBIRD satellite mission: Sub-kelvin instrument,” *J. Low Temp. Phys.*, vol. 193, no. 5, pp. 1048–1056, Dec. 2018.
- [43] G. W. Wilson *et al.*, “The TolTEC camera: an overview of the instrument and in-lab testing results,” in *Proc. SPIE, Millimeter, Submillimeter, and Far-Infrared Detectors and Instrumentation for Astronomy X*, J. Zmuidzinas and J.-R. Gao, Eds., vol. 11453, Int. Soc. Opt. Photon. SPIE, 2020, pp. 1–20.
- [44] T. de Graauw *et al.*, “The Herschel-heterodyne instrument for the far-infrared (HIFI)*,” *Astron. Astrophys.*, vol. 518, p. L6, Jul. 2010.
- [45] M. Carter *et al.*, “The EMIR multi-band mm-wave receiver for the IRAM 30-m telescope,” *Astron. Astrophys.*, vol. 538, p. A89, 2012.
- [46] C. M. Caves, “Quantum limits on noise in linear amplifiers,” *Phys. Rev. D*, vol. 26, pp. 1817–1839, Oct. 1982.
- [47] C. Matt Bradford *et al.*, “Z-Spec: A broadband millimeter-wave grating spectrometer - design, construction, and first cryogenic measurements,” in *Proc. SPIE, Millimeter and Submillimeter Detectors for Astronomyn II*, vol. 5498, Int. Soc. Opt. Photon. SPIE, Oct. 2004.

- [48] C. Ferkinhoff *et al.*, “ZEUS-2: a second generation submillimeter grating spectrometer for exploring distant galaxies,” in *Proc. SPIE, Millimeter, Submillimeter, and Far-Infrared Detectors and Instrumentation for Astronomy V*, J. Z. Wayne S. Holland, Ed., vol. 7741, Int. Soc. Opt. Photon. SPIE, Jul. 2010.
- [49] A. Endo *et al.*, “Wideband on-chip terahertz spectrometer based on a superconducting filterbank,” *J. Astron. Telesc. Instrum. Syst.*, vol. 5, no. 3, pp. 1–12, Jun. 2019.
- [50] C. N. Thomas *et al.*, “Progress on the CAmbridge Emission Line Surveyor (CAMELS),” in *Proc. 26th Int. Symp. Space THz Technol.*, Mar. 2015.
- [51] S. Bryan *et al.*, “WSPEC: a waveguide filter-bank focal plane array spectrometer for millimeter wave astronomy and cosmology,” *J. Low Temp. Phys.*, vol. 184, no. 1, pp. 114–122, Jul. 2016.
- [52] G. Cataldo *et al.*, “Second-generation design of Micro-Spec: A medium-resolution, submillimeter-wavelength spectrometer-on-a-chip,” *J. Low Temp. Phys.*, vol. 193, no. 5, pp. 923–930, Dec. 2018.
- [53] J. Redford *et al.*, “The design and characterization of a 300 channel, optimized full-band millimeter filterbank for science with SuperSpec,” in *Proc. SPIE, Millimeter, Submillimeter, and Far-Infrared Detectors and Instrumentation for Astronomy IX*, J. Zmuidzinas and J.-R. Gao, Eds., vol. 10708, Int. Soc. Opt. Photon. Austin, TX, US: SPIE, Jul. 2018, pp. 187–194.
- [54] European Southern Observatory (ESO). Integral field units. [Online]. Available: <https://www.eso.org/public/teles-instr/technology/ifu/>
- [55] R. Güsten *et al.*, “CHAMP: the Carbon Heterodyne Array of the MPIfR,” in *Proc. Adv. Technol. Millimeter Wave, Radio, and Terahertz Telescopes*, T. G. Phillips, Ed., vol. 3357, Int. Soc. Opt. Photon. SPIE, 1998, pp. 167–177.
- [56] C. Kasemann *et al.*, “CHAMP+: A powerful submm heterodyne array,” in *Proc. 19th Int. Symp. Space Terahertz Technol.*, Groningen, Apr. 2008.
- [57] K. Sunada, C. Yamaguchi, N. Nakai, K. Sorai, S. K. Okumura, and N. Ukita, “BEARS: SIS 25-beam array receiver system for the NRO 45-m telescope,” in *Proc. Radio Telescopes*, H. R. Butcher, Ed., vol. 4015, Int. Soc. Opt. Photon. SPIE, 2000, pp. 237 – 246.
- [58] C. K. Walker *et al.*, “Pole STAR: An 810 GHz array receiver for AST/RO,” in *Proc. 12th Int. Symp. on Space Terahertz Technology*, 2001, pp. 540–552.

- [59] C. E. Groppi *et al.*, “Desert STAR: a 7-pixel 345-GHz heterodyne array receiver for the Heinrich Hertz Telescope,” in *Proc. Millimeter and Submillimeter Detectors for Astronomy*, T. G. Phillips and J. Zmuidzinas, Eds., vol. 4855, Int. Soc. Opt. Photon. SPIE, 2003, pp. 330–337.
- [60] U. U. Graf *et al.*, “SMART: the KOSMA submillimeter array receiver for two frequencies,” in *Proc. Millimeter and Submillimeter Detectors for Astronomy*, T. G. Phillips and J. Zmuidzinas, Eds., vol. 4855, Int. Soc. Opt. Photon. SPIE, 2003, pp. 322–329.
- [61] K.-F. Schuster *et al.*, “A 230 GHz heterodyne receiver array for the IRAM 30 m telescope,” *Astron. Astrophys.*, vol. 423, no. 3, pp. 1171–1177, 2004.
- [62] J. V. Buckle *et al.*, “HARP/ACSiS: a submillimetre spectral imaging system on the James Clerk Maxwell Telescope,” *Mon. Not. R. Astron. Soc.*, vol. 399, no. 2, pp. 1026–1043, Oct. 2009.
- [63] C. Groppi *et al.*, “Test and integration results from SuperCam: a 64-pixel array receiver for the 350 GHz atmospheric window,” in *Proc. SPIE, Millimeter, Submillimeter, and Far-Infrared Detectors and Instrumentation for Astronomy V*, W. S. Holland and J. Zmuidzinas, Eds., vol. 7741, Int. Soc. Opt. Photon. SPIE, 2010, pp. 267–278.
- [64] S. Heyminck, U. U. Graf, R. Güsten, J. Stutzki, H. W. Hübbers, and P. Hartogh, “GREAT: the SOFIA high-frequency heterodyne instrument,” *Astron. Astrophys.*, vol. 542, p. L1, 2012.
- [65] C. Risacher *et al.*, “First supra-THz heterodyne array receivers for astronomy with the SOFIA observatory,” *IEEE Trans. Terahertz Sci. Technol.*, vol. 6, no. 2, pp. 199–211, Mar. 2016.
- [66] L. W. Looney *et al.*, “Realizing 3D spectral imaging in the far-infrared: FIFI LS,” in *Proc. SPIE, Airborne Telescope Systems*, R. K. Melugin and H.-P. Roeser, Eds., vol. 4014, Int. Soc. Opt. Photon. SPIE, 2000, pp. 14–22.
- [67] A. Poglitsch *et al.*, “The photodetector array camera and spectrometer (PACS) on the Herschel Space Observatory*,” *Astron. Astrophys.*, vol. 518, p. L2, Jul. 2010.
- [68] M. J. Griffin *et al.*, “The Herschel-SPIRE instrument and its in-flight performance*,” *Astron. Astrophys.*, vol. 518, p. L3, Jul. 2010.
- [69] M. Mirzaei *et al.*, “ μ -spec spectrometers for the EXCLAIM instrument,” in *Proc. SPIE, Millimeter, Submillimeter, and Far-Infrared Detectors and Instrumentation for Astronomy X*, J. Zmuidzinas and J.-R. Gao, Eds., vol. 11453, Int. Soc. Opt. Photon. SPIE, Dec. 2020, pp. 128–139.

- [70] C.-T. Li *et al.*, “TIME millimeter wave grating spectrometer,” in *Proc. SPIE, Millimeter, Submillimeter, and Far-Infrared Detectors and Instrumentation for Astronomy IX*, J. Zmuidzinas and J.-R. Gao, Eds., vol. 10708, Int. Soc. Opt. Photon. SPIE, 2018, pp. 540–547.
- [71] C. M. Bradford *et al.*, “X-Spec: a multi-object trans-millimeter-wave spectrometer for CCAT,” in *Proc. SPIE, Millimeter, Submillimeter, and Far-Infrared Detectors and Instrumentation for Astronomy VII*, W. S. Holland and J. Zmuidzinas, Eds., vol. 9153, Int. Soc. Opt. Photon. SPIE, 2014, pp. 622–633.
- [72] J. Redford *et al.*, “SuperSpec: Device characterization and preparation for telescope deployment and observations,” *Bull. Am. Astron. Soc.*, vol. 53, no. 6, Jun. 2021.
- [73] P. Barry *et al.*, “Design and preliminary results of the spectroscopic focal plane for the south pole telescope summertime line intensity mapper,” in *Proc. 19th Int. Workshop on Low Temp. Detectors*, Jul. 2021.
- [74] A. Endo *et al.*, “First light demonstration of the integrated superconducting spectrometer,” *Nat. Astron.*, vol. 3, no. 11, pp. 989–996, Nov. 2019.
- [75] K. Kohno *et al.*, “Large format imaging spectrograph for the Large Submillimeter Telescope (LST),” in *Proc. SPIE, Millimeter, Submillimeter, and Far-Infrared Detectors and Instrumentation for Astronomy X*, J. Zmuidzinas and J.-R. Gao, Eds., vol. 11453, Int. Soc. Opt. Photon. SPIE, 2020, pp. 128–138.
- [76] J. Geach *et al.*, “The case for a ‘sub-millimeter SDSS’: a 3D map of galaxy evolution to $z \sim 10$,” *Bull. Am. Astron. Soc.*, vol. 51, no. 3, May 2019.
- [77] D. Obreschkow, H.-R. Klöckner, I. Heywood, F. Levrier, and S. Rawlings, “A Virtual sky with extragalactic HI and CO lines for the Square Kilometre Array and the Atacama Large Millimeter/Submillimeter Array,” *Astrophys. J.*, vol. 703, no. 2, pp. 1890–1903, Sep. 2009.
- [78] Y. B. Zeldovich and R. A. Sunyaev, “The interaction of matter and radiation in a hot-model universe,” *Astrophys. Space Sci.*, vol. 4, no. 3, pp. 301–316, Jul. 1969.
- [79] T. Mroczkowski *et al.*, “Astrophysics with the spatially and spectrally resolved Sunyaev-Zeldovich effects,” *Space Sci. Rev.*, vol. 215, no. 1, p. 17, Feb. 2019.
- [80] J. Delabrouille *et al.*, “Microwave spectro-polarimetry of matter and radiation across space and time,” *Exp. Astron.*, Jul. 2021.

- [81] D. T. Chung, M. P. Viero, S. E. Church, and R. H. Wechsler, “Forecasting [CII] line-intensity mapping measurements between the end of reionization and the epoch of galaxy assembly,” *Astrophys. J.*, vol. 892, no. 1, p. 51, Mar. 2020.
- [82] H. Fröhlich, “Theory of the superconducting state. I. The ground state at the absolute zero of temperature,” *Phys. Rev.*, vol. 79, pp. 845–856, Sep. 1950.
- [83] N. Bohr, “I. on the constitution of atoms and molecules,” *London, Edinburgh Dublin Philos. Mag. J. Sci.*, vol. 26, no. 151, pp. 1–25, 1913.
- [84] E. Schrödinger, “Quantisierung als eigenwertproblem,” *Ann. Phys.*, vol. 384, no. 4, pp. 361–376, 1926.
- [85] H. Kamerlingh Onnes, “Further experiments with liquid helium G. on the electrical resistance of pure metals etc. VI. on the sudden change in the rate at which the resistance of mercury disappears,” in *Proc. KNAW*, vol. 14 II, Amsterdam, Jan. 1912, pp. 818–821.
- [86] W. Meissner and R. Ochsenfeld, “Ein neuer effekt bei eintritt der supraleitfähigkeit,” *Naturwis.*, vol. 21, no. 44, pp. 787–788, Nov. 1933.
- [87] J. Bardeen, “Theory of the Meissner effect in superconductors,” *Phys. Rev.*, vol. 97, pp. 1724–1725, Mar. 1955.
- [88] F. London and H. London, “The electromagnetic equations of the supraconductor,” *Proc. R. Soc. Lond. A*, vol. 149, no. 866, pp. 71–88, 1935.
- [89] J. Bardeen, L. N. Cooper, and J. R. Schrieffer, “Theory of superconductivity,” *Phys. Rev.*, vol. 108, pp. 1175–1204, Dec. 1957.
- [90] L. N. Cooper, “Bound electron pairs in a degenerate Fermi gas,” *Phys. Rev.*, vol. 104, pp. 1189–1190, Nov. 1956.
- [91] D. C. Mattis and J. Bardeen, “Theory of the anomalous skin effect in normal and superconducting metals,” *Phys. Rev.*, vol. 111, pp. 412–417, Jul. 1958.
- [92] R. Matick, *Transmission Lines for Digital and Communication Networks: An Introduction to Transmission Lines, High-frequency and High-speed Pulse Characteristics and Applications*. McGraw-Hill, 1969.
- [93] R. L. Kautz, “Picosecond pulses on superconducting striplines,” *J. Appl. Phys.*, vol. 49, no. 1, pp. 308–314, 1978.
- [94] A. R. Kerr, “Surface impedance of superconductors and normal conductors in EM simulators,” Electronics Division, National Radio Astronomy Observatory, Green Bank, West Virginia, Tech. Rep. 302, Feb. 1996.

- [95] R. F. Broom and P. Wolf, “Q factor and resonance amplitude of Josephson tunnel junctions,” *Phys. Rev. B*, vol. 16, pp. 3100–3107, Oct. 1977.
- [96] R. Barends, “Photon-detecting superconducting resonators,” Ph.D. dissertation, Delft University of Technology, 2009.
- [97] H. G. Leduc *et al.*, “Titanium nitride films for ultrasensitive microresonator detectors,” *Appl. Phys. Lett.*, vol. 97, no. 10, p. 102509, 2010.
- [98] CST Microwave Studio (2018). Dassault Systèmes Simulia Corp. [Online]. Available: <https://www.3ds.com/products-services/simulia/products/cst-studio-suite/>
- [99] Sonnet em (17.56). Sonnet Software, Inc. [Online]. Available: <https://www.sonnetsoftware.com/>
- [100] D. M. Pozar, *Microwave engineering*, 4th ed. Hoboken, NJ: Wiley, 2012.
- [101] R. Collin, *Foundations for Microwave Engineering*, 2nd ed. Hoboken, NJ: John Wiley & Sons, Inc., 1992.
- [102] M. D. Shaw, J. Bueno, P. Day, C. M. Bradford, and P. M. Echternach, “Quantum capacitance detector: a pair-breaking radiation detector based on the single Cooper-pair box,” *Phys. Rev. B*, vol. 79, p. 144511, Apr. 2009.
- [103] A. Peacock *et al.*, “Single optical photon detection with a superconducting tunnel junction,” *Nature*, vol. 381, no. 6578, pp. 135–137, May 1996.
- [104] P. K. Day, H. G. LeDuc, B. A. Mazin, A. Vayonakis, and J. Zmuidzinas, “A broadband superconducting detector suitable for use in large arrays,” *Nature*, vol. 425, no. 6960, pp. 817–821, Oct. 2003.
- [105] J. Gao, J. Zmuidzinas, A. Vayonakis, P. Day, B. Mazin, and H. Leduc, “Equivalence of the effects on the complex conductivity of superconductor due to temperature change and external pair breaking,” *J. Low Temp. Phys.*, vol. 151, no. 1, pp. 557–563, Apr. 2008.
- [106] P. J. de Visser, “Quasiparticle dynamics in aluminium superconducting microwave resonators,” Ph.D. dissertation, Delft University of Technology, 2014.
- [107] B. A. Mazin, “Microwave kinetic inductance detectors,” Ph.D. dissertation, California Institute of Technology, 2005.
- [108] R. M. J. Janssen *et al.*, “High optical efficiency and photon noise limited sensitivity of microwave kinetic inductance detectors using phase readout,” *Appl. Phys. Lett.*, vol. 103, no. 20, p. 203503, Nov. 2013.

- [109] J. Gao *et al.*, “A semiempirical model for two-level system noise in superconducting microresonators,” *Appl. Phys. Lett.*, vol. 92, no. 21, p. 212504, May 2008.
- [110] J. Gao, J. Zmuidzinas, B. A. Mazin, H. G. LeDuc, and P. K. Day, “Noise properties of superconducting coplanar waveguide microwave resonators,” *Appl. Phys. Lett.*, vol. 90, no. 10, p. 102507, 2007.
- [111] J. van Rantwijk, M. Grim, D. van Loon, S. Yates, A. Baryshev, and J. Baselmans, “Multiplexed readout for 1000-pixel arrays of microwave kinetic inductance detectors,” *IEEE Trans. Microw. Theory Tech.*, vol. 64, no. 6, pp. 1876–1883, Jun. 2016.
- [112] S. McHugh *et al.*, “A readout for large arrays of microwave kinetic inductance detectors,” *Rev. Sci. Instrum.*, vol. 83, no. 4, p. 044702, Apr. 2012.
- [113] A. Pascual Laguna *et al.*, “Terahertz band-pass filters for wideband superconducting on-chip filter-bank spectrometers,” *IEEE Trans. Terahertz Sci. Technol.*, vol. 11, no. 6, pp. 635–646, Nov. 2021.
- [114] H. Pickett, R. Poynter, E. Cohen, M. Delitsky, J. Pearson, and H. Müller, “Submillimeter, millimeter, and microwave spectral line catalog,” *J. Quant. Spectrosc. Radiat. Transf.*, vol. 60, no. 5, pp. 883–890, Nov. 1998.
- [115] P. Hargrave, S. Withington, S. A. Buehler, L. Kluft, B. Flatman, and P. K. Dongre, “THz spectroscopy of the atmosphere for climatology and meteorology applications,” in *Proc. Next-Gener. Spectrosc. Technol. X*, M. A. Druy, R. A. Crocombe, S. M. Barnett, and L. T. Profeta, Eds., vol. 10210, Int. Soc. for Opt. and Photon. SPIE, Apr. 2017, pp. 149–161.
- [116] H. Dole *et al.*, “The cosmic infrared background resolved by Spitzer - Contributions of mid-infrared galaxies to the far-infrared background,” *Astron. Astrophys.*, vol. 451, no. 2, pp. 417–429, May 2006.
- [117] C. M. Casey *et al.*, “Characterization of SCUBA-2 450 um and 850 um selected galaxies in the COSMOS field,” *Mon. Not. R. Astron. Soc.*, vol. 436, no. 3, pp. 1919–1954, Oct. 2013.
- [118] U. U. Graf, C. E. Honingh, K. Jacobs, and J. Stutzki, “Terahertz heterodyne array receivers for astronomy,” *J. Infrared Millim. Terahertz Waves*, vol. 36, no. 10, pp. 896–921, Oct. 2015.
- [119] P. F. Goldsmith and M. Seiffert, “A flexible quasioptical input system for a submillimeter multiobject spectrometer,” *Publ. Astron. Soc. Pac.*, vol. 121, no. 881, pp. 735–742, Jun. 2009.

- [120] K. Basu *et al.*, “‘SZ spectroscopy’ in the coming decade: Galaxy cluster cosmology and astrophysics in the submillimeter,” *Bull. Am. Astron. Soc.*, vol. 51, no. 3, May 2019.
- [121] J. Delabrouille *et al.*, “Exploring cosmic origins with CORE: Survey requirements and mission design,” *J. Cosmol. Astropart. Phys.*, vol. 2018, no. 04, pp. 014–014, Apr. 2018.
- [122] J. Zmuidzinas *et al.*, “Coherent Detection and SIS Mixers,” in *Proc. Far-IR, Sub-mm & mm Detect. Technol. Workshop*, Jan. 2002, p. 68.
- [123] A. Endo, “Superconducting on-chip spectrometry for millimeter-submillimeter wave astronomy,” *IEICE Trans. Electron.*, vol. E98.C, no. 3, pp. 219–226, Mar. 2015.
- [124] A. Kovács *et al.*, “SuperSpec: Design concept and circuit simulations,” in *Proc. SPIE, Millimeter, Submillimeter, and Far-Infrared Detectors and Instrumentation for Astronomy VI*, J. Z. Wayne S. Holland, Ed., vol. 8452, Int. Soc. Opt. Photon. SPIE, Jul. 2012, pp. 748–757.
- [125] G. Che, “Advancements in kinetic inductance detector, spectrometer, and amplifier technologies for millimeter-wave astronomy,” Ph.D. dissertation, Arizona State University, 2018.
- [126] S. Hähnle *et al.*, “Suppression of radiation loss in high kinetic inductance superconducting co-planar waveguides,” *Appl. Phys. Lett.*, vol. 116, no. 18, p. 182601, May 2020.
- [127] A. Endo *et al.*, “Design of an integrated filterbank for DESHIMA: On-chip submillimeter imaging spectrograph based on superconducting resonators,” *J. Low Temp. Phys.*, vol. 167, no. 3, pp. 341–346, Jan. 2012.
- [128] E. Shirokoff *et al.*, “MKID development for SuperSpec: an on-chip, mm-wave, filter-bank spectrometer,” in *Proc. SPIE, Millimeter, Submillimeter, and Far-Infrared Detectors and Instrumentation for Astronomy VI*, J. Z. Wayne S. Holland, Ed., vol. 8452, Int. Soc. Opt. Photon. SPIE, Jul. 2012, pp. 209–219.
- [129] C. J. Galbraith, R. D. White, L. Cheng, K. Grosh, and G. M. Rebeiz, “Cochlea-based RF channelizing filters,” *IEEE Trans. Circuits Syst. I*, vol. 55, no. 4, pp. 969–979, May 2008.
- [130] G. L. Matthaei, L. Young, and E. M. T. Jones, *Microwave Filters, Impedance-matching Networks, and Coupling Structures*, ser. Artech House Microwave Library. Norwood, MA: Artech House Books, 1980, ch. 16, p. 973.

- [131] A. Endo *et al.*, “On-chip filter bank spectroscopy at 600–700 GHz using NbTiN superconducting resonators,” *Appl. Phys. Lett.*, vol. 103, no. 3, p. 032601, Jul. 2013.
- [132] D. A. Frickey, “Conversions between S, Z, Y, H, ABCD, and T parameters which are valid for complex source and load impedances,” *IEEE Trans. Microw. Theory Tech.*, vol. 42, no. 2, pp. 205–211, Feb. 1994.
- [133] A. Endo *et al.*, “Superconducting coplanar waveguide filters for submillimeter wave on-chip filterbank spectrometers,” *J. Low Temp. Phys.*, vol. 184, no. 1, pp. 412–417, Jul. 2016.
- [134] M. Naruse *et al.*, “Superconducting submicron-CPW resonators for on-chip THz filterbank,” in *Proc. 31st Int. Symp. Superconductivity (ISS 2018)*, Tsukuba, Japan, Dec. 2018.
- [135] GRASP, Ticra tools 20.1. Ticra. [Online]. Available: <https://www.ticra.com/software/grasp/>
- [136] A. Neto and S. Maci, “Green’s function for an infinite slot printed between two homogeneous dielectrics—Part I: Magnetic currents,” *IEEE Trans. Antennas Propag.*, vol. 51, no. 7, pp. 1572–1581, Jul. 2003.
- [137] L. Ferrari *et al.*, “Antenna coupled mkid performance verification at 850 GHz for large format astrophysics arrays,” *IEEE Trans. Terahertz Sci. Technol.*, vol. 8, no. 1, pp. 127–139, Jan. 2018.
- [138] Z. Chen *et al.*, “Fabrication and characterization of aluminum airbridges for superconducting microwave circuits,” *Appl. Phys. Lett.*, vol. 104, no. 5, p. 052602, Feb. 2014.
- [139] O. Yurduseven, J. Bueno, S. Yates, A. Neto, J. Baselmans, and N. Llombart, “Incoherent detection of orthogonal polarizations via an antenna coupled mkid: Experimental validation at 1.55 thz,” *IEEE Trans. Terahertz Sci. Technol.*, vol. 8, no. 6, pp. 736–745, Nov. 2018.
- [140] S. J. C. Yates *et al.*, “Photon noise limited radiation detection with lens-antenna coupled microwave kinetic inductance detectors,” *Appl. Phys. Lett.*, vol. 99, no. 7, p. 073505, Aug. 2011.
- [141] ———, “Clean beam patterns with low crosstalk using 850 GHz microwave kinetic inductance detectors,” *J. Low Temp. Phys.*, vol. 176, no. 5, pp. 761–766, Sep. 2014.

- [142] L. Ferrari *et al.*, “Kinetic inductance detectors (KIDs) for the SAFARI instrument on SPICA,” in *Proc. Space Telescopes and Instrumentation 2010: Optical, Infrared, and Millimeter Wave*, J. M. O. Jr., M. C. Clampin, and H. A. MacEwen, Eds., vol. 7731, Int. Soc. Optics Photon. SPIE, Aug. 2010, pp. 1551–1559.
- [143] “Electric characterization LTC 9300/9500 series,” Fujifilm Electronic Materials, Tech. Rep., 2017.
- [144] A. Endo *et al.*, “Simulating the radiation loss of superconducting submillimeter wave filters and transmission lines using Sonnet EM,” in *Proc. SPIE, Millimeter, Submillimeter, and Far-Infrared Detectors and Instrumentation for Astronomy X*, J. Zmuidzinas and J.-R. Gao, Eds., vol. 11453, Int. Soc. Optics Photon. SPIE, 2020, pp. 436–447.
- [145] S. van Berkel, A. Garufo, N. Llombart Juan, and A. Neto, “A quasi-analytical tool for the characterization of transmission lines at high frequencies [EM programmer’s notebook],” *IEEE Antennas Propag. Mag.*, vol. 58, no. 3, pp. 82–90, Jun. 2016.
- [146] J. Gao, J. Zmuidzinas, B. Mazin, P. Day, and H. Leduc, “Experimental study of the kinetic inductance fraction of superconducting coplanar waveguide,” *Nucl. Instrum. Methods Phys. Res. A*, vol. 559, no. 2, pp. 585–587, Apr. 2006, proc. 11th Int. Workshop on Low Temp. Detectors.
- [147] A. Megrant *et al.*, “Planar superconducting resonators with internal quality factors above one million,” *App. Phys. Lett.*, vol. 100, no. 11, p. 113510, 2012.
- [148] R. Barends *et al.*, “Minimal resonator loss for circuit quantum electrodynamics,” *Appl. Phys. Lett.*, vol. 97, no. 2, p. 023508, 2010.
- [149] B. T. Buijtendorp *et al.*, “Characterization of low-loss hydrogenated amorphous silicon films for superconducting resonators,” in *Proc. SPIE, Millimeter, Submillimeter, and Far-Infrared Detectors and Instrumentation for Astronomy X*, J. Zmuidzinas and J.-R. Gao, Eds., vol. 11453, Int. Soc. Opt. Photon. SPIE, Dec. 2020, pp. 459–472.
- [150] M. Spirito, G. Gentile, and A. Akhnoukh, “Multimode analysis of transmission lines and substrates for (sub)mm-wave calibration,” in *Proc. 82nd ARFTG Microw. Meas. Conf.*, Nov. 2013, pp. 1–6.
- [151] A. D. O’Connell *et al.*, “Microwave dielectric loss at single photon energies and millikelvin temperatures,” *App. Phys. Lett.*, vol. 92, no. 11, p. 112903, Mar. 2008.

- [152] S. Hailey-Dunsheath *et al.*, “Optical measurements of SuperSpec: a millimeter-wave on-chip spectrometer,” *J. Low Temp. Phys.*, vol. 176, no. 5, pp. 841–847, Sep. 2014.
- [153] S. Hähnle *et al.*, “Superconducting microstrip losses at microwave and submillimeter wavelengths,” *Phys. Rev. Applied*, vol. 16, p. 014019, Jul. 2021.
- [154] L.-H. Hsieh and K. Chang, “Simple analysis of the frequency modes for microstrip ring resonators of any general shape and correction of an error in the literature,” *Microw. Opt. Technol. Lett.*, vol. 38, no. 3, pp. 209–213, Jun. 2003.
- [155] Matlab (R2020b). The Mathworks, Inc. [Online]. Available: <https://www.mathworks.com/products/matlab.html>
- [156] D. J. Thoen, V. Murugesan, K. Karatsu, A. Pascual Laguna, A. Endo, and J. J. A. Baselmans, “Combining UV-and electron-beam lithography for superconducting bandpass filters in mm/sub-mm astronomy,” in *Proc. SPIE, Millimeter, Submillimeter, and Far-Infrared Detectors and Instrumentation for Astronomy X*, J. Zmuidzinas and J.-R. Gao, Eds., vol. 11453, Int. Soc. Opt. Photon. SPIE, Dec. 2020.
- [157] D. J. Thoen, B. G. C. Bos, E. A. F. Haalebos, T. M. Klapwijk, J. J. A. Baselmans, and A. Endo, “Superconducting NbTiN thin films with highly uniform properties over a \varnothing 100 mm wafer,” *IEEE Trans. Appl. Supercond.*, vol. 27, no. 4, pp. 1–5, Jun. 2017.
- [158] S. J. C. Yates *et al.*, “Surface wave control for large arrays of microwave kinetic inductance detectors,” *IEEE Trans. Terahertz Sci. Technol.*, vol. 7, no. 6, pp. 789–799, Nov. 2017.
- [159] S. Hähnle, J. Bueno, R. Huiting, S. J. C. Yates, and J. J. A. Baselmans, “Large angle optical access in a sub-kelvin cryostat,” *J. Low Temp. Phys.*, vol. 193, no. 5, pp. 833–840, Dec. 2018.
- [160] T. Guruswamy, D. J. Goldie, and S. Withington, “Quasiparticle generation efficiency in superconducting thin films,” *Supercond. Sci. Technol.*, vol. 27, no. 5, p. 055012, Mar. 2014.
- [161] O. Noroozian, P. K. Day, B. H. Eom, H. G. Leduc, and J. Zmuidzinas, “Crosstalk reduction for superconducting microwave resonator arrays,” *IEEE Trans. Microw. Theory Tech.*, vol. 60, no. 5, pp. 1235–1243, May 2012.
- [162] A. Pascual Laguna, D. Cavallo, J. J. A. Baselmans, and N. Llombart, “Focused connected array antenna as a broadband beam-steering feed for quasi-optical systems,” *IEEE Trans. Antennas Propag.*, accepted for publication.

- [163] C. A. Fernandes, E. B. Lima, and J. R. Costa, "Broadband integrated lens for illuminating reflector antenna with constant aperture efficiency," *IEEE Trans. Antennas Propag.*, vol. 58, no. 12, pp. 3805–3813, Dec. 2010.
- [164] O. Yurduseven, D. Cavallo, and A. Neto, "Wideband dielectric lens antenna with stable radiation patterns fed by coherent array of connected leaky slots," *IEEE Trans. Antennas Propag.*, vol. 62, no. 4, pp. 1895–1902, Apr. 2014.
- [165] J. M. Edwards, R. O'Brient, A. T. Lee, and G. M. Rebeiz, "Dual-polarized sinusoidal antennas on extended hemispherical silicon lenses," *IEEE Trans. Antennas Propag.*, vol. 60, no. 9, pp. 4082–4091, Sep. 2012.
- [166] S. Bruni, A. Neto, and F. Marliani, "The ultrawideband leaky lens antenna," *IEEE Trans. Antennas Propag.*, vol. 55, no. 10, pp. 2642–2653, Oct. 2007.
- [167] R. Olsson, P. S. Kildal, and S. Weinreb, "The Eleven antenna: A compact low-profile decade bandwidth dual polarized feed for reflector antennas," *IEEE Trans. Antennas Propag.*, vol. 54, no. 2, pp. 368–375, Feb. 2006.
- [168] G. Cortes-Medellin, "Non-planar quasi-self-complementary ultra-wideband feed antenna," *IEEE Trans. Antennas Propag.*, vol. 59, no. 6, pp. 1935–1944, Jun. 2011.
- [169] A. Akgiray, S. Weinreb, W. A. Imbriale, and C. Beaudoin, "Circular quadrupledridged flared horn achieving near-constant beamwidth over multi octave bandwidth: Design and measurements," *IEEE Trans. Antennas Propag.*, vol. 61, no. 3, pp. 1099–1108, Mar. 2013.
- [170] C. Granet, A. Dunning, M. Bowen, D. B. Hayman, J. Stevens, and K. W. Smart, "A wide-band 4–12.25 GHz feed system for the Australia Telescope 22m-diameter antenna," in *Proc. 2019 Int. Conf. Electromagn. Adv. Appl. (ICEAA)*, 2019, pp. 0600–0605.
- [171] C. Granet and J. S. Kot, "A 3.5–12.3 GHz bullet-horn feed concept," in *Proc. 15th Eur. Conf. Antennas Propag. (EuCAP)*, 2021.
- [172] Z. Ying, A. A. Kishk, and P.-S. Kildal, "Broadband compact horn feed for prime-focus reflectors," *Electron. Lett.*, vol. 31, pp. 1114–1115(1), Jul. 1995.
- [173] M. Abbas-Azimi, F. Mazlumi, and F. Behnia, "Design of broadband constant-beamwidth conical corrugated-horn antennas [Antenna Designer's Notebook]," *IEEE Antennas Propag. Mag.*, vol. 51, no. 5, pp. 109–114, Oct. 2009.
- [174] A. Gonzalez, K. Kaneko, and S. Asayama, "Recent work on (sub-)mm-wave ultra wideband corrugated horns for radio astronomy," in *Proc. 11th Eur. Conf. Antennas Propag. (EuCAP)*, 2017, pp. 3327–3331.

- [175] B. Lee, A. Gonzalez, K. Kaneko, R. Sakai, and J.-W. Lee, “Design and characterization of 275–500 GHz corrugated horns and optics for a wideband radio astronomy receiver,” in *Proc. 14th Eur. Conf. Antennas Propag. (EuCAP)*, 2020.
- [176] S. O. Dabironezare, G. Carluccio, A. Pascual Laguna, S. Hähnle, J. J. A. Baselmans, and N. Llombart, “Quasi-optical system for the ASTE telescope with 1:3 bandwidth at sub-mm wave,” in *Proc. 44th International Conference on Infrared, Millimeter, and Terahertz Waves (IRMMW-THz)*, Paris, France, Sep. 2019.
- [177] S. O. Dabironezare *et al.*, “Wide band quasi-optical system for DESHIMA 2.0 spectrometer: Beam pattern experimental validation,” in *Proc. 45th Int. Conf. Infrared, Millimeter, and Terahertz Waves (IRMMW-THz)*, Nov. 2020.
- [178] R. Datta *et al.*, “Large-aperture wide-bandwidth antireflection-coated silicon lenses for millimeter wavelengths,” *Appl. Opt.*, vol. 52, no. 36, pp. 8747–8758, Dec. 2013.
- [179] T. Matsumura *et al.*, “Millimeter-wave broadband antireflection coatings using laser ablation of subwavelength structures,” *Appl. Opt.*, vol. 55, no. 13, pp. 3502–3509, May 2016.
- [180] D. Rosen *et al.*, “Epoxy-based broadband antireflection coating for millimeter-wave optics,” *Appl. Opt.*, vol. 52, no. 33, pp. 8102–8105, Nov. 2013.
- [181] A. Nadolski *et al.*, “Broadband, millimeter-wave antireflection coatings for large-format, cryogenic aluminum oxide optics,” *Appl. Opt.*, vol. 59, no. 10, pp. 3285–3295, Apr. 2020.
- [182] A. Suzuki *et al.*, “Multi-chroic dual-polarization bolometric detectors for studies of the cosmic microwave background,” *J. Low Temp. Phys.*, vol. 176, no. 5, pp. 650–656, Sep. 2014.
- [183] A. Goldin *et al.*, “Design of broadband filters and antennas for SAMBA,” in *Proc. SPIE, Millimeter and Submillimeter Detectors for Astronomy*, T. G. Phillips and J. Zmuidzinas, Eds., vol. 4855, Int. Soc. Opt. Photon. SPIE, Feb. 2003, pp. 163–171.
- [184] P. K. Day *et al.*, “Antenna-coupled microwave kinetic inductance detectors,” *Nucl. Instrum. Methods Phys. Res. A*, vol. 559, no. 2, pp. 561–563, Apr. 2006.
- [185] J. Sayers *et al.*, “The status of MUSIC: the multiwavelength sub-millimeter inductance camera,” in *Proc. SPIE, Millimeter, Submillimeter, and Far-Infrared Detectors and Instrumentation for Astronomy VII*, W. S. Holland and J. Zmuidzinas, Eds., vol. 9153, Int. Soc. Opt. Photon. SPIE, 2014, pp. 57–74.

- [186] R. C. Hansen, *Phased Array Antennas*. John Wiley & Sons, Ltd, 2009, ch. 14, pp. 503–510.
- [187] W. D. Fitzgerald, “Limited electronic scanning with a near-field cassegrainian system,” Lincoln Lab., Massachusetts Institute of Technology, Tech. Rep., 1971.
- [188] C. Wilson, “Electronically steerable field reflector techniques,” in *1965 Antennas Propag. Soc. Int. Symp.*, vol. 3, 1965, pp. 211–216.
- [189] S. Anlage, H. Snortland, and M. Beasley, “A current controlled variable delay superconducting transmission line,” *IEEE Trans. Magn.*, vol. 25, no. 2, pp. 1388–1391, Mar. 1989.
- [190] G. Bordier *et al.*, “Superconducting coplanar switch and phase shifter for CMB applications,” *J. Low Temp. Phys.*, vol. 184, no. 3, pp. 547–552, Aug. 2016.
- [191] G. Che *et al.* (2017) A superconducting phase shifter and traveling wave kinetic inductance parametric amplifier for W-band astronomy.
- [192] B. Ho Eom, P. K. Day, H. G. LeDuc, and J. Zmuidzinas, “A wideband, low-noise superconducting amplifier with high dynamic range,” *Nat. Phys.*, vol. 8, no. 8, pp. 623–627, Aug. 2012.
- [193] J. Bueno *et al.*, “Full characterisation of a background limited antenna coupled KID over an octave of bandwidth for THz radiation,” *Appl. Phys. Lett.*, vol. 110, no. 23, pp. 233 503:–233 503:5, Jun. 2017.
- [194] J. W. Sherman, III, “Properties of focused apertures in the Fresnel region,” *IRE Trans. Antennas Propag.*, vol. 10, no. 4, pp. 399–408, Jul. 1962.
- [195] J. Musil, “Properties of antennas focused in the Fresnel zone,” *Czech. J. Phys. B*, vol. 17, no. 10, pp. 874–888, Oct. 1967.
- [196] R. C. Hansen, “Focal region characteristics of focused array antennas,” *IEEE Trans. Antennas Propag.*, vol. 33, no. 12, pp. 1328–1337, Dec. 1985.
- [197] Y. Li and E. Wolf, “Focal shifts in diffracted converging spherical waves,” *Opt. Commun.*, vol. 39, no. 4, pp. 211–215, Oct. 1981.
- [198] A. Ludwig, “The definition of cross polarization,” *IEEE Trans. Antennas Propag.*, vol. 21, no. 1, pp. 116–119, Jan. 1973.
- [199] J. Ruze, “Lateral-feed displacement in a paraboloid,” *IEEE Trans. Antennas Propag.*, vol. 13, no. 5, pp. 660–665, Sep. 1965.

- [200] N. Llombart, S. O. Dabironezare, G. Carluccio, A. Freni, and A. Neto, “Reception power pattern of distributed absorbers in focal plane arrays: A Fourier optics analysis,” *IEEE Trans. Antennas Propag.*, vol. 66, no. 11, pp. 5990–6002, Nov. 2018.
- [201] W. J. Smith, in *Handbook of Optics*, 3rd ed., ser. Handbook of Optics, M. Bass *et al.*, Eds. McGraw-Hill Education, 2009, vol. 2, ch. 1, pp. 1.8–1.10.
- [202] D. Cavallo and A. Neto, “A connected array of slots supporting broadband leaky waves,” *IEEE Trans. Antennas Propag.*, vol. 61, no. 4, pp. 1986–1994, Apr. 2013.
- [203] D. Cavallo, W. H. Syed, and A. Neto, “A 5:1 connected slot array loaded with artificial dielectric layers,” in *Proc. IEEE Int. Symp. Phased Array Syst. Technol. (PAST)*, Waltham, MA, US, Oct. 2016, pp. 1–4.
- [204] HFSS, Ansys Electronics Desktop 2019 R3.7. Ansys Inc. [Online]. Available: <https://www.ansys.com/products/electronics/ansys-hfss>
- [205] D. Paris, W. Leach, and E. Joy, “Basic theory of probe-compensated near-field measurements,” *IEEE Trans. Antennas Propag.*, vol. 26, no. 3, pp. 373–379, May 1978.
- [206] E. Gandini, A. Tamminen, A. Luukanen, and N. Llombart, “Wide field of view inversely magnified dual-lens for near-field submillimeter wavelength imagers,” *IEEE Trans. Antennas Propag.*, vol. 66, no. 2, pp. 541–549, Feb. 2018.
- [207] N. Beschoor Plug, “Towards on-chip superconducting phase shifters,” Master’s thesis, Delft University of Technology, 2021.
- [208] D. A. Gandolfo, A. Boornard, and L. C. Morris, “Superconductive microwave meander lines,” *J. Appl. Phys.*, vol. 39, no. 6, pp. 2657–2660, 1968.
- [209] J. Pond, J. Claassen, and W. Carter, “Measurements and modeling of kinetic inductance microstrip delay lines,” *IEEE Trans. Microw. Theory Techn.*, vol. 35, no. 12, pp. 1256–1262, Dec. 1987.
- [210] H. T. Su, Y. Wang, F. Huang, and M. J. Lancaster, “Superconducting delay lines,” *J. Supercond. Nov. Magn.*, vol. 21, no. 1, pp. 7–16, Jan. 2008.
- [211] A. Semenov, I. Devyatov, M. Westig, and T. Klapwijk, “Effect of microwaves on superconductors for kinetic inductance detection and parametric amplification,” *Phys. Rev. Applied*, vol. 13, p. 024079, Feb. 2020.
- [212] J. Zmuidzinas, “Superconducting microresonators: Physics and applications,” *Annu. Rev. Condens. Matter Phys.*, vol. 3, no. 1, pp. 169–214, 2012.

- [213] C. Bockstiegel *et al.*, “Development of a broadband NbTiN traveling wave parametric amplifier for MKID readout,” *J. Low Temp. Phys.*, vol. 176, no. 3, pp. 476–482, Aug. 2014.
- [214] S. Chaudhuri, J. Gao, and K. Irwin, “Simulation and analysis of superconducting traveling-wave parametric amplifiers,” *IEEE Trans. Appl. Supercond.*, vol. 25, no. 3, pp. 1–5, Jun. 2015.
- [215] W. Shan, Y. Sekimoto, and T. Noguchi, “Parametric amplification in a superconducting microstrip transmission line,” *IEEE Trans. Appl. Supercond.*, vol. 26, no. 6, pp. 1–9, Sep. 2016.
- [216] S. Shu *et al.*, “Nonlinearity and wide-band parametric amplification in a (nb,ti)n microstrip transmission line,” *Phys. Rev. Research*, vol. 3, p. 023184, Jun. 2021.
- [217] J. Luomahaara, V. Vesterinen, L. Grönberg, and J. Hassel, “Kinetic inductance magnetometer,” *Nat. Commun.*, vol. 5, no. 1, p. 4872, Sep. 2014.
- [218] A. Kher, P. K. Day, B. H. Eom, J. Zmuidzinas, and H. G. Leduc, “Kinetic inductance parametric up-converter,” *J. Low Temp. Phys.*, vol. 184, no. 1, pp. 480–485, Jul. 2016.
- [219] M. R. Vissers, J. Hubmayr, M. Sandberg, S. Chaudhuri, C. Bockstiegel, and J. Gao, “Frequency-tunable superconducting resonators via nonlinear kinetic inductance,” *Appl. Phys. Lett.*, vol. 107, no. 6, p. 062601, 2015.
- [220] A. A. Adamyan, S. E. Kubatkin, and A. V. Danilov, “Tunable superconducting microstrip resonators,” *Appl. Phys. Lett.*, vol. 108, no. 17, p. 172601, 2016.
- [221] H. Kurokawa, F. Nabeshima, and A. Maeda, “Current and magnetic field dependences of a superconducting coplanar waveguide resonator,” *Jpn. J. Appl. Phys.*, vol. 58, no. 3, p. 033001, Feb. 2019.
- [222] S. Zhao, S. Withington, D. J. Goldie, and C. N. Thomas, “Nonlinear properties of supercurrent-carrying single- and multi-layer thin-film superconductors,” *J. Low Temp. Phys.*, vol. 199, no. 1, pp. 34–44, Apr. 2020.
- [223] R. Basu Thakur *et al.*, “Superconducting on-chip Fourier transform spectrometer,” *J. Low Temp. Phys.*, vol. 200, no. 5, pp. 342–352, Sep. 2020.
- [224] F. B. Faramarzi *et al.*, “An on-chip superconducting kinetic inductance Fourier transform spectrometer for millimeter-wave astronomy,” *J. Low Temp. Phys.*, vol. 199, no. 3, pp. 867–874, May 2020.
- [225] G. N. Gol’tsman *et al.*, “Picosecond superconducting single-photon optical detector,” *Appl. Phys. Lett.*, vol. 79, no. 6, pp. 705–707, 2001.

- [226] B. T. Buijtendorp *et al.*, “Hydrogenated amorphous silicon carbide: A low-loss deposited dielectric for microwave to submillimeter wave superconducting circuits,” 2021.
- [227] K. K. Davis *et al.*, “Complex field mapping of large direct detector focal plane arrays,” *IEEE Trans. Terahertz Sci. Technol.*, vol. 9, no. 1, pp. 67–77, Jan. 2019.
- [228] K. Kouwenhoven, “Dielectric loss measurements at sub-K temperatures and terahertz frequencies,” Master’s thesis, Delft University of Technology, 2018.
- [229] J.-S. Hong, *Microstrip Filters for RF/Microwave Applications*, 2nd ed. Wiley, 2011.
- [230] G. L. Matthaei, L. Young, and E. M. T. Jones, *Microwave Filters, Impedance-matching Networks, and Coupling Structures*, ser. Artech House Microwave Library. Norwood, MA: Artech House Books, 1980, ch. 4, p. 99.
- [231] J. W. Kooi *et al.*, “Quantum limited sis receiver technology for the detection of water isotopologue emission from comets,” *IEEE Trans. Terahertz Sci. Technol.*, vol. 10, no. 6, pp. 569–582, Nov. 2020.
- [232] A. S. Kher, “Superconducting nonlinear kinetic inductance devices,” Ph.D. dissertation, California Institute of Technology, 2017.
- [233] H. L. Hortensius, E. F. C. Driesssen, T. M. Klapwijk, K. K. Berggren, and J. R. Clem, “Critical-current reduction in thin superconducting wires due to current crowding,” *App. Phys. Lett.*, vol. 100, no. 18, p. 182602, 2012.
- [234] S. O. Dabironezare, “Fourier optics field representation for the design of wide field-of-view imagers at sub-millimetre wavelengths,” Ph.D. dissertation, Delft University of Technology, 2020.
- [235] S. Hähnle *et al.*, “An ultrawideband leaky lens antenna for broadband spectroscopic imaging applications,” *IEEE Trans. Antennas Propag.*, vol. 68, no. 7, pp. 5675–5679, Jul. 2020.

Summary

The mysteries of the early Universe are largely enshrouded in dust, product of the violent process of star formation. Due to the vast distances of our Universe, infrared light emitted by the heated dust back in those early stages can still be observed today, which has been observed to contribute to about half of the total cosmic background radiation. Gases fueling star-formation also radiate, but in the form of emission lines, which leave distinct spectral signatures that allow the study of the underlying physical processes. Given the expansion of the Universe, the evolutionary information is encoded in the cosmological redshift observed, making the far-infrared or terahertz (THz) regime specially suited for probing star-formation. Superconducting on-chip broadband THz imaging spectrometers with moderate spectral resolution coupled to large telescopes will allow the investigation the early Universe processes over large cosmological volumes. In this dissertation we propose two enabling technologies toward the advancement of this on-chip superconducting instruments: a broadband and moderate spectral resolution channelizing filter-bank, and a broadband phased array antenna as a reflector feed with beam-steering capabilities.

Octave-band THz channelizing filter-banks with moderate spectral resolution of the order $R = 500$ are investigated in this work. These systems allow for a size reduction of several orders of magnitude compared to conventional spectrometers with similar spectral resolution. The proposed filters are half-wavelength resonators, which naturally provide a free-spectral range of an octave. The performance of those filters, both when in isolation and when embedded in a filter-bank, is analyzed using a newly-developed circuit model. This tool also provides design insights such as the required filter ordering and separation within the filter-bank to enable an efficient circuit. The actual implementation of the superconducting filter-bank on a chip is investigated for two of the main on-chip technologies: co-planar waveguide (CPW) and microstrip. Despite the easier manufacturing of co-planar circuitry, that technology is not suited for channelizing THz filter-banks as it suffers from radiation issues. Instead microstrip technology is non-radiative and, although it suffers from the moderate dissipation in deposited dielectrics such as a-Si, it provides a very reliable platform to build THz filter-banks. Half-wavelength I-shaped resonators are proposed as suit-

able filtering structures with which frequency-sparse filter-banks have been built to test their performance in semi-isolation. The measurements were based on both a frequency response characterization of the filters as well as their optical efficiency, showing good agreement between the two. The measured performance of these filters showed pass-bands with an average peak coupling efficiency of 27% and a spectral resolution $R \approx 940$. The coupling is significantly better than earlier results based upon planar technology.

The coupling between the quasi-optical reflector system of a telescope and the on-chip filter-bank requires of a broadband antenna. Currently, broadband integrated anti-reflection-coated lenses are being developed for this purpose, but their manufacturing is specially complicated for cryogenics and require mechanical actuators to perform beam scanning in the case of a multi-object spectrometer. In this dissertation, we propose a broadband phased-array antenna concept with electronic beam-steering that exploits two key properties of superconductors in its feeding network: the negligible conductor loss and the tunable kinetic inductance with a bias current. The focused connected array antenna concept proposed is based on the broadband impedance matching enabled by the connected arrays and the largely frequency-independent far fields of near-field focused apertures. To demonstrate this concept we designed, fabricated and tested two low frequency (3–6 GHz) prototypes in PCB technology: one pointing broadside and another one scanning. The measured fields met the predictions to a large degree and provided with a reflector aperture efficiency in excess of 60% over an octave of bandwidth and allowing to scan one half-power beamwidth at the lowest frequency with a frequency-averaged scan loss of 0.2 dB. Both the directivity and the gain were measured, allowing to report the losses, which chiefly originated from the tin-finished copper lines in the PCB. As a result, we can expect a highly-efficient reflector feed at THz frequencies with beam-steering capabilities in the near future.

The beam-steering concept proposed for the phased-array antenna relies on the current-dependent kinetic inductance of superconducting lines. With this effect, the phase velocity of biased superconducting lines may be modified, allowing thereby an electronic tuning of the phase-shift introduced. Prior to the integration of such phase-shifters with the phased-array antenna, we devised an on-chip platform based a tunable Fabry-Pérot resonator to quantify the phase-shifting capabilities at THz frequencies. In this concept, the dc bias currents are injected in the proximity of the edges of the resonator through 9th order Chebyshev stepped-impedance low-pass filters, whose high rejection mitigates any possible disturbance to the THz resonances. Using a circuit model including the resonator and the low-pass filters, as well as the simulated properties of the superconducting buried microstrip lines used in the designs, we anticipate an expected maximum tuning of $d\phi/\phi = -df/f \approx 2\%$. With such tuning range millimeter-long tunable delay lines will be required for THz superconducting phased-array.

Samenvatting

De mysteries van het vroege heelal zijn grotendeels omhuld door stof dat is ontstaan bij het geweldig heftige geboorteproces van sterren. Door de uitgestrektheid van ons heelal, kan het infrarode licht dat het verhitte stof uitzond in die vroege stadia van-dag de dag nog worden geobserveerd. Dit infrarode licht is ongeveer de helft van al de kosmische achtergrond straling. De gassen die de geboorte van een ster voeden, zenden ook licht uit, maar met specifieke spectrale kenmerken, emissielijnen, waaruit de onderliggende fysieke processen kunnen worden afgeleid. Door het uitdijken van het heelal, is de evolutionaire informatie gecodeerd in the kosmologische roodverschuiving. Dat maakt het ver-infrarode, of terahertz (THz), regime bijzonder geschikt voor het bestuderen van de geboorte van sterren. Supergeleidende, *on-chip*, breedbandige, THz, beeldvormende spectrometers met middelmatige resolutie en gekoppeld aan grote telescopen, zullen het mogelijk maken om de processen in het vroege heelal te onderzoeken over grote kosmologische volumes. In dit proefschrift worden twee technologieën voorgesteld die de ontwikkeling van deze on-chip supergeleidende instrumenten bevorderen: een breedbandige en kanaliserende filterbank met middelmatige resolutie, en een breedbandige *phased array* antenne die gebruikt kan worden als een bundelsturende invoer-reflector.

In dit werk worden THz kanaliserende filterbanken behandeld die een octaaf beslaan en een middelmatige resolutie hebben van $R = 500$. Deze instrumenten zijn meerder orders van grootte kleiner dan conventionele spectrometers met een vergelijkbare resolutie. De filters zijn *half-wavelength* resonatoren, die op een natuurlijke wijze voor een vrij spectraal bereik van een octaaf zorgen. De prestaties van de filters, zowel geïsoleerd als in een filterbank, worden bestudeerd met behulp van een nieuw ontwikkeld circuitmodel. Dit model verschaft ook ontwerpinzichten voor een efficiënt circuit, zoals de vereiste filterordening en onderlinge afstand binnen de filterbank. Voor de realisatie van de supergeleidende on-chip filterbank worden twee van de belangrijkste technologieën bestudeerd: de *co-planar waveguide* (CPW) en de *microstrip*. Ondanks de eenvoudigere fabricage van CPW circuits, is die technologie niet geschikt voor het kanaliseren van THz-filterbanken, omdat hierbij de stralingsverliezen groot zijn. Microstrip technologie heeft dit probleem niet en hoewel er wel

enige dissipatie plaatsvindt in het gedeponeerde diëlectricum zoals a-Si, biedt deze technologie een betrouwbaar platform voor de fabricage van THz filterbanken. I-vormige resonatoren van een halve golflengte zijn geschikte filterstructuren. Om de prestaties van deze resonatoren semi-geïsoleerd te testen, zijn filterbanken met ver uit elkaar liggende frequenties geproduceerd. Zowel de frequentie response als de optische efficiëntie zijn gemeten, wat een goede overeenkomst tussen de twee liet zien. Er is een doorlaatbandbreedte met een gemiddelde piek koppeling efficiëntie van 27% en een spectrale resolutie van $R \approx 940$ gemeten. De koppeling is significant beter dan eerdere resultaten met CPW circuits.

Er is een breedbandige antenne nodig voor het koppelen van de quasi-optische reflector van een telescoop en de on-chip filterbank. Hiervoor worden er momenteel breedbandige, geïntegreerde lenzen met anti-reflectie coating ontwikkeld. Echter is de fabricage van deze lenzen voor cryogene toepassingen erg gecompliceerd en voor een spectrometer voor meerdere objecten zijn mechanische actuatoren nodig om de bundel te sturen. In dit proefschrift wordt een breedbandige phased-array antenne concept met elektronische bundelsturing gepresenteerd. Dit concept gebruikt twee belangrijke eigenschappen van de supergeleiders in het voedingsnetwerk: de te verwaarlozen conductor verliezen en de met biasstroom regelbare kinetische inductie. Dit gefocusseerde, verbonden array antenneconcept is gebaseerd op de breedbandige impedantie-aanpassing die mogelijk is door de verbonden arrays en de grotendeels frequentie-onafhankelijke verre velden van gefocusseerde aperture in het nabije veld. Om dit concept te demonstreren, zijn er twee prototypes met een lage frequentie (3-6 GHz) in PCB-technologie ontworpen, gefabriceerd en getest: één naar boven gericht en één die scant. De gemeten velden kwamen goed overeen met de verwachtingen. Er werd een reflector-apertuur efficiëntie van meer dan 60% gehaald, over een bandbreedte van een octaaf. Het scannen van één half vermogen bundelbreedte op de laagste frequentie, zorgde voor een frequentiegemiddeld scanverlies van niet meer dan 0.46 dB. Zowel de gerichtheid als de versterking zijn gemeten, waardoor de verliezen berekend konden worden. Die waren voornamelijk afkomstig van de vertinde koperen lijnen in de PCB. We kunnen daarom op korte termijn een zeer efficiënte, bundelsturende invoer-reflector verwachten op THz frequenties.

Het bundelsturende concept voor phased array antennes is gebaseerd op de stroomafhankelijkheid van de kinetische inductie van supergeleidende transmissielijnen. Hierdoor kan de voortplantingssnelheid in de transmissielijnen worden gewijzigd, waardoor een faseverschuiving elektrisch kan worden geïntroduceerd. Voorafgaand aan de integratie van zulke faseverschuivers met een phased-array antenne, hebben we een on-chip platform ontworpen met Fabry-Pérot resonatoren om de faseverschuiving capaciteiten op THz frequenties te kunnen kwantificeren. In dit ontwerp worden de DC biasstromen geïnjecteerd in de buurt van de randen van de resonator door middel van een negende orde Chebyshev laagdoorlaatfilter met getrapte impedantie. De hoge onderdrukking van deze filters vermindert alle mogelijke verstoringen van de THz

resonanties. Vanuit een circuitmodel, dat zowel de resonatoren als de laagdoorlaatfilters behelst en de supergeleidende eigenschappen van de microstrip transmissielijnen meeneemt, verwachten wij een maximale faseverschuiving van $d\phi/\phi = -df/f \approx 2\%$. Hierdoor zullen er millimeter lange, afstembare vertragingslijnen nodig zijn voor THz supergeleidende *phased-arrays*.

List of Publications

Journal Papers

- J1.** A. Pascual Laguna, D. Cavallo, J. J. A. Baselmans, and N. Llombart, “Focused connected array antenna as a broadband beam-steering feed for quasi-optical systems,” *IEEE Trans. Antennas Propag.*, accepted for publication.
- J2.** A. Pascual Laguna, K. Karatsu, D. J. Thoen, V. Murugesan, A. Endo and J. J. A. Baselmans, “Terahertz band-pass filters for wideband superconducting on-chip filter-bank spectrometers,” *IEEE Trans. Terahertz Sci. Technol.*, vol. 11, no. 6, pp. 635–646, Nov. 2021.
- J3.** T. Takekoshi, K. Karatsu, J. Suzuki, Y. Tamura, T. Oshima, A. Taniguchi, S. Asayama, T. J. L. C. Bakx, J. J. A. Baselmans, S. Bosma, J. Bueno, K. W. Chin, Y. Fujii, K. Fujita, R. Huiting, S. Ikarashi, T. Ishida, S. Ishii, R. Kawabe, T. M. Klapwijk, K. Kohno, A. Kouchi, N. Llombart, J. Maekawa, V. Murugesan, S. Nakatsubo, M. Naruse, K. Ohtawara, A. Pascual Laguna, K. Suzuki, D. J. Thoen, T. Tsukagoshi, T. Ueda, P. J. de Visser, P. P. van der Werf, S. J. C. Yates, Y. Yoshimura, O. Yurduseven and A. Endo, “DESHIMA on ASTE: On-sky responsivity calibration of the integrated superconducting spectrometer,” *J. Low Temp. Phys.*, vol. 199, no. 1, pp. 231–239, Apr. 2020.
- J4.** A. Endo, K. Karatsu, Y. Tamura, T. Oshima, A. Taniguchi, T. Takekoshi, S. Asayama, T. J. L. C. Bakx, S. Bosma, J. Bueno, K. W. Chin, Y. Fujii, K. Fujita, R. Huiting, S. Ikarashi, T. Ishida, S. Ishii, R. Kawabe, T. M. Klapwijk, K. Kohno, A. Kouchi, N. Llombart, J. Maekawa, V. Murugesan, S. Nakatsubo, M. Naruse, K. Ohtawara, A. Pascual Laguna, K. Suzuki, D. J. Thoen, T. Tsukagoshi, T. Ueda, P. J. de Visser, P. P. van der Werf, S. J. C. Yates, Y. Yoshimura, O. Yurduseven and J. J. A. Baselmans, “First light demonstration of the integrated superconducting spectrometer,” *Nat. Astron.*, vol. 3, no. 11, pp. 989–996, Nov. 2019.

- J5.** A. Endo, K. Karatsu, A. Pascual Laguna, B. Mirzaei, R. Huiting, D. J. Thoen, V. Murugesan, S. J. C. Yates, J. Bueno, N. van Marrewijk, S. Bosma, O. Yurduseven, N. Llombart, J. Suzuki, M. Naruse, P. J. de Visser, P. P. van der Werf, T. M. Klapwijk and J. J. A. Baselmans, “Wideband on-chip terahertz spectrometer based on a superconducting filterbank,” *J. Astron. Telesc. Instrum. Syst.*, vol. 5, no. 3, pp. 1–12, Jun. 2019.

Conference Papers

- C1.** A. Taniguchi, K. Karatsu, Y. Tamura, T. Takekoshi, T. J. L. C. Bakx, T. Oshima, J. Bueno, B. Buijtendorp, Y. Fujii, K. Fujita, R. Huiting, T. Ishida, S. Ishii, R. Kawabe, K. Kohno, A. Kouchi, N. Llombart, J. Maekawa, V. Murugesan, S. Nakatsubo, A. Pascual Laguna, D. J. Thoen, P. P. van der Werf, S. J. C. Yates, S. O. Dabironezare, S. Hähnle, J. J. A. Baselmans, M. Gouwerok, M. Rybak, K. Matsuda, S. Brackenhoff, A.-K. Doing, H. Akamatsu, T. Kitayama, A. Endo, “Development of an integrated superconducting spectrometer for science-grade astronomical observations,” in *Proc. 19th Int. Workshop Low Temp. Detectors (LTD)*, Jul. 19–29 2021.
- C2.** A. Pascual Laguna, D. Cavallo, J. J. A. Baselmans and N. Llombart, “Focused connected array as a wideband beam-steering feed for quasi-optical systems,” in *Proc. 15th Eur. Conf. Antennas Propag. (EuCAP 2021)*, Mar. 22–26 2021.
- C3.** A. Pascual Laguna, K. Karatsu, J. Bueno, S. O. Dabironezare, D. J. Thoen, V. Murugesan, A. Endo and J. J. A. Baselmans, “Filter-bank for broadband sub-mm wave superconducting on-chip spectrometers,” in *Proc. SPIE, Millimeter, Submillimeter, and Far-Infrared Detectors and Instrumentation for Astronomy X*, J.,Zmuidzinas and J-R.,Gao, Eds., vol. 11453, Int. Soc. Opt. Photon. SPIE, online forum, Dec. 14–18 2020.
- C4.** A. Endo, A. Pascual Laguna, S. Hähnle, K. Karatsu, D. J. Thoen, V. Murugesan and J. J. A. Baselmans, “Simulating the radiation loss of superconducting submillimeter wave filters and transmission lines using Sonnet EM,” in *Proc. SPIE, Millimeter, Submillimeter, and Far-Infrared Detectors and Instrumentation for Astronomy X*, J.,Zmuidzinas and J-R.,Gao, Eds., vol. 11453, Int. Soc. Opt. Photon. SPIE, online forum, Dec. 14–18 2020.

- C5.** A. Endo, K. Karatsu, Y. Tamura, T. Oshima, A. Taniguchi, T. Takekoshi, S. Asayama, T. J. L. C. Bakx, S. Bosma, J. Bueno, B. T. Buijtendorp, K. W. Chin, Y. Fujii, K. Fujita, E. Huijten, R. Huiting, S. Ikarashi, T. Ishida, S. Ishii, R. Kawabe, T. M. Klapwijk, K. Kohno, A. Kouchi, N. Llombart, J. Maekawa, V. Murugesan, S. Nakatsubo, M. Naruse, K. Ohtawara, A. Pascual Laguna, K. Suzuki, D. J. Thoen, T. Tsukagoshi, T. Ueda, P. J. de Visser, P. P. van der Werf, S. J. C. Yates, Y. Yoshimura, O. Yurduseven, S. O. Dabironezare, S. Hähnle and J. J. A. Baselmans, "DESHIMA on ASTE: On-sky performance and upgrade to ultra wideband," in *Proc. SPIE, Millimeter, Submillimeter, and Far-Infrared Detectors and Instrumentation for Astronomy X*, J.,Zmuidzinas and J-R.,Gao, Eds., vol. 11453, Int. Soc. Opt. Photon. SPIE, online forum, Dec. 14–18 2020.
- C6.** S. O. Dabironezare, K. Karatsu, S. J. C. Yates, A. Pascual Laguna, V. Murugesan, D. J. Thoen, A. Endo, J. J. A. Baselmans and N. Llombart, "Broadband quasi-optical system for on-chip filter-bank spectrometer operating at sub-mm wavelengths," in *Proc. SPIE, Millimeter, Submillimeter, and Far-Infrared Detectors and Instrumentation for Astronomy X*, J.,Zmuidzinas and J-R.,Gao, Eds., vol. 11453, Int. Soc. Opt. Photon. SPIE, online forum, Dec. 14–18 2020.
- C7.** K. Karatsu, Z. Zhang, A. Pascual Laguna, S. O. Dabironezare, A. Endo, D. J. Thoen, V. Murugesan and J. J. A. Baselmans, "Development of absolute frequency calibration system for superconducting integrated spectrometer," in *Proc. SPIE, Millimeter, Submillimeter, and Far-Infrared Detectors and Instrumentation for Astronomy X*, J.,Zmuidzinas and J-R.,Gao, Eds., vol. 11453, Int. Soc. Opt. Photon. SPIE, online forum, Dec. 14–18 2020.
- C8.** D. J. Thoen, V. Murugesan, K. Karatsu, A. Pascual Laguna, A. Endo and J. J. A. Baselmans, "Combining UV-and electron beam lithography for superconducting bandpass filters in mm/sub-mm astronomy," in *Proc. SPIE, Millimeter, Submillimeter, and Far-Infrared Detectors and Instrumentation for Astronomy X*, J.,Zmuidzinas and J-R.,Gao, Eds., vol. 11453, Int. Soc. Opt. Photon. SPIE, online forum, Dec. 14–18 2020.
- C9.** E. Huijten, Y. Roelvink, S. A. Brackenhoff, A. Taniguchi, T. J. L. C. Bakx, K. B. Marthi, S. Zaalberg, J. J. A. Baselmans, K. W. Chin, R. Huiting, K. Karatsu, A. Pascual Laguna, Y. Tamura, T. Takekoshi, S. J. C. Yates, M. van Hoven and A. Endo, "TiEMPO: Open-source time-dependent end-to-end model for simulating ground-based submillimeter astronomical observations," in *Proc. SPIE, Millimeter, Submillimeter, and Far-Infrared Detectors and Instrumentation for Astronomy X*, J.,Zmuidzinas and J-R.,Gao, Eds., vol. 11453, Int. Soc. Opt. Photon. SPIE, online forum, Dec. 14–18 2020.

- C10.** A. Endo, K. Karatsu, Y. Tamura, T. Oshima, A. Taniguchi, T. Takekoshi, T. J. L. C. Bakx, J. Bueno, S. Brackenhoff, S. O. Dabironezare, S. Hähnle, R. Huiting, T. Ishida, R. Kawabe, K. Matsuda, K. Kohno, N. Llombart, V. Murugesan, [A. Pascual Laguna](#), M. Rybak, D. J. Thoen, P. P. van der Werf, S. J. C. Yates and J. J. A. Baselmans, “DESHIMA: Integrated superconducting spectrometer for ultra-wideband millimeter/submillimeter wave astronomy” in *Proc. of 33rd Int. Symp. Superconductivity (ISS2020)*, Tsukuba, Japan, Dec. 1–3 2020.
- C11.** [A. Pascual Laguna](#), K. Karatsu, A. Neto, A. Endo and J. J. A. Baselmans, “Sub-mm-wave superconducting on-chip filter bank for astronomy,” in *Proc. of 45th Int. Conf. Infrared, Millimeter, and Terahertz Waves (IRMMW-THz 2020)*, Buffalo, New York, USA, Nov. 8–13 2020.
- C12.** [A. Pascual Laguna](#), K. Karatsu, D. J. Thoen, V. Murugesan, A. Endo and J. J. A. Baselmans, “Wideband superconducting integrated filter-bank for THz astronomy,” in *Proc. 14th Eur. Conf. Antennas Propag. (EuCAP 2020)*, Copenhagen, Denmark, Mar. 15–20 2020.
- C13.** [A. Pascual Laguna](#), D. Cavallo, J. J. A. Baselmans, and N. Llombart, “Broadband beam-steering with focused connected arrays in quasi-optical systems,” in *Proc. 14th Eur. Conf. Antennas Propag. (EuCAP 2020)*, Copenhagen, Denmark, Mar. 15–20 2020.
- C14.** [A. Pascual Laguna](#), K. Karatsu, A. Neto, A. Endo and J. J. A. Baselmans, “Wideband sub-mm wave superconducting integrated filter-bank spectrometer,” in *Proc. 4th Int. Conf. on Infrared, Millimeter, and Terahertz Waves (IRMMW-THz 2019)*, Paris, France, Sep. 1–6 2019.
- C15.** [A. Pascual Laguna](#), K. Karatsu, A. Neto, A. Endo and J. J. A. Baselmans, “On the design of wideband sub-mm wave superconducting integrated filter-bank spectrometers,” in *Proc. 18th Int. Workshop on Low Temperature Detectors (LTD)*, Milan, Italy, Jul. 22–26 2019.
- C16.** M. Naruse, K. Karatsu, [A. Pascual Laguna](#), O. Yurduseven, D. J. Thoen, V. Murugesan and J. J. A. Baselmans, “Superconducting submicron-CPW resonators for on-chip THz filterbank,” in *Proc. 31st Int. Symp. Supercond. (ISS 2018)*, Tsukuba, Japan, Dec. 12–14 2018.
- C17.** A. Endo, K. Karatsu, Y. Tamura, T. Oshima, A. Taniguchi, T. Takekoshi, S. Asayama, T. J. L. C. Bakx, S. Bosma, J. Bueno, K. W. Chin, Y. Fujii, K. Fujita, R. Huiting, S. Ikarashi, T. Ishida, S. Ishii, R. Kawabe, T. M. Klapwijk, K. Kohno, A. Kouchi, N. Llombart, J. Maekawa, V. Murugesan, S. Nakatsubo, M. Naruse, K. Ohtawara, [A. Pascual Laguna](#), K. Suzuki, D. J. Thoen,

T. Tsukagoshi, T. Ueda, P. J. de Visser, P. P. van der Werf, S. J. C. Yates, Y. Yoshimura, O. Yurduseven and J. J. A. Baselmans, “DESHIMA on ASTE: First astronomical light captured with an integrated superconducting spectrometer,” in *Proc. Millimeter, Submillimeter, and Far-Infrared Detectors and Instrumentation for Astronomy IX*, SPIE Astronomical Telescopes + Instrumentation, vol. 10708, Austin, Texas, United States, Jun. 10–15 2018.

- C18.** A. Pascual Laguna, D. Cavallo, N. Llombart, J. J. A. Baselmans and A. Neto, “Focused superconducting connected array for wideband sub-mm spectrometers,” in *Proc. 12th Eur. Conf. Antennas Propag. (EuCAP 2018)*, London, United Kingdom, Apr. 9–13 2018.

Thesis Co-Supervised

- T1.** N.E. Beschoor Plug, “Towards on-chip superconducting phase shifters,” M.Sc. thesis, Delft University of Technology, Delft, the Netherlands, May 2021.

Propositions Accompanying the Doctoral Thesis

- I A tomographic view of the vast cosmic distances out to the early Universe can be mapped to the nanoscale structures of broadband on-chip filter-bank imaging spectrometers. This is ‘cosmo-nano-science’. (This proposition pertains to this dissertation.)
- II Low-loss microstrip technology is key for advanced on-chip solutions at terahertz frequencies. (This proposition pertains to this dissertation.)
- III Antennas in focusing quasi-optical systems improve their operational bandwidth by being placed out of focus. (This proposition pertains to this dissertation.)
- IV “Goed gereedschap is het halve werk” (“a good tool is half the work”) —Dutch saying. But a bad tool brings a good occasion to learn more.
- V “The real world relies on the intelligence of antifragility. (...) If there is something in nature you don’t understand, odds are it makes sense in a deeper way that is beyond your understanding. So there is a logic to natural things that is much superior to our own. (...) What Mother Nature does is rigorous until proven otherwise; what humans and science do is flawed until proven otherwise.” —*Antifragile*, N. N. Taleb.
- VI In a doctorate, the amount of relevant output and knowledge generated scales with the amount of supervision received; however, the abilities acquired as an independent researcher do so inversely proportional. The hard work remains a constant.
- VII Universities should protect and enforce the highest level of education and not degrade its quality due to extraneous forces.
- VIII The business model of most scientific journals is unjustifiably lucrative. A 2005 Deutsche Bank AG report referred to it as a “bizarre triple-pay” system, in

which “the state funds most research, pays the salaries of most of those checking the quality of research, and then buys most of the published product”. As long as scientific reputation is linked to those renowned journals, there is no easy way out of the system; not even with the intervention of research-funding institutions.

IX “All designs are wrong, it is just a matter of how wrong.” — E. R. Musk.
However, perfectionism immobilizes and frustrates in the asymptotic path to Knowledge.

These propositions are regarded as opposable and defendable, and have been approved as such by the promotores prof. dr. ir. J. J. A. Baselmans and prof. dr. ing. A. Neto.

Acknowledgements

This doctoral work would not have been possible without the support of many people who directly or indirectly participated of this dissertation. This work has been fruit of the synergetic collaboration between the Technology group, in SRON, and the Terahertz Sensing group, in the Delft University of Technology. Because of this cooperation, I have had the privilege to interact with great scientists of very diverse fields of expertise, leading to very rich interactions.

I want to start thanking my promotor, prof. dr. ir. Jochem J. A. Baselmans and prof. dr. ing. Andrea Neto, who supported me throughout the extend of this journey. I have learned a great deal from you two and I had fun talking with you. Jochem, thank you for trusting me to participate of the technological development of the MOSAIC and DESHIMA projects. I learn so much every time I talk to you. You are one of the most knowledgeable persons I know. The problem is that your mouth can keep up with the speed of your brain, so the mere mortals around you only dream of following your full train of thought. Your continuous support and our lengthy conversations, despite your busy agenda, have helped me a lot with the detailed technicalities as well as to reflect on the big picture. Andrea, I am very grateful to have had the opportunity to interact with you during these years. You inspired me to retake the dreaded path of electromagnetics I had abandoned years ago, and I am glad you did. You have been very supportive and helpful every time I needed expert engineering assistance, even for the ‘almost-embarrassing’ doubts. Your enthusiasm for research and deep knowledge of electromagnetics are admirable. Thank you both.

I continue thanking those who, despite their many other duties aside this project, always found some time to steer my efforts in a sensible direction: prof. dr. Nuria Llombart Juan, dr. Daniele Cavallo and dr. Angelo Freni. Nuria, I am tremendously grateful for our interactions. I have learned a lot from you, both technically and professionally. Your advice and energy have left a profound impression on me. Daniele, you always spot the root of my doubts and show me a way out of seemly unsolvable problems. I am truly grateful for your support, which has been instrumental to get where I am. Angelo, thank you for sharing your vast knowledge of electromagnetic theory with me, especially through your precise and neat explanatory notes.

I want to give special shout-out to the people contributing to the development of the filter-bank chips. Dr. Kenichi Karatsu, one of the best scientists in the group, who carefully scripted the mask-making of the filter-banks and patiently guided me through the measurements of the filter-banks. Dr. Akira Endo, who always manages to ask critical questions (a great thing!), proposes nice design ideas; and who taught me, among other things, how to simulate properly in Sonnet and how to convey a message with beautiful illustrations. Ing. David J. Thoen, who always knows somebody and some tool for the task, and whose clean-room magic, together with that of Vignesh Murugesan, provides us with impeccable sub-micron-featured devices. Thank you all!

I also want to thank dr. Marco Spirito, dr. Pascal Aubry for lending a hand and/or equipment for the experiments conducted in this dissertation.

Besides the many people that contributed directly to this work, a great amount of people helped making a nice work place, which at some point felt almost like a second home judging by the amount of hours spent there.

Special thanks to our amazing secretarial team, both at SRON and at the university. In particular, many thanks to Everdine M. C. de Vreede-Volkers, whose fantastic support through the years made everything run so smoothly at the university that we forgot how complicated things would be without her. I enjoyed very much our conversations, which are always a good occasion to practice our Dutch and Spanish (I am also forgetting the latter).

Although I mostly sat at the university, the people at SRON were always present and supportive. Dr. ir. Henk F. C. Hoevers, thank you for your kindness throughout this time, I look forward to meeting you more often in Leiden. Dr. Juan Bueno López, I enjoyed a lot our conversations (except those relating to our cherished CST), how you teach me complicated physical phenomena in engineering terms and even some of your jokes! Dr. ir. Pieter J. de Visser, I have to thank you for easing this poor engineer the understanding of concepts of superconductivity and MKIDs through your own dissertation. Ing. Robert Huiting, I am truly amazed by the detail level of your CAD drawings; no wonder why everything came together nominally in the ASTE telescope. Dr. Stephen J. C. Yates, our optics expert in SRON. I need to thank you in particular for the chopper design of DESHIMA, as I think my filter-bank designs have part of the ‘culprit’ for making the wheel spin so fast.

My (long) days at the office in the university became more enjoyable with the company of great office mates and fellow graduate students aboard the same boat. These bunch of souls would become true friends through the years. I miss our fun pre-Covid times in the office; but also outside at conferences, bars, house parties, etc.

I want to start by thanking those in my office (at least until the recent EWI havoc), as we have de facto shared a large part of our lives over the last five years. Dr. ir. Shahab O. (van) Dabironezare, with whom I enjoyed cracking (edgy) jokes, having nice conversations and from whom I also learned a lot (about quasi-optical systems). Soon-to-be dr. Sebastian Hähnle, with whom I shared nice conversations,

both technical and personal, with the excuse of hydrating. There are so many ways in which my thesis has benefited from your work, and for that, I am also grateful. To name a few: low-loss microstrips, automated mask-making and a wide opening angle cryostat, also known as the ‘the Beast’. Dr. Cristina Yepes, our adopted office mate who brought, together with her inseparable buddy dr.ir. Harshitha Thippur Shivamurthy, new energy and plenty of laughter to our office. Dr. Paolo M. Sberna, with whom I had the whole spectrum of conversations, with a strong bias towards ridiculously funny interactions. Ir. Riccardo Ozzola, who was brave enough to substitute *calcio storico* for golf, and *fiorentina* for *kroket*. Although shortly, I also had the chance to meet ir. Nuri van Marrewijk and ir. Andrea Degasperi, who mustered confidence to change paths. I hope you are doing fine.

Those who were not in my office, also made a huge impact during these years. Dr. Marta Arias Campo, you are a great professional and a wonderful person. Thank you for all the conversations and fun times together. I wish we could live closer by. The same goes for dr. ir. Sven L. van Berkel, who left to one of the places we only dream of, the Jet Propulsion Laboratory. I had a lot of fun and great conversations with you, including the one that made up my mind to come to the group. The younger bunch also brought lots of nice interactions which I cherish. Ir. Arturo Fiorellini Bernardis, who teaches us how to maximize the gains, both from spherical antenna domains as well as from training sessions. Ir. Sjoerd Bosma, who always keeps us updated of interesting reads, conferences, as well lunch or beer time. Ir. Ralph M. van Schelven, who apparently can mountain-bike faster than I do (TBC). Ir. Huasheng Zhang, thanks to whom I do not need GRASP or impossibly long CST simulations. Ir. Sander(s) J. van Katwijk, our IT expert and fellow feeding network sufferer thanks to whom I will never ran out of RAM (let us say because of the efficient Matlab functions I borrowed from you). Ir. Kevin Kouwenhoven, who is apparently as good at stacking layers for LEKID’s as for cakes. Ir. Bruno T. Buijtendorp, who deposits the best a-Si(C) films on the planet. Ir. Steven de Rooij, our advocate for open science, who kindly translated the summary of this thesis into Dutch. Ir. Nina E. Beschoor Plug, who was the first student I worked with. Nina, I really enjoyed our interactions and it was a pleasure to supervise your work because the learning was bidirectional. Furthermore, we share the hobby of mountain-biking, so you default to a VIP list.

I cannot forget to acknowledge the former senior Spartans of the Terahertz Sensing group. Dr. Waqas H. Syed, my daily supervisor during my internship in the first days with the group, a ‘mere’ six years ago. Dr. Giorgio Carluccio, the friendliest and most helpful low-profile genius. Dr. Erio Gandini, a wizard of optics and super fun company. Dr. Ozan Yurduseven, unbeatable runner and the reason why I often backup my files. And finally, my great friends and (spicy-)food lovers dr. Alessandro Garufo and dr. Darwin J. Blanco. I am especially grateful for all the fresh energy and cohesion that Darwin infused in the group when he arrived, as well as for becoming my gym buddy for all sorts of funnily-named lessons I shall not spell out here.

Wonderful people have passed by the group during these years. Luckily, our group has recently grown with the incorporation of the brilliant minds of dr. María Alonso del Pino, dr. Mátus Rybák and new master and Ph.D. students. I look forward to interacting with all of you soon.

I will also remember the ‘cadeautjes’ we received periodically from dr. Ioan (Hansi) Lager and dr. Daniele Cavallo. Somehow, despite all the frustration these infused on me, the tedious task of correcting exams managed to give me some occasional laugh out of ‘mathematical desperation’ and a great occasion to keep the basics in-line.

A big part of my life over the last years has been devoted to this work, but it is thanks to those in the ‘outer world’ that I gathered true quality time. To them I extend my gratitude and an apology for being physically/mentally absent at times.

I would like to acknowledge those who made the Netherlands a nice place to live in. In the beginning there was Alex and my Erasmus friends Jeske and Sanne, who introduced me to the country of the windmills and canals. Rosario, Sid, Álvaro and Ela joined soon afterwards, leaving very cherished memories in me. More recently I have enjoyed the friendship of Daniel, Natalia, Laura, Giannis, Carlos, Elisa and all the NACO team. Because of the rainy and gloomy weather of the Netherlands, we tend to spend a lot of time at home. Housemates become then our true daily companions. Stefan, Elgar, Nasim, Mario Alberto; I keep great memories with you all. Mario, I learn a lot from you; Alberto, I enjoy your company.

Finally I would like to come back *home*.

I want to dedicate a few words thanking my (almost) lifelong friends: César, Dani, Javi, Carlos, Sole, Rebeca, Alejandro, Lumbrieras, Andrés, Otero. A pesar de vivir tan lejos, nuestra amistad se mantiene inmune al tiempo y la distancia. Gracias por ello y por hacerme sentir un ‘gato maragato’.

To my lovely girlfriend, Ángela, who interestingly was the first person I met in the Netherlands. Gracias por tu amor y comprensión durante los altibajos de estos años. Aprendo mucho de ti y me ayudas a mantener los pies en el suelo. Gracias por tantas cosas... Te quiero.

To the family overseas: Ángela, Fernando y Daniel. Gracias por hacer que me sienta como en mi propia casa con vosotros.

To my family. En especial a mis padres, Juan Antonio y Yolanda, que me lo han dado todo. Gracias por haber apoyado y facilitado todas mis decisiones para haber llegado a donde estoy hoy. A mis hermanas, Marta e Inés, que tan bien me conocen y con las que tantos buenos recuerdos guardo. A mis tíos, primos y abuelos, también a los que ya no están. Soy muy afortunado de tener una familia como vosotros, tan cercana y cariñosa. Os quiero y os echo mucho de menos.

*Alejandro Pascual Laguna
Delft, August 2021*

About the author



Alejandro Pascual Laguna was born on August 22nd, 1992 in Madrid, Spain. He received the B.Sc. degree in telecommunications engineering from ICAI School of Engineering, Universidad Pontificia Comillas, Madrid (Spain), in 2014. During the last year of his bachelor's degree studies, he spent a year at Chalmers University of Technology, Gothenburg (Sweden). In 2016 he received the M.Sc. degree (cum laude) in Electrical Engineering from Delft University of Technology, Delft (The Netherlands).

Since December 2016 he has been with SRON Netherlands Institute for Space Research working towards the Ph.D. degree from the Delft University of Technology. During this time, his research interests included on-chip solutions for efficient broadband sub-mm wave imaging spectrometers based on Kinetic Inductance Detectors. This research has been carried out under the supervision of prof. dr. ir. J. J. A. Baselmans and prof. dr. ing. A. Neto as promotors. The research has resulted in 5 journal publications and 18 contributions at various international conferences. During his Ph.D. he has co-supervised one M.Sc. student in the THz Sensing group.

